Flame Propagation in a Straight Duct with a 90° Curved Section

by

Gordon Macrae McAlary

A thesis submitted to the Department of Mechanical Engineering

in partial fulfillment of the requirements for the degree

Master of Science (Engineering)

Queen's University

Kingston, Ontario, Canada

May, 1999

Abstract

Work was performed to commission a flame propagation duct with an attached 90° bend. This work included the testing, fabrication and installation of associated hardware and flame detection instrumentation.

A testing program was initiated to investigate flame propagation in the duct utilizing propane/air mixtures. The testing program entailed the characterization of flame front propagation at subsonic velocities. This work also included the detailed study of the interactions of the propagating flame front and secondary flows developed in the 90° bend. These secondary flows were the result of the induced motion of the unburned gas ahead of the flame front.

The results from this investigation indicated that flame propagation in the straight inlet section of the duct was characterized by distinctive velocity variation patterns for lean and very rich mixture conditions. For slightly rich mixtures, the flame propagation velocities were relatively steady, however a velocity variation pattern was still discernible.

ii

Acknowledgments

I would like to thank my supervisor, Dr. Andrzej Sobiesiak for his guidance and financial support in the undertaking of this project. I also would like to extend my thanks to certain individuals who provided help in various tasks associated with my research. Andy Bryson, Geoff Brooks and John Garner for help in various machine shop duties and gas bottle acquisition and disposition. Mark Cunningham, Allan McPhail and Dr. Darko Matovic for suggestions on circuit designs and instrumentation arrangements. Dr. Carolyn Small for the use of her LECROY oscilloscope. Dave Smith and his crew at Queen's TV (QTV) for their help in image processing. Etta Cerisano, Gayle Laporte, Barb Higgins, Jackie Paquin, and Barbra Brousseau for help in keeping my paperwork associated with suppliers, and department and university affairs in order.

The financial support of this research project by the Natural Sciences and Engineering Research Council, School of Graduate Studies and Research and the Department of Mechanical Engineering at Queen's University is gratefully acknowledged.

I would like to express my thanks to the numerous friends and colleagues that I have met during my stay in Kingston. A special thanks go to my office colleagues, past and present, Jamie Wentzell, Paulo Pagot, and Stu McIlwain.

Finally, this work could not have taken place without the support and love of my family. This includes my distant cousins the Robison clan in Napanee, for whom I've come to know quite well and have enjoyed many happy occasions with during the past two and half years.

Table of Contents

List of Figures

List of Tables

Nomenclature

A	area (m^2), or mass of air (kg)
a	hydraulic diameter of FPD (m)
c_p	specific heat at constant pressure (J/ kg-K)
D	mass diffusivity (m^2/s)
D_h	hydraulic diameter (m)
Dn	Dean number
E	activation energy (J/kg)
F	mass of fuel (kg)
H, h	duct height (m)
L	spacing between photodiodes (m)
ΔL	differences in photodiode detection length (m)
Le	Lewis number ($Le = \alpha/D$)
MW	molecular weight (kg/kg-mole)
n	number of moles
P_{fuel}	fuel pressure (kPa)
P_{tot}, P_{TOTAL}	total mixture pressure (kPa)
Q	thermal energy (J/kg)
R	gas constant (J/kg-K)
R	mean radius of bend (m)
R_i, r_i	inner radius of bend (m)
R_o, r_o	outer radius of bend (m)
Re	Reynolds number
S_F, S_{FLAME}	flame propagation velocity (m/s)
ΔS_F^P	flame propagation velocity error due to differences related to detection measurements (m/s)
ΔS_F^ϕ	flame propagation velocity error due to differences related to mixture composition (m/s)
S_L	burning velocity (m/s)
t	time
Δt	time difference (s)
T	temperature (K)
T_b	burned gas temperature (K)
T_u	unburned gas temperature (K)
U_u, S_{mix}	unburned gas velocity with respect to duct (m/s)
V	velocity
$\dot{W}$	reaction rate (J/kg-s)
W, w	duct width (m)
x	mole ratio
Y	mass fraction of a species
Y_r, Y_u	mass fraction of a reactant species, or unburned gas

α	thermal diffusivity (m^2/s)
δ, R/a	curvature ratio
ϕ	equivalence ratio
μ	viscosity ($N\text{-}s/m^2$)
v_u	velocity of unburned gas (m/s)
v_b	velocity of burned gas (m/s)
ρ	density (kg/m^3)
ρ_b	density of burned gas (kg/m^3)
ρ_u	density of unburned gas (kg/m^3)
τ_c	elastic collision time (s)
$\tau_r(T)$	characteristic reaction time (s)

Abbreviations

CCD	Charge-Coupled Device
DC	Direct Current
EMI	Electromagnetic Interference
FPD	Flame Propagation Duct
fps	frames per second
LDV	Laser Doppler Velocimetry
RTV	Room Temperature Vulcanizing
SCR	Silicon Controlled Rectifier
VAC	Volts, Alternating Current

Chapter One

Introduction

1.1 Objectives

The subject of this thesis is to detail the experimental work conducted with a newly fabricated, but untested Flame Propagation Duct (FPD). The objectives of this work were two-fold. The first objective was to complete the work necessary for the commissioning of the FPD. Attendant to this work was the development of the associated equipment, instrumentation, signal processing circuitry and testing techniques needed for satisfactory operation of the FPD apparatus. The second objective was to experimentally investigate flame propagation in bends utilizing the FPD. The investigation involved the characterization of flame front propagation through the straight section of a duct, and the effect of downstream flow structures on the flame front as it traveled through a 90° bend.

1.2 Description of Problem

The FPD used for these experiments was comprised of a long straight section, a 90° bend, and a shorter, straight exit section attached to the back end of the bend. The FPD was filled with a combustible mixture of propane and air at atmospheric pressure and temperature and left to rest. The mixture was ignited at the closed end of the long straight section, while the exit section was left open to the atmosphere. After ignition, a flame front propagated down the straight section into the bend. The volume expansion of the burned gas induced the motion of unburned gas ahead of the flame front. Studies in laminar fluid flow through a curved duct indicated secondary flows in the form of torroidal vortices would evolve. These vortices would develop not only in the bulk flow (Dean vortices), but also in the boundary layer on the concave surface of the curve (Görtler vortices). It was postulated that these types of vortex structures would be present in the unburned gas flow by the time the flame front approached the bend. When the flame front reached this disturbed portion of flow, stretching and folding of the flame front by the vortical fluid motion would result in a considerable distortion of the flame. These effects of the flame front and vortex interactions constituted the investigative work associated with the second objective.

1.3 Previous Work

Initial work in this area of research was conducted by Sato, Sakai, and Chiga [1]. A high speed camera was used to determine the flame propagation velocities through a straight inlet section and 90° bend. Schlieren techniques and a timeline tracer method were used in conjunction with the camera to visualize the flow of the unburned gas ahead of the

flame front. They also performed numerical studies using an incompressible, two-dimensional, cold-flow model without combustion.

For a closed inlet and open outlet configuration, Sato *et al.* concluded that flame fronts become distorted as they propagate into the bend along or close to the inner wall. Subsequent timeline tests, as observed and numerically simulated, closely approximated the deformed shape of the flame fronts. Experiments to determine flame front propagation velocities indicated that the flame fronts accelerate through the bend regardless of the mixture composition. Sato *et al.* attributed these bend effects to the flow conditions of the unburned gas preceding the flame front.

1.4 Differences from Other Work

The investigation detailed in this thesis differs from Sato *et al.* in two ways. First, the experimental FPD apparatus used for this investigation was of a much larger scale. The Sato apparatus had a 2 cm x 2 cm square duct cross section. A 10 cm straight section was attached to the front of the bend and a 20 cm length was attached behind the bend. The FPD in this investigation had a rectangular duct cross section of 5.08 cm x 2.54 cm. The straight, inlet section ahead of the bend was 1.67 m. The straight exit section after the bend had a length of 30.5 cm. The curvature ratio (δ) was different for both ducts. The duct used by Sato *et al.* had a curvature ratio of 1.0 while the FPD used in this study had a curvature ratio of 2.25.

Second, Sato *et al.* did not explicitly refer to secondary flows. They only made mention of an undefined, "rotating forced flow " in the duct bend. Experiments undertaken in this investigation were conducted with the aim of providing evidence that secondary flows affect flame front propagation in a bend.

1.5 Applications

Most flame propagation studies have concentrated on detonations. Many of these involved the use of shock tubes. Flame propagations at subsonic velocities, or deflagrations can occur as initial and transition stages in the development of detonation waves. Although this was a deflagration study, the results are applicable to a number of subjects. Chief among these being deflagrations and transitions to detonations in pipe networks. For instance, many pipe networks in industrial settings utilize components such as tees, elbows and valves. Gas pipelines and pneumatic grain ducts are just two examples of pipe networks which transport combustible components. If the right reactant concentrations and appropriate ignition conditions are present, it is possible that initially slow flame front propagation may transition to detonation. This may lead to catastrophic results such as destruction of property and possible loss of life. It is of interest to know if the geometry of the pipe network contributes to flame quenching or acceleration.

The results of these experiments also have some application to the design of internal combustion engines. Within the cylinder environs of a spark ignition engine, a homogeneous mixture of fuel and air exists prior to ignition. At ignition, a flame kernel develops which begins to progress outward through the combustible mixture in the form

of a flame front. If a shaped engine head (i.e. one with convex and concave surfaces) is used, the contours will have an effect on the flame front propagation velocity and flame front profile.

Another application of this research is in the design of flame arresters. Most flame arresters typically quench flames through the use of configurations which restrict flame propagation. These devices use small passages to break down a large flame front into many smaller ones. Inside these passages, thermal energy is rapidly removed from the combustion reactions. This leads to reduced flame propagation velocities.

Results from this investigative research have shown that for some conditions, flames are quenched in the FPD bend. This leads to the possibility that the use of bends or corners similar to the FPD configuration may result in another method to quench flames.

1.6 Experimental Approach

The approach used through the course of the experiments involved determining flame propagation velocities primarily by use of photodiodes. Individual tests were performed for a number of different propane and air mixtures. As the development of secondary flows was dependent on unburned gas velocity, the flame propagation velocities on entrance into and through the bend were used to indicate the development of secondary flow structures in the bend.

Schlieren diagnostics and a timeline tracer method were used to visualize the initial development of the secondary flow structures. A high speed digital camera was utilized for recording flame front behavior and timeline progression in the bend.

Features of this project included the fabrication and use of custom designed circuits for photodiode signal processing and time delays for the timeline tracer method. Another aspect was to use equipment that could easily be modified or fabricated for use in the experiments. This was shown in the construction of circuits using inexpensive, off-the-shelf components, and the modification of an existing thermocouple time constant tester for excitation of the time line tracer wires.

The use of these devices and the development of testing techniques and procedures provided a starting point for project work with the FPD. In the course of testing, capabilities and limitations of the equipment and instruments were quickly discovered. An important limitation was the fact that the photodiodes used were only sensitive to the visible portion of light. Other photodiodes were tried but results were even poorer. This necessitated the development of an indirect lighting technique in order to get acceptable signals from the photodiodes when faint flame fronts were produced.

1.7 Organization of Thesis

The following chapters detail various aspects of the project.

Chapter 2: details the theory involved with flame front propagation through a straight duct and a flow in a bend.

Chapter 3: discusses the various apparatus used in testing and the procedures developed for the experimentation regime.

Chapter 4: presents the results.

Chapter 5: discusses the results.

Chapter 6: communicates the conclusions drawn on the testing and the proposed recommendations should future work be carried out.

Chapter Two

Literature Review and Theory

2.1 Introduction

Flame propagation in a curved duct encompasses several individual phenomena. These phenomena include; laminar flame propagation, premixed combustion, secondary flow development in a bend, and flame and flow structure interaction.

2.2 Premixed Combustion Process

Although it was not within the scope of this investigation to detail the actual mechanisms of premixed flame combustion, a summary of pertinent combustion theory with reference to premixed flames and flame front propagation is merited.

Premixed combustion is a complex process involving heat transfer, chemical kinetics, and fluid flow. The process is governed by the mass, momentum, energy, and species laws of conservation. The equation of state is also necessary. Clavin [2] utilized a simple, one-

step model describing the exothermic, irreversible reactions of combustion. This model is summarized below:

$$\text{Reactants} \rightarrow \text{Products} + \text{Heat release} \qquad (1)$$

$$\dot{W} = - \rho_u Y_r / \tau_r(T) \qquad (2)$$

$$\text{where:} \qquad \tau_r(T) = \tau_c \exp(E/RT)$$

$$T_b - T_u = Q Y_u / C_p \qquad (3)$$

Equation (1) describes combustion as a process in which the reaction between two or more fuel and oxidant species results in the creation of product species, and the liberation of heat energy. The rate at which these reactions take place is shown as the global reaction rate in equation (2). The global reaction rate is a function of mass concentration, density of the reactant species and a characteristic reaction time which in itself is dependent on the elastic collision time (τ_c), and temperature of the reaction. A high reaction rate is therefore characterized as having a small characteristic reaction time and a high reaction temperature. If the reaction temperature remains high and a sufficient quantity of reactant species remain available, then the combustion process becomes self-sustaining. Excess energy not necessary to keep the global reaction rate high, is released as heat. As shown in equation (3), this is manifested as an increase in temperature of the product species.

2.3 Flame Propagation

In the context of a self-sustaining combustion zone, reactants must continually be brought into the localized reaction area and products discharged. In a deflagration, the reactant

and product flow velocities are subsonic. The combustion zone itself is referred to as a flame front which can be either stationary or moving. For constant pressure combustion, the equation of state dictates that the density of the products is less than the density of the reactants. If the flame front is used as the Lagrangian frame of reference, then given a constant cross sectional area, continuity requires that the velocity of the product species (v_b) is greater than the velocity of the reactant species (v_u).

$$\rho_u v_u A = \rho_b v_b A \qquad (4)$$

If the frame of reference is now removed from the flame front and replaced by the unburned gas flow, then continuity is preserved and the (v_u) term is replaced by the velocity of the advancing flame front. This velocity is defined by Shepherd and Lee [3] as the burning velocity (S_L) of the flame front. For propane and air mixtures, the maximum burning velocity is 44 cm/s. The burning velocity is lower for fuel lean and fuel rich mixtures.

Figure 2.1 shows a simplified arrangement of a propagating flame front in a duct. The starting point of the flame front is at the ignition point near the closed end of the duct. The other end of the duct is open.

Upon ignition, a flame kernel forms near the ignition source. Since the unburned gas is initially stagnant, the flame front must move in order to preserve continuity. Consequently, the kernel expands outward until it reaches the duct walls. Further

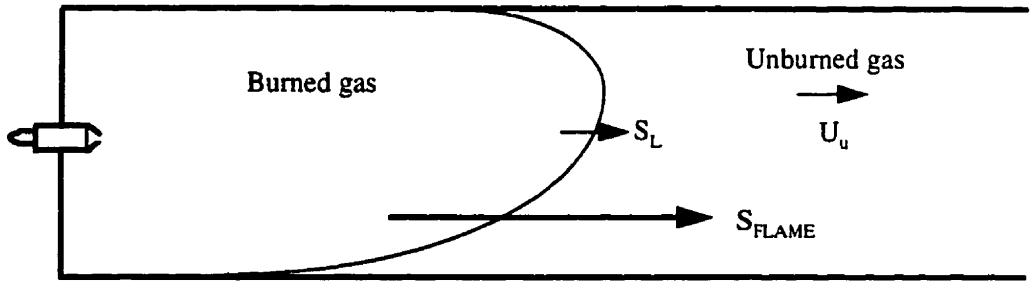

Fig. 2.1 Propagating flame front in duct.

expansion only occurs in the direction of the unburned gas. The burning velocity is dependent only on mixture composition, pressure and temperature. Due to the one-end open configuration of the duct, there is an even pressure distribution across the flame front interface. Therefore, the burned gas volume is greater than the unburned gas it displaces. This makes itself evident as a displacement of the unburned gas towards the open end of the duct.

As the flame front begins near the ignition point, the unburned gas which was initially stagnant, now begins to accelerate in the direction of the open end of the duct. Using the duct as the Eulerian frame of reference, the observed flame front propagating through the duct has a flame propagation velocity (S_{FLAME}) at any discrete moment composed of two components. These components being the burning velocity (S_L) and the velocity due to the expansion of the burned gases. The induced movement of the unburned gas is related to the flame propagation velocity by the following equation.

$$v_u = (\rho_b / \rho_u) (S_{FLAME} - S_L) \qquad (5)$$

It is possible for a flame front propagating in a horizontal duct to have a planar shape, however it is an unstable state. Generally, wall effects and convection tend to distort the flame front shape. Previous studies as discussed by Matalon and Metzener [4], show that a hydrodynamic instability is formed across the flame front due to the density gradient between the burned and unburned gases. This instability is also referred to as the Darrieus and Landau instability. The instability results in the flame front becoming asymmetrically curve shaped with the convex leading edge oriented in the direction of flame propagation.

2.4 Flow in Curved Ducts

Flow in curved ducts has been extensively studied by numerous researchers. Most of the research has involved the study of secondary flow formations in bends. These secondary flows are a consequence of centrifugal flow instabilities. The Rayleigh's circulation criterion states that for a flow instability to exist, the following empirical condition must be satisfied:

$$d[(rV)^2]/dr < 0 \qquad (6)$$

This is schematically shown in Fig. 2.2, where fluid flows through a bend with a convex inner radius and concave outer radius. In this situation near the outer surface of the bend, an incremental increase outward in the positive radial direction results in a negative velocity gradient. Consequently, the Raleigh criterion is satisfied and a region of unstable flow develops along the outer wall of the duct.

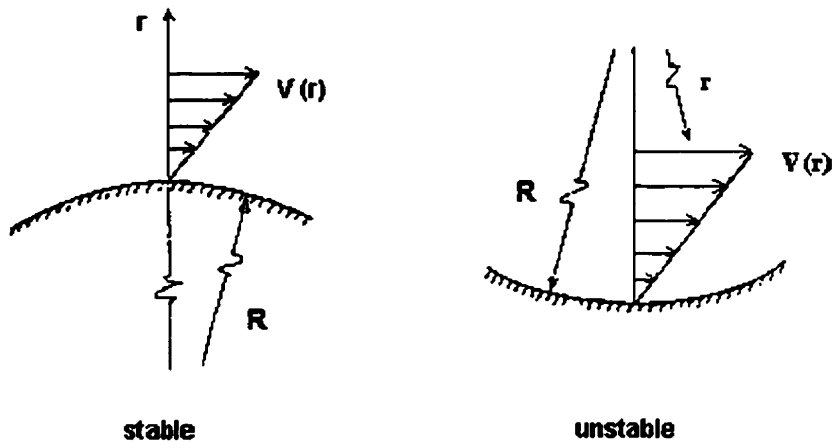

Fig. 2.2 Conditions for the development of flow instabilities. (Saric)

The secondary flow structures developed from the instabilities are characterized as a pair of symmetrical, counter-rotating vortices oriented in the flow direction. At higher bulk flow velocities, it is also possible to form structures with four or even six vortices. These vortex structures are classified as Dean vortices and are depicted in Fig. 2.3. Dean vortices have been studied experimentally by Humphrey *et al.* [5], Hille *et al.* [6], and Bara *et al.* [7]. Numerical modeling has been conducted by not only these researchers but also by Pratap and Spalding [8], Hassager *et al.* [9], and Soh [10].

Dean vortices develop in the bulk volume of the flow. However, similar streamwise-oriented, counter-rotating structures also develop within the boundary layer of the flow along the concave surface of the bend. Here again, the secondary flow vortices develop due to the instabilities resulting from the same conditions shown in Fig. 2.2. These boundary layer instabilities also satisfy the Raleigh criterion. The resulting smaller scale

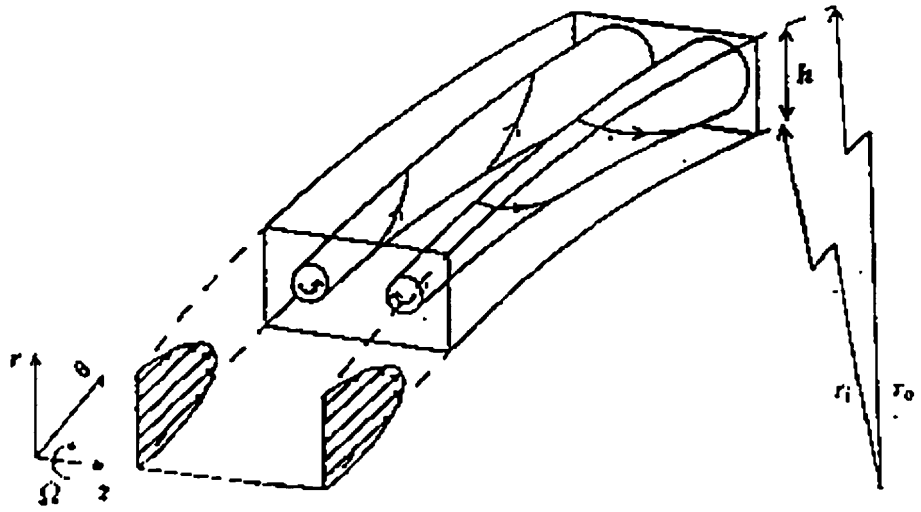

Fig. 2.3 Dean vortices in bend.

vortices are generally classified as Görtler vortices, and unlike Dean vortices, develop in multiple side-by-side arrangements as shown in Fig. 2.4.

Curved duct flow is characterized by two parameters. These parameters are the Dean number and the curvature ratio. Various researchers have promoted many variants of the

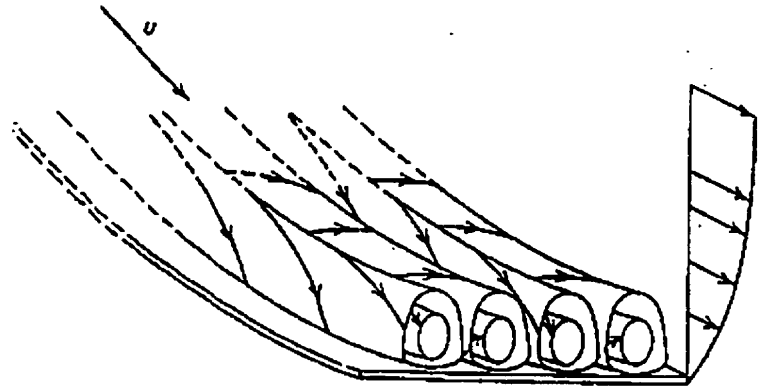

Fig. 2.4 Görtler vortices along concave surface of bend. (Saric)

definition of the Dean number. For the purposes of this thesis, the following definition is used.

$$Dn = Re / (R/a)^{0.5} \qquad (7)$$

In this equation, Re is the Reynolds number and (R/a) is the curvature ratio. In the present work, (R) is considered the mean radius of the duct (R = 7.62 cm), and (a) is the characteristic length as defined by the hydraulic diameter (a = 3.39 cm).

The Dean number is a measure of the magnitude of the secondary flows which are the result of the interactions of inertia, centrifugal and viscous forces. Understandably, for very slow flow velocities or large curvature ratios (slight curvature), development of Dean vortices does not occur. Figure 2.5 shows the development of Dean vortices in water flow through a square duct. Experimental results by Bara *et al.* [7] showed that with increasing Dn numbers, the Dean vortices fully evolved within a smaller arc of the bend.

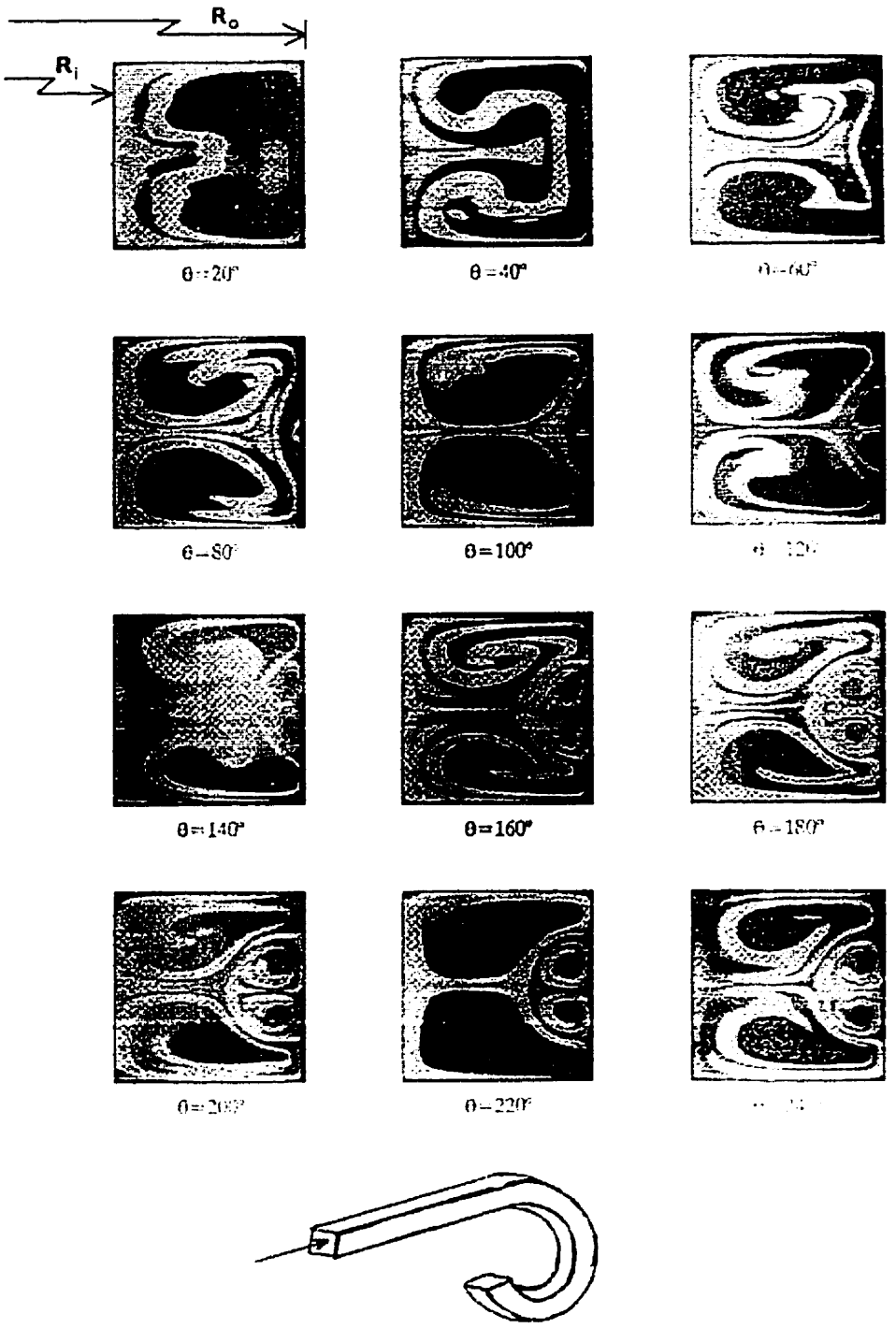

Fig. 2.5 Development of secondary flow structures in a bend. Dn = 149.9. (Bara)

Berger *et al.* [11] summarized the findings of flow in curved pipes by other researchers. This extensive summary detailed Dean vortices for many flow conditions.

2.4.1 Small Dean number regime

For the present FPD apparatus, the small Dean number regime was comprised of flows in the bend of Dn < 64. In this regime, previous studies have indicated that the core flow of fluid with the maximum axial velocity moves slightly off-center towards the outer surface. This is due to the centrifugal forces exerted on the fluid. A slight positive pressure gradient develops between the outer and inner surfaces. The result is that fluid near the walls begins to move from the outer bend region to the inner bend region along the duct perimeter. This causes fluid near the inner bend region to be directed to the outer bend region through the center of the duct perpendicular to the primary axial flow. These secondary flow movements form the basis of Dean vortices. The centers of the Dean vortices are approximately located along the axial centerline of the duct.

2.4.2 Intermediate Dean number regime

The intermediate Dean number regime encompassed those flows in the FPD bend in the approximate range of 64 < Dn < 400. Previous studies have indicated that the core flow of fluid moves further outward towards the outer surface of the bend. The pressure gradient becomes greater and the resulting symmetrical Dean vortices become stronger. With increasing Dn number, the centers of the Dean vortices move further radially toward the outer surface. Secondary boundary layers begin to form, and intermixing with the axial boundary layers becomes more pronounced. The axial boundary layer near the outer surface may contain Görtler vortices.

2.4.3 Large Dean number regime

The large Dean number regime encompassed the remaining attributes of secondary flow development of laminar flows through the FPD bend up to approximately Dn = 3333. In this regime, previous studies have indicated that the core flow increases in axial velocity, the core flow and centers of the Dean vortices continue to move towards the outer surface. However, there is a limit to these outward movements as the axial and secondary boundary layers remain. The increased circumferential forces cause thinning of the boundary layers near the outer bend surface. This further promotes intermixing of fluid between the core flow, axial and secondary boundary layers, resulting in further strengthening of the Dean vortices. With the movement of the Dean vortices closer to the outer bend, the secondary boundary layer near the inner surface of the bend thickens.

At higher Dean numbers, the development of an additional smaller set of Dean vortices can occur in the region of the outer bend. Other studies have shown that six-vortex structures can also develop.

2.4.4 Entry flow

The core flow of fluid into a bend is considered inviscid. The effects of the development of secondary flow are mainly seen in the boundary layers. As the secondary boundary layers grow, the core flow is seen to constrict. This results in the acceleration of the core flow into the bend.

For all Dean number values, this idealized view of developing flow remains valid to a distance into the bend of O(a). Numerical studies have indicated that there is a crossover point in the bend where the location of largest wall shear changes from being on the inner bend surface to being on the outer bend surface. The wall shear is initially greater near the inner wall since the boundary layer in this region is thin. This is due to the shorter wall length compared to the outer wall length. However, at some later point, the wall shear near the outer bend becomes larger. This is in part to the movement of the core flow towards the outer surface and the resultant thinning of the boundary layer. With increasing Dean number, this crossover point moves closer to the entrance to the bend.

For large Dean number, the centrifugal, inertia and viscous effects balance within a distance of $O((aR)^{0.5})$. Furthermore, the magnitude of the secondary flow begins to increase. The outward displacement of the core flow becomes more of an effect of the secondary flow rather than the core flow itself. This causes a high pressure region to develop with the result being that the secondary boundary layers continue to remain thin relative to the thick inner boundary layer.

2.4.5 Entry conditions

Researchers have implemented different entry conditions for their experimental, analytical and numerical investigations. These conditions have included (1) uniform axial velocity, (2) straight pipe Poiseuille flow, and (3) uniform total pressure. However,

experimental results have indicated that regardless of inlet conditions in circular pipes, the flow rapidly evolves into a potential vortex structure with the maximum axial velocity near the inner surface. This occurs before the curvature effects of the bend influence the flow development. Bara *et al.* (7) experimented with a square cross-sectioned duct in which the maximum axial velocities were observed near the outer surface. Therefore, the potential vortex structure may not exist in ducts of square or rectangular cross-section.

2.4.6 Unsteady laminar flow (Developing flow)

In a bend of defined length, developing flow is almost always the characteristic flow condition. This is the flow condition which describes the unburned gas flow in the tests conducted for this experimental investigation.

Numerical investigations have indicated that in developing flow, the skin friction in the boundary layers increases when the flow is accelerating. The opposite occurs when the flow is decelerating. As a result, in the inlet section of the bend where fluid flow is accelerating, the maximum wall shear crossover point is extended further into the bend relative to steady flow.

2.4.7 Finite bend

As previously mentioned, the development of secondary flows in bends results in pressure variation between the inner and outer bend regions. Previous studies have

shown that in a 90° bend, such as the one used on the current FPD, the maximum pressure gradient occurs at 45°. The inlet of the bend experiences a pressure gradient of approximately 40 - 50% of the maximum. At the bend exit, the pressure gradient is 20-40% of the maximum. This indicates that the secondary flow structures influence the flow upstream and downstream of the bend.

2.4.8 Turbulent flows

The development of secondary flow structures in bends occurs for flows of turbulent nature. These flows are characterized by Dean numbers greater than those for laminar flows. Numerical and experimental investigations by Humphrey *et al.* [12] and Taylor *et al.* [13] have indicated that the effects of high Reynolds number flows in bends are similar to those of laminar flow.

The high flow velocity in turbulent flow causes large shearing stresses in the boundary layers. However, the stabilizing effect of the inner surface region reduces the turbulence energy in the boundary layers at these locations. The destabilizing surface along the concave outer bend intensifies turbulent energy. The result of secondary flows is that fluid is continuously exchanged between these two regions of the duct. This hinders the development of larger scale turbulent structures in the flow.

2.5 Interactions of Vortices with Flame Fronts

Previous investigations of flame front and flow vortex interactions have been centered around the study of turbulent effects on flames, Lee and Santavicca [14]. These interactions are also important to the mechanisms leading to detonations. These investigations have entailed flame front propagation into vortices in the direction parallel to the vortex axes. However, in the case of flame propagation in a bend, the flame front direction is parallel to the axes of the secondary flow vortices.

Shepard and Lee [3] have disclosed that for moderate flame velocities, the interactions by flames and vortices result in stretching and folding of the flame fronts. Furthermore, with strong vortices, it is possible for the flame front to be further stretched by becoming entrained in the vortices. If the strain on the flame front is large, then the flame front may be quenched in the interior of the vortices.

A numerical study by Lee and Santavicca [14] has indicated that for counter-rotating vortices, the vortex tangential velocity and to a lesser extent, vortex size dictate the effects of interactions. For example, if the vortex tangential velocities are O(2) higher than the burning velocity, then the flame front can be stretched and wrapped completely around the vortices creating reactant pockets.

2.6 Summary of Events in the FPD Under Investigation

From the literature review, theory, previous work cited and experience, the following sequence of events occurs.

1). A quiescent combustible gas mixture is introduced into a duct and allowed to stabilize at atmospheric conditions.

2). The duct end near the bend is opened. At the closed end, a spark is used to ignite the mixture. A flame front develops. This flame front extends across the cross sectional area of the duct and shortly thereafter begins to propagate in the direction of the unburned gas.

3). Thermal expansion of the burned gas products begins to drive the unburned gas ahead of the flame front. Sustained combustion causes the acceleration of the burned gas to some maximum flow velocity.

4). The transient nature of the flame propagation and unburned gas flow causes the gas to go through the laminar, transition and possibly turbulent flow regimes. The unburned gas flow results in the development of secondary flows in the bend.

5). When the flame front has propagated to the inlet to the bend, the secondary flow structures interact with the flame front. The interactions may possibly cause distortion and stretching of the flame front.

Chapter Three

Experimental Apparatus and Procedures

3.1 Introduction

This chapter describes the apparatus utilized and the procedures developed to undertake this research program. Aspects pertaining to construction, modification and commissioning activities are discussed more in detail in appropriate appendices.

3.2 Flame Propagation Duct

A schematic of the major test apparatus components is shown in Fig. 3.1. The main piece of equipment was the Flame Propagation Duct (FPD). A photograph of the FPD is shown in Fig. 3.2. The FPD had a constant rectangular cross section, H = 5.08 cm x W = 2.54 cm, through both the straight and curved sections. The straight inlet section was 168 cm in length. The exit section after the bend was 30 cm in length. The 90° bend had internal and external radii of 5.08 cm and 10.16 cm respectively. This resulted in a curvature

ratio of 2.25. The sides of the straight section were fabricated from 12.7 mm thick clear Plexiglas panels. Glass panes 6 mm thick formed the sides of the curved section.

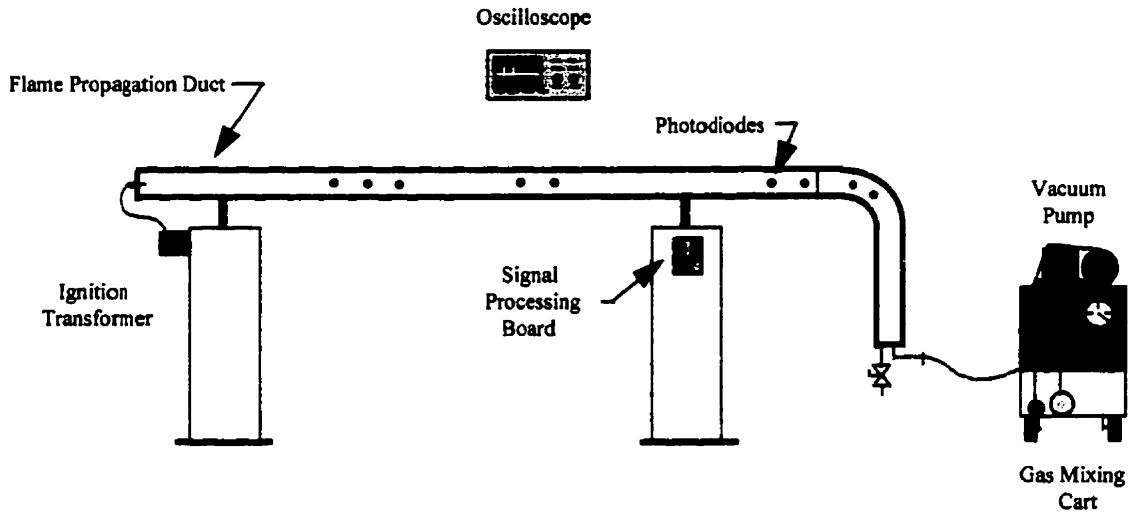

Fig. 3.1 Schematic of major test apparatus components.

Remaining structural components such as the duct top, bottom, endplates and clamp pieces were composed of machined aluminum parts. The endplate at the end of the longer straight section featured a threaded opening for a centrally mounted spark plug. The endplate for the short vertical section after the bend had two off-center openings. One opening was for the vacuum and gas fill piping connection. The other opening was 7.1mm in diameter and was connected to the surroundings through a valve. The valve remained open during experiments and was used to exhaust the flow of unburned gas ahead of the flame front. In this manner, it served the role of equalizing the pressure between the FPD and the environment. The opening was only about 3 % of the cross sectional area of the duct.

Fig. 3.2 Photograph of Flame Propagation Duct.

This FPD was designed by Acton [15] and manufactured in the Mechanical Engineering machine shop. A feature of the design was that the modular arrangement of the duct components allowed for extension of the duct to longer lengths. Another aspect was that bends of different curvature could be easily removed and installed. This flexibility in the design however, necessitated the requirement for a large number of seams. In order for an acceptable vacuum to be obtained within the FPD, these seams needed to be sealed. Much effort was exerted in trying to get the FPD to seal. The final arrangement involved the use of RTV silicone compound in conjunction with rubber O-ring cord to seal the side panels to the aluminum frame members. Automobile gasket sealant and kraft paper gaskets were used to seal the seams between adjacent aluminum frame members. In the event, the FPD was never able to hold a leak tight vacuum. A 3.1 ml/s leakage rate

during the FPD filling procedure was deemed acceptable in order to proceed with the experimental investigation.

Plexiglas panels could not be used in conjunction with Schlieren visualization in the bend area. These Plexiglas panels were replaced with glass panels. Quartz glass was considered, but the expense was prohibitive. The final arrangement used plate glass panels that prior to cutting, were tested in a Schlieren device for acceptable light transmission qualities. Due to the inelastic nature of glass, glass pieces as cut to fit the bend profile failed from stress concentrations in the area of the sharp inner radius. Modifications were made to the aluminum frame members of the bend structure. These changes allowed the use of glass pieces shaped with only straight cuts.

A final modification made to the duct was the installation of thermocouple wires in the entry region of the bend. This required drilling a series of holes on the top and bottom frame members. These filament wires were activated for millisecond durations to heat up unburned gas flowing through the duct. The result was a vertical tracer line of lower density gas flowing in the stream of the bulk gas flow. These lines were easily visualized with the use of a Schlieren apparatus. Their displacement in time and shape illustrated the velocity field of the unburned gas.

Further details of the FPD and activities relating to its commissioning are given in Appendices A and B.

3.2 Ignition System

The ignition system for the FPD consisted of a high voltage transformer, a relay, switch and a spark plug. The transformer was obtained from a heating and air conditioning equipment supplier. It was a common transformer used mainly for ignition of oil or gas fired home heating furnaces. This particular unit operated on 120 VAC, but outputted at 10,000 volts DC with a current rating of 20 mA. The electrical discharge was transferred to a spark plug through an automobile type spark plug wire. Control of the transformer was through a mechanical relay. The relay was a safety device which allowed control of the high AC voltage by a simple low voltage DC switch circuit. DC power in this case was provided by the instrumentation power supply. The ignition switch was connected to the relay and instrumentation power supply through a 3 meter length wire cord. This allowed the operator to assume a safe distance from the FPD during tests.

The spark plug was a common automobile type (MOTORCRAFT type ASF 32C). The spark gap was widened to approximately 2 mm to facilitate ignition of lean gas mixtures. Further details and a schematic of the ignition circuit are described in Appendix I.

3.3 Gas Mixture Preparation Cart

The purpose of the gas mixture preparation cart was to prepare a combustible mixture of propane and air for use in the FPD. An existing mobile laboratory cart was taken in hand for modifications. SWAGELOK compression fittings, on-off valves, check valves and metering valves were used for fabrication. All tubing and most of the fittings were of

brass construction. A stainless steel, thick-walled sample cylinder of 2250 ml volume was used as the storage container for the flammable mixture. Mixture preparation was done by the partial pressure method. This method is described in Appendix E.

Fuel and oxidizer gases were supplied from two, high pressure, industrial gas cylinders. The fuel used was Instrument Grade, 99.5% propane as supplied by WELDCO. The oxidizer was dry air supplied by BOC GASES.

The key component of the apparatus, necessary for producing accurate gas mixtures was the ASHCROFT type 1082 test pressure gauge. This gauge was a combination vacuum and pressure gauge. The vacuum side of the gauge was delineated in inches of mercury (in Hg). The pressure side of the gauge was delineated in pounds per square inch (psig). The pressure gauge had a stated accuracy of 0.25%. Its maximum operational pressure was 700 kpa (100 psig). Consequently, gas regulators were required to reduce the output pressure from the individual gas cylinders.

A vacuum pump was installed on top of the mixture preparation cart. The vacuum pump was used to initially evacuate the sample cylinder and internal piping prior to preparing a gas mixture. For tests, the pump was used to evacuate the FPD prior to filling with the test mixture. The vacuum pump was an EDWARDS type ES50 and had a maximum vacuum draw of 1×10^{-2} torr.

3.4 Instrumentation and Signal Processing

Flame propagation velocities were measured by a series of photodiodes attached at specified locations along the FPD. The photodiodes were manufactured by VACTEC and were designated type VTP3310LA. These photodiodes had their maximum sensitivity in the visible light spectral range. Nine photodiodes were used in testing. The photodiodes could be relocated along the FPD so as to characterize flame propagation along the entire duct. In the course of this testing program, three photodiode configurations were implemented. These configurations are labeled AA, BB, and CC in the test data tables.

Signals from the photodiodes were sent to a custom-built signal processing board. The signal processing boards amplified the outputs from each individual photodiode. The amount of amplification was different for each photodiode. The circuit then combined these signals from four or five photodiodes into one distinct "summed" waveform signal. This allowed for the display of all photodiode signals on a two channel oscilloscope.

A LECROY 9400A oscilloscope was used to determine the time difference between photodiode signals. A feature of this oscilloscope was that the waveform could be expanded to more precisely determine the time difference between photodiode signals. For all tests, the oscilloscope was set up for SINGLE RUN operation. Triggering of the run was done by using a loop of wire to create a low voltage DC signal from otherwise undesirable EMI noise. The EMI noise was produced by the high voltage ignition transformer when the ignition switch was closed.

Appendix F details the photodiode specifications and their installation configurations. A supplementary backlighting procedure is also discussed. The signal processor circuits are described in Appendix G. Appendix H discusses the details of the signal waveforms obtained with the oscilloscope.

3.5 High Speed Camera

A black and white, high speed CCD camera was used for recording the motion of flame fronts propagating through the FPD bend. This unit was a Motionscope 500 camera manufactured by REDLAKE but sold by OPTICON. It had a maximum frame rate of 500 frames/sec. A Pentax/Comiscar TV type lens was used for these recordings. This lens had a 6 mm aperture and a 1:1.4 focal length. The high speed camera was also used in conjunction with the Schlieren apparatus to record the motion of timelines in the unburned gas flow. These recordings were conducted with another Pentax/Comiscar lens. This lens had a 6 mm aperture and a 1:1.2 focal length.

Images from the high speed camera were digitally stored in an internal buffer memory. About 2000 images could be stored before the memory was overwritten. A switch on the camera control was used to disable the overwrite mode. The remote "pickle" switch was used for this purpose. A GRABIT frame grabber device was purchased to download images from the camera memory into a personal computer. LVIEW PRO software was used for image processing.

3.6 Schlieren System

Schlieren visualization is a technique which uses light to differentiate density gradients in a fluid. The basic principle of Schlieren visualization is that density gradients within a fluid causes transmitted light to refract at different angles. Through the use of an appropriate apparatus, a columnar light beam can be produced and passed through a heterogeneous fluid under investigation. The perturbed light beams are focused by a lens or converging mirror. Deviations in the angles of the refracted light beams are amplified by the use of a knife edge or Schlieren diaphragm located at the focal point of the collated light beams. The resulting image can be displayed on a screen for recording by a camera.

The Schlieren apparatus used for these experimental investigations was designed, fabricated and tested for a Mech 460 Design Project. A 100 watt Xenon lamp mounted on a 2-axis traversing mechanism was used as the light source. The resulting columnar beam was approximately 18 cm in diameter. Since images were to be recorded by the black and white high speed camera, a simple knife edge rather than a color Schlieren diaphragm was acceptable. Once all the lens and mirrors were satisfactorily adjusted, the images produced by the apparatus were of very good quality. The Schlieren system was set up to visualize conditions of the flow in the confines of the FPD bend. Specifically, timeline tracers in the unburned gas flow and temperature gradients of the flame fronts were to be observed. Appendix K details the Schlieren apparatus used in this project.

3.7 Timeline Device

In order to visualize the flow patterns of the unburned gas flow in the FPD bend, it was decided to use a timeline procedure. As previously discussed, creating a timeline involved heating a localized area in the bulk flow of a fluid. A Schlieren device was then used to visualize the less dense fluid in relation to the heavier bulk fluid around it.

The timeline arrangement consisted of a 76 micron diameter, thermocouple wire installed vertically in the channel at the inlet to the bend. This wire in turn was heated by a modified thermocouple time constant tester. The one used for these experiments was built by the University of Waterloo electronic shop. This device allowed for the varying of the current as well as the duration of the electrical impulse to the thermocouple wire. Initiation of the impulse was originally performed by a push-button switch mounted on the tester. The initiation circuit was altered by bypassing the switch and connecting the wire leads to the output of a simple, custom-built time delay circuit. This circuit allowed for time delays of 1 to 100 milliseconds between an input signal and a respective output signal. Due to the transient nature of the unburned gas flow in the bend, varying the time delay allowed for the initiation of a timeline at different flow conditions. Time delay circuits are further detailed in Appendix J.

3.8 Procedures

The initial task in conducting a test run was to prepare a mixture of propane and air using the mixture preparation apparatus. This involved applying a vacuum to the storage tank,

and filling the tank at pressures corresponding to the desired mixture composition. Once filled, the mixture in the tank was allowed to stabilize for at least 10 minutes prior to filling the FPD. The vacuum pump hose was attached to the FPD apparatus and a vacuum was applied. Filling of the FPD with the gas mixture was then undertaken. The FPD was filled to atmospheric pressure. The mixture was allowed to stabilize to a quiescent state for at least 2 minutes prior to ignition.

The ignition system, instrumentation circuits, oscilloscope and if required, the CCD camera were turned on and checked for proper operation. It was important to set the oscilloscope to the desired measurement parameters. Sampling rate, signal scale, and trigger mode were the more important adjustments. Once the oscilloscope was ready for triggering, the main FPD valve was opened. For safety and a broader view of flame propagation in the FPD, the operator was positioned about 2 meters from the FPD. Ignition of the mixture was done by closing the ignition switch. In most cases, ignition was quick and the flame front propagated through the FPD in less than 1 second. For mixtures of very rich or lean composition, more than one operation of the ignition switch may have been warranted. In these cases, the oscilloscope would have been reset after every switch operation otherwise photodiode signals would not have been displayed.

Once the flame front had passed through the FPD, the resulting waveform could be viewed on the oscilloscope. Cursors and expansion settings were adjusted to determine the time differences between the various photodiode signals. These time values were recorded in a lab notebook.

The high speed CCD camera was used in some test runs to record flame front propagation in the FPD bend. This device was set up on a tripod approximately 1.2 m from the face of the FPD bend. Besides the ignition switch, the camera "pickle" switch also needed to be activated for these tests. When a satisfactory test run had been conducted, video images were downloaded from the camera memory into the personal computer via utilization of the GRABIT frame grabber device. Images were stored in the computer as bitmap files for subsequent processing.

For a specific test mixture composition, attempts were made to obtain at least 10 trials for each of the three photodiode configurations. All tests were conducted during the summer of 1998. However, tests for a specific mixture composition were not all conducted on the same day. This was done so as to diminish the effects of excessively high humidity or temperature on the collected data.

For timeline experiments, the same procedures were implemented except photodiodes and the oscilloscope operations were not used. In their place, the Schlieren apparatus and modified Thermocouple tester were utilized.

The thermocouple tester was connected to the thermocouple wire installed in the FPD. The Schlieren system was set up with the high speed CCD camera recording Schlieren images projected on a small screen. The potentiometer on the time delay circuit was then adjusted for an approximate time delay. The actual delay was determined later by

analyzing the high speed camera images. Again, ignition of the gas mixture and recording of the Schlieren images were initiated by closing the ignition and camera "pickle" switches.

Chapter Four

Results

4.1 Introductory Remarks

The experimental trials were conducted with various mixtures of propane and air. The composition of the mixtures was defined by the equivalence ratio (ϕ). In this work, the equivalence ratio is a mass based characteristic variable which relates the fuel to air ratio of the test mixture with respect to the stoichiometric fuel to air ratio. The following equation symbolizes the relationship between the fuel to air ratios.

$$\phi = (F/A)_{test} / (F/A)_{stoich}$$

The test plan involved the combustion of gas mixtures which spanned the range from ϕ = 0.6 to ϕ = 2.0. Equivalence ratios were varied by 0.1 increments. The increments were reduced to 0.05 to more precisely specify the equivalence ratios where the flame propagation limits were encountered.

Appendix L contains the raw data results from the initial FPD commissioning tests. These tests were conducted with BERNZOMATIC propane. This type of propane contained a mixture of propane and higher order hydrocarbons. Consequently, a commercial grade propane was obtained and used for the remaining trials. The raw data results from these trials are presented in Appendix M.

4.2 Flame Propagation Limits

The lean and rich flame propagation limits were determined for specific mixture compositions as measured by equivalence ratio. The criterion set for the determination of a flame propagation limit was a mixture composition where a flame front developed and propagated through the entire length of the FPD.

Under this definition, the lower limit of flame propagation occurred for a mixture composition of $\phi = 0.85$. Fourteen trials were conducted at this equivalence ratio. All the trials resulted in flame fronts which propagated through the entire duct. Fifty trials were conducted at an equivalence ratio of $\phi = 0.80$. In 38 trials, flame fronts were quenched either in the bend of the FPD or just after the bend.

The upper flame propagation limit occurred for a mixture composition of $\phi = 1.80$. Fifty-three trials were conducted at this equivalence ratio. In all the trials, the developed flame fronts propagated through the entire length of the FPD. Nine trials were conducted at an

equivalence ratio of ϕ=1.85. Of these trials, six resulted in flame front propagation through the entire length. However, the remaining trials resulted in the quenching of the flame fronts prior to entering the bend.

4.3 Flammability Limits

Mixture compositions could be ignited beyond the lean and rich flame propagation limits. However, in these cases, the developed flame fronts quenched at some point in the FPD. Extending the mixture compositions further into the lean and rich regimes resulted in no ignition of the mixture. Compared to the flame propagation limits, the equivalence ratios which delineate the lean and rich flammability limits were not precise boundaries.

The criteria set for mapping of the lean and rich flammability limits were mixture compositions where ignition was difficult or impossible to achieve. At the lean flammability limit, ignition was characterized by a long spark duration of more than 5 seconds, or a series of many short duration sparks. If a flame front did develop through this effort, it was very slow and was quenched in the straight inlet section of the FPD. Ignition at the rich flammability limit was characterized by a single, short-duration spark. The resulting flame fronts propagated through the straight section of the FPD very slowly and were quenched before entering the bend.

From these experiments, the lean flammability limit was found to be for a mixture composition of ϕ = 0.75. At this equivalence ratio, six trials resulted in no ignition of the

mixture. However, four of the ten trials resulted in ignition of the mixture and the development of a slow moving flame front. Three of these flame fronts were quenched near the midpoint of the straight entrance channel of the FPD. One flame front was quenched just before entering the bend of the FPD.

The rich flammability limit for this experimental program was found to be for a mixture composition of ϕ = 2.0. Of the nine trials, eight flame fronts developed but were quenched before entering the FPD bend. One trial resulted in the development of a flame kernel around the spark. This kernel was observed to have a diameter of about 1 cm. It did not evolve into a flame front and it disappeared once the spark was deactivated.

4.4 Flame Propagation Velocities

Figures 4.1, 4.2 and 4.3 are summary graphs which compare the average flame propagation velocities of the various mixtures. Figures 4.4 to 4.14 are graphs showing average flame propagation velocities and standard deviations for individual mixture compositions of ϕ = 0.8 to ϕ =1.8. In all these charts, the axial length is considered along the centerline of the duct. The 90° bend begins at the axial length of 166 cm and ends at the axial length of 178 cm.

These figures show that the average flame propagation velocities vary considerably with mixture composition and location within the duct. However, there are two distinct

patterns of behavior in the flame propagation velocity. One pattern is seen in the inlet section of the FPD while the other is in the bend.

Figure 4.1 shows the average flame propagation velocities for mixture compositions of ϕ =1.1 to ϕ = 1.4. From the ignition point at the 0 cm location, the flame fronts initially evolve and accelerate as they progress into the first 30 cm of the inlet section. Between the 30 cm and 53 cm locations along the duct length, the average flame propagation velocities decrease. The propagation velocities then increase abruptly in the short distance between the 53 cm and 58 cm locations along the duct length. From the 58 cm location to the 151 cm location, the average flame propagation velocities remain constant with only small variations. At the 151 cm location, the flame fronts undergo a deceleration until just prior to entering the FPD bend. For the inlet section of the FPD, the average flame propagation velocities for these mixture compositions are on the order of about 10 m/s with variations generally not exceeding 8 m/s.

Average flame propagation velocities for mixture compositions of ϕ = 0.8 to ϕ = 1.1 are shown in Fig. 4.2. Dramatic variations in the average flame propagation velocities along the inlet section of the FPD are shown for these cases. The velocity changes can be as much as 35 m/s in a length of 5 cm. This is shown between the 53 cm and 58 cm locations along the duct.

At the higher equivalence ratios of 1.5 to 1.8 (Fig. 4.3), again the average flame propagation velocities change dramatically along the inlet section of the duct. At an

equivalence ratio of 1.8, the maximum change in the inlet duct section is about 30 m/s within a 5 cm axial length. Similar to Fig. 4.2, this maximum velocity change also occurs between the 53 cm and 58 cm locations along the duct.

However, with the exception of $\phi = 1.8$, the mixture compositions in Fig. 4.3 encounter their largest individual variations near the 144 cm location. Prior to this region, the mixture compositions of $\phi = 1.5$, 1.6, and 1.7 exhibit relatively small variations in their average flame propagation velocities.

Together, these first three figures show the wavering velocity profile of the flame fronts prior to entering the bend. The velocity profiles have distinctive patterns. A noteworthy feature is the consistent acceleration and slowing pattern experienced by the flame fronts. This is most pronounced by the flame front decelerations and subsequent accelerations between the 30 cm and 58 cm locations along the FPD. This occurs for all tested mixture compositions. Flame front decelerations are also noted for almost all mixture compositions prior to the flame fronts entering the bend.

These graphs show that at any specific location along the inlet duct section, the flame front is either undergoing an acceleration or a deceleration. The mixture composition has a major effect on the velocity variations. Even with these velocity variations, a pattern is still distinguishable.

Tempering of the velocity variations occurs for the slightly rich mixture conditions. Approaching the rich flame propagation limit, the velocity variations in the inlet section are small until the flame fronts reach the 140 cm region. This is with the exception of ϕ = 1.8. When the mixture compositions approach the lean flame propagation limit, the pattern of accelerations and decelerations is similar to the rich mixture compositions. However, larger velocity variations are encountered.

Figures 4.1, 4.2, and 4.3 show that flames decelerate prior to entering the bend with the exception of ϕ = 1.8. For most mixture compositions, the average flame propagation velocity at the entrance to the bend does not exceed 6.2 m/s. For the exceptional case of ϕ = 1.8, the resulting average flame propagation velocity at the bend entrance is 13.2 m/s. However, as Fig 4.14 shows, the standard deviation at location 161 cm and for this ϕ = 1.8 mixture is high, and it therefore necessitates some reservation of this specific value.

For the mixtures with compositions of ϕ =0.9 to ϕ =1.8, the average flame propagation velocity of the flame fronts increases as they propagate through the bend. The maximum average flame propagation velocity occurs either just before exiting the bend, or immediately after exiting the bend. This again is dependent on the mixture composition. The slightly rich mixtures result in maximum velocities occurring in the bend. The lean and very rich mixtures generally show maximum velocities occurring outside the bend. The velocity level of the flame fronts near the bend exit does not exceed 18.6 m/s.

Upon exiting the bend, the average flame propagation velocities generally decrease through the exit length of the duct. For the two mixture compositions of ϕ =1.0 and ϕ =1.8, a slight increase in the average flame propagation velocity is shown for flame fronts progressing through the exit length of the duct. However, these equivalence ratios also had relatively high standard deviations at the end locations of the exit duct (Figures 4.6 and 4.14).

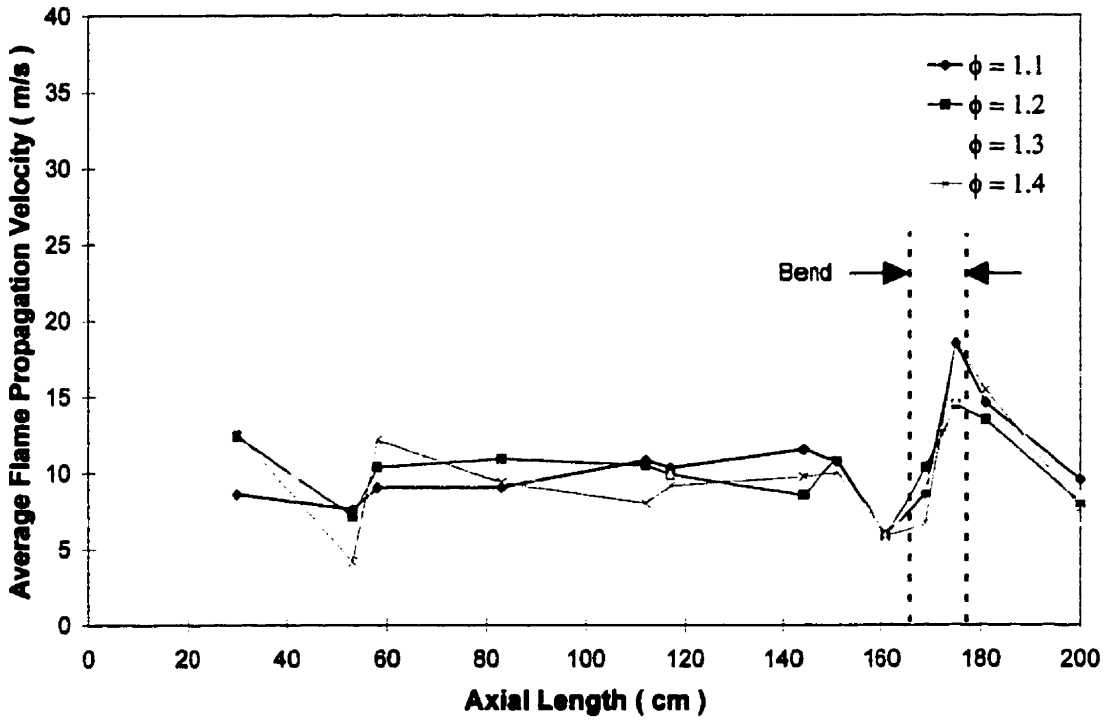

Fig. 4.1 Average flame propagation velocities for slightly rich mixture compositions.

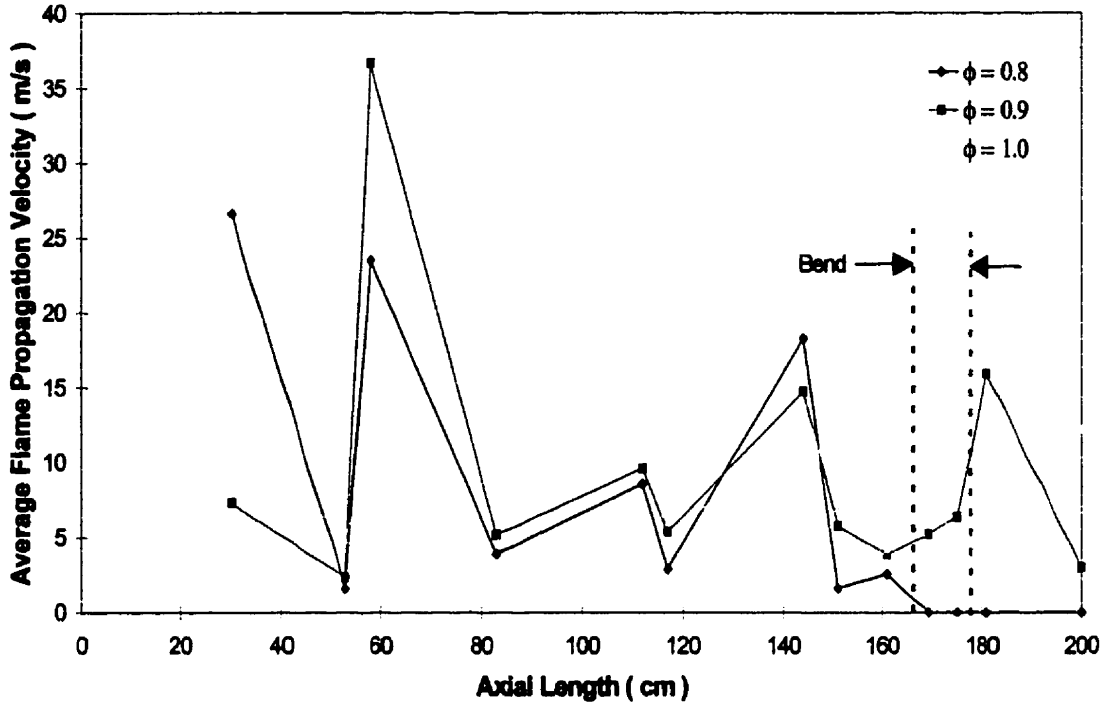

Fig. 4.2 Average flame propagation velocities for lean and stoichiometric mixture compositions.

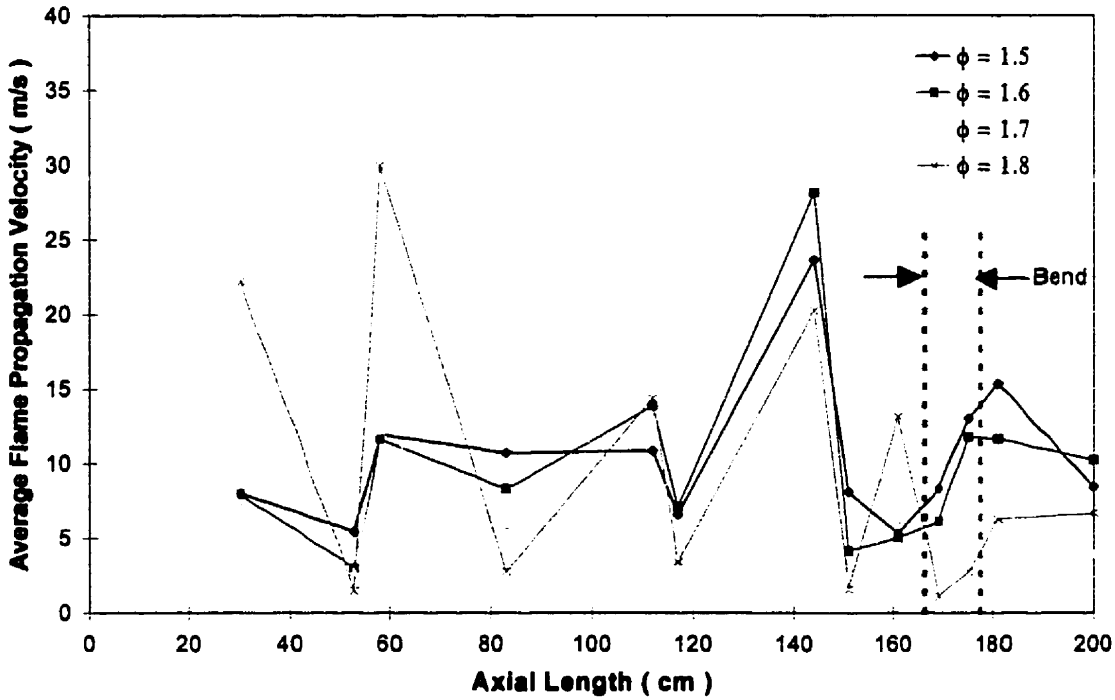

Fig. 4.3 Average flame propagation velocities for very rich mixture compositions.

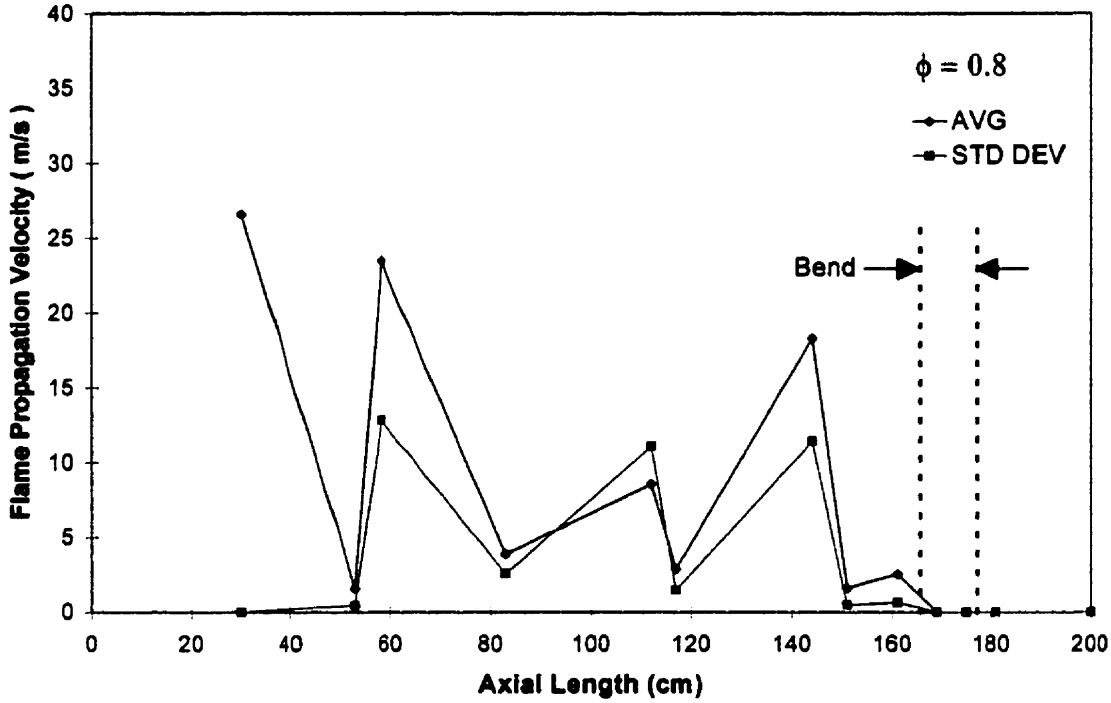

Fig. 4.4 Average flame propagation velocities and standard deviations for $\phi = 0.8$.

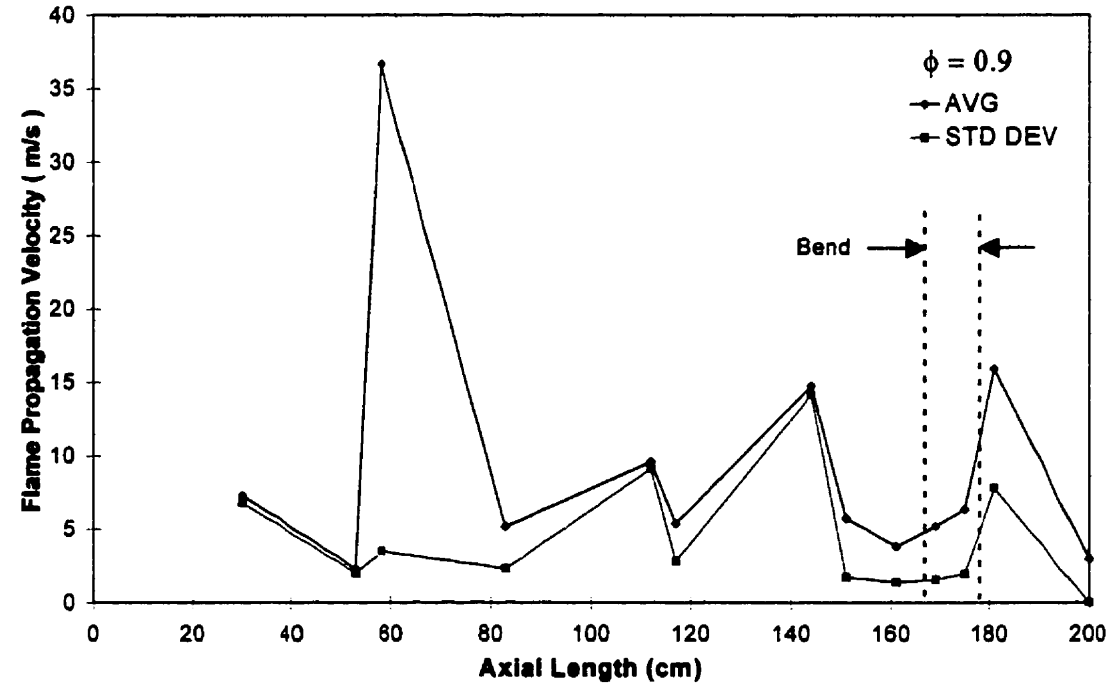

Fig. 4.5 Average flame propagation velocities and standard deviations for $\phi = 0.9$.

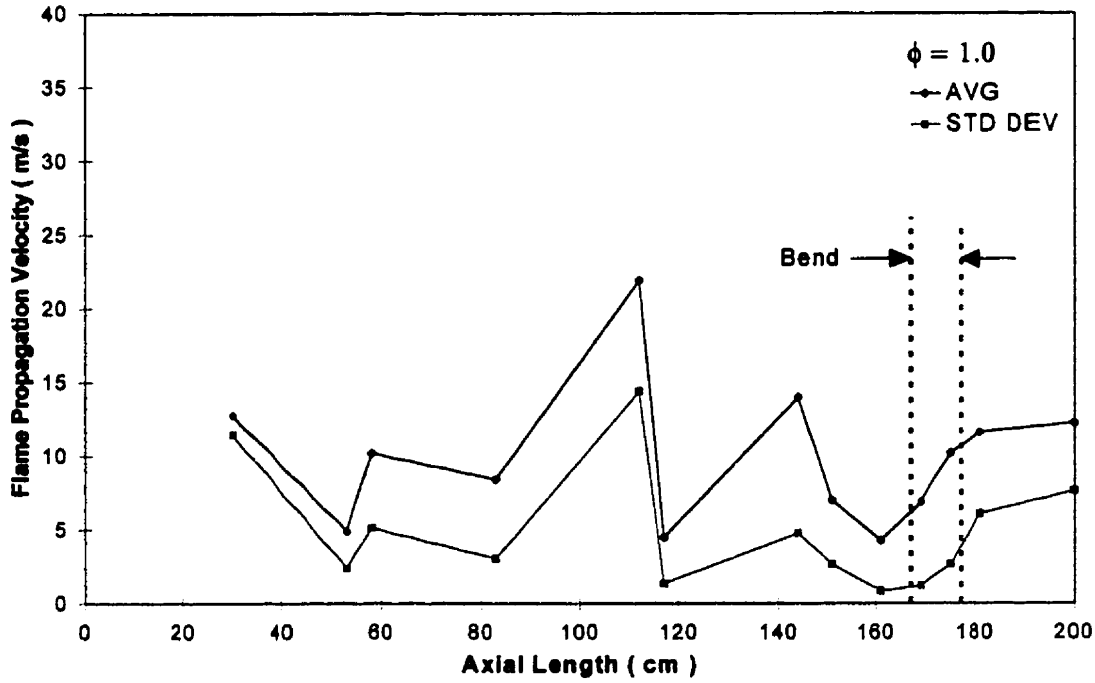

Fig. 4.6 Average flame propagation velocities and standard deviations for $\phi = 1.0$.

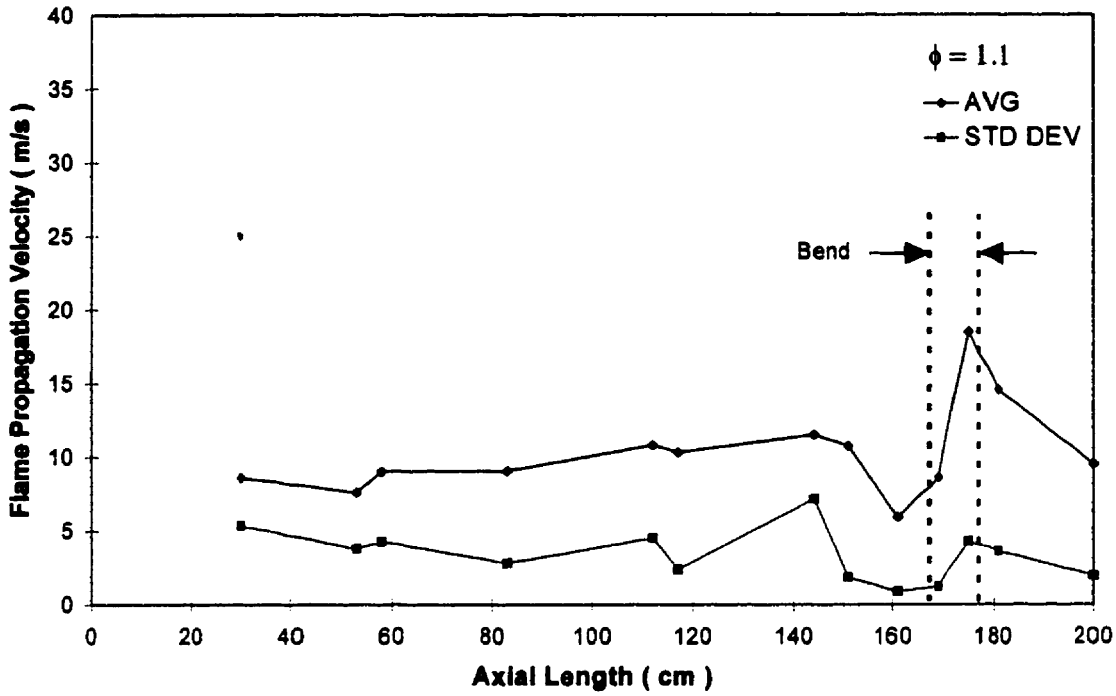

Fig. 4.7 Average flame propagation velocities and standard deviations for $\phi = 1.1$.

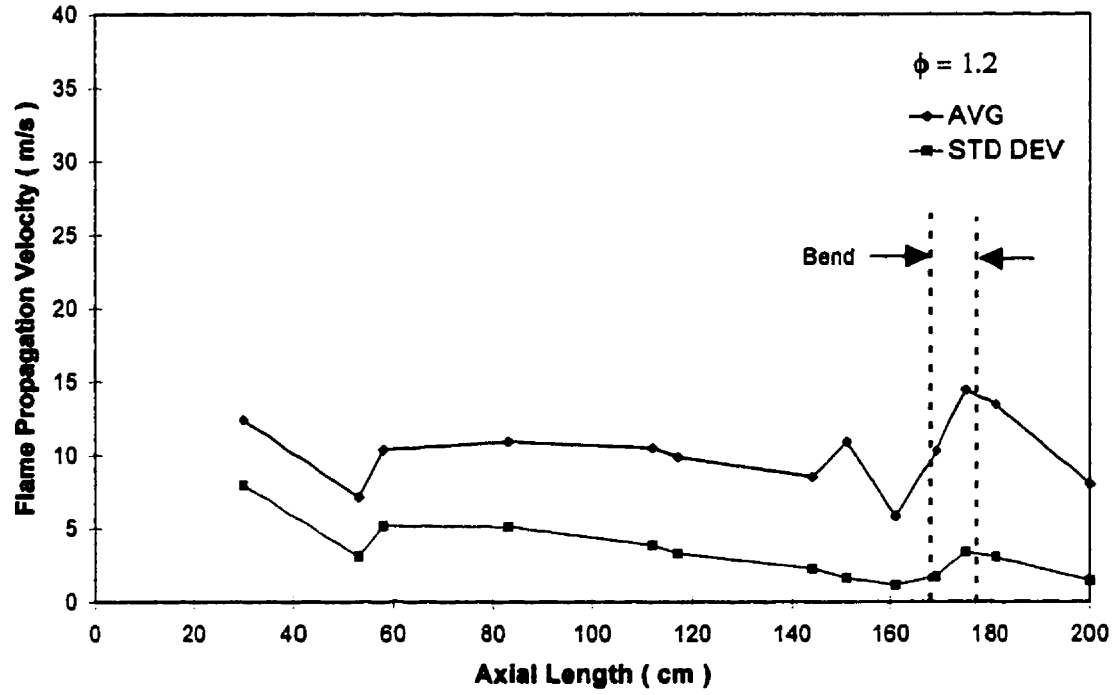

Fig. 4.8 Average flame propagation velocities and standard deviations for $\phi = 1.2$.

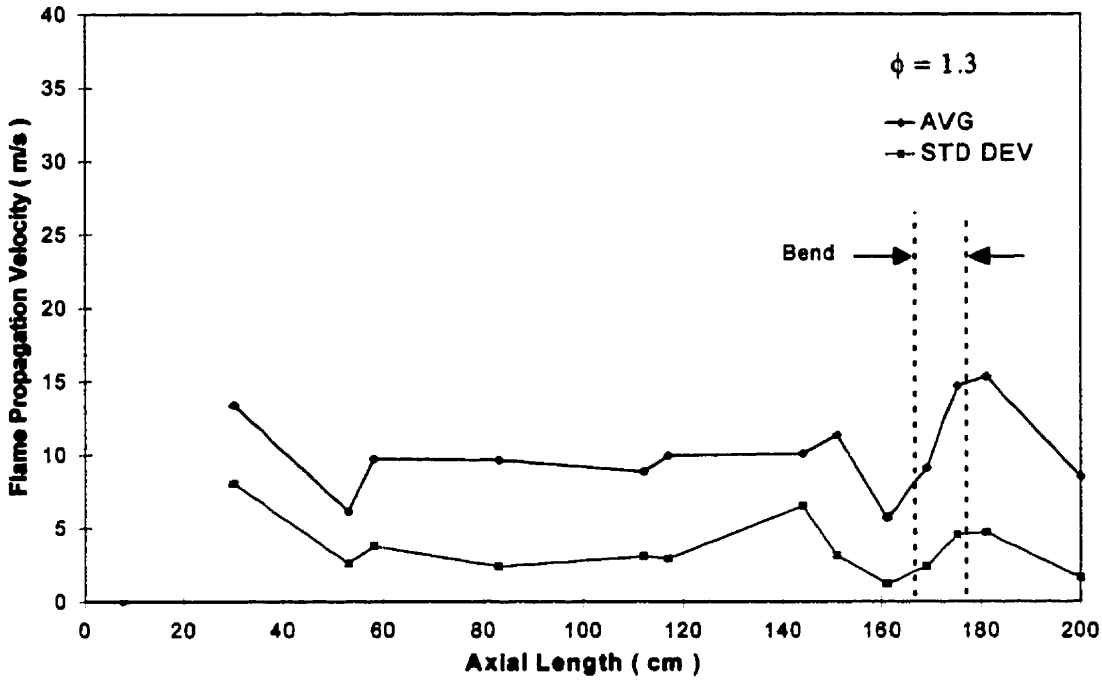

Fig. 4.9 Average flame propagation velocities and standard deviations for $\phi = 1.3$.

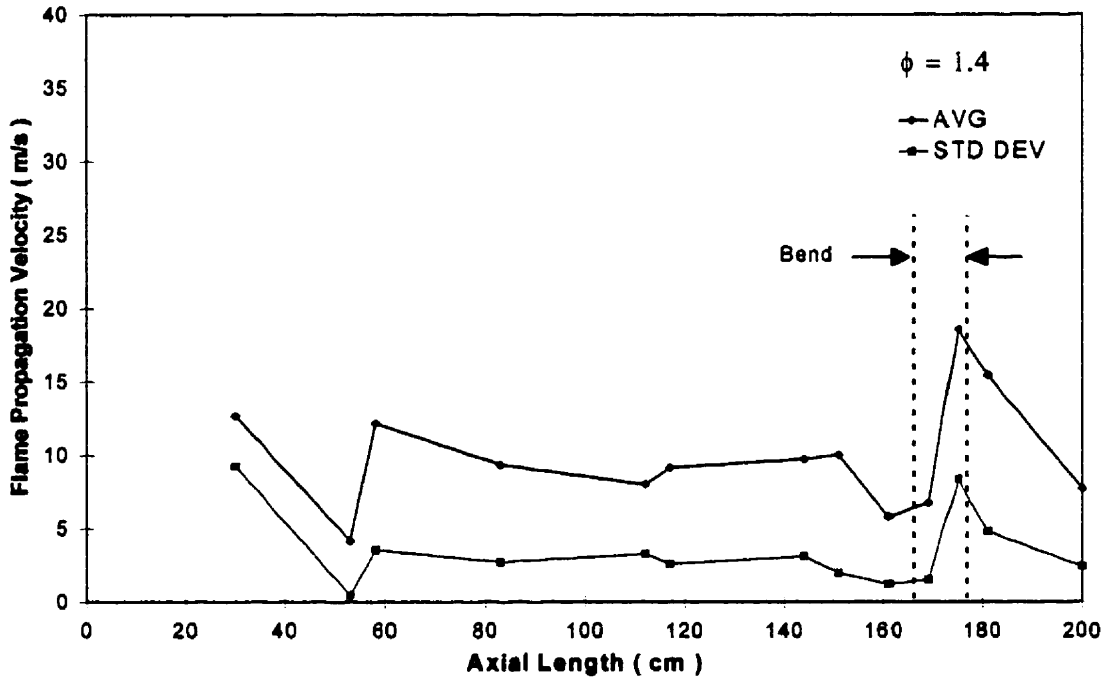

Fig. 4.10 Average flame propagation velocities and standard deviations for $\phi = 1.4$.

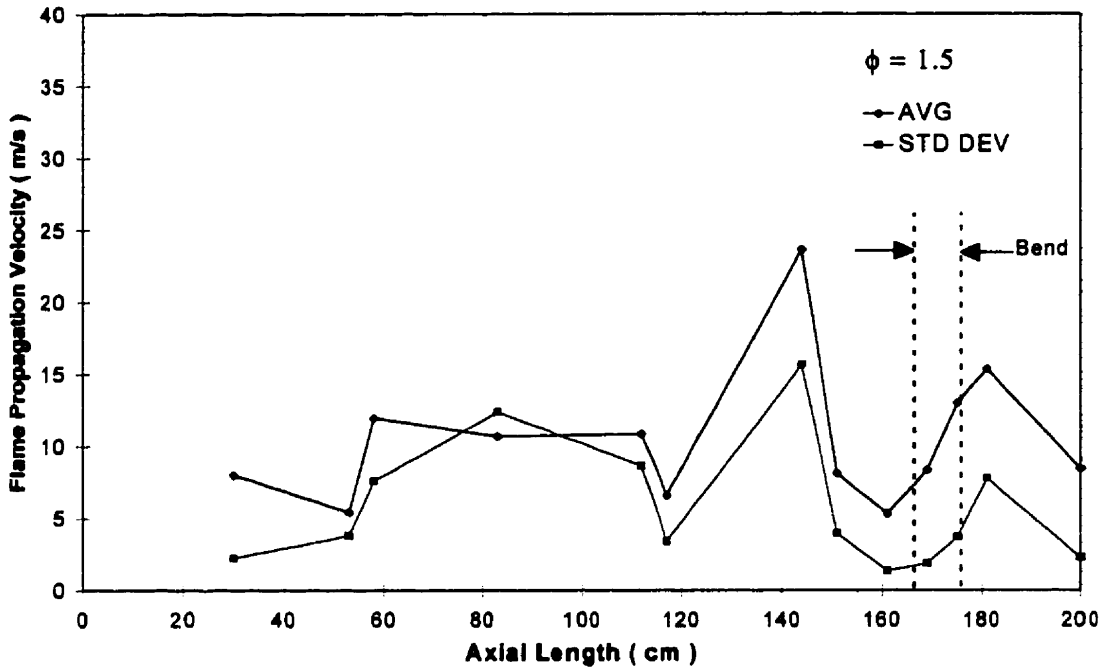

Fig. 4.11 Average flame propagation velocities and standard deviations for $\phi = 1.5$.

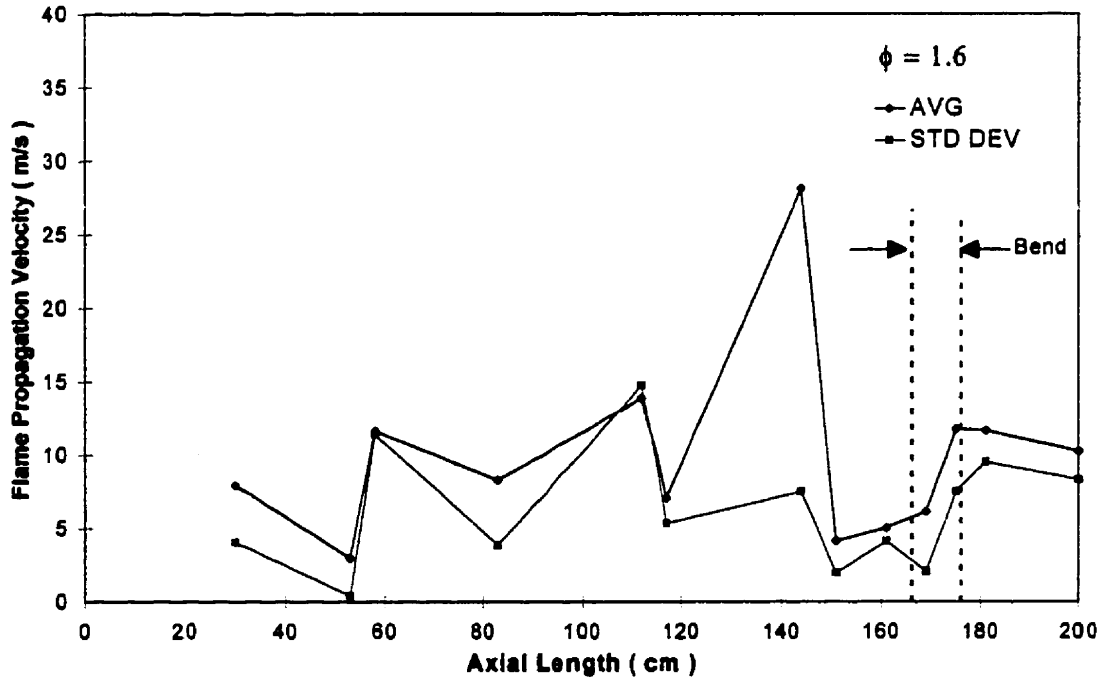

Fig. 4.12 Average flame propagation velocities and standard deviations for $\phi = 1.6$.

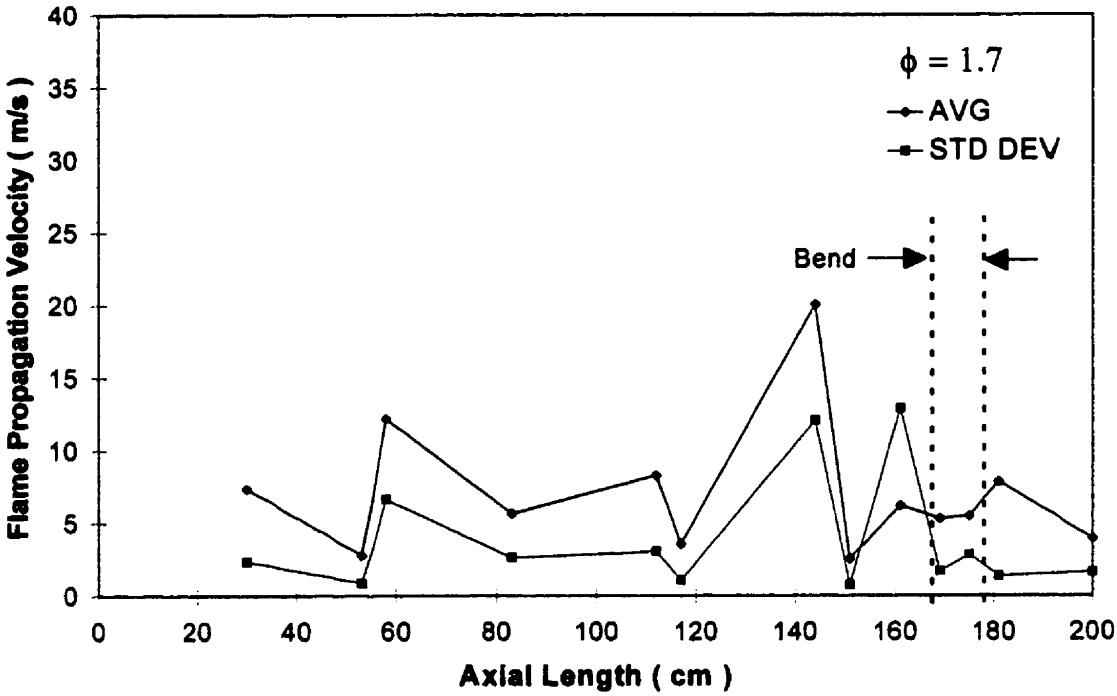

Fig. 4.13 Average flame propagation velocities and standard deviations for $\phi = 1.7$.

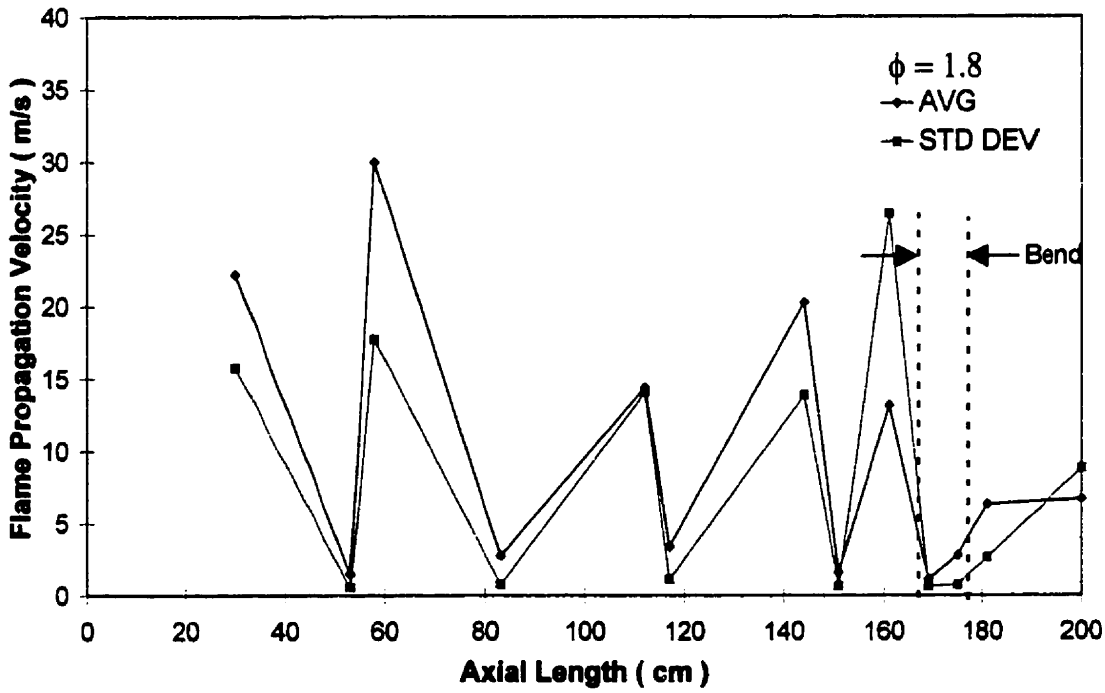

Fig. 4.14 Average flame propagation velocities and standard deviations for $\phi = 1.8$.

The standard deviations shown in Figures 4.4 to 4.11 indicate that there is a low variance among the data points obtained for the location near the entrance of the FPD bend. The standard deviations at this location are 2 m/s or less for the mixture compositions of ϕ = 0.8 to ϕ = 1.5. The very rich conditions are exceptions with higher variances. For a mixture of ϕ = 1.6 (Fig. 4.12), a slightly high standard deviation of 4.15 m/s results. For the conditions of ϕ = 1.7 and ϕ = 1.8 (Fig. 4.13 and 4.14), the standard deviations are 12.9 m/s and 26.4 m/s respectively.

Where large variations in the average flame propagation velocities occur (ϕ = 0.8 to 1.0 and ϕ = 1.5 to 1.8), the standard deviations appear to follow the actual flame propagation velocity trends. The standard deviations are high for the high average velocities and low for the low average velocities. The mixture conditions of ϕ = 1.1 to 1.4 show that for these conditions of relatively steady flame velocities in the inlet section of the FPD, relatively low standard deviations of 5 m/s or less are the result.

4.5 Flame Front Contours

A series of contour plots starting at Fig 4.15 shows the leading edge of flame fronts propagating through the FPD bend. Each plot is a composite of single frames obtained from the high speed CCD camera for one individual trial. They are representative of typical flame front propagations for a specific equivalence ratio. The plots were processed in a negative format which displays black pixels as white and vice versa. This allows for easier visualization of the flame fronts and better contrast to more accurately

determine their contours. An added benefit is that the photodiode shield locations are also easily discernible.

For those individual trials where photodiode data was obtained, graphs are also presented which compare flame propagation velocities calculated from this method, and from the analysis of the contour plots.

Analysis of the first one or two flame front contours of each plot shows distinct profiles for different equivalence ratio conditions. These contours are roughly 5 cm in front of the entrance to the bend. The flame fronts for ϕ = 0.9 and 1.0, and for the very rich conditions of ϕ = 1.5 to 1.8 appear to have an elongated parabolic profile. For the slightly rich conditions of ϕ = 1.1 to 1.4, the flame front profile has a "top hat" like appearance.

The flame fronts upon entering the bend, have the tips of their leading edges either at the midplane level or slightly above the midplane. As the flame fronts proceed into the bend, the tip of the leading edge gradually moves inward toward the inner surface of the bend. By the time the flame fronts are halfway through the bend, the tips of the leading edges are very close or relatively near the inner surface of the bend. The flame fronts proceed through the latter half of the bend in a similar manner.

The contour plots extend down into the exit length of the FPD approximately 8 cm from the exit of the bend. Upon exiting the bend, the tips of the leading edges of the flame fronts begin to move back toward the centerline. The final contours for the plots of

$\phi = 0.9$ and 1.0 and $\phi = 1.5$ to 1.8 show that the flame front tips are now off-centered with the tips located between the duct centerline and the outer surface of the straight exit length.

The contour plots show an interesting occurrence near the outer surface of the bend. For mixture compositions of $\phi = 1.1$ and 1.2, the flame front propagates proceeds quickly near the outer surface of the bend. This is shown as one or two flame front contours near that region of the bend. The other contour plots indicate that as the equivalence ratio of the mixture increases above $\phi = 1.2$, the concentration of contour lines increases near the outer bend. This also occurs when the equivalence ratio is decreased below $\phi = 1.1$. The high concentration of contour lines for these cases is indicative of slow flame front propagation along the outer radius region of the bend. The result is that the flame front is extended or stretched as it proceeds through the latter half of the bend and into the exit length. Speculation as to the reasons for the slow flame propagation in this region will be discussed in the next chapter.

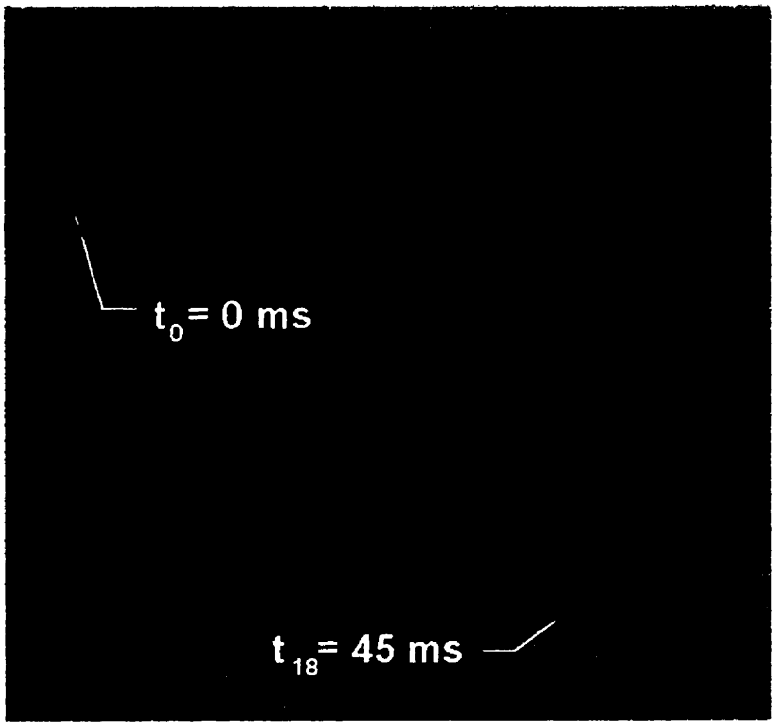

Fig 4.15 Flame front contours for $\phi = 0.9$. Test # 242, 400 fps.
Time spacing between contours: $\Delta t = 2.5$ ms.

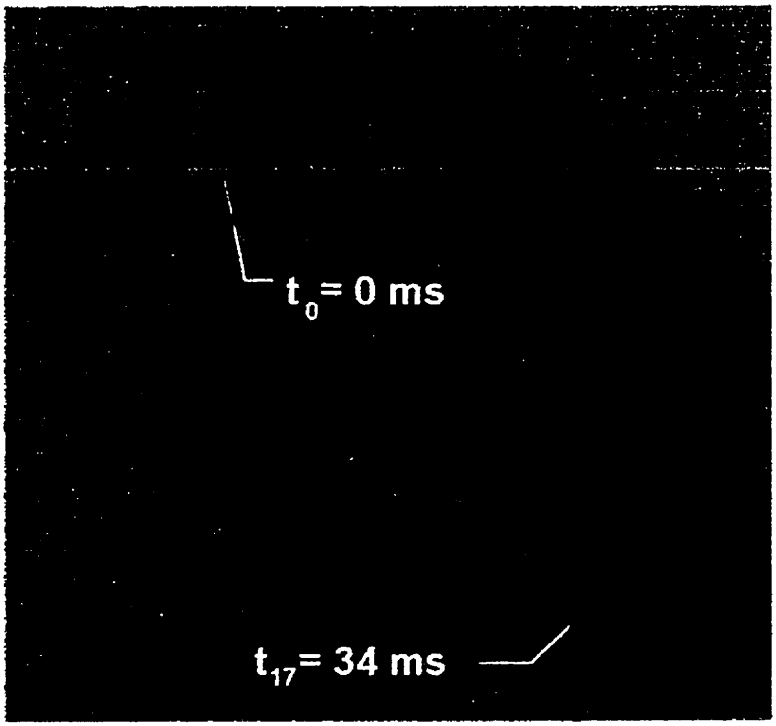

Fig 4.16 Flame front contours for $\phi = 1.0$. Test # 186, 500 fps.
Time spacing between contours: $\Delta t = 2.0$ ms.

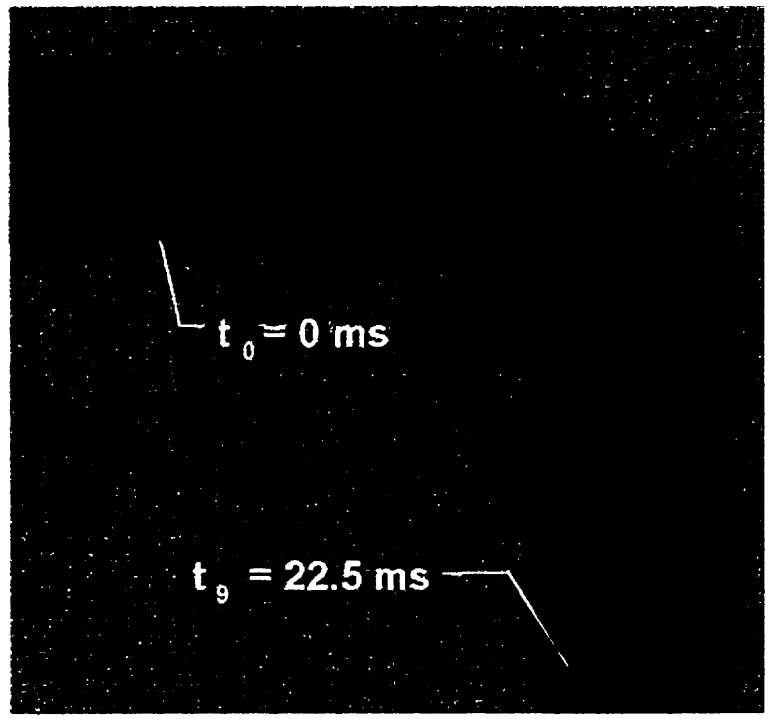

Fig 4.17 Flame front contours for $\phi = 1.1$. Test # 192, 400 fps. Time spacing between contours: $\Delta t = 2.5$ ms.

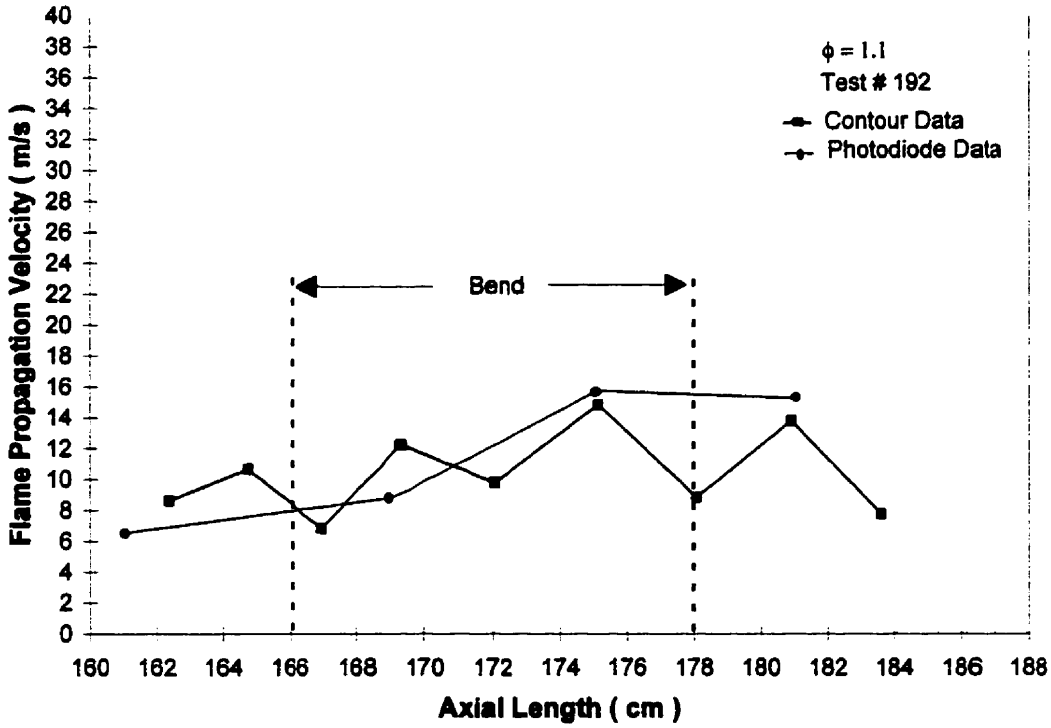

Fig 4.18 Comparison of centerline flame propagation velocities for Test # 192, as obtained from photodiode and contour analyses.

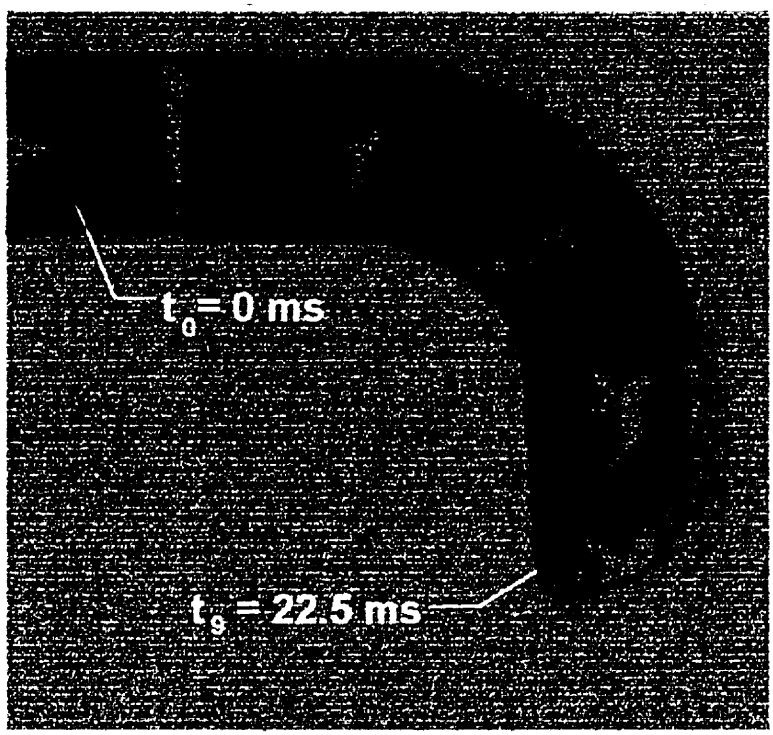

Fig 4.19 Flame front contours for $\phi = 1.2$. Test # 198, 400 fps. Time spacing between contours: $\Delta t = 2.5$ ms.

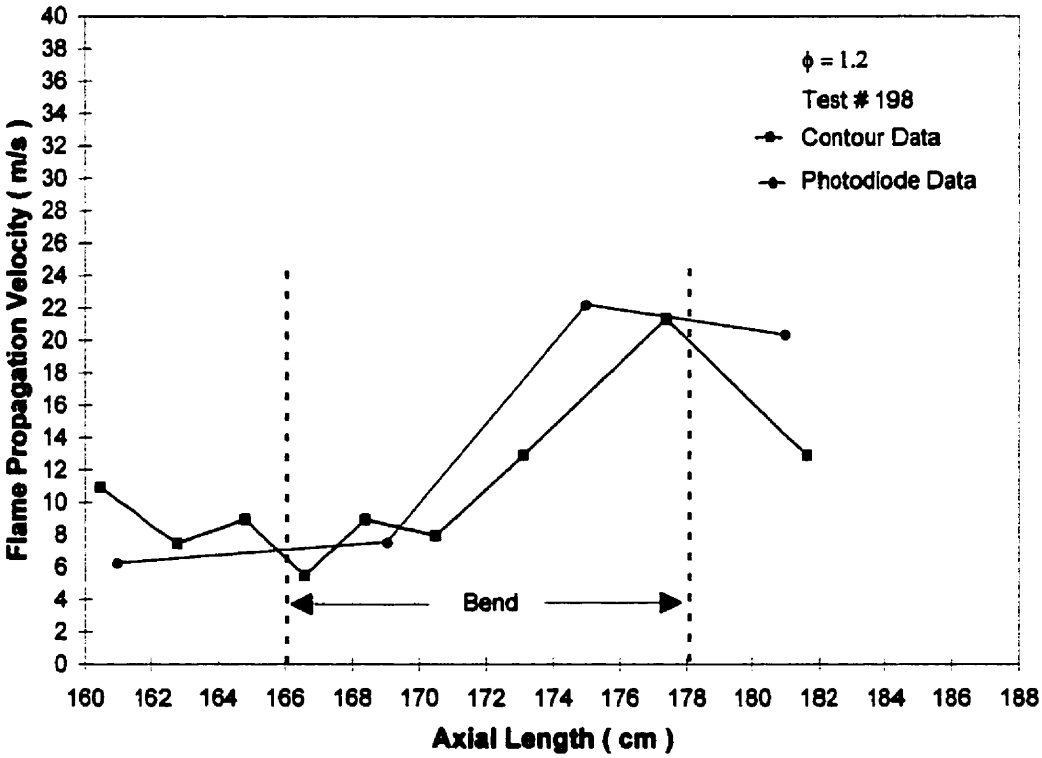

Fig 4.20 Comparison of centerline flame propagation velocities for Test # 198, as obtained from photodiode and contour analyses.

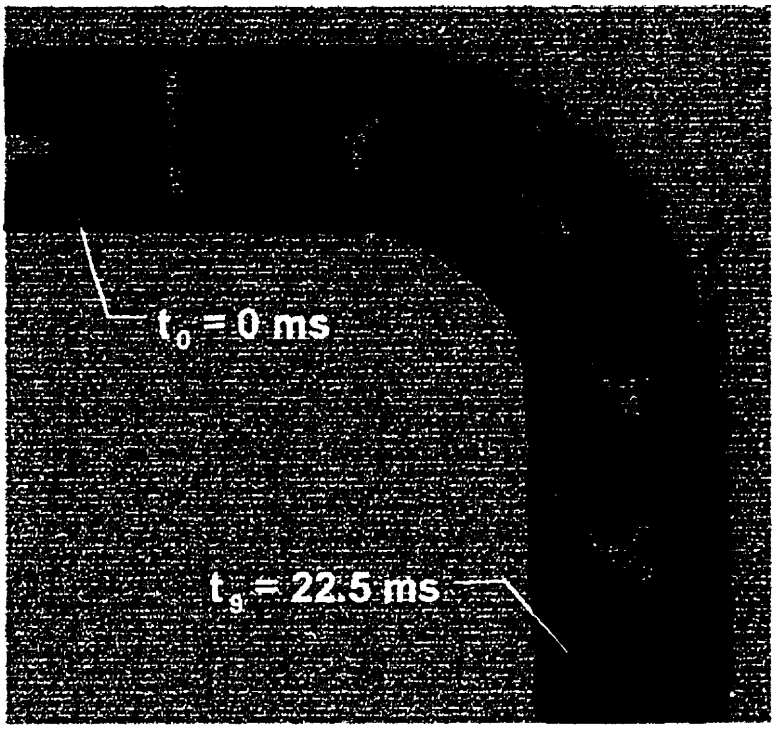

Fig 4.21 Flame front contours for $\phi = 1.3$. Test # 202, 400 fps. Time spacing between contours: $\Delta t = 2.5$ ms.

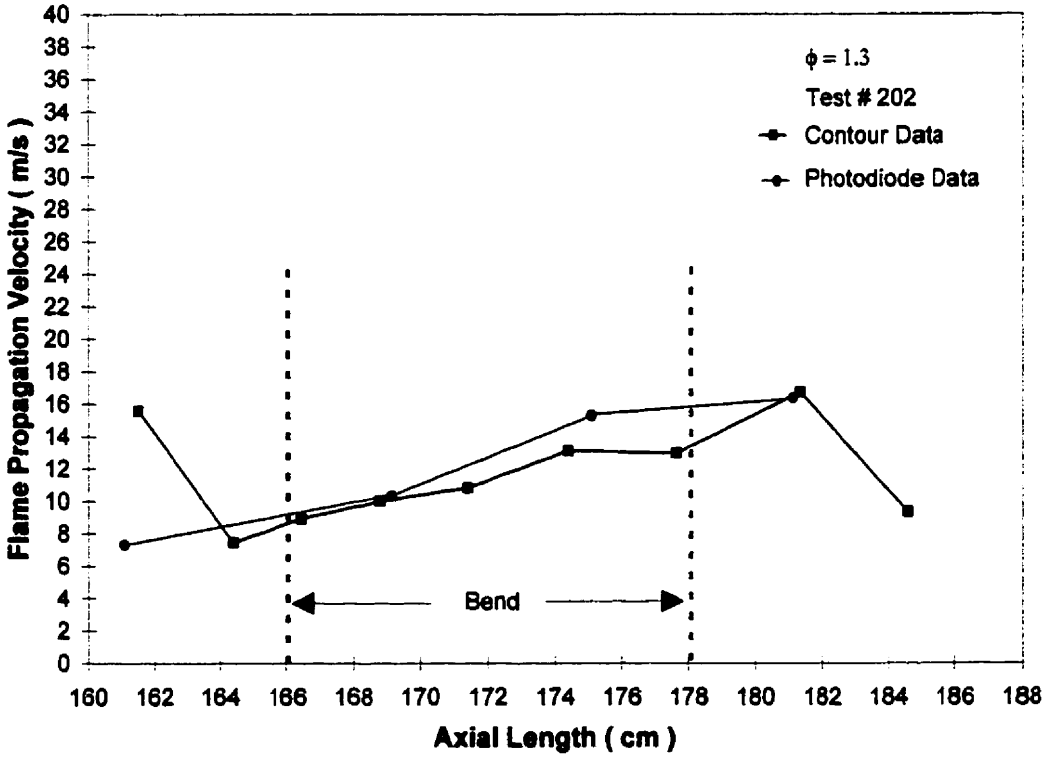

Fig 4.22 Comparison of centerline flame propagation velocities for Test # 202, as obtained from photodiode and contour analyses.

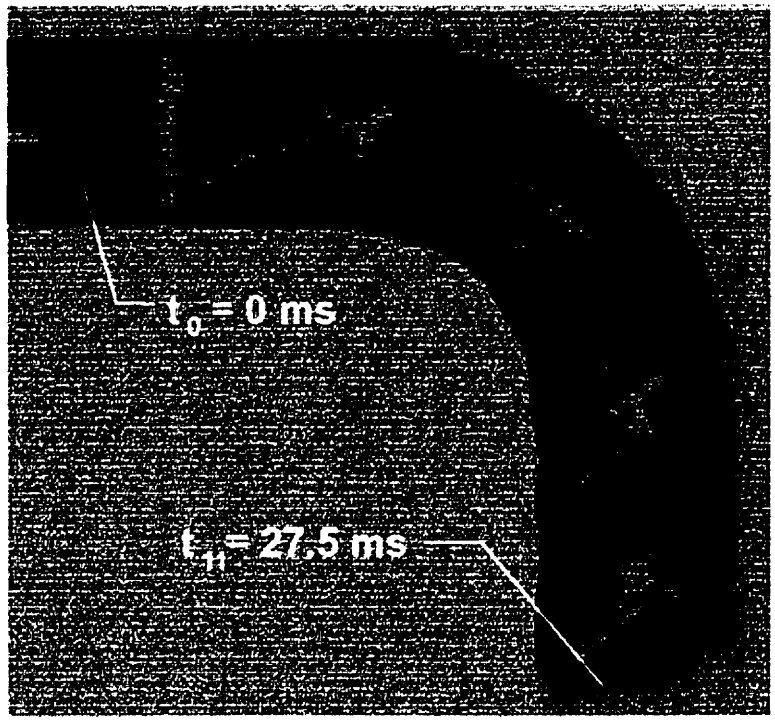

Fig 4.23 Flame front contours for $\phi = 1.4$. Test # 206, 400 fps. Time spacing between contours: $\Delta t = 2.5$ ms.

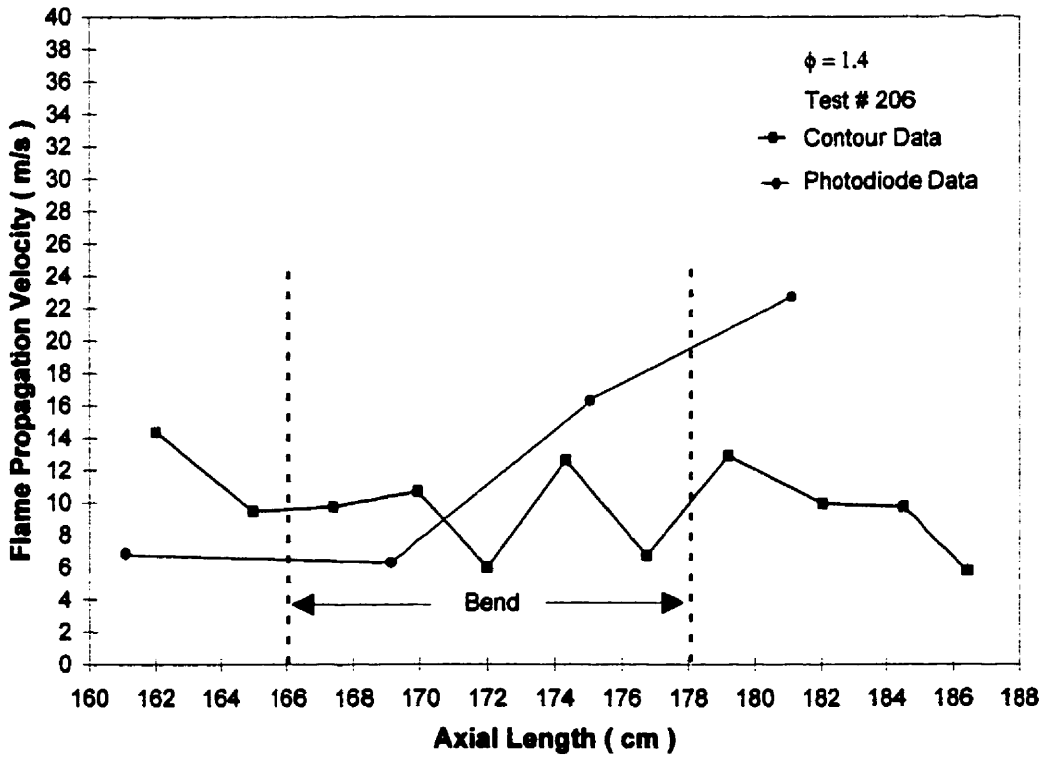

Fig 4.24 Comparison of centerline flame propagation velocities for Test # 206, as obtained from photodiode and contour analyses.

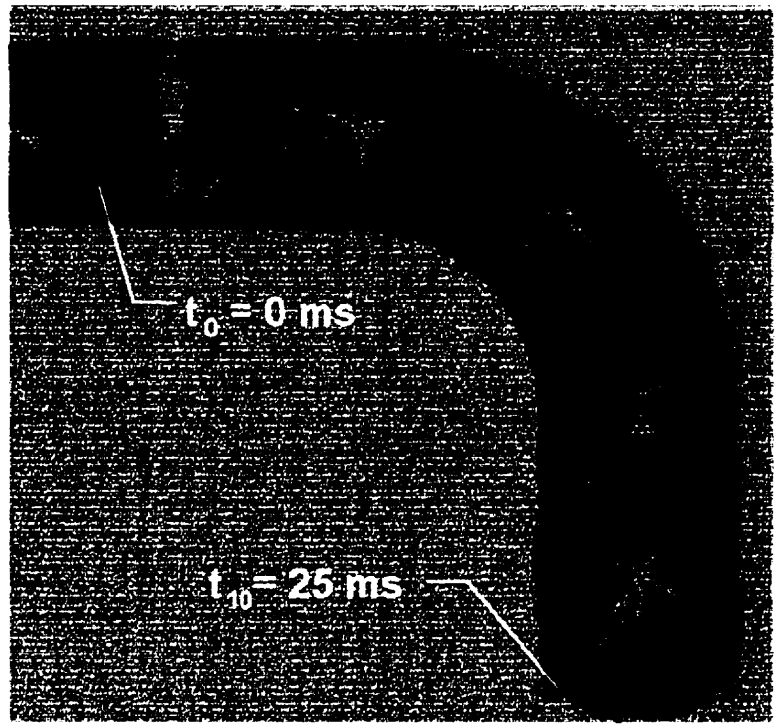

Fig 4.25 Flame front contours for $\phi = 1.5$. Test # 213, 400 fps. Time spacing between contours: $\Delta t = 2.5$ ms.

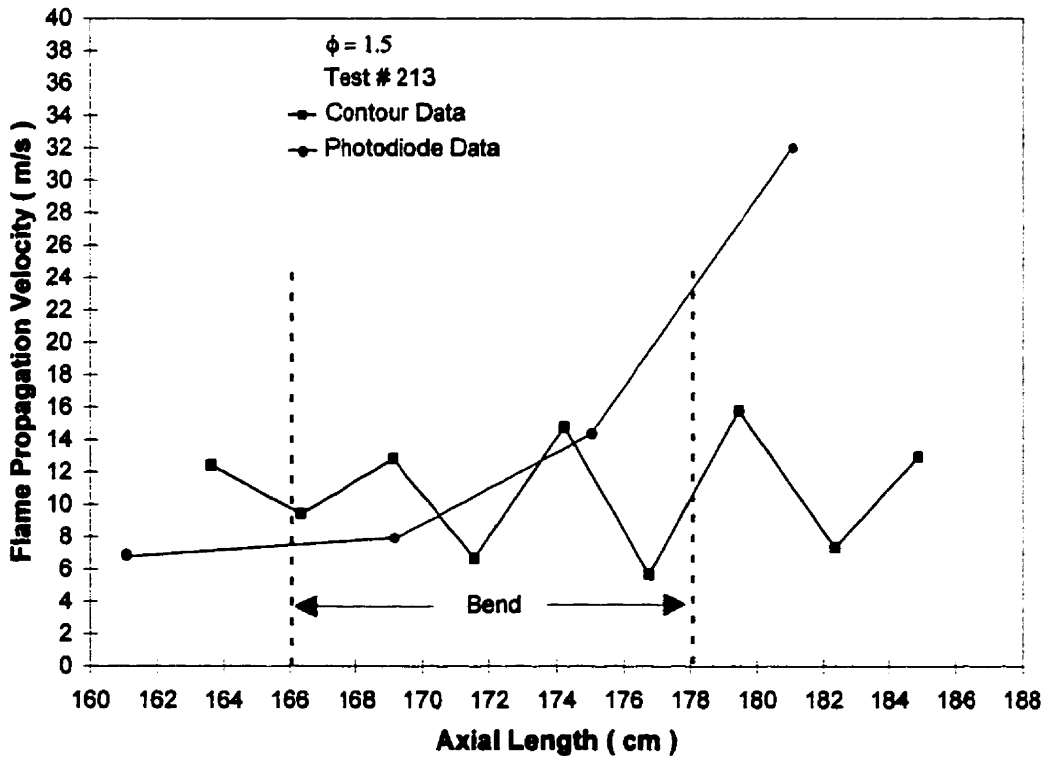

Fig 4.26 Comparison of centerline flame propagation velocities for Test # 213, as obtained from photodiode and contour analyses.

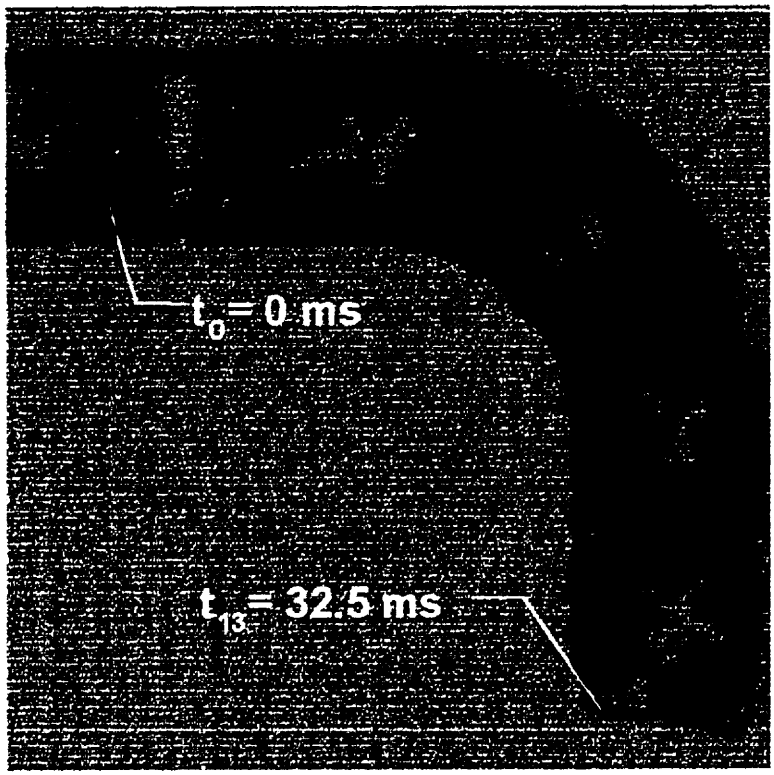

Fig 4.27 Flame front contours for $\phi = 1.6$. Test # 218, 400 fps.
Time spacing between contours: $\Delta t = 2.5$ ms.

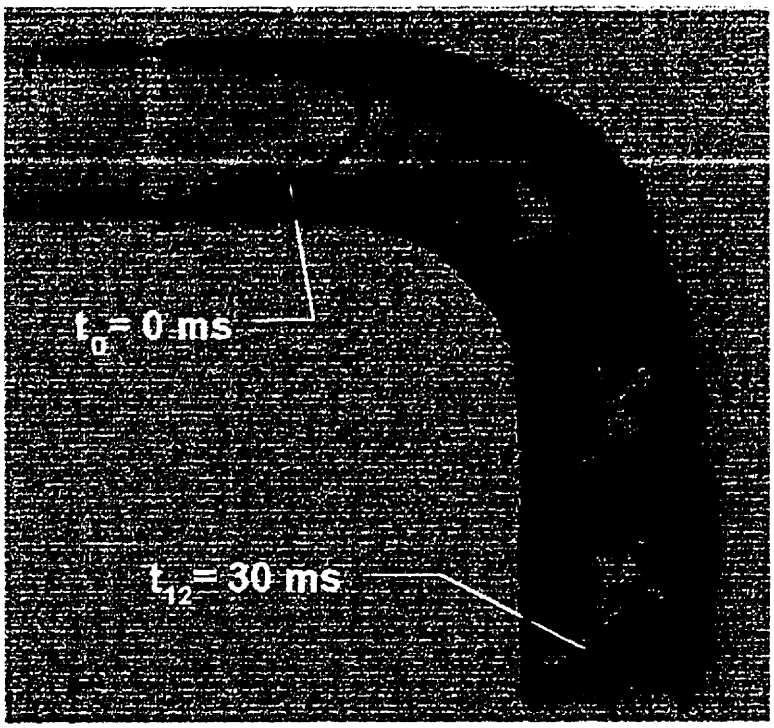

Fig 4.28 Flame front contours for $\phi = 1.7$. Test # 224, 400 fps.
Time spacing between contours: $\Delta t = 2.5$ ms.

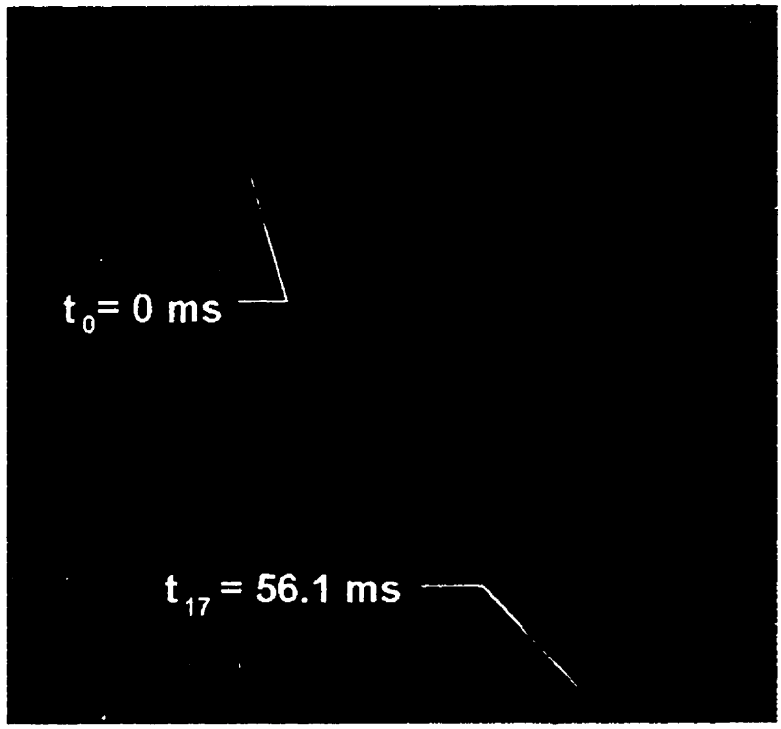

Fig 4.29 Flame front contours for $\phi = 1.8$. Test # 229, 300 fps.
Time spacing between contours: $\Delta t = 3.3$ ms.

4.6 Velocity Comparisons from Photodiode and Contour Methods

Photodiode data was obtained for Tests # 192, 198, 202, 206, and 213. Graphs were developed which compare the flame propagation velocity as obtained from the photodiode data and analysis of the respective contour plots. These graphs are shown in Figures 4.18, 4.20, 4.22, 4.24 and 4.26.

The first three figures show the comparisons for mixture compositions of $\phi = 1.1$, $\phi = 1.2$, and $\phi = 1.3$. The graphs indicate that flame propagation velocities determined through both methods correlate closely for the regions in and bordering the bend. With the exception of the first data points, the graph for mixture composition of $\phi = 1.3$ (Fig. 4.22)

shows the best agreement between both methods. Yet, among these three graphs, it has the largest difference between any two corresponding plotted points. At the location near 161 cm, the velocity difference between the methods is 8.1 m/s.

In the cases of mixture compositions of ϕ = 1.1 and ϕ =1.2, velocities obtained from photodiode data are slightly less than the values obtained from contour analysis in the region of the entrance and first half of the bend. In the region of the latter half of the bend and bend exit, velocity values from the photodiode data are slightly higher than those values obtained from contour analysis.

Figures 4.24 and 4.26 show the comparisons for mixture compositions of ϕ = 1.4 and ϕ =1.5. These graphs do not exhibit as close an agreement between the methods as the previous graphs. Similar to the graphs for ϕ = 1.1 and ϕ =1.2, the velocity values obtained from photodiode data are slightly less than those values obtained from contour analysis for the regions of the bend entrance and first half of the bend. In the region of the latter half of the bend and bend exit, the values obtained from the photodiode data are somewhat higher than the corresponding values obtained from contour analysis. However, in the region immediately after the bend, the velocity values from the photodiode method are much higher than the values obtained from contour analysis. At the location near 181 cm, the velocity differences between the methods is 11.7 m/s for the mixture composition of ϕ = 1.4 and 20.8 m/s for the mixture composition of ϕ =1.5.

Together, the five graphs show that more detailed velocity information can be obtained from analysis of the contour plots than from the photodiode data. The graphs indicate that velocity variations as seen in the inlet length of the duct are still present as the flame fronts propagate through the bend. The photodiode data does not show this effect.

4.7 Timeline Tracer

The Timeline Tracer Method, as previously detailed in Chapter 3, was a technique in which a heated column of unburned gas was formed by filament wires near the bend entrance. The heated column was convected together with the unburned gas flow ahead of the propagating flame front.

This method was used for the last 37 tests (Tests # 636 to # 672) of the test regimen. Of these tests, only one (Test # 643) resulted in the observation of a discernible timeline progression. The composite image of this test is shown in Fig. 4.30. The timeline was obtained for a mixture composition of $\phi = 1.4$, with the timeline forming approximately 100 ms after ignition of the gas mixture. The flame propagation for this test appeared to start off much slower than previous tests at this equivalence ratio. This resulted in the formation of a timeline during the initial development of unburned gas flow in the bend. Except near the inner surface, the timeline remained intact throughout its progress through the bend. In the other tests, the timeline was seen to dissipate immediately after being formed.

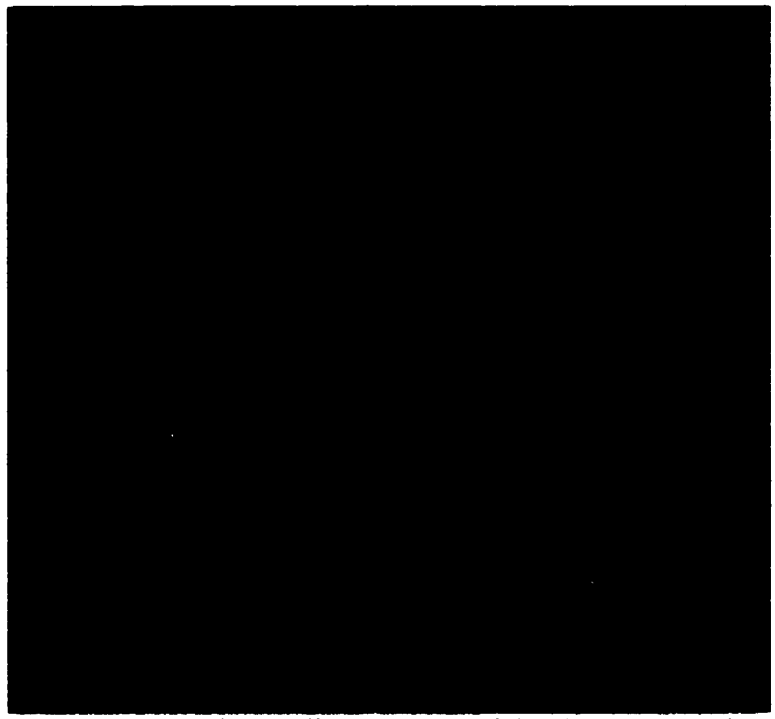

Fig 4.30 Composite Schlieren image of timeline progression. Test # 643, $\phi = 1.4$, 250 fps. Time spacing between timelines: $\Delta t = 12$ ms.

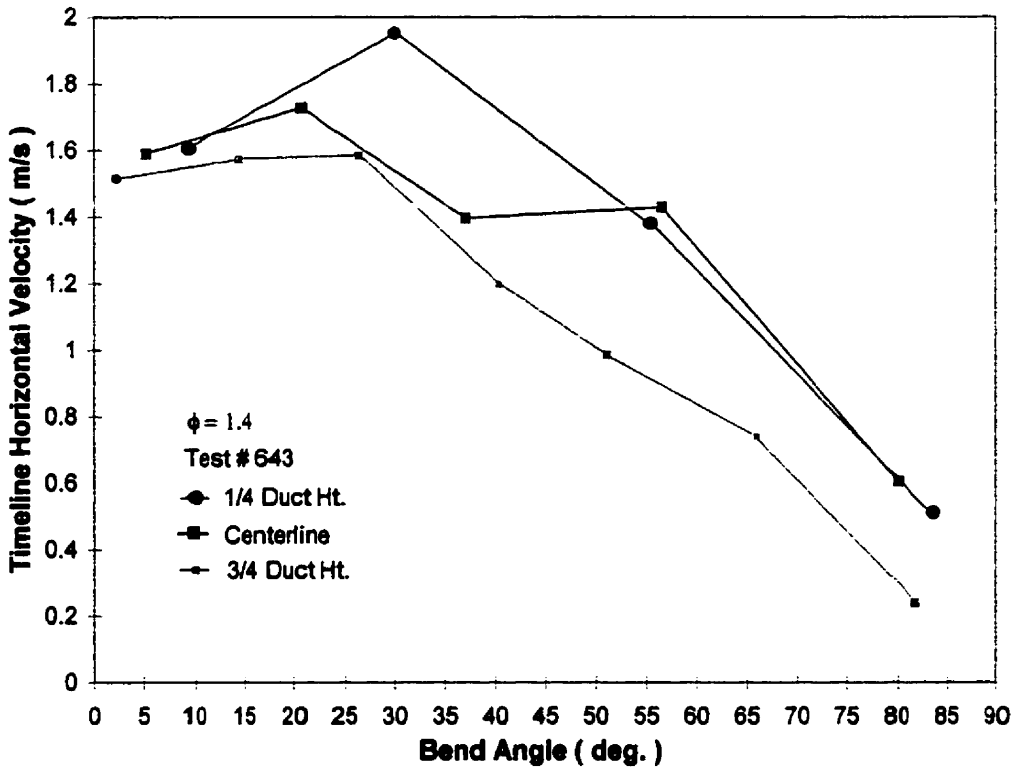

Fig 4.31 Horizontal velocities of timeline for 1/4 height, centerline, and 3/4 height planes. Test # 643.

Test # 643 was the first test performed from a new mixture batch. Subsequent tests from the same mixture batch resulted in fast flames normally expected for an equivalence ratio of 1.4. This variation among tests within a mixture batch was a common occurrence throughout the testing program. It will be discussed more in detail in the next chapter.

Since Fig. 4.30 is a time lapse composite image, a large distance separating the lines represents the timeline progressing quickly. This is shown clearly just before the timeline enters the bend. On the other hand, a close grouping of lines is indicative of a slowly progressing timeline. This is shown near the outer surface of the bend.

Figure 4.31 displays the timeline velocities in the horizontal direction for discrete points as measured at the 1/4 duct height, centerline and 3/4 duct height planes. Upon entering the bend, the timeline has an approximate horizontal velocity of 1.58 m/s. Consequently, the bulk flow of the unburned gas is also moving at this velocity. Therefore at this snapshot in time, the unburned gas has a "top hat" velocity profile. The graph shows that as the timeline progresses through the bend, the horizontal velocity at the different planes varies. At the 1/4 height and 3/4 height planes, the timeline accelerates in the first 1/3 of the bend. The timeline decelerates as it progresses through the remaining part of the bend. At the centerline plane, the timeline is seen to accelerate in the first 20° of the bend. It then decelerates for approximately 20° before it undergoes a slight horizontal acceleration. From 58° onwards to the end of the bend, the timeline continues to decelerate.

The timeline not only has a horizontal velocity component, but also a vertical component. This is indicated by the stretching of the timeline, particularly in the latter section of the bend. Near the inner surface of the bend, the timeline disappears entirely. This suggests that in this region, there are strong velocities in both directions.

Figure 4.32 shows the contour plot of the flame front progressing through the bend for Test #643. The time separation between the timeline entering the bend and the flame front entering the bend is approximately 400 ms. This flame front propagation is similar to others as shown in previous contour plots. The flame front enters into the bend with an asymmetrically curved profile. The leading edge of the flame front then moves closer to, and remains near the inner surface as it proceeds through the bend.

Figure 4.33 is a graph of the flame propagation velocities as measured at the 1/4 duct height, centerline and 3/4 duct height planes. Compared to the velocities of the unburned gas flow shown in the previous timeline graph, the flame propagation velocities are much higher. This indicates that the unburned gas continued to accelerate through the bend in the interim between timeline progression and flame front progression. The graph shows that in the bend, the flame front undergoes accelerations and decelerations at different points along the leading edge. Initially, the leading edge of the flame front has its highest velocity at the 1/4 duct height plane. As the flame front progresses through the bend, the points of the leading edge near the centerline and 3/4 duct height planes continue to

Fig 4.32 Composite Schlieren image of flame front contours. Test # 643, $\phi = 1.4$, 250 fps. Time spacing between contours: $\Delta t = 4.0$ ms.

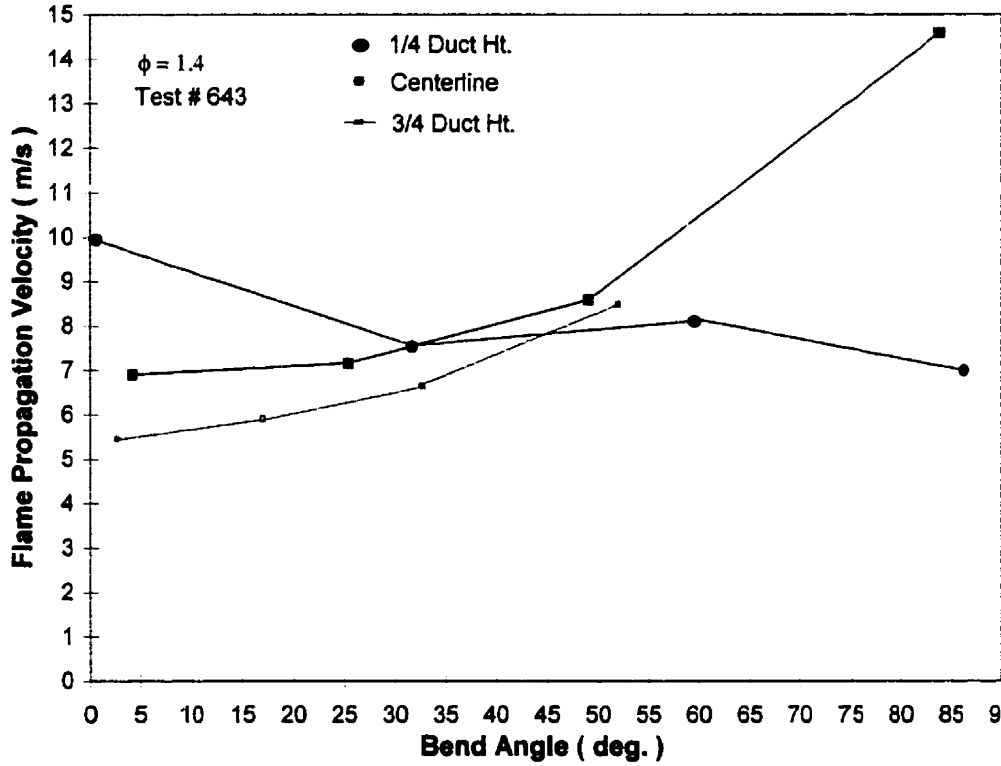

Fig 4.33 Comparison of 1/4 height, centerline, and 3/4 height, flame front contour velocities for Test # 643.

accelerate. The point of the leading edge at the 1/4 duct height plane slows down as the flame front goes through the bend.

The largest change in axial velocity occurs at the centerline plane. The flame front leading edge enters the bend at this plane at 6.9 m/s. It exits the bend at this plane at an axial velocity of 14.6 m/s. The velocity variations between for the other two planes are about the same. The flame front leading edge enters the bend at the 1/4 duct height plane at 10.0 m/s and leaves the bend at 6.9 m/s. At the 3/4 duct height plane, the flame front goes into the bend at an axial velocity of 5.4 m/s and leaves the bend at 8.5 m/s.

4.8 Comparison of Schlieren and Visible Images of Flame Fronts

Figure 4.34 shows representative images of flame fronts proceeding through the FPD bend. The two left images are consecutive visible flame images processed from Test # 206. These images were further enhanced using a negative pixel format similar to that used for the contour plots. The two right images are Schlieren flame images processed from Test # 656. These images were contrast enhanced. Both tests are for a mixture composition of ϕ = 1.4. The image sets were obtained using the high speed CCD camera at a frame recording speed of 400 fps. The time lapse between the visible images is 2.5 ms. The Schlieren images have a time lapse of 5.0 ms. This is due to a slower flame propagation during the Schlieren test.

Fig. 4.34 Side by side comparison of visible (left) and Schlieren (right) flame images. Visible images: Test # 206, $\phi = 1.4$, 400 fps, Time lapse $\Delta t = 2.5$ ms. Schlieren images: Test # 656, $\phi = 1.4$, 400 fps, Time lapse $\Delta t = 5.0$ ms.

The overall shape of the flame front profile for both image sets are somewhat different. The differences reflect the particular characteristics of the Schlieren method. The Schlieren images show a dark area in the leading edge profile of the flame front. The dark area has a uniform shading across the entire profile of the flame front. This dark area is indicative of a density gradient within the flame front. In the absence of a pressure gradient, the density gradient is only attributable to temperature differences. Knowing that the highest temperatures of combustion occur in the combustion zone, it can be

concluded that the dark areas in the Schlieren images are at higher temperatures than the gray or white regions.

The areas of high temperature in the Schlieren images are much narrower than the corresponding areas shown on the visible images. In fact, the zone of combustion in the visible images extends further back along the inner and outer surfaces of the duct bend. These rear combustion areas along the duct surfaces must be at a lower temperature than the main combustion zone of the flame front. The lower temperature in those regions may be a consequence of the high heat transfer rate between the combustion products and the relatively cool duct surfaces.

4.9 Other Observations

4.9.1 Full Duct Images

Figure 4.35 shows the images of a typical propagating flame front through the entire duct. These images are for a preliminary test performed to determine test procedures and to check out apparatus operation. The images were recorded using a standard, 30 fps home camcorder. Each subsequent image therefore represents a time increment of 33 ms. As a result, the entire duration of this trial was a little less than 0.8 seconds. The negative pixel format was again used for processing of the images to better display the flame front features.

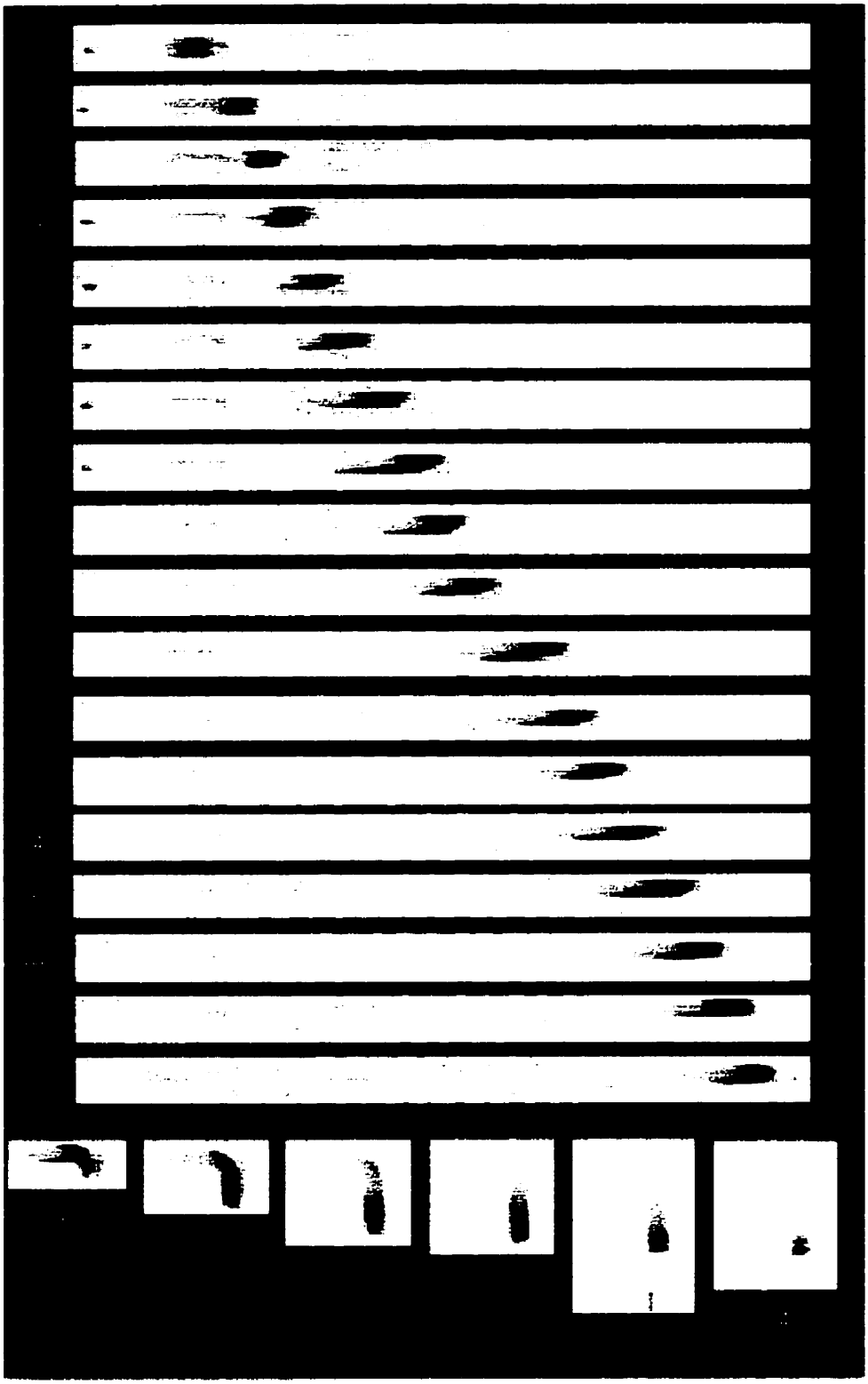

Fig. 4.35 Flame front progression through FPD . Preliminary test with BERNZOMATIC propane. $\phi = 0.8$, 30 fps. Time interval between images: $\Delta t = 33.3$ ms.

For this particular test, the propane used was a BERNZOMATIC brand torch propane. This propane is used for propane torches, camping stoves, gas barbecues, etc. The contents of this transportation grade propane were about 95% propane. The remaining constituents were higher order hydrocarbons. The equivalence ratio for this test mixture was $\phi = 0.8$.

Image 1 through 18 are consecutive images which show the flame front progressing through the straight inlet section of the FPD. The leftmost black spot in the first eight images is the ignition spark. The first image shows that the flame front has propagated quickly through the first 1/12 th of the inlet section (approximately 15 cm). The flame front then continues to propagate but at a slower velocity. By the fifth image, the flame front profile has distinctly become more parabolic-shaped, but with a slight distortion. It also begins to stretch out in the lengthwise axial direction.

Image 8 clearly shows the flame front with the distorted and stretched, asymmetrically curved profile. At this point, the flame front is about halfway through the inlet section. Its propagation velocity from ignition has averaged about 3 m/s. The flame front proceeds through the remaining half of the inlet section with a slightly lower average flame propagation velocity (approximately 2.5 m/s). Image 17 and 18 in particular, show a noticeable reduction in propagation velocity of the flame front just as the flame front begins to enter the bend.

Image 19 through 24 show the flame front progressing through the bend and into the exit section. The flame front proceeds into the bend along the inside surface of the bend as shown in image 19. Comparing images 19, 20, 21 and 22 shows that the flame front propagation velocity varies as it leaves the bend and proceeds into the exit section. Once the flame front reaches the end of the exit section, combustion of the unburned gas continues even while the unburned gas is escaping through the pressure equalization valve. This is shown in image 23 where the black smear in the lower portion of the image is the combustion occurring in the escaping gas stream just outside of the FPD equalization valve. Image 24 shows the last moments of combustion of the residual unburned gas remaining in the FPD.

4.9.2 Quenching Phenomenon

Figure 4.36 shows the images of a propagating flame front which is quenched in the bend of the FPD. The equivalence ratio for this test mixture was $\phi = 0.8$. Images were recorded using the high speed CCD camera at a frame rate of 180 fps. The images are arrayed in a column arrangement with succeeding images displayed one under the other.

The first column shows how the flame front enters the bend. Its behavior at this point is not abnormal in comparison to the behavior of other flame fronts. In the second column, the images show that the forward movement of the flame front begins to stagnate. The latter images in the column show that combustion continues, however the combustion zone remains stationary at a point slightly over halfway through the bend. This location is at the axial length of 174 cm. The flame front begins to waver back and forth and it

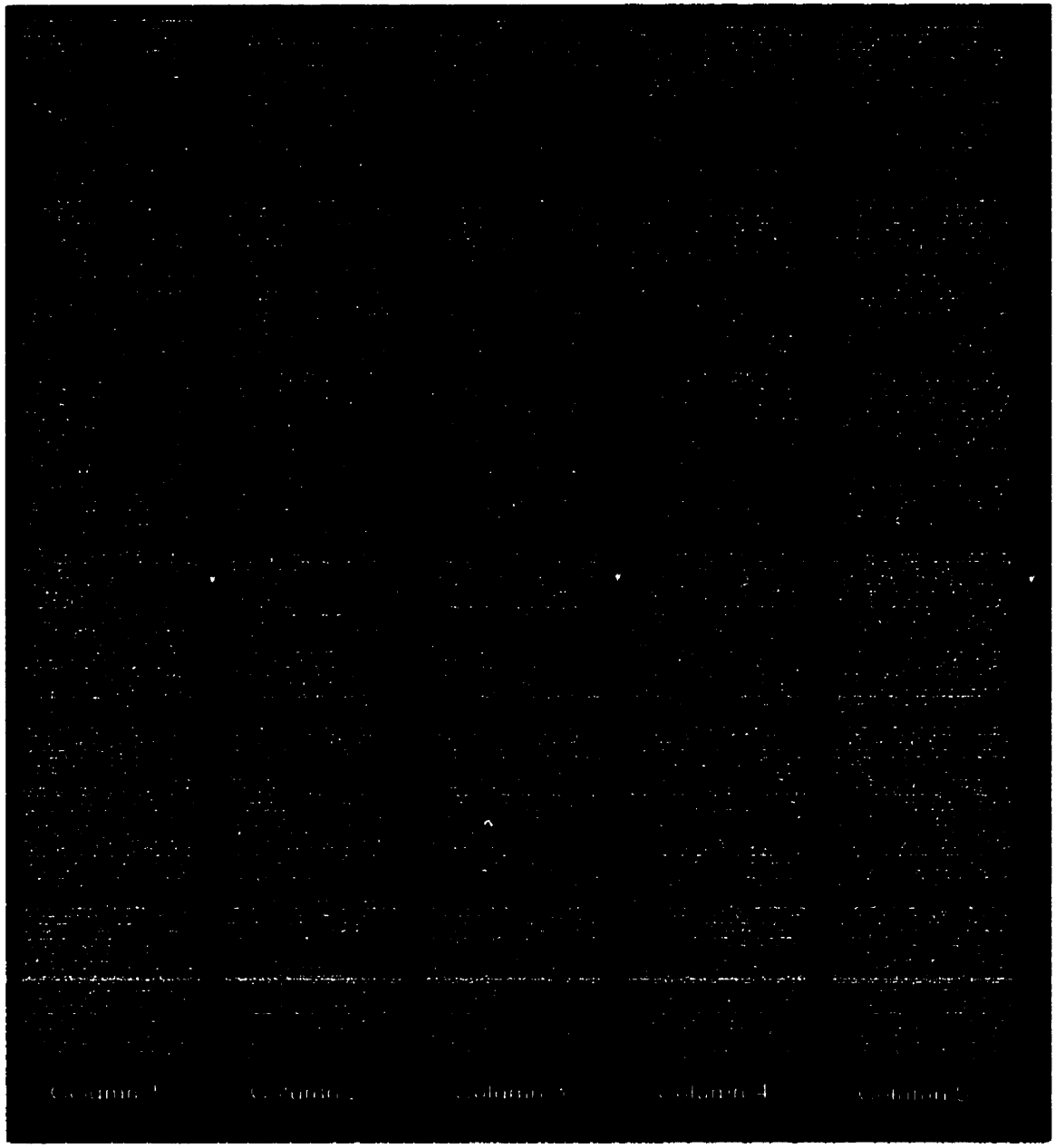

Fig. 4.36 Quenching of a flame front in a bend. Test # 248, $\phi = 0.8$, 180 fps. Time interval between images: $\Delta t = 5.6$ ms.

remains in this region for approximately 28 milliseconds. This is shown in Fig. 4.37, which graphs the flame front position along the axial centerline with respect to time.

Column 3 shows the flame front breaking away from its initial stationary position. It then proceeds forward through the bend and into the straight exit section. In column 4, the flame front is seen to slow down and finally stop at a second stationary point in the exit section. This is also shown in Fig. 4.37 at the axial length location of 181 cm. The first three images in column 5 show the sustained combustion and flame front wavering at the second stationary point. The graph shows that at this location, the flame front wavering occurs between the 178 cm and 181 cm locations along the axial length of the FPD. The flame front wavers for 125 ms. The final images in Column 5 show the cessation of the combustion reactions and the quenching of the flame front.

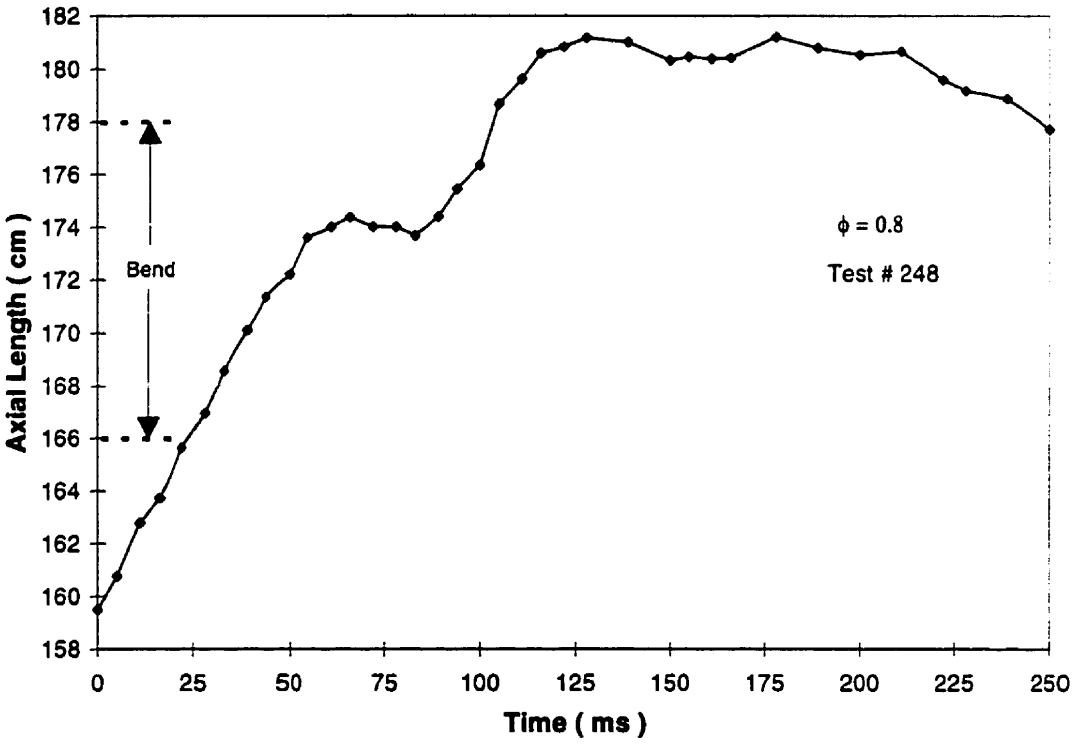

Fig. 4.37 Quenching of a flame front in a bend. Flame front location along axial centerline, with respect to time. Test # 248, $\phi = 0.8$.

Flame front waverings were observed for other test conditions as well. These conditions were for mixture compositions of $\phi < 0.9$ and $\phi > 1.7$.

4.9.3 Large Scale Turbulent Flame Fronts

It was also observed that some flame profiles were wrinkled and rough with large scale eddies. Other flame fronts showed convoluted fold structures within the flame. These characteristics are evidence of turbulent, premixed combustion.

Figure 4.38 shows images of a particular behavior exhibited by some turbulent flame fronts. The main characteristic of this type of flame front was the cyclic expansion and contraction of the combustion zone as the flame front progressed through the bend.

The expansion and contraction phenomenon was observed only for three tests out of the entire test regime. The equivalence ratio for this test mixture was $\phi = 1.2$. Images were recorded using the high speed CCD camera at a frame rate of 400 fps. Similar to the arrangement in Fig. 4.36, images are arrayed in columns in which succeeding images are displayed one under the other.

The first column shows the flame front entering the last few centimeters of the inlet duct section. As previously shown in other figures, the dark areas differentiate the combustion zone. Image 1 in the first column shows an even shading of the combustion area. The leading edge of the flame front is blunt and does not have the smooth, asymmetrically

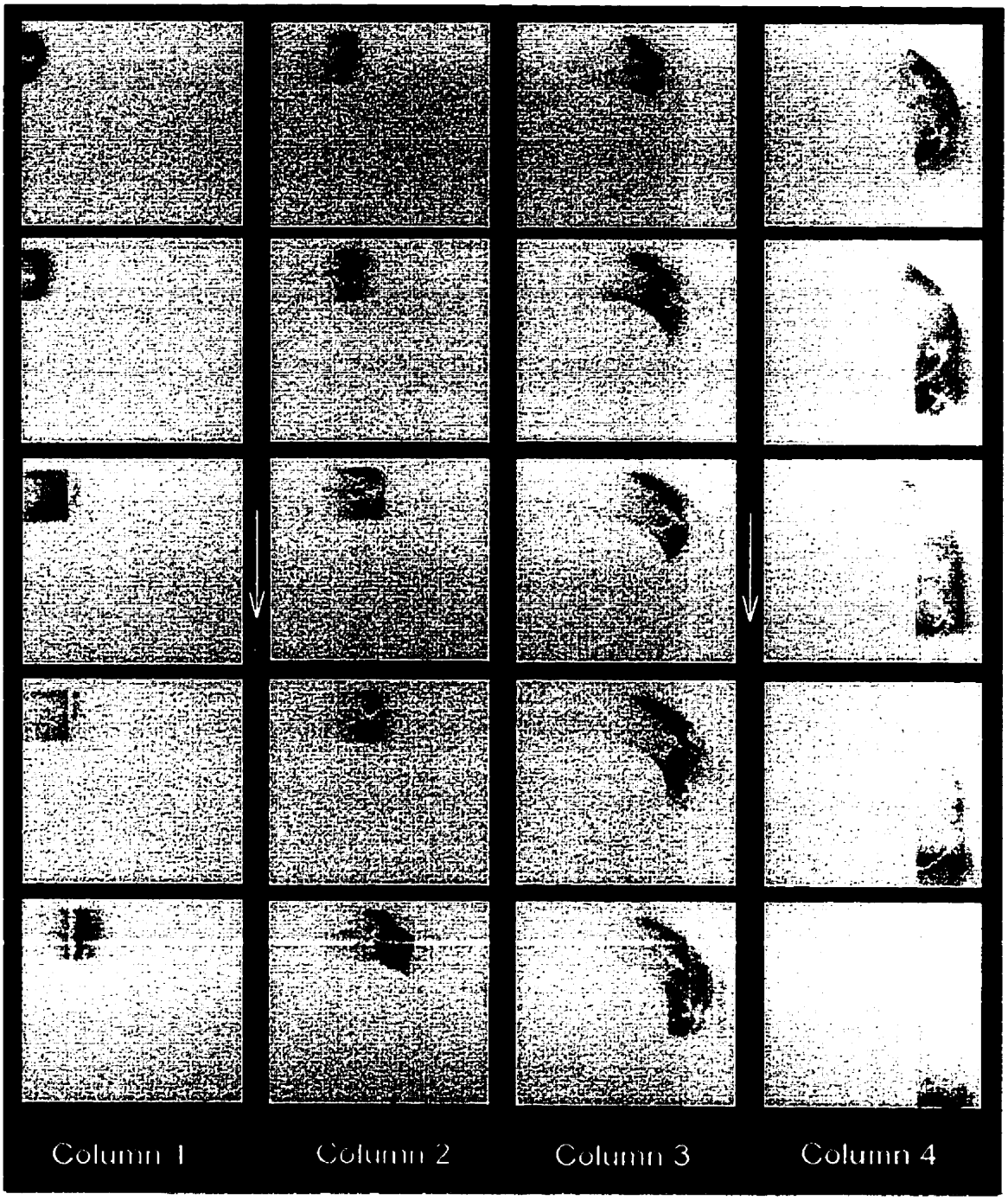

Fig. 4.38 Turbulent flame front phenomenon. Test # 197, $\phi = 1.2$, 400 fps. Time interval between images: $\Delta t = 2.5$ ms.

curved profile normally expected. Image 2 has about the same area, but there is a darker shading at the leading edge of the flame front. Image 3 and 4 are similar. There is an even shading of the extended combustion zone (Image 3), and then the combustion zone is shortened and the zone itself is slightly darker at the leading edge (Image 4).

The last image in Column 1 and the first image in Column 2 form another flame front expansion/contraction set. This effect continues as the flame front progresses into the bend as shown in the images in Column 3. The flame front proceeds into the bend with the leading edge near the inner surface. Column 4 shows the flame front entering the exit section of the FPD. Again, the phenomenon continues to occur.

The last image in Column 2 clearly shows the convoluted structure of the flame front. Although this image only provides information in two dimensions, the complexity shown necessitates a three dimensional effect in which the flame structure is folded in among itself.

Chapter Five

Discussion

5.1 Introductory Remarks

This chapter will link the results of the tests with combustion and fluid mechanics. This will provide evidence that flame front propagation through a 90° bend is affected by downstream flow structures in the bend. Further to this will be an analysis of the sources of errors in the test results. This analysis will provide information to gauge the relative quality and confidence level of the obtained test data.

5.2 Flammability Limits

From Turns [16], the lean limit of flammability for propane/air mixtures is $\phi = 0.51$. The rich limit of flammability is $\phi = 2.83$. These limits were determined by the "tube method". This method employs a long, vertically-oriented tube of circular cross section. Ignition of the test mixture occurs at the bottom of the tube.

The lean flammability limit in this work was determined to be $\phi = 0.75$. The differences between the measured and the literature value can be attributed to the square cross section and horizontal orientation of this FPD. Part of the difference can also be attributed to the precision in producing repeatable mixture compositions. This will be discussed later in the Sources of Error section of this chapter.

The richest mixture composition tested was for an equivalence ratio of $\phi = 2.0$. This mixture composition was less than the rich limit of flammability as indicated in the literature.

5.3 Unburned Gas Flow in Bend

As discussed in Chapter 2, curved duct flow is characterized by the development of secondary flows. The extent of the secondary flow development in the bend is quantified by the Dean number. Since the bend geometry remained the same throughout the test regimen, the curvature ratio remains constant and the Dean number is therefore strictly dependent on the Reynolds number.

The Reynolds number is described by the following equation:

$$Re = D_h S_{mix} / (\mu / \rho)$$

where: S_{mix} is the unburned mixture velocity ahead of the flame front.
D_h is the characteristic length equal to the hydraulic diameter of the duct. ($D_h = 3.386$ cm)
μ is the viscosity of the unburned mixture. ($\mu = 1.80 \times 10^{-5}$ N s /m^2)
ρ is the unburned mixture density. ($\rho = 1.20$ kg / m^3)

The main component in all the test mixtures was air. All tests were performed at atmospheric pressure. The temperature of the gas mixtures did not vary more than 3° C over the course of the test period. As a consequence, the density and viscosity of the gas mixtures were considered constant. As a result, the largest dependent factor in the Reynolds number is the unburned mixture velocity.

Table 5.1 shows Reynolds and Dean numbers for a range of unburned gas velocities. Regarding the Dean number, it must be remembered that the unburned gas velocity is initially zero prior to ignition. As a flame front develops and begins to propagate through the FPD, the unburned gas undergoes transient changes in its mainstream velocity. Consequently, the unburned gas flow in the bend steadily develops through the low, intermediate and high Dean number regimes.

The propagation velocity of the flame is an important parameter in analysis of the flame and flow structure interactions. The region near the entrance to the bend is where the flame front will begin to interact with the developed and evolving flow structures in the bend. An estimate of the unburned gas velocities can be obtained from the continuity equation. Consequently, the unburned gas velocity profiles at this location most accurately details the conditions of the flow structures in the bend.

Velocity (m/s)	Re	Dn
0	0	0
0.5	1129	752
1.0	2257	1505
1.5	3386	2257
2.0	4514	3010
2.5	5643	3762
3.0	6772	4514

Table 5.1 Gas velocities with corresponding Reynolds and Dean numbers.

It has been observed that the flame propagation velocities continually change as the flame front progresses through the FPD. Since the initial interactions between the flame and flow structures are of short duration, the flow conditions just prior to the interactions can be considered as quasi-steady state.

Figure 5.1 compares the average unburned gas velocities 5 cm in front of the bend (location 161 cm) for different mixture compositions as characterized by equivalence ratio. The velocities stay below 0.85 m/s, with the Dean number not exceeding 1250. These velocities were calculated assuming no heat transfer from the burned gas to the environment. With heat transfer, the density ratio (ρ_b /ρ_u) increases. This results in slightly higher unburned gas velocities from those shown in the figure. The velocities for the rich conditions of ϕ =1.6, 1.7 and 1.8 have been revised from the flame propagation velocity plots shown in Chapter 4. Data values considered grossly out of the norm were removed, so as to reduce the standard deviations. The corresponding Dean numbers are also plotted as a secondary field.

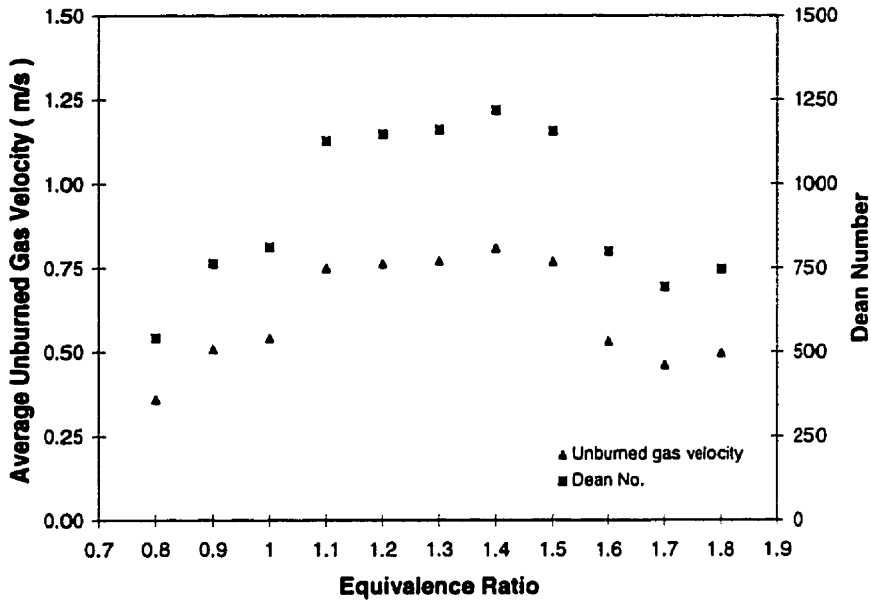

Fig. 5.1 Effect of equivalence ratio on average unburned gas velocities and Dean number at bend entrance.

The graph can be broken down into 3 distinct regions. The first region envelops the slightly rich mixtures ($1.1 < \phi < 1.5$). Here, the highest average unburned gas velocities are encountered.

In the region delineating stoichiometric and lean mixtures ($\phi \leq 1.0$), the average unburned gas velocities at the bend entrance are seen to decrease the closer the mixture composition approaches the lean flammability limit.

A similar decrease is seen in the region delineating very rich mixtures ($\phi \geq 1.6$). In this region, the average unburned gas velocities decrease as the mixture compositions

approach the rich flammability limit. However, the average velocity decreases are more gradual compared to what is seen with the lean mixtures.

The development of secondary flows in the form of Dean vortices can only occur for laminar flows. The accepted critical value of the laminar to turbulent Reynolds number is Re = 2300 ~ 2400. Berger [11] argues that flow in curved pipes has been shown to be more stable than in straight pipes. As a result, the laminar to turbulent transition point is at a higher critical Reynolds number. Berger also contends that the transition point may be two or more times larger than the accepted value of Re = 2300 ~ 2400. Therefore, according to Table 5.1 and Fig. 5.1, the flow of unburned gas through the bend can be characterized as laminar.

Figure 4.30 shows the composite Schlieren image of the timeline progression in the unburned gas flow. Since no dissipation of the timeline is seen, the flow could be described as laminar. In addition, the subsequent timeline velocity graph (Fig. 4.31) shows that the unburned gas remains in the laminar regime.

The appearance of a flame front provides some quantitative information about the motion of the flow ahead of the flame. Figure 5.2 shows untouched images of flame fronts in the 5 cm ahead of the bend. Except for the ϕ = 0.8 image, all images are from the tests reflected in Figs. 4.15 through 4.28. The image for ϕ = 0.8 was obtained from Test # 248 (also see Fig 4.36, Flame quenching).

Comparing these images shows that there are distinct differences in the flame fronts produced from different mixture compositions. Flame fronts produced from lean mixtures of equivalence ratio $\phi < 1.0$ and rich mixtures of $\phi \geq 1.6$ have smooth and distinct leading edges. There are extended "regions" behind the leading edges which are evenly luminescent. These "regions" may simply be the projected side views of the parabolic surfaces of the thin combustion zone. These parabolic flame front profiles are similar to a Poiseuille flow profile, which describes laminar, incompressible flow in pipes. None of the Schlieren trials showed evidence of pressure waves during flame propagation through the bend. Therefore, the assumption of incompressible gas flow appears valid. Since the flame front is the interface between the burned and unburned gases, defining the parabolic profile of the flame front as the Poiseuille flow is a valid supposition. This would then define the unburned gas flow for these mixture compositions as laminar.

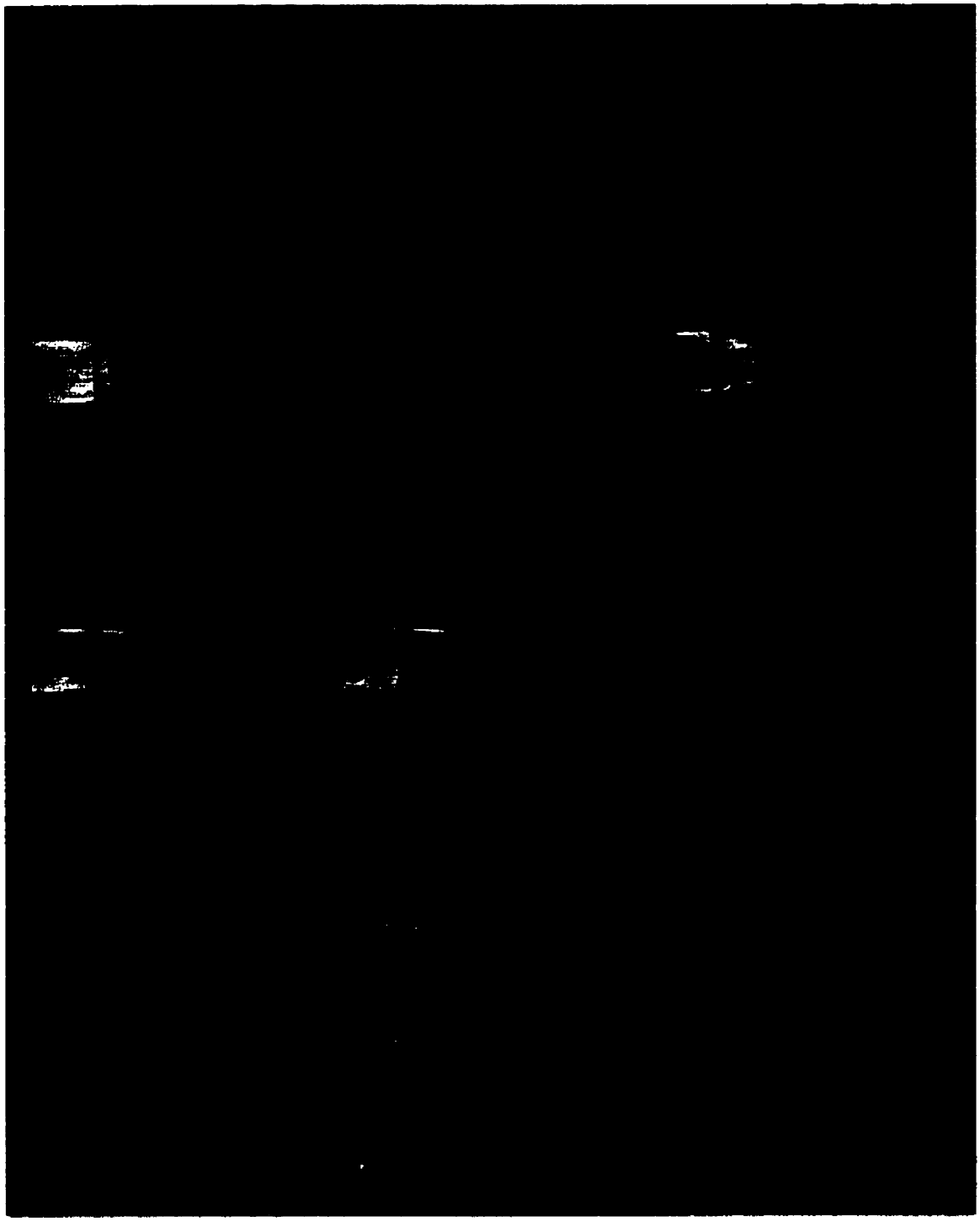

Fig. 5.2 Comparison of flame fronts near bend entrance for different mixture compositions.

The flame fronts for mixture compositions of $1.5 \geq \phi \geq 1.0$ show extended combustion regions behind the leading edges. These regions appear to be wrinkled with areas of slight distortion or striations. The regions also have varying luminescence. The leading edges of the combustion zone are fuzzy and not as distinct as those for the lean and very rich mixture conditions. These characteristics are evidence of the beginnings of turbulent flame propagation. No large-scale, duct size, easily discernible eddies are visible. Therefore, the turbulent structures are of smaller scale. Turns [16] and Kuo [17] describe this flame regime as the wrinkled laminar flame regime.

Kuo [17] states that fine scale turbulence occurs in the range of $2300 \leq Re \leq 6000$. This correlates to the upper values of Reynolds number in this work and makes the existence of wrinkles possible.

Using these arguments, unburned gas velocities below 1.0 m/s are clearly flows that are laminar in character. Unburned gas flow with velocities above 1.0 m/s are not as well characterized. The flame fronts may be laminar, in transition, or turbulent in nature.

5.4 Flame Front Profiles in Entrance and First Half of Bend

The tests performed in this research program resulted in the collection of flame propagation velocity data and visual images of flame front profiles in the FPD bend. The nature of the flow induced by the propagating flame fronts is transitionary and non-steady. Therefore, a complete understanding of the complicated phenomenon of secondary flow and flame front interactions can not be ascertained with a project of this

limited scope. However, the flame front and flow interactions can be characterized by the collected data. The characterizations can be substantiated by previous research in secondary flow structures in bends.

In all cases shown in Fig. 4.15 through 4.29, flame fronts propagate through the bend with the leading edge of the flame front close to the inner surface of the bend. This was seen to occur for all mixture conditions and flame front velocity regimes. The literature citations provide evidence to the possible causes of this flame front behavior.

As previously stated, the development of secondary flows is dependent on centrifugal, viscosity and inertia effects. Increasing the velocity of the fluid flow at the bend entrance results in higher centrifugal forces due to axial acceleration. This causes the core flow or the part of the flow not affected by boundary effects, to move closer to the outer surface of the bend. As a result, the boundary layer near the outer surface thins and the layer near the inner surface thickens. The displacement of the boundary layer along the outer surface promotes the development of secondary flows. These secondary flows, in the form of Dean vortices, remove high momentum fluid from the outer surface and direct it longitudinally towards the inner bend. This redirection of fluid occurs along the sidewalls of the duct. To satisfy continuity, the low momentum fluid along the inner bend is directed back towards the outer bend. This outward directed flow is a crossflow through the centerline of the duct.

Berger's [11] paper contends that the development of the secondary flow results in a pressure differential between the inner and outer regions of the bend. The high pressure in the outer region forms a stagnation point which results in a high resistance to fluid flow in that region. The maximum pressure variation, and subsequently the highest flow resistance occur approximately 45° through the bend. As a result, the streamwise velocity of the fluid decreases near the outer surface and increases near the inner surface. Experimental work by Bara [7], Humphrey [5] [12], Taylor et al. [13], and numerical work by Pratap, et al. [8] provide additional evidence of this effect.

In the first half of the bend, the flame front proceeds into a region where there is a longitudinal pressure variation. The streamwise flow of unburned gas ahead of the flame front is accelerated in the region of the inner bend. The gas flow profile then becomes distorted. The result is that the propagating flame front is stretched to match the profile of the unburned gas flow.

Figures 5.3, 5.4, and 5.5 display the axial flame propagation velocities at the 1/4 height, centerline and 3/4 height positions in the bend. The figures show that in the first half of the bend, the flame propagation velocities, and conversely the unburned gas velocities are greater near the inner surface than near the outer surface.

The flame speed is also affected by the pressure gradient, since flame speed is inversely dependent on pressure. Consequently, a slight increase in the flame speed would be expected for the flame front near the inner surface compared to the portion of the flame

front near the outer surface. This effect would tend to elongate the flame front profile further in the region of the inner surface.

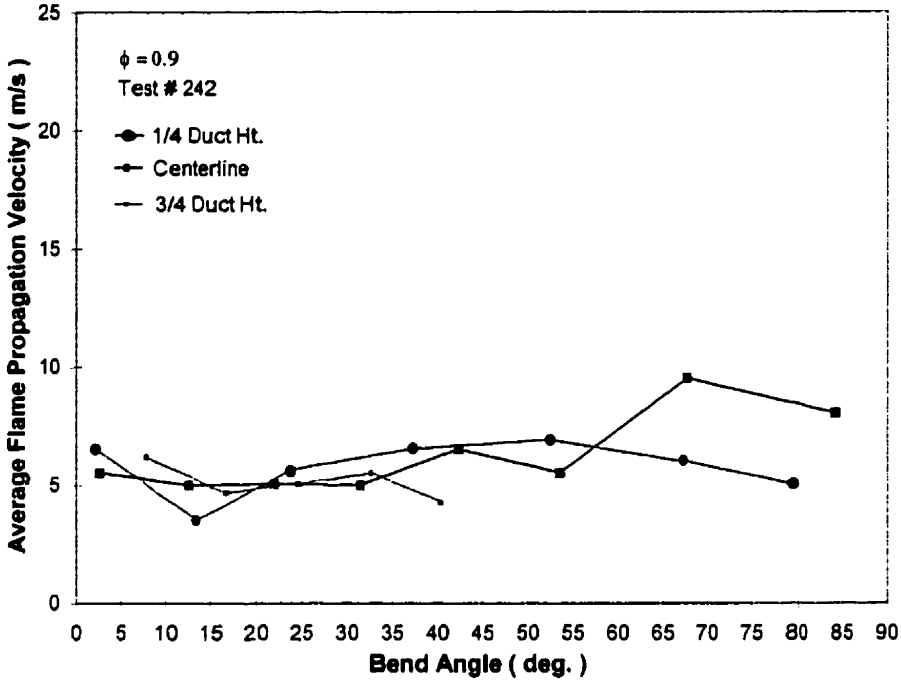

Fig. 5.3 Comparison of 1/4 height, centerline, and 3/4 height, flame front contour velocities for Test # 242.

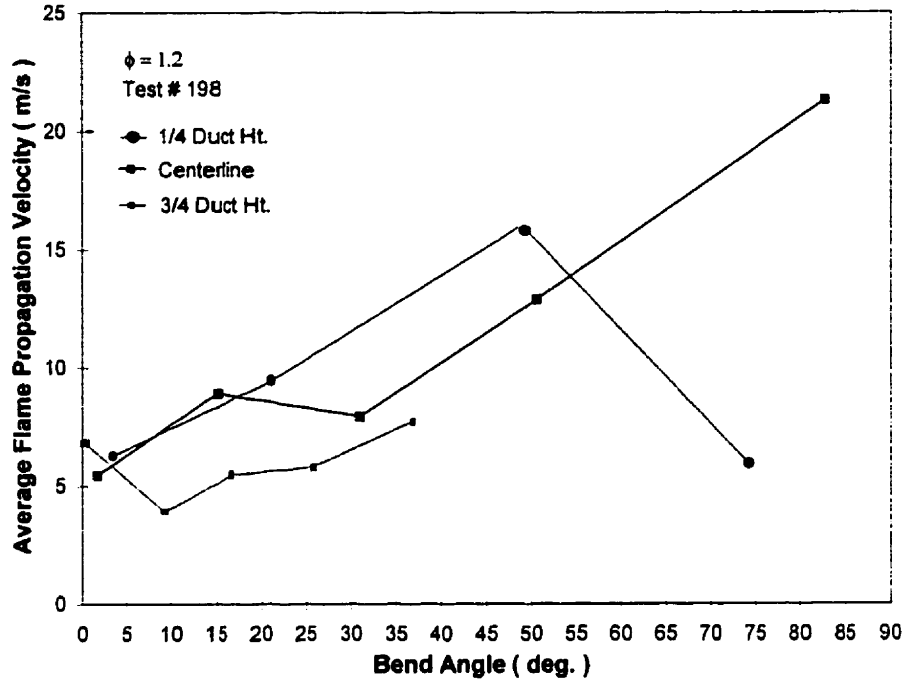

Fig. 5.4 Comparison of 1/4 height, centerline, and 3/4 height, flame front contour velocities for Test # 198.

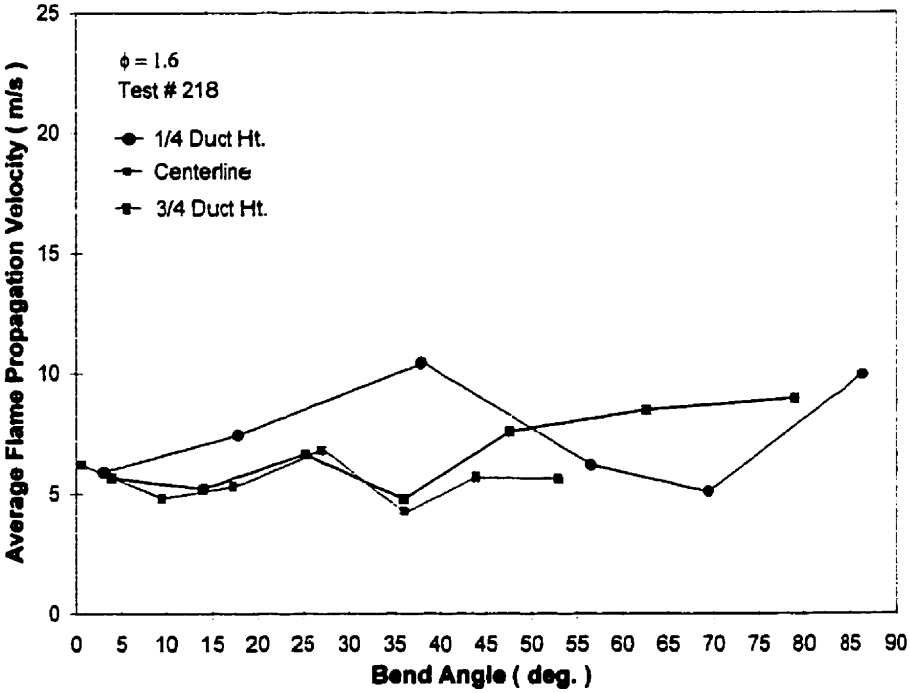

Fig. 5.5 Comparison of 1/4 height, centerline, and 3/4 height, flame front contour velocities for Test # 218.

With stretching of the flame front, the possibility of quenching exists. However, the confluence of the secondary flow vortices near the inner surface reduces this possibility due to the negative flame stretching resulting from this interaction, Lee and Santavicca [14]. The surface area along the inner section of the bend is smaller than a comparable straight section. In addition, Kalb and Seader [18], [19] indicate that the temperatures of the secondary flows which merge in the inner bend region are close to the side wall temperatures. This results in small temperature gradients between the unburned gas and the inner wall. Subsequently, these effects result in a low convective heat transfer rate near the inner surface compared to other regions of the FPD. Since heat transfer to the FPD structure is minimal, the combustion reactions are sustained.

The overall effect of flame stretching and slight increase in flame speed is the sharpening of the flame front leading edge in the vicinity of the inner surface. This is shown in the flame front contour figures in Chapter 4. In most of the figures, the most pronounced sharpening of the leading edge of the flame fronts occurs near the halfway location of the bend.

Bara [7], Humphrey [5] [12], Taylor et al. [13] have shown experimentally that the pressure differential results in effects that can be observed in the fluid flow upstream from the entrance to the bend. Again in the contour figures in Chapter 4, this effect is shown by the gradual movement of the tip of the flame front from above the centerline toward the bottom surface of the bend entrance.

In comparison to the work of Sato *et al.* [1], the flame front profiles in the entrance and first half of the bend are very similar. This suggests that scale of the duct has minimal effects on the shape of the propagating flame front. Figure 5.6 shows an example of a flame front profile obtained by Sato for an equivalence ratio $\phi = 1.0$.

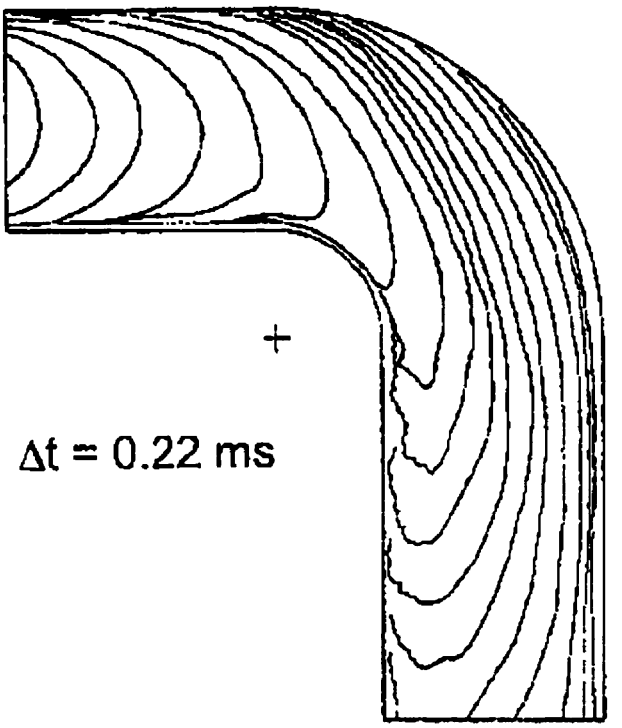

Fig. 5.6 Typical flame front contour profile through bend by Sato, Sakai and Chiga. Front end of duct closed, back end open. $\phi = 1.0$.

5.5 Flame Front Profiles in Second Half of Bend and Exit

In the latter half of the bend, the influence of the secondary flows begins to wane due to the decrease in the inertia of the core flow. As a result, the pressure gradient between the

inner and outer surfaces decreases. This causes the flow along the inner surface to decelerate.

The flame front contour figures from Chapter 4 show that in the second half of the bend, the leading edge tips of the flame fronts move from near the inner surface back towards the axial centerline. With further progression into the exit section of the FPD, the sharp leading edges of the flame front profiles become more curved shaped.

The shape of the flame front profile is dependent on the unburned gas flow conditions. Consequently, the flame propagation velocities reflect the changes in the flow of the unburned gas. As shown in Fig. 5.3, 5.4 and 5.5, the flame propagation velocities from approximately 45^{0} onwards are now greatest at the centerline positions.

5.6 Timeline Results

The timeline progression in Fig. 4.30 reveals the nature of the unburned gas flow ahead of the flame front. Granted, this was the only discernible timeline captured, its existence provides further evidence to the development of secondary structures in the bend.

The Sato timeline progression shown in Fig. 5.7 is very similar to the images captured in Test # 643. Although not shown in Fig. 4.30, the dashed line denoting a boundary layer or secondary flow development near the inside surface of Fig. 5.7 was also observed in Test # 643.

The timelines in the Sato case and in Test # 643 are distinctive in that as the timeline progresses through the bend, it becomes stretched and bow-shaped. These effects are most pronounced near the inner surface of the bend. Also, the distance between adjacent timeline views is large near the inner surface region and small near the outer surface. As Sato purports, this evidence implies that the gas flow velocity is greater near the inner regions than in the outer bend regions. It is also consistent with the development of a stagnant region near the outer bend and the attendant formation of secondary flows.

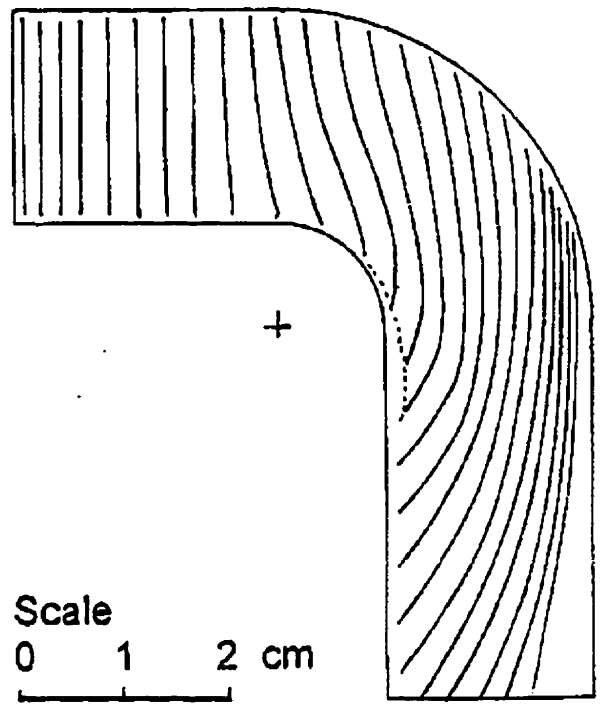

Fig. 5.7 Timeline variation through bend by Sato, Sakai and Chiga. Front end of duct closed, back end open. $\phi = 1.0$. Time interval between timelines: $\Delta t = 0.22$ ms.

It would be expected that the secondary flows such as Dean vortices would distort or dissipate timelines simply because of their vortical structures. This would be especially evident if the timeline shifts off the axial centerline. It is highly probable that this is what

happened to the timelines formed in the other tests. However, if the timeline remains centered, then the only secondary flow component is the longitudinal crossflow from the inner bend surface to the outer bend surface. The timeline would then remain intact.

5.7 Combustion and Flame Profiles Along Outer Bend

The contour figures in Chapter 4 (Fig. 4.15 to 4.29) show high concentrations of flame front contours in the vicinity of the outer surface of the bend. These high concentrations of contours are apparent in all the figures except for the ones for mixture compositions of ϕ = 1.1, 1.2 and 1.3. The close spacing of the contour lines indicates that flame propagation velocities in this region are low compared to the velocities in other regions of the bend. The figures also imply that flame propagation in this region occurs more in the radial direction than in the axial direction.

In the outer region of the bend, the unstable boundary layer along the concave wall results in the development of Görtler vortices. With increased Dn number, the Görtler vortices can breakdown into turbulence which should speed up the flame.

The interaction of these respective boundary layers and the dynamics of the secondary flows can result in conditions where fluid from the interior of the duct can be easily convected to the boundary layer near the outer surface of the bend. These turbulent or "turbulent-like" conditions would suggest that upon advancement of the flame front, rapid combustion would ensue. However, it is just the opposite.

As discussed by Berger [11], a number of studies have indicated that heat transfer rates are higher in coiled pipes than in straight pipes. It has been shown that the high heat transfer involves the additional mixing resulting from the secondary flows. The mechanism for heat transfer in this case is different than most researched cases due to the dynamics of a propagating flame front inside a duct.

The outer surface area of the bend is larger than for a comparable straight duct. This results in a large heat transfer area. There is also the situation where the secondary flows are separating into two individual recirculating streams near the outer bend region. These flow streams are at a high temperature due to the preheating of the unburned gas which is being cross convected from the inner surface to the outer surface. Consequently, a large temperature gradient develops between the unburned gas and outer wall surface. As a result, the local Nu number is high in this region, Kalb and Seader [18], [19].

In addition, the section of a flame front propagating near the outer surface undergoes positive flame stretching due to the separation of the crossflow. This positive flame stretching increases the heat transfer area of the flame front which results in high heat transfer from the flame. The overall result of these high heat transfer effects is that the combustion reactions slow down near the outer bend surface.

Once a flame front has progressed through a portion of a bend segment, the secondary flows in that segment cease. However, due to inertia, movement of the unburned gas

continues in the remaining portion of the segment near the outer bend surface. Heat transfer increases and the combustion reactions slow down. As the flame front proceeds slowly outward towards the outer surface, only unburned gas in the boundary layer remains. This gas gets squeezed between the advancing flame front and outer wall.

It is speculated that two actions are occurring at this time. The first action is the combustion of some unburned gas. The second action has the remaining unburned gas being drawn along the outer surface since it is still forms part of the unburned gas mass still moving further down in the duct. Görtler or turbulent vortices could then still be present. This continuous motion may aid in the convective transfer of heat from the flame front to the outer surface. This would have the effect of reducing the rate of preheating of the reactants near the flame front.

Referring back to the figures in Chapter 4, the concentration of contours near the outer surface indicates that the combustion reactions continue in this region, even when the leading edge of the flame front has extended some distance into the exit section of the FPD. However, reactants must still be available for combustion. The distance between adjacent contours is small. This suggests that the advancing flame propagation velocity is on the order of magnitude of the laminar burning velocity. Near the wall, the contours are even closer together. The implication here is that the flame propagation velocity, or more accurately, the flame speed is decreasing further due to the high heat transfer to the wall. However, quenching of the flame does not occur and the consequence is simply a decrease in the combustion rate.

5.8 Flame Propagation Velocities

5.8.1 Straight Inlet Section

The graph in Fig. 4.1 shows that the flame front propagations for mixture equivalence ratios between $\phi = 1.1$ and $\phi = 1.4$ are characterized by relatively steady average flame propagation velocities through the straight inlet section of the FPD. However, a pattern of slight variation in the flame propagation velocities is evident.

This range of mixture compositions resulted in the formation of "strong" flame fronts which were inclined to quickly advance forward through the FPD without exhibiting any oscillatory behavior. These flame fronts were not appreciably affected by the physical boundary conditions of the FPD and heat transfer to the environment was of insignificant concern. A distinct, loud "whack" sound was also exhibited by these flame fronts as they exited the FPD through the valve opening. These flame fronts also tended to be turbulent-like near the bend entrance as shown in Fig. 5.2.

In Figs. 4.2 and 4.3, the graphs show that for mixture conditions less than $\phi = 1.1$ and greater than $\phi = 1.4$, large variations in the average flame propagation velocities are evident in the straight inlet section of the FPD. This behavior is evident as well in Fig. 5.8 where the velocity vs. time graph is shown. This velocity profile was determined from analysis of the video images of the flame front progression through the FPD as

shown in Fig. 4.35. The profile is plotted only for flame propagation through the inlet section of the FPD and ends at the entrance to the bend.

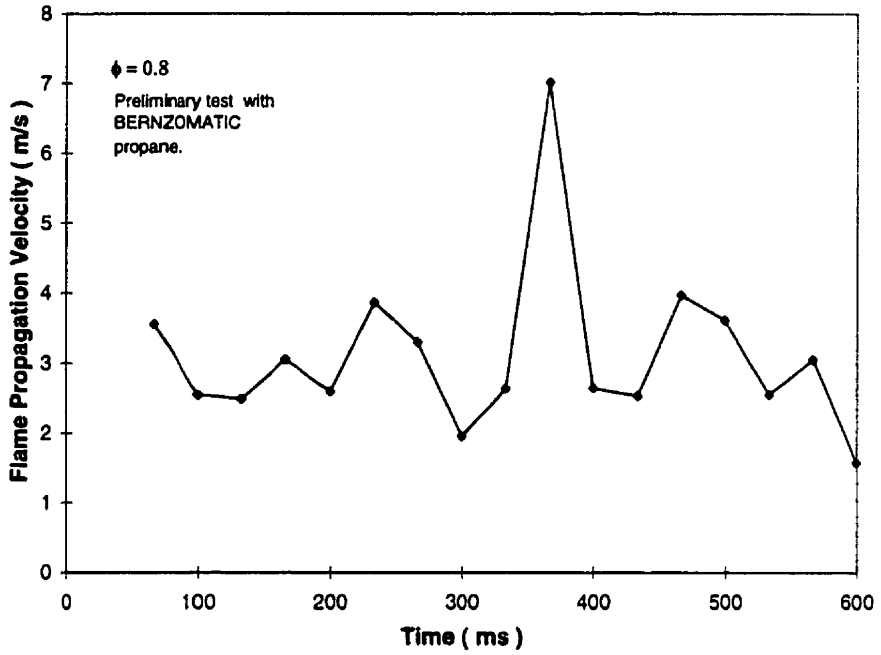

Fig. 5.8 Flame propagation velocity profile through straight inlet section of FPD. Data obtained from contour analysis of images in Fig. 4.35.

The flame front propagations for mixture conditions less than ϕ =1.1 and greater than ϕ = 1.4 are characterized as "weak". These "weak" flames usually started out slowly just after ignition. Only when the flame fronts were approximately 30 to 40 cm downstream of the spark plug, did they begin to accelerate. In addition, some "weak" flame front propagations were observed to oscillate to some degree in the duct. In general, the flame fronts did not oscillate back and forth more than 5 to 10 cm. These oscillatory flame propagations were mainly seen to occur for the very rich mixture conditions. However oscillatory flame behavior was also observed for many tests conducted with mixture composition of ϕ = 0.8.

As shown in Fig. 5.2, the flame fronts for the "weak" mixture conditions are mostly laminar in the bend entrance region. When these flame fronts exited the FPD through the valve opening, they usually created a low "whistle" or "whisp" sound.

5.8.2 Bend and Exit Sections

The flame propagation velocity stabilization effect, which slows the flame down, is seen to occur at the entrance to the bend. This adds further confirmation that the flow dynamics of the unburned gas in the bend has upstream effects. For all mixture compositions with the exception of ϕ =1.8, the average flame propagation velocities at the entrance to the bend are less than 6.2 m/s. More significantly, the standard deviations for all the mixture conditions of $\phi < 1.7$ are low at this duct position. This implies that regardless of the flame front behavior in the straight inlet section of the FPD, the existence of the bend tends to have a stabilizing influence on the average flame propagation velocity in this region. For the slightly rich mixture conditions of ϕ =1.1 to ϕ =1.4, the stabilizing influence is manifested as a decrease in the average flame propagation velocity in comparison to the mean velocity experienced in the rest of the straight section. For the mixture conditions of $\phi < 1.1$ and $\phi > 1.4$, the stabilizing influence is reflected in a reduction in the variation in propagation velocity.

The graphs in Figs. 4.1, 4.2, and 4.3 show that average flame propagation velocities for all mixture compositions increase as the flame fronts progress through the bend. Figures 4.18, 4.20,4.22, 4.24, and 4.26 indicate that this is not necessarily always the case. It is

expected that the flame propagation velocities calculated from the contours are more indicative of the actual conditions. This is because there are more contour data points than photodiode data points. Therefore, for the test cases in Fig 4.24 and Fig. 4.26, the contours indicate that the average flame propagation velocity does not increase over the length of the bend.

Using a high speed camera to record flame propagations through the bend and then performing contour analysis provided more details to obtain accurate flame propagation velocities than using the photodiode method. However, contour analysis proved to be more time consuming than using the photodiode system. In the region of the bend, the data from the photodiodes is rough and should be viewed with a degree of skepticism. This is because the flame front profiles change as they propagate through the bend. The photodiodes are only illuminated by the flame front profile along the centerline. Therefore, the resulting photodiode data does not necessarily reflect the region of greatest axial propagation velocity.

The graphs show that the average flame propagation velocities decrease as the flame fronts exit the bend and proceed through the straight exit section of the FPD. The exceptions being for the mixture conditions of $\phi = 1.0$ and $\phi = 1.8$. The entrance region of the straight exit section of the FPD (position 181 cm) continues to see profile changes in the flame fronts as seen in the contour images of Figs. 4.15 to 4.29. As a result, the considerations in the previous paragraph remain valid and the photodiode data from this duct position must be viewed as being coarse as well.

The data obtained from the photodiode set at the end of the exit section (position 200 cm) was not substantiated by high speed camera images. However, in this region, the unburned gas is severely restricted in its passage through the exit valve. This would cause the unburned gas velocity to decrease. Also, the contour images show that the flame front profiles in the region far down from the bend exit are now only slightly distorted and are developing "top hat" and more axially symmetric profiles. This suggests that once the flame front is near the end of the exit section, its profile may be symmetrical and similar to the flame front profile at the entrance to the bend. As a result of these factors, the flame propagation velocities calculated from the photodiode data at position 200 cm may in fact be sound.

Although the photodiode data results in coarse average flame propagation velocities in the region of the bend and immediately after, they do reflect actual trends. In most trials, high speed video show that the flames indeed speed up in the bend and slow down in the exit section.

Figure 5.9 shows the flame propagation velocities for varying equivalence ratio from the study by Sato *et al.* [1]. The flame propagation velocities between the ignition point and bend entrance continuously increase for mixture compositions of $\phi \geq 0.6$. For the mixture composition of $\phi = 0.6$, a short region of constant flame propagation velocity is seen.

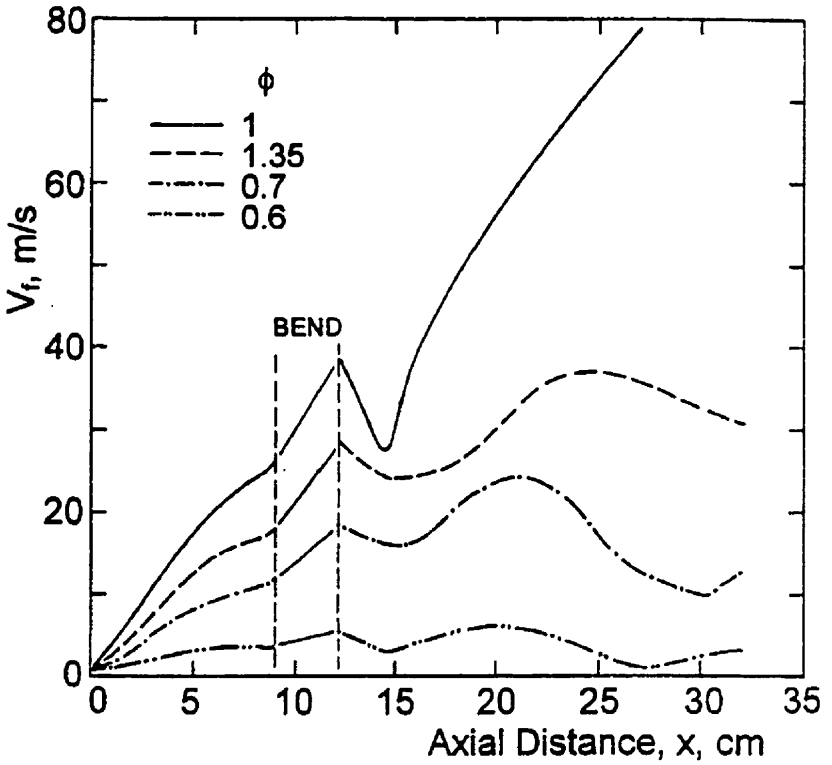

Fig. 5.9 Flame propagation velocities obtained by Sato, Sakai and Chiga. Front end of duct closed, back end open.

The graph shows that there are no large velocity variations in the inlet section, although there is a slight slowing of the flame fronts just before they enter the bend . This is in contrast to what was seen in the present work where large velocity variations were observed and distinct, local velocity minimums were measured near the bend entrance. However it must be noted that the Sato duct apparatus had a short inlet section of 10 cm in comparison to the 168 cm long inlet section of this FPD. In addition, the Sato apparatus also had a fully open back end condition.

At the entrance to the bend, Sato measured flame propagation velocities on the order of 18 to 22 m/s. This is 3 to 4 times higher than the flame propagation velocities measured at the bend entrance in the present study.

Sato *et al.* determined their results in the bend region by straight line interpolation of the bend entrance and bend exit propagation velocities. This method although crude, does verify that the flame propagation velocity increases as the flame front propagates through the bend. The same conclusion can be drawn in the present study.

In Sato's exit section, the flame propagation velocities are seen to decrease in the immediate region after the bend. The propagation velocities then begin to increase again after a distance of approximately 3 cm from the bend exit. This trend was observed in this work as well.

A scaling factor of F_s=1.69 was calculated using the ratio of the hydraulic diameters of the present FPD and the Sato duct. Length comparisons indicate that the exit sections of both apparatus are proportionally the same. The 3 cm length in the Sato duct correlates to a length of 5 cm in the FPD. This is near the 181 cm axial location on the FPD. At this location, Fig. 4.1 shows that there is also a decrease in flame propagation velocity from the bend exit for the same mixture compositions of $\phi = 1.1$ and $\phi = 1.4$ used by Sato. It is noted that the mixture equivalence ratio denoted as $\phi = 1$ in the graph, is referred to as $\phi = 1.06$ in the Sato paper.

The Sato graph shows that for mixture equivalence ratios of ϕ =1.06 and ϕ =1.35, they observed higher flame propagation velocities at the duct end than at the exit from the bend. For the mixture composition of ϕ = 1.06 , this was seen as a continuous acceleration through the exit section after the initial deceleration out of the bend. The flame propagation velocity profile for mixture composition of ϕ =1.35 shows some variation as the flame front proceeds through the exit section. However, the final flame propagation velocity was still higher than the velocity at the exit from the bend.

These exit section flame propagation velocities are much higher than the comparable velocities obtained in the FPD. In the latter part of the exit section, Sato indicates that flame fronts accelerate for the mixture compositions of ϕ = 1.06 and ϕ = 1.35. In the present study, flame front deceleration is evident in the latter part of the exit section. These contrasts can be explained by the fact that Sato's duct had the capability of fully opening the duct end. In the present FPD, the fully opened condition refers to a valve opening which has an open area that is 3% of the duct cross section. The result is that unburned gas flow from the duct end is restricted. This causes the gas to decelerate as it approaches the duct end and limits velocity development within the duct.

5.9 Visible and Schlieren Images

The Schlieren images shown in Fig. 4.34 indicate that the highest density gradients occur in the vicinity of the leading edge. This is valid as combustion theory stipulates that the highest combustion temperatures occur in this region. The visible images show that the combustion zone extends for some distance behind the leading edge of the flame front.

When these images are compared side by side with the Schlieren images, it can be concluded that there is a temperature gradient within the combustion zone. The high temperatures are attained at the leading edge of the flame front, while the regions further behind the leading edge attain lower temperatures.

Both sets of images show characteristics of turbulence. In the case of the visible images, these characteristics are evident as convoluted, unevenly shaded structures in the combustion zone. The Schlieren images show the turbulent structures as striations behind the leading edge of the flame fronts.

Interestingly, the Schlieren images do not show any density gradients in the unburned gas flow ahead of the flame front. As previously described, with the development of secondary flows in the bend, it is expected that pressure gradients will form. These pressure gradients would result in density gradients that the Schlieren system should be able to resolve.

The absence of evidence of pressure gradients may be explained by the fact that the pressure gradients caused by secondary flows are small in these cases. The Schlieren apparatus used in this project may simply not have the resolution to detect these small pressure gradients.

5.10 Quenching of Flame Front

The quenching phenomenon as shown in Fig. 4.36 only occurred for very lean and very rich mixture conditions. In these instances, the cause of the quenching phenomenon is the removal of heat from the combustion reactions. For these very rich and very lean mixture compositions, quenching occurs when the rate of heat transfer from the reactions exceeds the rate of heat generation in the combustion zone.

The locations where flame quenching occurred did not necessarily always happen in the bend as shown in this example. In many cases, flames were quenched in the inlet or exit sections of the FPD.

It was observed that oscillatory or wavering motion by the flame front and quenching were accompanying phenomena . In many instances, a flame front would waver, but it would not necessarily be quenched. On the other hand, any flame front that was quenched almost always exhibited some degree of oscillatory behavior.

As indicated by Brailovsky [20], oscillatory flame propagation occurs when the thermal diffusivity of the mixture is exceeded by the molecular diffusivity of the limiting reactant. In essence, the Lewis number (Le) can no longer be approximated as unity. The result is that stable, forward projecting flame propagation reverts to an unstable, oscillatory mode.

Further investigation of quenching and oscillatory flame propagation was beyond the scope of this project. However, the observed phenomena does seem to conform to the

above interpretation. In the flame front, heat transfer to the wall reduces the temperature of the burned gas. This, in turn, reduces the rate of heat convection from the burned gas to the unburned gas. The flame front begins to oscillate. If the rate of heat transfer to the walls increases, then the flame front is quenched.

5.11 Turbulence

As previously discussed, the flame front characteristics and flow conditions were not limited to the laminar regime. Many images of turbulent flame fronts were recorded during this research project. An example of such a flame front is shown in Fig. 5.10. This flame front profile is similar to the images shown in Fig. 4.38.

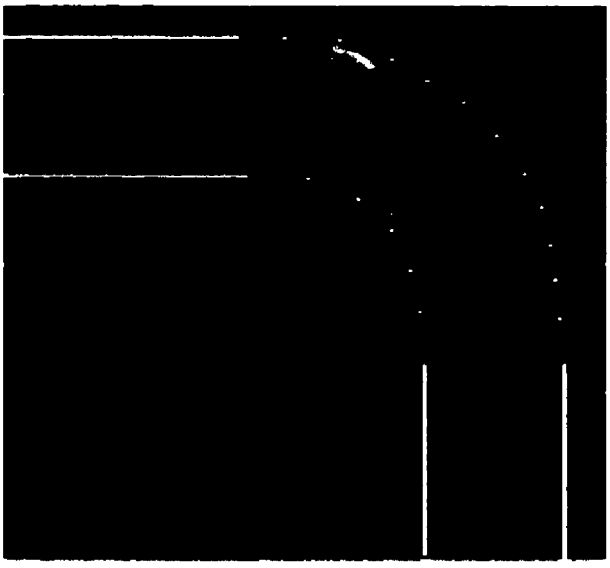

Fig 5.10 Image of turbulent flame front in bend. Test # 208, $\phi = 1.4$.

Since the combustion zone behind the leading edge appears turbulent, the flow of the burned gas behind the flame is turbulent. Whether the unburned gas ahead of the flame front is laminar or turbulent is not easily discernible. According to Turns [16], wrinkling

of the flame front requires the presence of vortices in the upstream flow. However, as discussed in a previous section of this chapter, the measurement of flame propagation velocities greater than 1.0 m/s will not necessarily disclose more detail about the unburned gas flow regime. Large scale wrinkles present in Fig. 5.10 could develop due to secondary flows (large structures) or due to Le < 1 conditions.

Laminar flow is a prerequisite for the development of Görtler and Dean vortices. However, in every test conducted in this project, it was observed that the tip of the leading edge of the flame fronts always proceeded near the inner surface of the bend. Some of these tests involved turbulent flows of the unburned gas ahead of the flame fronts. Therefore, secondary flows in the form of Görtler and Dean vortices could not exist for these conditions.

In this work, Dean numbers are somewhat higher compared to other research where Dean vortices were clearly identified. However, this does not exclude the development and existence of secondary flows in this case. In fact, the effects of secondary flows intensify with higher Dn number. Görtler vortices are replaced by turbulent boundary layers and Dean vortices transform to even higher energy, large eddy-type structures. Taylor [13] and Humphrey [12] showed in their work that the characteristics of turbulent flow in a bend are similar to those of laminar flow. As a result, the flame front propagation profiles through the bend would exhibit similarities in the flow regime limited to transition to detonation.

The flame propagation shown in Fig. 4.38 is unusual. This "stop and go" phenomena is not like the oscillatory behavior described earlier for "weak" flame front propagations. Figure 5.11 is a composite of the individual images from Fig. 4.38. The figure shows that the flame front does not propagate backward, but only hesitates in advancing forward.

As shown in Fig. 5.1, slightly rich mixture conditions resulted in high average flame propagation velocities. The hesitant nature of the flame front propagation suggests that the unburned gas flow is also unsteady or pulsating. It is speculated that fast flames may induce resonant sound/pressure waves in the duct which could cause this effect.

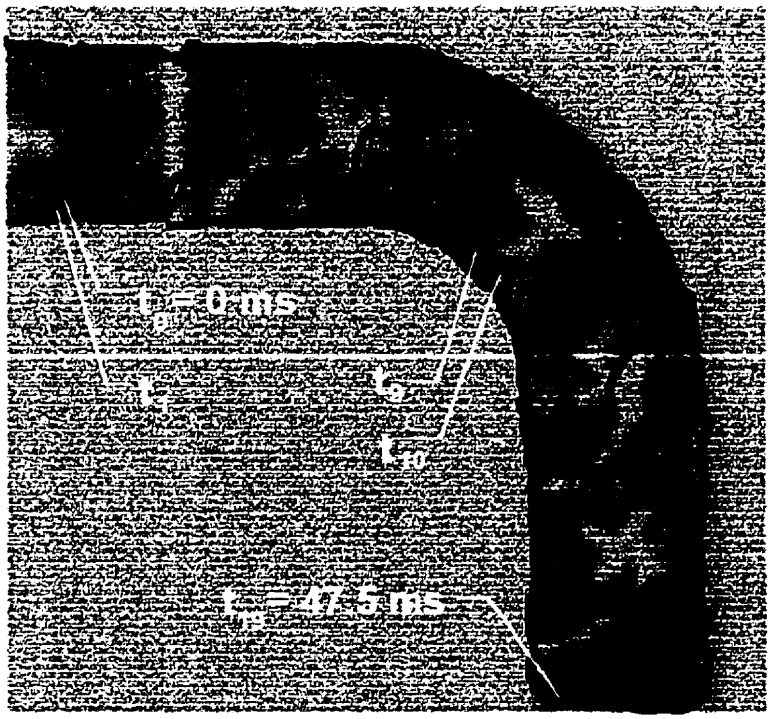

Fig. 5.11 Flame front contours for Test # 197, $\phi = 1.2$, 400 fps.
Time interval between images: $\Delta t = 2.5$ ms.

5.12 Sources of Error

There are several sources of error which influence the accuracy of the flame propagation velocity measurement determinations. These include natural or inherent errors, errors due to the preparation of the test mixtures, and errors due to the methods used in flame front detection.

The variations in the average flame propagation velocities as shown in the straight inlet section of the FPD may be due to a number of factors. As described in Chapter 4, Figs. 4.4 through 4.14 show the respective standard deviations for the velocity data for the tested mixture compositions. High flame propagation velocities have high standard deviations while low flame propagation velocities have low standard deviations.

5.12.1 Natural Differences

One factor is the natural differences due to the physics of flame propagation. The photodiodes are used to determine time averaged velocities over a specified distance along the FPD. Propagating flame fronts from different trials do not have the same velocity profiles through the duct. Therefore, the flame fronts may not be reaching their maximum or minimum local velocities at the same locations in the FPD for every trial of a specified mixture composition. As a result, the collected time difference data covers a range of flame front accelerations and decelerations for each photodiode set. With high average flame propagation velocities, the range of accelerations and decelerations may be large. This would be evident as large standard deviations. With low average flame

propagation velocities, the range of accelerations and decelerations may be small. This would result in small standard deviations.

The error associated with flame velocities can be determined from the following expression developed from a Taylor expansion and root sum square method using the length (L) and time (t) variables of velocity. This expression relates the error strictly to the physical measurement of these variables.

$$\Delta S_F^P = S_F \sqrt{\left(\frac{\Delta L}{L}\right)^2 + \left(\frac{\Delta t}{t}\right)^2}$$

Although the natural differences may contribute a fraction to the total error, the expression indicates that with increasing flame velocity (S_F), the error (ΔS_F^P) and consequently, the standard deviation also increases.

5.12.2 Instrumentation for Velocity Determination

The second factor in errors is the instrumentation. High velocity flame fronts pass through a photodiode set in a small period of time. The ability to resolve time differences is subjective since the operator must manipulate cursors on the oscilloscope screen. Particularly for small time differences, errors in resolving the time difference result in large errors in calculating the velocity. Whereas for large time differences, errors in resolving the time difference do not have a large effect on the calculated velocity. Subsequently, little variation would result for the low propagation velocity calculations while high variation would result for the high propagation velocities.

Another consideration would be the response time of the photodiode circuits. Although assumed to be instantaneous, the photodiodes and their respective circuits do add some time delay to the processing of the signals. A number of factors can affect the response time and no doubt their effects are not the same for all individual photodiodes nor for all tests. Such factors may be the light intensity of the flame in front of the photodiode, different resistances of the wire leads, and the different variations in performance of the individual electronic circuit components. The effect of these factors would be extremely low for the low flame propagation velocities for the same reason explained in the previous paragraph. However, for the high velocity calculations, the response time may form a large portion of the total time difference signal. In this case, the response time is not negligible and may contribute to the large deviations in the collected data.

Signals were sent from the processing circuits to the oscilloscope. The LECROY oscilloscope used for this project allowed for the expansion of the signal waveforms. However, there was a limit to how small the difference between the time signals could be resolved. Generally, each photodiode signal could be resolved to within 0.1 ms. It was ultimately the observer, who manipulated the oscilloscope cursors, that had the largest impact on time difference determinations. With small time differences, observer error in resolving the times would result in large variations in the calculation of the propagation velocities.

Analysis of the data showed that signal differences less than 1 ms resulted in propagation velocities which appeared exceedingly high compared to the other velocities. These high propagation velocities were on the order of 50 m/s or more. Subsequently, because of these suspect propagation velocities and the potential observer error in resolving very small time differences, time differences less than 1 ms were not used in calculating flame propagation velocities. Forty-eight time difference values were treated this way.

Photodiodes were securely attached to the FPD during the tests. However, the photodiodes as purchased, had a broad detection view angle. This view angle was reduced through the use of photodiode shields. These shields are described in Appendix F.

Flame propagation velocities were determined assuming that the detection of the flame front by the photodiodes occurred when the flame front passed through the center of the view angle. This may not have always happened with the result being that errors in the measurement length are possible.

The profiles of the flame fronts did not change drastically as the flame fronts propagated through the straight, inlet section of the FPD. Consequently, propagation velocity errors in this region were mainly due to flame front detection and time difference resolution as described above. However, in the bend and exit sections of the FPD, the flame front profiles change dramatically. These profile changes contribute to the differences between

the propagation velocities obtained from the photodiode method and the contour analysis of high speed photographic images.

As shown in the graphs in Figs. 4.18 to 4.26, the photodiode method can result in propagation velocities that are as much as twice the propagation velocities obtained from the flame front contour analysis. Another contribution to the differences is that the flame propagation velocities calculated from the photodiode data are averaged over a duct length of 5, 6, or 10 cm. The velocities obtained from contour analysis are averaged over distances of less than 3 cm.

Taking these considerations into account, in the region of the bend and exit sections of the FPD, flame propagation velocities obtained from contour analysis of images are more accurate than the propagation velocities obtained from photodiode data. Using the above expression for the error resulting from physical measurements of time and length, an approximate relative error of 21 % was calculated for flame propagation velocities in the straight inlet section of the FPD.

5.12.3 Mixture Preparation

The partial pressure method utilized in preparing test mixtures proved reliable. The high accuracy pressure gauge and consistency in performing the mixture preparations were crucial to obtaining accurate test mixtures.

Looking strictly at the capabilities of the pressure gauge, the error in flame propagation velocity due to the mixture preparation procedures can be expressed in the following equation.

$$\Delta S_F^{\Phi} = \sqrt{\left(\frac{\delta S_F}{\delta P_{tot}} \Delta P_{tot}\right)^2 + \left(\frac{\delta S_F}{\delta P_{fuel}} \Delta P_{fuel}\right)^2}$$

A polynomial equation was developed from the data used to develop the graph in Fig. 5.1. This equation relates the flame propagation velocity with the equivalence ratio. In turn, an additional equation was developed which expresses the equivalence ratio in terms of the total mixture pressure (P_{tot}) and the fuel pressure (P_{fuel}) as measured by the pressure gauge.

From this analysis, the relative error in flame velocities due to differences in mixture composition can be as much as 53%. This relative error is for the lean mixture composition of $\phi = 0.8$. For mixture compositions of $\phi \geq 1.0$, the relative errors are less than 17%.

Prior to running tests, a number of gas mixture samples were prepared and tested with a gas analyzer. These tests were conducted to confirm that the mixture preparation procedures are correct and to gauge the accuracy of the gas mixture samples with respect to a standard. The gas analyzer was calibrated with a certified 1.06% propane in air gas mixture. Mixture samples were prepared using the Gas Mixture Cart and collected in mylar balloons. The results of the gas analysis of the mixture samples are shown in

Appendix O. These results show that compared to the actual (measured) fuel ratios of the mixture compositions, the calculated fuel ratio values differ by less than 12% for the mixture equivalence ratios used in the test regime.

The mixture compositions were all richer than what was calculated. This confirms that the procedures used to produce the mixture samples were consistent. The degree of error was a concern however. This was looked at in more detail.

The partial pressure method utilized gauge markings on a pressure gauge to determine the amount of air and propane needed for a specific mixture composition. As described in Appendix E, the test gauge used on the Gas Mixture Cart had two scales. A vacuum scale and a pressure scale. The vacuum scale was used to mark the fuel pressure. The major markings on the vacuum section of the gauge were close together. The arc length between the markings was about 1 cm. Therefore, obtaining the precise fuel pressure called for in the mixture preparation spreadsheet program could be difficult. The major markings on the pressure section of the gauge were further apart on the scale. This allowed for more precise measuring of the total mixture pressure.

Using the actual fuel ratios from the gas analysis information, it was possible to back-calculate the exact gauge markings needed for the actual mixture. These exact gauge markings could be compared to the sample fuel gauge mark called for in the mixture preparation spreadsheet program. Differences between the gauge mark used to produce the sample and the exact, back calculated value were less than 3%. This was with the

assumption that the total mixture pressure was precisely at the required gauge mark. The 3% difference is considered very good considering that the ability to obtain the ultimate vacuum pressure in the mixture tank could vary.

The vacuum pump used in evacuating the mixture tank in the Gas Mixture Cart was an Edwards Type ES 50. This pump was a rotary vane type which used oil as the sealing mechanism. Although a very simple pump to operate, it had one major disadvantage for applications of this nature. This type of pump could not achieve its ultimate vacuum pressure if too much water vapor condensed in the oil. Tests were conducted during the summer months where on some days, the humidity level was very high. On these days, water vapor would condense in the oil and the ultimate vacuum pressure achieved would be 2 to 3 kPa less than normal. The inability to achieve the maximum vacuum was not taken into consideration when using results from the mixture preparation spreadsheet program. This resulted in mixture compositions leaner than desired. In hindsight, this should have been looked at more closely. This effect is reflected in the relative error estimates presented earlier in this section. The consequence of the humidity is most pronounced for the lean mixtures due to the small fuel ratios involved. For the higher equivalence ratio mixtures, where fuel ratios are larger, the effect due to humidity is less pronounced.

This problem of not achieving ultimate vacuum when high humidity conditions prevailed also affected the evacuation of the FPD for trials. More importantly, the FPD could not be made leak tight. Therefore, during the FPD fill operation, air would infiltrate into the

FPD until it reached atmospheric pressure. Over the course of the test regime, air infiltration tests were performed on the FPD to gauge the leakage rate. The results of the air infiltration tests are shown in Appendix P.

The effect of air infiltration, and in some cases not achieving ultimate vacuum in the FPD resulted in the dilution of the test mixture inside the FPD. During the filling operations, it was imperative to fill the FPD in the shortest time possible to reduce the amount of dilution air. A fill time criteria of less than 90 seconds was used over the course of the tests. As the gas mixture entered the FPD from the mixture tank, the vacuum pressure in the FPD decreased. Since the pressure differential between the atmosphere and inside the FPD decreased, the rate of air infiltration also decreased.

The FPD fill rate varied from test to test and was not measured. Therefore it was not possible to compare mixture fill rates to air infiltration rates to gauge the effect of dilution of the gas mixture charge inside the FPD. However, a worst case condition could be analyzed to estimate the effect. This condition would be to evacuate the FPD and allow air infiltration into the FPD for 90 seconds. At the end of this time, a gas mixture charge would instantaneously fill the FPD to atmospheric pressure. Using the curves displayed in Fig. P.1, the ideal gas law, the volume of the FPD, and the fuel ratios for various mixture compositions, an analysis was performed to estimate the effect of air infiltration on mixture compositions using this worse case scenario. The analysis indicated that this worst case scenario would reduce the fuel ratio of the gas mixture from the mixture tank by only 12%.

Typically, five mixture charges could be obtained from a gas mixture batch produced in the Gas Mixture Cart. As each succeeding charge was withdrawn from the mixture tank, the pressure in the tank decreased. The initial mixture charges would fill the FPD very quickly (~ 15 - 20 seconds). The fourth and fifth charges would take longer. In most tests, the fifth charge would take 65 to 75 seconds to fill the FPD. Only for a few tests did the fill time come close to the 90 second criteria. As a result, the 12% error figure is considered conservative.

5.12.4 Analysis of Variance

Over the course of testing, it was observed that in some instances, the first charge from mixture batches would produce flame fronts that appeared to propagate faster than flame fronts from succeeding charges. This effect was observed over the entire range of tested mixture compositions. It was felt that this may have been due to the air infiltration effects discussed in the previous section.

Analysis of Variance (ANOVA) techniques were employed to investigate whether these observations were attributable to variations in the flame propagation velocities. The ANOVA technique was applied to the data from mixture compositions of ϕ = 0.9, 1.2 and 1.6. The data was sorted into separate groups. These groups represent the trials conducted with one mixture batch. Subsequently, all the first trials from each mixture batch were collected and average flame propagation velocities calculated. This same procedure was used for the second, third, fourth, and fifth trials in each batch.

The statistical package in MS EXCEL was used for this ANOVA investigation. The results from the investigation are shown in Appendix Q. The most important parameter is the variance ratio (F) between the columns. In these cases, the columns refer to the trial number in a batch. These (F) values are compared to the critical variance ratio (F_{crit}) values. For all three mixture compositions, the (F) values are less then their respective critical values. This implies that there are no significant differences in the variations between the trials.

As a result, although it may have appeared that flame front propagation in some individual trials was characteristically different than others, the propagation velocities themselves were not statistically different. This simple ANOVA investigation adds credibility and confidence in the collected data.

Chapter Six

Recommendations and Conclusion

Work was performed to commission an existing, yet unfinished flame propagation duct apparatus. Additionally, a gas mixture preparation cart was constructed. Flame detection instrumentation was fabricated and operation procedures were devised. A test program was implemented which resulted in the completion of 672 individual tests. Flame propagation velocity data was obtained to aid in the characterization of flame propagation through the FPD. High speed images were also recorded of flame propagation in the bend. A Schlieren apparatus in conjunction with the high speed camera and a timeline technique were used to analyze the unburned gas flow ahead of propagating flame fronts in the bend.

6.1 Recommendations

The objectives of this project were to get an FPD to an operational state, and to perform an initial investigation of the characterization of flame front propagation at atmospheric pressure in the FPD. This study illuminated the deficiencies encountered in trying to understand the interactions of secondary flow structures with propagating flame fronts in the bend. The following recommendations pertain to alleviating these deficiencies should future studies in this area be conducted.

I. With the present apparatus arrangement, the development of secondary flow structures in the bend was evident only by the effects observed on the timeline and flame fronts. There was no direct observation or measurement of secondary flows. In addition, the observed effects could only be discerned in two dimensions whereas secondary flows are a three dimensional phenomenon. Therefore, to fully understand the characteristics of the unburned gas flow in the bend, future work must be directed at 3-D visualization and measurement. Ideally, a non-intrusive technique such as Laser Doppler Velocimetry (LDV) could be utilized. This would require the installation of an optical viewport in the outer radius of the bend to allow for measurements in the radial direction.

II. Further work should be directed at reducing the air infiltration rate into the FPD. This is especially important should sub-atmospheric testing be undertaken. Air

leakage would not only alter the operation pressure, but it would also make the test mixture leaner. It is suggested that the primary source of leaks is the gaskets between the aluminum structural members. It is suspected that the sealant impregnating these paper gaskets does not fully cure at room temperature. A substitute sealant should be procured.

III. More photodiodes and closer spacing of photodiode sets would provide more accurate determination of average flame propagation velocities. It would also reduce the number of tests needed to be performed to fully characterize flame propagation. This would also provide a better description of how the velocities vary across the inlet section of the FPD.

IV. The signal waveforms obtained from the photodiodes were displayed on an oscilloscope. However, the waveform data could not be digitally recorded for future reference. All analysis of the waveform had to be performed after every test. The use of a data acquisition system would allow for recording of this waveform information. This would have the additional advantage of removing the subjective interpretation of a signal waveform profile by the observer.

V. Mixture conditions that produced faint flame fronts resulted in photodiode data that was more suspect than photodiode data obtained from more luminescent flame fronts. The backlighting procedure is not an ideal method to improve flame detection by the photodiodes. Also, although the signal processing circuits

performed adequately for this project, they would not be considered efficient. For instance, the MOD 2 circuit uses 40 MΩ resistances. This excessively high resistance requirement implies that a better circuit could probably be substituted.

Efforts should be made to try to improve the detection capability of faint flame fronts by the photodiodes. These efforts could be improvements in the photodiode circuits or new circuits all together. Experiments with other types of photodiodes could also be conducted. If ultraviolet type photodiodes are used, a method of installing them on the inside surfaces of the FPD must be devised.

VI. Pressure measurements would provide additional information concerning flame propagation in the FPD. Pressure transducers could be installed in the straight inlet section, bend and exit sections of the FPD. Additionally, a pressure differential transducer to measure delta P between the inner and outer regions of the bend would provide further evidence of secondary flow development in the bend.

VII. It would be beneficial to have more than one timeline to provide more detail of the transient changes occurring in the unburned gas flow ahead of the propagating flame front. Rather than use the TC Tester to create single pulse timelines, it would be better to devise a heater circuit that cycles on and off over the course of an entire flame propagation. A possible arrangement would be to modify the time

delay circuit to control a relay switch. This would result in the formation of a series of timelines in the unburned gas flow.

VIII Modifications should be made to the duct endplate to allow for a larger opening. The current arrangement has a small opening for the pressure equalization valve. This opening is also off-center. It is believed that this configuration and the small flow area may be a cause of the velocity variations and flame front profile changes in the bend as observed in this test program. An ideal arrangement would be one where the duct end could be fully opened.

6.2 Conclusions

The following conclusions have been drawn from the experimental investigation and analysis of data.

I. In a 90° bend of strong curvature, the development of secondary flows in the unburned gas causes stretching and distortion of flame fronts propagating through the bend. The leading edges of the flame fronts proceed through the bend near the inner surface.

II. The presence of a 90° bend reduces variations in the flame propagation velocities in the region of the bend entrance. Regardless of mixture composition, the

resulting flame fronts have a relatively constant flame propagation velocity at the bend entrance.

III. Within the bounds of the experiments, flame propagation limits for the FPD were determined for propane/air mixture compositions of $0.85 < \phi < 1.8$. For leaner and richer mixture conditions, occasional instances of flame propagation were observed.

IV. Flame propagation through the FPD is non-steady. Flame propagation velocity was observed to vary as the flame fronts progressed through the inlet section. The variations in flame propagation velocity from the mean were seen to be small for mixture compositions of $1.1 < \phi < 1.4$. Larger variations in the mean flame propagation velocity were seen for mixture compositions of $\phi < 1.1$ and $\phi > 1.4$.

V. The technique of using photodiodes to determine flame propagation velocities was found to be simple, reliable and fast. However, the technique fails when flame fronts are faintly luminescent or if the flame front distorts appreciably over a short distance. The use of a high speed camera and subsequent flame front contour analysis can alleviate these disadvantages, but at the cost of higher time requirements.

List of References

1. Sato, K., Sakai, Y., Chiga, M., *XXVI Symposium (Int.) on Combustion*, 1996.

2. Clavin, P., *Annu. Rev. Fluid Mech.*, **26** pp. 321-352, 1994.

3. Shepherd, J.E., Lee, J.H.S., On the transition from deflagration to detonation. 1990.

4. Matalon, M., Metzener, P., *J. Fluid Mech.* **336** pp. 331-350, 1997.

5. Humphrey, J.A.C., Taylor, A.M.K.P., and Whitelaw, J.H., *J. Fluid Mech.* **83** pp. 509-527, 1977.

6. Hille, P., Vehrenkamp, R., and Schulz-Dubois, E.O., *J. Fluid Mech.* **151** pp. 219-241, 1985.

7. Bara, B., Nandakumar, K., and Masliyah, J.H., *J. Fluid Mech.* **244** pp. 339-376, 1992.

8. Pratap, V.S., Spalding, D.B., *The Aeronautical Quarterly* **26** pp. 219-228, 1975.

9. Hassager, O., Henriksen, P., Townsend, P., Webster, M.F., and Ding, D., *Computers Fluids.* **20** pp. 373-386, 1991.

10. Soh, W.Y., *J. Fluid Mech.* **188** pp. 337-361, 1988.

11. Berger, S.A., Talbot, L., Yao, L.S., *Annu. Rev. Fluid Mech.*, **15** pp. 461-512, 1983.

12. Humphrey, J.A.C., Whitelaw, J.H., Yee, G., *J. Fluid Mech.* **103** pp. 443-463, 1981.

13. Taylor, A.M.K.P., Whitelaw, J.H., Yianneskis, M., *Transactions of the ASME* **104** pp. 350-359, 1982.

14. Lee, T.W., and Santavicca, D.A., *Combust. Sci and Tech.* **90** pp 211-229, 1993.

15. Acton, J., MECH 460 Thesis, Department of Mechanical Engineering, Queen's University, 1995.

16 Turns, S.R., *An Introduction to Combustion: Concepts and Applications*, McGraw-Hill, 1996.

17. Kuo, K.K., *Principles of Combustion*, J. Wiley and Sons, 1986.

18. Kalb, C.E., Seader, J.D., *Int. J. Heat and Mass Transfer***15** pp. 801-817, 1972.

19. Kalb, C.E., Seader, J.D., *AIChE J.* **20** pp. 340-346, 1974.

20. Brailovsky, I., Sivashinsky, G., *Combust. Sci and Tech.* **87** pp 389-400, 1992.

21. Rakib, Z., Sivashinsky, G., *Combust. Sci and Tech.* **59** pp 247-260, 1988.

22. Blint., R.J., *Combust. Sci and Tech.* **49** pp 79-92, 1986.

23. Finley, W.H., Keller, J.B., and Ferziger, J.H., *J. Fluid Mech.* **194** pp. 417-456, 1988.

24. Saric, W.S., *Annu. Rev. Fluid Mech.*, **26** pp. 379-409, 1994.

25. Deacon, D., MECH 460 Thesis, Department of Mechanical Engineering, Queen's University, 1993.

26. Coughlin, R.F., Driscoll, F.F., *Operational Amplifiers and Linear Integrated Circuits*, Prentice Hall, 1977.

27. National Semiconductor Corp, Circuit Application Manuals, 1987.

28. Teodorczyk, A., Lee, J.H.S., Knystautas, R., *XXIII Symposium (Int.) on Combustion*, pp. 735-741, 1990.

29. Incropera, F.P., Dewitt, D.P., *Introduction to Heat Transfer,* J. Wiley and Sons, 1985.

30. Panton, R.L., *Incompressible Flow*, J. Wiley and Sons, 1984.

31. Catlin, C.A., Fairweather, M., Ibrahim, S.S., *Combust. and Flame* **102**, pp. 115-128, 1995.

32. Mees, P.A.J., Nandakumar, K., Masliyah, J.H., *J. Fluid Mech.* **314** pp. 227-246, 1996.

33. Andrews, G.E., Bradley, D., *Combust. and Flame* **19**, pp. 275-288, 1972.

34. Bartlamä, F., Schröder, K., *Combust. and Flame* **66**, pp. 237-248, 1986.

35. Andreev, M.A., Stepanov, A.M., Translated from *Fizika Goreniya i Vzryva* **23**, pp. 31-40, 1987.

Appendix A: FPD Fabrication Drawings

The following figures show the fabrication drawings and details of the FPD.

Fig. A.1 FPD fabrication drawing #1 (Acton).

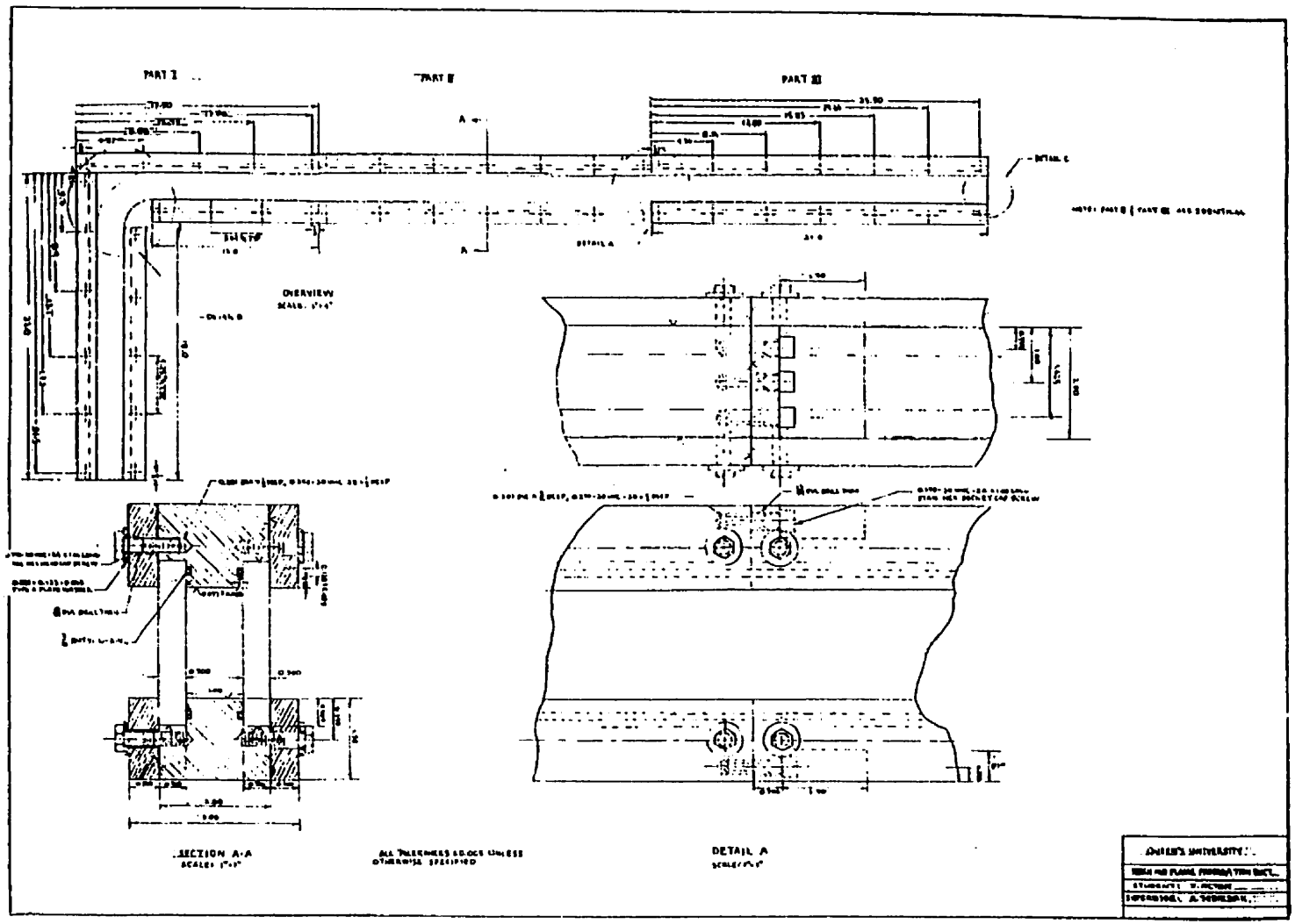

Fig. A.2 FPD fabrication drawing #2 (Acton).

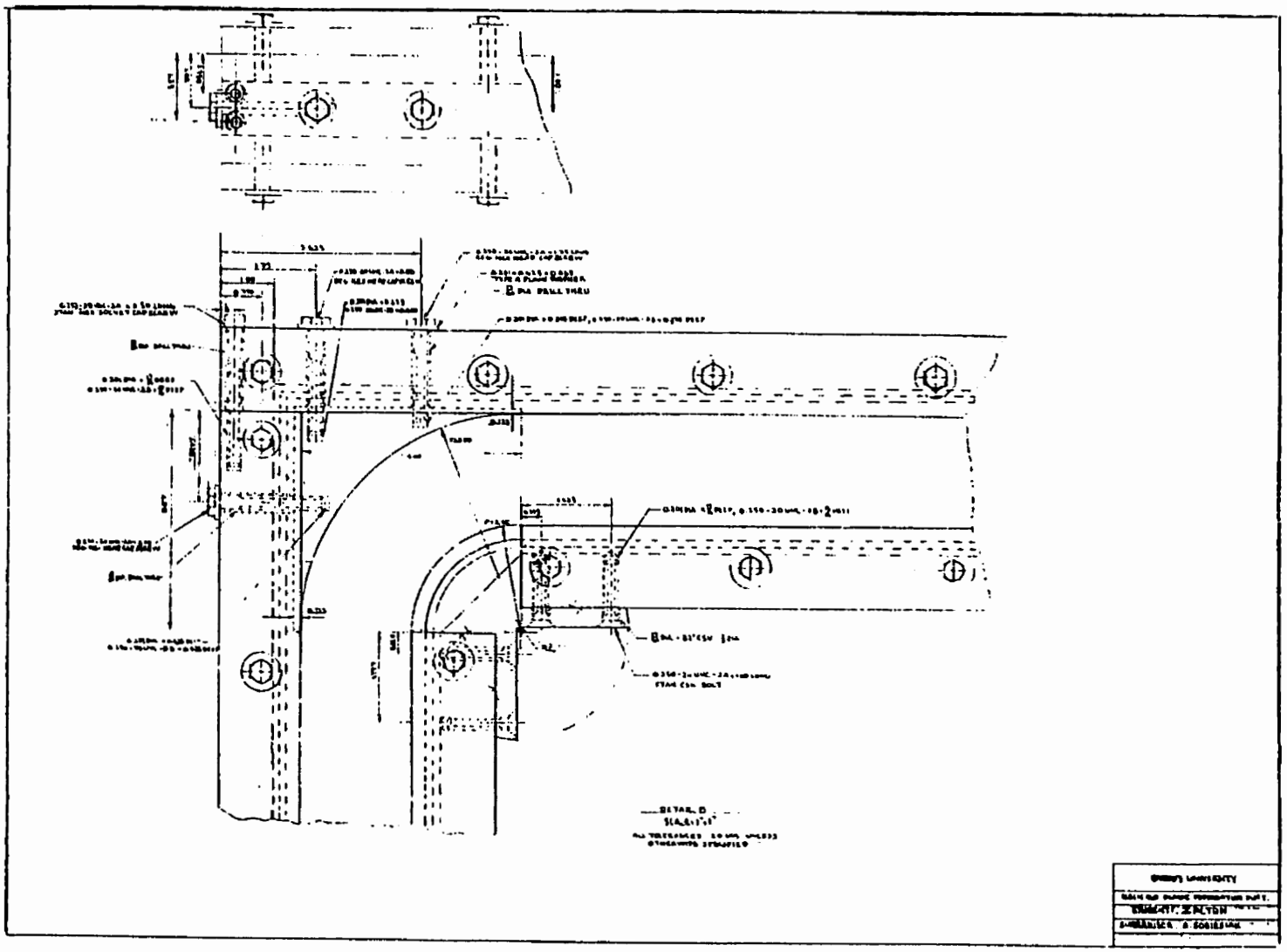

Fig. A.3 FPD fabrication drawing #3 (Acton).

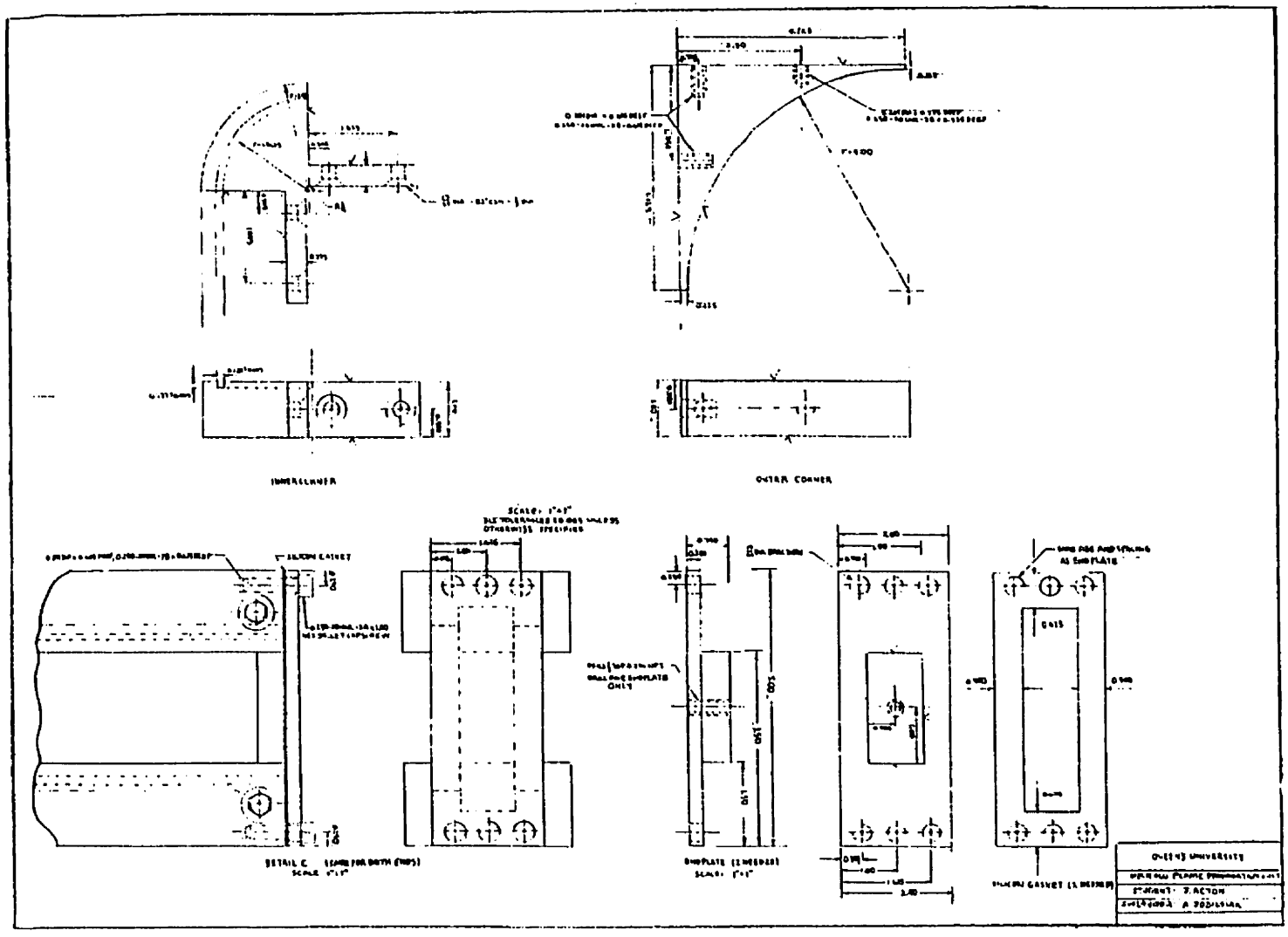

Appendix B: Construction of FPD Test Apparatus

B.1 Modifications to FPD

The aluminum structural parts for the FPD test apparatus were manufactured by the Mechanical Engineering Machine Shop at Queen's University. Clear Plexiglas side panels were also machined. The parts were fitted together with O-ring rubber cord to seal the Plexiglas panels to the FPD frame. At the time of construction, the FPD was not tested for vacuum integrity. Testing with the Schlieren apparatus proved the incompatibility of using Plexiglas for the observation windows in the area of the FPD bend. The FPD was then stored for approximately 2 years.

The FPD was removed from storage for use in this project. All components of the FPD were disassembled and cleaned. It was decided that the Plexiglas panels would be cut in the region of the entrance to the bend. Quartz glass would be used in place of the removed Plexiglas sections. Quartz glass does not cause smearing of the Schlieren images as does Plexiglas. Quotes were obtained for 12 mm thick quartz panels cut to the required specifications. The quotes were deemed too expensive for this project. It was then decided to use inexpensive, 6 mm thick plate glass for the Schlieren windows. However, it was necessary to check the orientation of the glass to produce minimal Schlieren smearing, prior to cutting the pieces.

The aluminum frame pieces of the FPD were reassembled using gaskets for the seams between the pieces. The gaskets were constructed out of Kraft paper from a paper

grocery bag. An automobile gasket cement compound (TiteSeal ™) was used to impregnate the Kraft paper. The pieces were set aside to allow the cement compound to air dry.

The Plexiglas panels were installed on both sides of the FPD. Additional O-ring cord was obtained to seal the panels to the FPD. The cord was installed in O-ring channels machined in the aluminum frame members. Wherever two aluminum pieces butted together, flexible silicon RTV (Room Temperature Vulcanizing) compound was used for additional sealing. The RTV sealant was also used to seal the butt seam formed between the Plexiglas panels and the glass panels. Figure B.1 shows the bend location of the FPD with O-ring, frame and Plexiglas details.

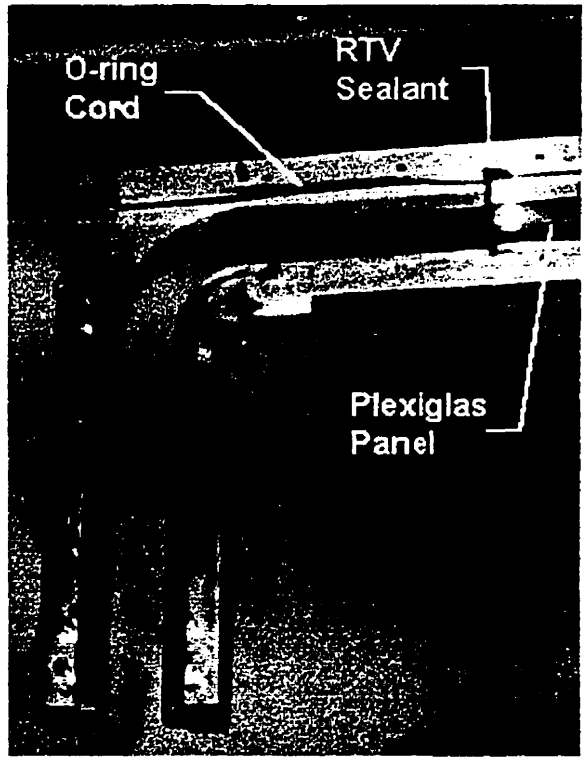

Fig. B.1 Bend location of the FPD with O-ring, frame and Plexiglas details.

Two 51 cm x 51 cm plate glass sheets were purchased from a local glass supplier. These sheets were then tested with the Schlieren apparatus to check the quality of the transmitted light. The sheets were oriented and matched together to obtain the best arrangement which resulted in good optical characteristics. Once this optimum arrangement was found, the rough dimensions of the panels were marked off with a black marker. The sheets were brought back to the supplier for cutting. Two sets of glass panels resulting in 4 pieces were cut. In cutting the glass panels to fit the FPD, it was necessary to cut a sharp radius along the inside bend of the glass panel. Figure B.2 shows the installation of the glass panel (marked with diagonal stripes), endplate and one clamp piece.

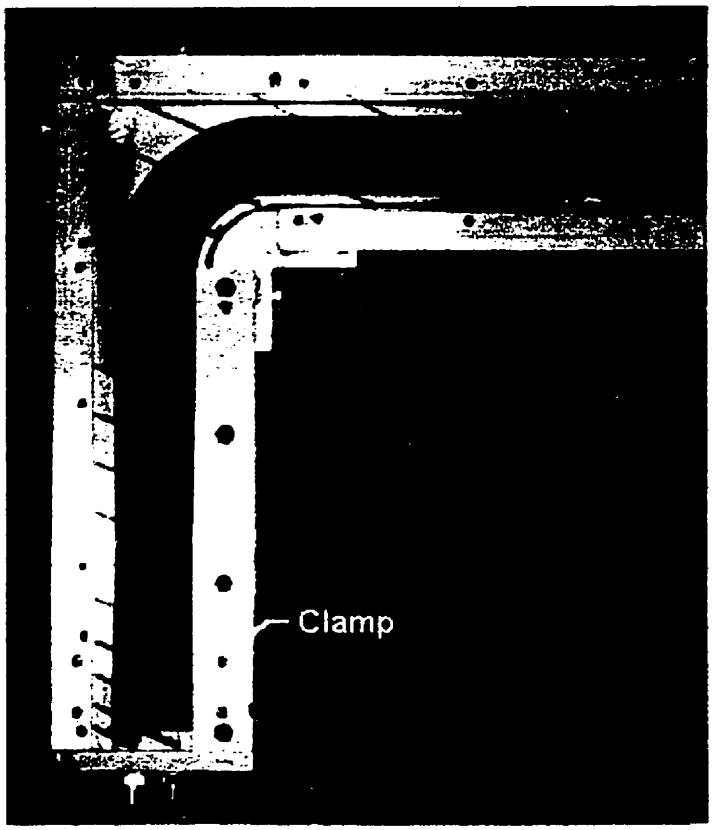

Fig. B.2 Installation of glass panel in FPD.

Clamp pieces were used to apply pressure against the Plexiglas and glass panels. In doing so, the O-ring seals were compressed. The RTV sealant was allowed to set for at least 24 hours. To check for vacuum integrity, a vacuum pump was connected to the FPD through a hose which was attached to a valve and fitting arrangement on the FPD endplate. A vacuum gauge was connected to the second fitting on the endplate. The vacuum pump was turned on and the air in the FPD was evacuated. The gauge was observed. When maximum vacuum was achieved, the isolation valve was closed and the vacuum pump turned off. Any air ingress into the FPD was indicated as a decrease in vacuum pressure as shown on the vacuum gauge. The first vacuum tests showed a decrease in pressure from 30 in Hg (101 kPa) to 20 in Hg (68 kPa) in 7.5 minutes. Since this indicated leakage, a water bottle with a small diameter tube was used to stream water along the seams of the FPD. Leaks were localized by the drawing in of the water into the FPD. Another method used to find leaks was to pressurize the FPD with air at pressures 1 to 2 psi (7 to 14 kPa) above atmospheric pressure. Then a soap and water solution was streamed along the FPD seams. Leaks were localized wherever expanding soap bubbles were seen. This method was abandoned after one or two instances, since it pushed the panels away from the seals which was opposite to the intended design. Also, there was a safety concern should the glass panels fail. With pressure in the FPD, a catastrophic failure could possibly have resulted in the shattering of glass fragments outward from the FPD. This could have potentially caused personal injury.

In trying to reduce the leakage rate by using the vacuum method to find leaks, one of the glass panels cracked. With this type of failure, the pressure in the FPD increased to

atmospheric pressure. Originally, it was though that the cracking was due to high clamping pressure on the glass panels. The glass panel was removed. The dried RTV sealant was removed and the entire bend area was cleaned. One of the glass panels from the other set was used for the replacement piece. However, the clamps around the glass panel were only tightened lightly for this installation. New RTV sealant was used and allowed to dry. When the FPD next underwent a vacuum test, the new glass panel cracked. Since there still remained an additional spare glass panel, it was decided to try one last time using a different procedure. The cracked panel was removed and the bend area prepared as before. The replacement panel was installed and RTV sealant applied in the respective locations. The RTV sealant was allowed to dry before the clamp pieces were installed and lightly tightened. When a vacuum was pulled on the FPD, the glass panel still cracked.

Analyzing the three cracked panels showed that all the cracks were located near the sharp inner radius. One of the cracked panels is shown in Fig. B.3. It was speculated that stress concentrations were localized at the inner radius due to the necessity of making a sharply curved cut. When a vacuum was applied in the FPD, the glass was strained and the result was that the highly stressed area near the bend failed. The failure was made evident as a crack that propagated outward.

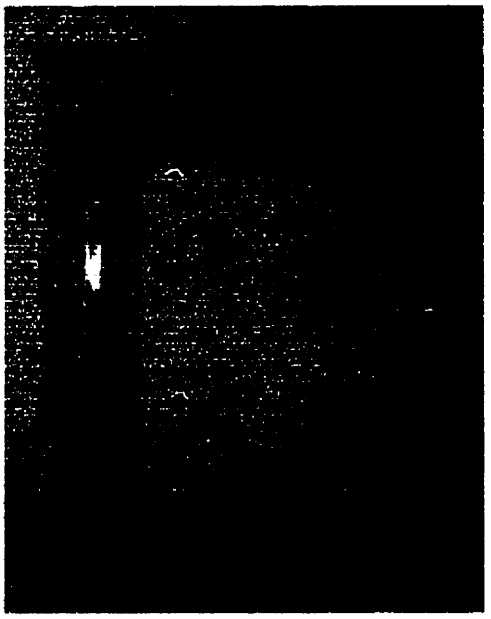

Fig. B.3 Glass panel with crack circled in black marker.

Three solutions to this problem were proposed. The first solution was to use thicker glass. However, discussions with glass suppliers revealed that cutting a sharp radius as desired for thicker glass of approximately 12 mm would not have been possible. The second solution was to try different types of clear plastic. Samples of 6 mm thick Lexan™ polycarbonate plastic were obtained. These samples were tested with the Schlieren apparatus to determine optical characteristics. Although Lexan ™ transmitted Schlieren light much better than Plexiglas, it did not equal the optical transmission characteristics of regular plate glass or quartz glass. Under flexion, Lexan™ displayed the same smear and striation patterns as Plexiglas.

The third solution was to use tempered glass. A local glass supplier provided quote and delivery time for two sets of tempered glass pieces. All work was to be performed in Guelph Ontario, so a drawing with dimensions and tolerance specifications was given to

the supplier. Two 51 cm x 51 cm plate glass sheets were purchased from the supplier and tested with the Schlieren apparatus. Rough outlines of the glass panels were marked on the sheets. The sheets along with an extra drawing copy were then returned to the supplier for shipment to Guelph. The tempered pieces were delivered 7 weeks later. On attempting to install the glass panels into the FPD, it was realized that the panels were cut oversize and not to specified tolerances. Clarification from the supplier indicated that the industry standard tolerance is 0.25" (6.35 mm). The sent drawing was specified with a tolerance of 0.125" (3.18 mm). The supplier should have picked up on this earlier or at least should have cleared up inconsistencies with what was desired and what was possible. In the event, payment was not made for these items and it was decided not to pursue this course of action further due to the lengthy turn around time.

The ultimate solution to this problem involved the use of glass panels that did not have sharp inner radii. The plan was to modify two of the frame sections to allow for the installation of panels made with only straight cuts. The two frame sections which support the glass panel near the inside edges were milled down to the level of the connector. This rendered the clamping bars as shown in Fig. B.2 useless. Additional workshop C-clamps were purchased for this purpose. Plate glass sheets were purchased and checked out on the Schlieren apparatus. Glass panels were cut out to the new shape. The frame pieces were reassembled and the new glass panels installed. Figure B.4 shows the final arrangement with the glass panel outlined in red.

Fig. B.4 Final glass panel arrangement.

The FPD was vacuum tested using the testing procedures as previously discussed. Neither glass panel cracked and they remained intact for the rest of the testing program. Vacuum testing showed that the FPD was not leak tight. Additional work was performed to try to find the leakage points. Eventually, it was decided to encase the O-ring cord in RTV sealant along the entire length of the FPD. This is also shown in Fig. B.4. Further tests using the vacuum method continued to indicate leakage. However, checking with the water stream proved that the major leaks had been sealed. It was therefore decided to proceed to actual testing even though the FPD was not leak tight. All testing was to be conducted at atmospheric pressure, so having the FPD under vacuum was only necessary for mixture filling operations. As long as the filling operations were of short duration, only a small amount of leakage air would enter into the FPD. Leakage rate was monitored over the course of testing.

B.2 Timeline wires

Modifications were made to the FPD when the flame propagation velocity measurement tests were finished. The modifications entailed the installation of two thermocouple wires in the entrance to the bend. These wires were installed in the vertical orientation. One wire (0.08 mm dia.) was installed through the mid plane of the duct while the other wire (0.05 mm dia.) was installed in the 1/4 plane of the duct. The wires were used as heater filaments to produce timelines in the unburned gas flow.

Four 1/8" (3.18 mm) dia. holes were drilled in the aluminum frame members. Two holes on the top section and two on the bottom section. Plastic isolation sleeves were glued into the holes. The thermocouple wire was threaded through these sleeves. RTV sealant was used to seal the thermocouple wire leads. Prior to tests, the leads were checked with a multimeter for electrical continuity and absence of grounding with the FPD framework. Alligator lead clips were used to connect the Thermocouple Tester to the thermocouple wires.

B.3 Note about Sealant and Gaskets

The Kraft paper/sealant gaskets may have been one of the sources of leakage. The TiteSeal ™ cement sealant had the consistency of molasses and was intended for use on automotive engines. There were indications that this sealant compound did not fully cure though air drying. Additional heat may have been required to properly cure the sealant. The use of a heat gun was considered after the assembly of the aluminum frame pieces. A heat gun was procured and used to heat the areas near the seams of the frame pieces. It

was inconclusive as to whether this procedure worked or not. The heat gun procedure was not pursued further due to reservations that the heat may warp the aluminum frames, soften the Plexiglas panels, and/or promote the development of cracks in the glass through thermal stress.

Appendix C: Mixture Preparation, FPD Fill, and Shutdown Procedures

Test mixtures composed of dry air and propane were prepared using the Gas Mixture Preparation Cart. This apparatus and the connections to the FPD are shown in Fig. C.1.

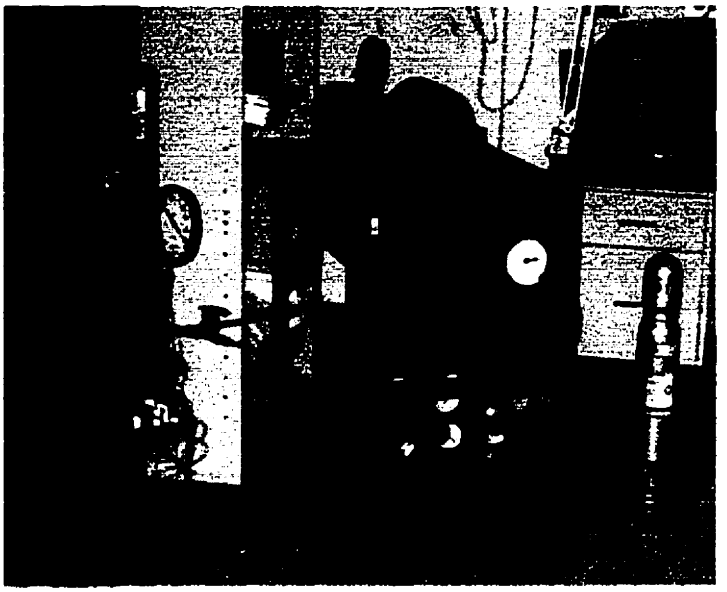

Fig. C.1 Gas Mixture Preparation Cart and connections to the FPD.

A schematic of the piping including valves is shown in Fig C.2. The valves, ports and gauge are identified for reference to the procedures.

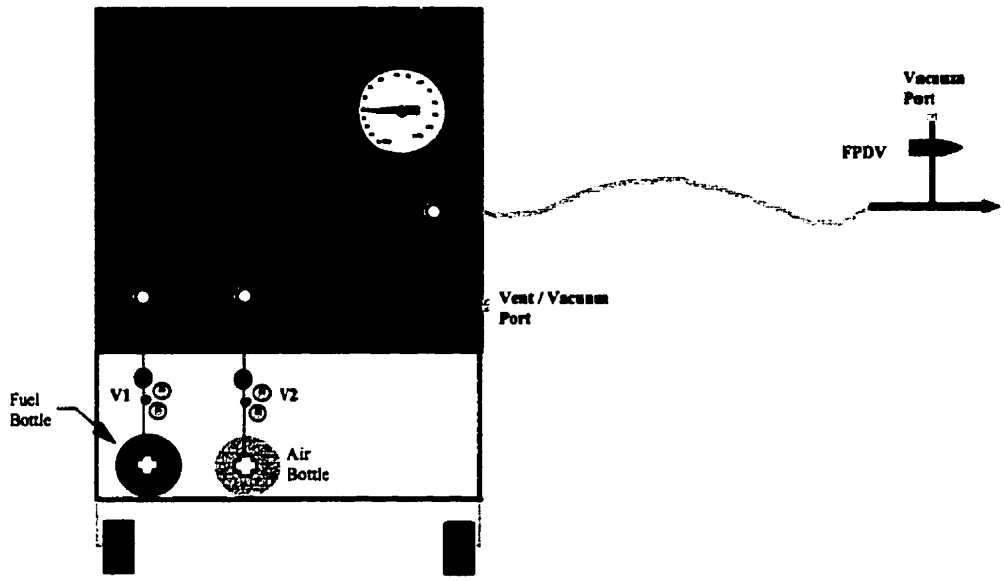

Fig. C.2 Schematic of piping arrangement for Gas Mixture Preparation Cart.

C.1 Mixture Preparation Procedure

1. For the desired equivalence ratio, calculate the required fuel pressure and final tank pressure.
2. Prior to any operations, check for tight regulator connections to fuel and air bottles.
3. Open the valves for the fuel and air bottles.
4. Adjust regulator valves (**V1**) and (**V2**) to desired operating pressures. Fuel regulator valve (**V1**) should be adjusted to a pressure of approximately 20 psig. Air regulator valve (**V2**) should be adjusted to a pressure of approximately 100 psig. Open the shut-off valves on the air and fuel regulators.
5. Confirm that valve 3 (**V3**), valve 4 (**V4**), valve 5 (**V5**), and valve 6 (**V6**) are in the closed position.
6. Attach vacuum pump hose to **Vent/Vacuum** port..
7. Open valve 6 (**V6**) and turn on vacuum pump.

8. Apply vacuum until gauge indicates 30 in Hg vacuum, or until maximum vacuum is obtained. Close valve 6 (**V6**) and then turn off the vacuum pump.
9. Fuel is the first component to be measured. Adjust fuel flow control valve (**FCV1**) to the fully opened position.
10. Open valve 3 (**V3**).
11. Monitor gauge. Fill mixture tank until gauge indicates the fuel pressure needed for the desired mixture equivalence ratio. As the gauge needle approaches the required pressure, the fuel flow control valve (**FCV1**) should be gradually closed to reduce the flow rate of the fuel. It is important to use the mirrored dial to reference the position of the needle against the dial. The mirrored dial reduces parallax error.
12. Once the needle indicates the desired fuel pressure, close valve 3 (**V3**).
13. Wait approximately half a minute. The pressure in the mixture tank may drop slightly. If this occurs, open valve 3 (**V3**) again. Close valve 3 (**V3**) when desired pressure is reached.
14. Air is used to pressurize the mixture tank to the desired final tank pressure. Adjust air flow control valve (**FCV2**) to the fully opened position.
15. Open valve 4 (**V4**).
16. Monitor gauge. Fill mixture tank until gauge indicates the final pressure needed for the desired mixture equivalence ratio. As the gauge needle approaches the required pressure, the air flow control valve (**FCV2**) should be gradually closed to reduce the flow rate of the air.
17. Once the needle indicates the desired fuel pressure, close valve 4 (**V4**).

18. Wait approximately one minute. The pressure in the mixture tank may drop slightly. If this occurs, open valve 4 (**V4**) again. Close valve 4 (**V4**) when desired pressure is reached. This step may need to be repeated until the final mixture pressure is reached and remains steady.
19. Allow the mixture to stabilize for 10 minutes prior to use in the FPD. At 90 psig, the mixture tank contains enough gas to charge the FPD to 1 atm pressure 4 or 5 times.

C.2 FPD Fill Procedure

1. To fill the FPD, attach the vacuum pump hose to the vacuum port on the tee and valve fitting as shown in Fig. C.1. Note that the braided FPD fill line remains attached to the FPD at all times.
2. Confirm that the pressure equalization valve on the FPD is in the closed position.
3. Turn on the vacuum pump to evacuate the FPD. Open the vacuum valve (**FPDV**) on the FPD as shown in Fig. C.1.
4. Monitor the vacuum pressure with the FPD vacuum gauge.
5. When maximum vacuum in the FPD is reached, close the FPD vacuum valve (**FPDV**) and immediately open valve 5 (**V5**). Fully open the mixture flow control valve (**FCV3**).
6. Monitor the FPD vacuum gauge. Adjust the mixture flow control valve (**FCV3**) if necessary. Close valve 5 (**V5**) when the gauge indicates 0 kPa.

C.3 Shutdown Procedure

1. Turn off all electrical equipment. This includes the oscilloscope, ignition transformer, instrumentation power supply, vacuum pump, etc.
2. Disconnect all power cords from outlets.
3. Confirm that the FPD pressure equalization valve is in the open position.
4. Disconnect the vacuum pump hose from the FPD or Gas Mixture Preparation Cart.
5. Open valve 6 (**V6**) to relieve pressure in the mixture tank.
6. Fully close the valves for the fuel and air bottles.
7. Open valve 3 (**V3**), and valve 4 (**V4**).
8. Fully open fuel flow control valve (**FCV1**) and air flow control valve (**FCV2**) to relieve pressure in the regulator valves.
9. Once the pressure is relieved, fully close the shut-off valves on the air and fuel regulators.
10. Close valve 3 (**V3**), valve 4 (**V4**), valve 5 (**V5**), and valve 6 (**V6**).
11. Close the flow control valves (**FCV1**), (**FCV2**), and (**FCV3**) to some intermediate position other than fully opened or fully closed.

Appendix D: Propane and Dry Air Specifications

Instrument grade propane (> 99.5% propane) Supplier: Air Products / Weldco Typical analysis (molar basis)	
propane	99.60 %
isobutane	0.30 %
ethane	624 ppm
methane	225 ppm
n-butane	14 ppm
water vapor	< 3 ppm
sulfur	< 0.5 ppm

Table D.1 Composition of propane.

Dry Air Supplier: BOC Gases Typical analysis (molar basis)	
nitrogen	78.03 %
oxygen	20.99 %
argon	0.94 %
carbon dioxide	300 ppm
hydrogen	< 100 ppm
neon	< 12 ppm
water vapor	< 10 ppm
helium	< 4 ppm
xenon	< 0.1 ppm

Table D.2 Composition of dry air.

Appendix E: Partial Pressure Method of Mixture Preparation

E.1 Theory

The partial pressure method was used to determine the reactant pressures necessary to make mixture compositions to the desired equivalence ratio. The equivalence ratio (ϕ) was defined as the stoichiometric air to fuel ratio with respect to the air to fuel ratio of the test mixture. The fuel and air parameters are mass quantities which are symbolized in the following equation.

$$\phi = (A / F)_{stoich} / (A / F)_{test}$$

For this test program, only two reactants were used. These reactants were propane and air. The stoichiometric equation which describes the chemical reaction between the two reactants is shown in the following equation.

$$C_3H_8 + 5 (O_2 + 3.76 N_2) \rightarrow 3 CO_2 + 4 H_2O + 18.8 N_2$$

Subsequently, for a stoichiometric reaction, 5 moles of air were needed for each mole of propane. The mass quantities of each reactant were related to the mole quantities of each reactant by the molecular weight.

$$m_{fuel} = MW_{fuel} \times n_{fuel}$$

$$m_{air} = MW_{air} \times n_{air}$$

Therefore, the stoichiometric air to fuel ratio for propane is calculated as:

$$(A / F)_{stoich} = (m_{air} / m_{fuel})_{stoich} = 15.58$$

Knowing this value, the test air to fuel ratio could be determined for a desired equivalence ratio.

The ideal gas equation of state can be manipulated to form Dalton's law of partial pressures. This law states that the pressure exerted by a gas component in a mixture of gases is related to the number of moles of that gas component. The summation of the pressures exerted by each gas component is equal to the total pressure of the gas mixture. Dalton's law of partial pressures is expressed with respect to the fuel component of the gas mixture in the following equation.

$$n_{fuel} / n_{total} = P_{fuel} / P_{total}$$

where:

$$n_{fuel} + n_{air} = n_{total}$$

These last relationships allowed for the use of easily measured pressures to produce test mixture compositions.

E.2 Application

A simple Microsoft Excel spreadsheet was developed to easily calculate the reactant fill pressures needed to produce a test mixture. The spreadsheet was developed for mixtures of propane and dry air. The input parameters were the desired equivalence ratio of the mixture and the desired fuel pressure. Two output parameters were calculated. The first parameter was the required fuel fill pressure as specified for the ASHCROFT Type 1082

test gauge. The second parameter was the total pressure of the mixture which was achieved using the dry air after the necessary fuel pressure had been reached.

The spreadsheet program is shown below in Fig. E.1. The cell formulae are displayed in blue.

	B	C	D	E	F	G	H	I	J
2									
3	**Gas Mixing Parameters**								
4									
5	Fuel:	Propane							
6	Oxidizer:	Air							
7									
8	Desired equivalence ratio:			**1.20**					
9									
10	Desired fuel pressure (in Hg)			**9.42**					
11									
12									
13	$(A/F)_{stoic}$ =		15.580						
14	$(A/F)_{test}$ =		12.983	(D13/E8)					
15									
16	MW_{air} =		28.850						
17	MW_{fuel} =		44.096						
18	MW_{mix} =		29.581	(D16*(1-D22))+(D17*D22)					
19									
20	x_{air} / x_{fuel} =		19.844	(D14*D17/D16)					
21									
22	$x_{fuel} = n_{fuel} / n_{total}$ =		0.048	(1/(D20+1))					
23									
24	P_{fuel} (psia)=		4.628	(E10*14.7/29.92)					
25									
26	P_{total} (psia) =		96.47	(D24/D22)					
27									
28	P_{total} (psig) =		81.77	(D26-14.7)					

	H	I	J
	Pressure Gauge Marks		
	P_{fuel} (in Hg) =	**20.50**	(29.92-E10)
	P_{total} (psig) =	**81.77**	(D28)

Fig. E.1 MS Excel spreadsheet program for test mixture preparation.

Appendix F: Photodiode Descriptions, Installations and Configurations

F.1 Photodiode Types

A number of inexpensive photodiodes with varying wavelength sensitivities were purchased to determine a suitable type that could be used for this project. The photodiodes were silicon types produced by VACTEC and purchased from ALLIED ELECTRONICS. A butane BBQ lighter was used to produce a flame in which the photodiodes were tested against. The photodiodes were held in place approximately 10 cm from the flame and the subsequent photodiode signals were measured on a digital voltmeter.

The VTP100 type was found to produce the strongest signal from these tests. This type of photodiode had a specified wavelength sensitivity in the infrared range of 725 to 1150 nm. Additional photodiodes of this type were purchased and connected to leads from the signal processing circuits. Once the signal processing circuits were tested and checked out, the photodiodes were installed in plastic shields. These shields were in turn attached to the side Plexiglas and glass panels of the FPD.

During the course of initial testing of the FPD, it was found that the propagating flame fronts were not being picked up by the photodiodes. This was due to the fact that propane flames do not emit infrared radiation except for rich mixture conditions. The VTP100 photodiodes were removed and it was decided to use photodiodes which were sensitive in the visible light region. The VTP3310LA type photodiode was connected to the signal

processing circuits. A number of tests were conducted with the FPD and it was found that this type of photodiode produced a satisfactory signal. The wavelength sensitivity for the VTP3310LA was in the range of 400 to 1150 nm. A number of photodiodes of this type were purchased and installed on the FPD.

A number of photodiodes sensitive in the ultraviolet region were also obtained. These photodiodes were purchased from BOSTON ELECTRONICS. The part number for these photodiodes was JECO.1 These ultraviolet photodiodes were more expensive than the visible light types, but testing indicated that the photodiodes could detect propane flames. The resulting signals however, were weak. This would have necessitated additional amplification circuitry to the signal processing circuits. Another disadvantage was that the ultraviolet photodiodes would have required installation on the inside surface of the Plexiglas and glass panels. This was due to the fact that these materials severely reduce the transmission of ultraviolet light.

F.2 Backlighting Procedures

The VTP3310LA photodiodes proved acceptable in detecting visible flame fronts propagating through the FPD. However, for those lean and rich mixture conditions which produced faint flame fronts, the photodiodes did not detect the flame fronts. For these situations, a backlighting procedure was devised and implemented.

The VTP3310LA photodiode had a small detection element encapsulated in clear plastic (see the accompanying specification sheet). The photodiode was cylindrical with a bulb-

shaped head. When installed on the FPD, the element was perpendicular to the axial length of the FPD. It was found that light directed to the back end of the photodiode also caused the photodiode to register a signal. It was surmised that since the rear end of the photodiode was clear plastic, light entering the photodiode in this manner was internally reflected off the bulb shaped head onto the detection element.

The backlighting procedure involved the use of a desktop fluorescent lamp which was placed approximately 50 to 80 cm in front of the FPD. The lamp would be adjusted to direct the light to the back ends of the photodiodes. The lamp would be moved backward or forward just enough to prevent the photodiodes from registering a signal on the oscilloscope. Once a faint flame front was produced, the additional light radiation would exceed the set photodiode threshold level, thereby resulting in a signal.

This procedure was only used during the collection of photodiode velocity data and not during the recording of flame front images. Backlighting was necessary for mixture conditions of $\phi \leq 1.0$ and $\phi \geq 1.6$.

F.3 Photodiode Shields

Photodiode shields were constructed from pieces of plastic tube and sheet stock. The purpose of these shields was to act as photodiode mounting structures and to reduce the field detection angle of the photodiodes. Limiting the field detection angle improved the accuracy of the velocity measurements.

PACKAGE DIMENSIONS inch (mm)

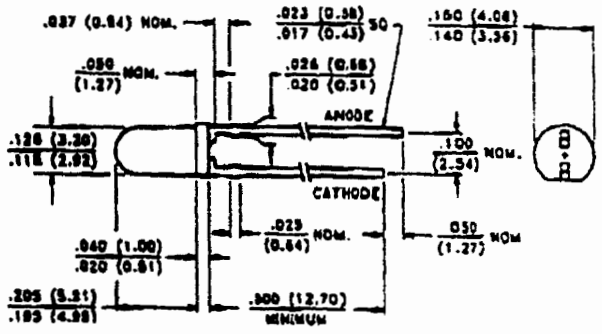

CASE 58A LONG T-1
CHIP ACTIVE AREA: .0011 in^2 (0.684 mm^2)

PRODUCT DESCRIPTION

Small area planar silicon photodiode in a clear, long T-1, endlooking package. These diodes exhibit low dark current under reverse bias and fast speed of response.

ABSOLUTE MAXIMUM RATINGS

Storage Temperature: -40°C to 100°C
Operating Temperature: -40°C to 100°C

ELECTRO-OPTICAL CHARACTERISTICS @ 25°C (See also VTP curves, pages 36-37)

SYMBOL	CHARACTERISTIC	TEST CONDITIONS	VTP3310LA						UNITS
			Min.	Typ.	Max.	Min.	Typ.	Max.	
I_{SC}	Short Circuit Current	H = 100 fc, 2850 K	24	36					µA
TC I_{SC}	I_{SC} Temperature Coefficient	2850 K		.20					% / °C
V_{OC}	Open Circuit Voltage	H = 100 fc, 2850 K		350					mV
TC V_{OC}	V_{OC} Temperature Coefficient	2850 K		−2.0					mV / °C
I_D	Dark Current	H = 0, V_R = 50 V			35				nA
R_{SH}	Shunt Resistance	H = 0, V = 10 mV		10					GΩ
C_J	Junction Capacitance	H = 0, V = 3 V			25				pF
R_R	Responsivity	940 nm		.016					A/(W/cm^2)
S_R	Sensitivity	@ Peak		.55					A/W
λ_{range}	Spectral Application Range		400		1150				nm
λ_p	Spectral Response – Peak			925					nm
V_{BR}	Breakdown Voltage		30	140					V
$\theta_{1/2}$	Angular Resp. – 50% Resp. Pt.			±20					Degrees
NEP	Noise Equivalent Power		1.8×10^{-13} (Typ.)						W/$\sqrt{Hz}$
D*	Specific Detectivity		5.3×10^{11} (Typ.)						cm$\sqrt{Hz}$ / W

Fig. F.1 Specification sheet for VTP3310LA type photodiode.

The photodiodes were held in place in the shields by friction. Figure B.4 shows the original arrangement for the infrared VTP100 type photodiodes. The black, rectangular photodiodes were fitted in the photodiode tubes. The tubes were 44 mm long and were glued to 3 mm thick styrene plastic bases. The bases were held in place to the side panels with duct tape.

The final arrangement with the VTP3310LA photodiodes used 3.6 mm diameter tubestock and 1.6 mm thick bases. The bases were reduced in area and some of them were made cross-shaped as shown in the contour images in Chapter 4. Transparent tape was used to secure these bases to the FPD side panels. Figure 3.2 shows a typical setting of how these photodiode shields were arranged.

The shield tubes were originally cut to 31.8 mm lengths. The first tests with these shields indicated that the photodiodes received insufficient light to register signals. The tubes were ultimately cut to 19 mm lengths to improve light detection. This resulted in a field detection angle of 10.7 °.

F.4 Photodiode Configurations

As mentioned in Chapter 3, three photodiode configurations (labeled AA, BB, and CC) were used to characterize the flame propagation velocities in the FPD. These configurations are shown in the following figure. Two sets of photodiodes remained in

the same locations for all three photodiode configurations. One set was located at the midpoint of the straight inlet section. The other set was at the entrance to the bend.

Configuration AA

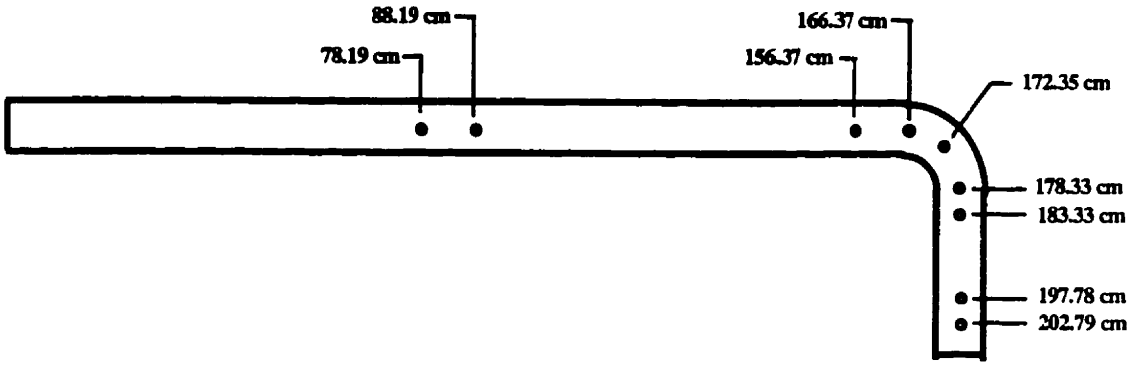

Configuration BB

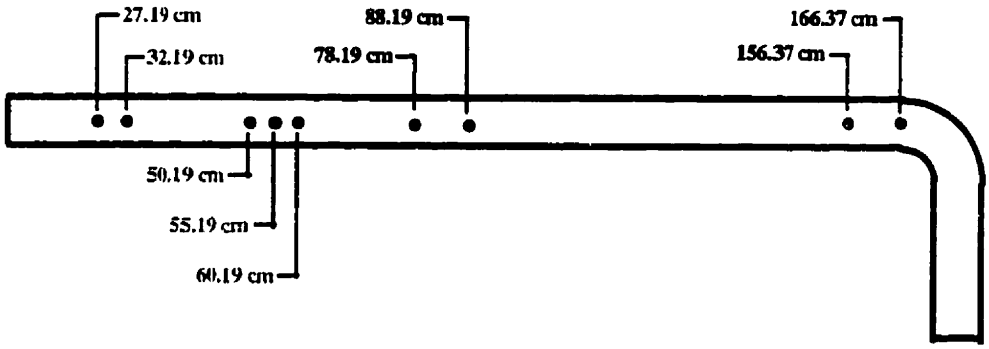

Configuration CC

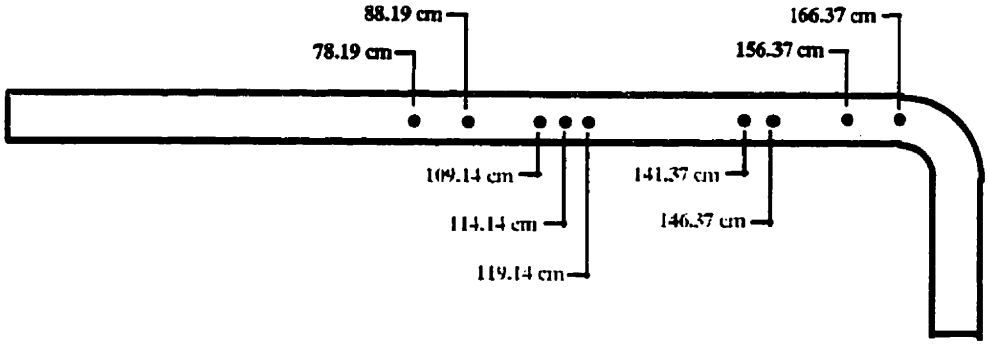

Fig. F.2 Photodiode configurations AA, BB and CC.

Appendix G: Signal Processor Circuits

The purpose of these circuits was to collect the signals from photodiodes and to manipulate them so that output signals could be displayed on an oscilloscope screen. The signals would be displayed in a characteristic waveform pattern.

The circuits were combinations of basic electronic designs obtained from published sources. All circuits were fabricated and tested using experimental breadboards and commercially available electronic components. The breadboards allowed for easy removal and installation of components to produce circuits which would operate to the desired requirements. Once a test circuit was deemed acceptable, the components were removed from the breadboard and hard-wired to phenolic circuit boards.

Over the course of this research program, it was found that the first circuit design (MOD 1) did not prove entirely satisfactory. Half the circuit was removed and a new circuit design was fabricated, tested and implemented. This circuit design (MOD 2) proved satisfactory and was used in the collection of the test data.

G.1 Processor Circuit MOD 1

The MOD 1 circuit was composed of 3 simple operational amplifier sub-circuits. These sub-circuits were obtained from NATIONAL SEMICONDUCTOR handbooks. The MOD 1 circuit schematic is shown in Fig. G.2. A 2-channel oscilloscope was used for

this project. However, the diagram shows the schematic for only one channel. The schematic for the other channel would be similar. The symbol legend for the circuit schematic is shown in Fig. G.1. A brief description of the 3 sub-circuits follows.

Sub-circuit 1: Photodiode Threshold Detector

This sub-circuit created a constant voltage signal when a photodiode detected light above a certain threshold level. The threshold level could be varied by changing the resistance of the **R1** and **R2** resistors. Initial tests showed that an acceptable threshold level was attained when **R1** = **R2** = 2.2 MΩ.

Sub-circuit 2: OR Gate

This sub-circuit detected an output signal from any one of the individual Photodiode Threshold Detectors. If an output signal was detected, a new signal was produced and sent on to the next sub-circuit.

Sub-circuit 3: One-Shot Multivibrator

This sub-circuit read the signal from the OR Gate and created a new voltage signal of only millisecond duration. The duration of the signal could be adjusted. For this application the duration was set to 2.5 ms. The "blip" signal could be read on one channel of the oscilloscope as $\mathbf{V_o}$.

During initial testing with propagating flame fronts in the FPD, a number of deficiencies became apparent with this circuit design. The foremost deficiency was the fact that the

OR Gate sub-circuit would produce an output signal regardless of the number of photodiodes illuminated at one time. It was initially speculated that a propagating flame front would only illuminate one photodiode at a time. Testing indicated that this was not the case.

Another deficiency was that the "blip" signals from the One-Shot Multivibrator sub-circuit were all of the same voltage level. Therefore, it was not always possible to correlate a "blip" signal to an individual photodiode. Again, the fact that a propagating flame front could illuminate more than one photodiode at a time made this deficiency a problem.

G.2 Processor Circuit MOD 2

The MOD 2 circuit was devised to alleviate the MOD 1 deficiencies. The schematic of this circuit is shown in Fig. G.3. The MOD 2 circuit used the existing Photodiode Threshold Detector sub-circuit of the original MOD 1 circuit. However, in the new design, the outputs from these detectors were shunted to ground through resistors. Each Photodiode Threshold Detector signal passed through a different resistance. This in effect created a voltage divider arrangement which resulted in a different voltage across each resistor. This voltage difference was used as the new signal. Consequently, each photodiode now had a specific, distinguishing voltage signal associated with it.

The signals were collected and sent to an N-Input Non-inverting Adder, or Summer sub-circuit. This circuit was described in **Operational Amplifiers and Linear Integrated**

Circuits by Coughlin and Driscoll. The Adder sub-circuit added the voltage signals together to produce an output signal $\mathbf{V_o}$. Similar to the MOD 1 circuit, this signal was read by one channel of the oscilloscope and displayed as a waveform on the oscilloscope screen.

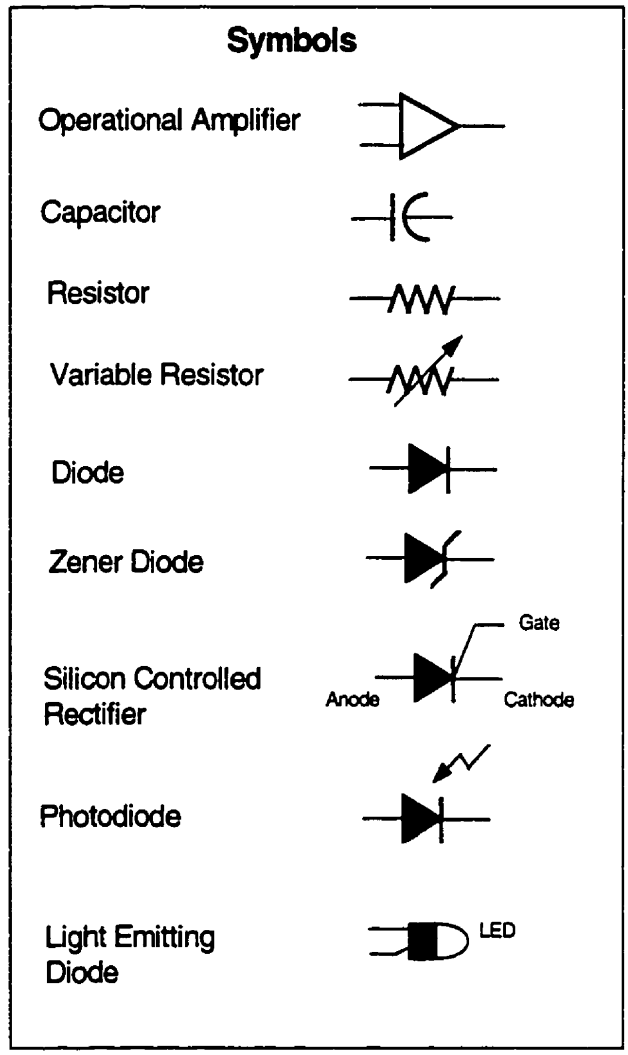

Fig. G.1 Symbol Legend for MOD 1 and MOD 2 circuit schematics.

Fig. G.2 Schematic of Signal Processing Circuit, MOD 1.

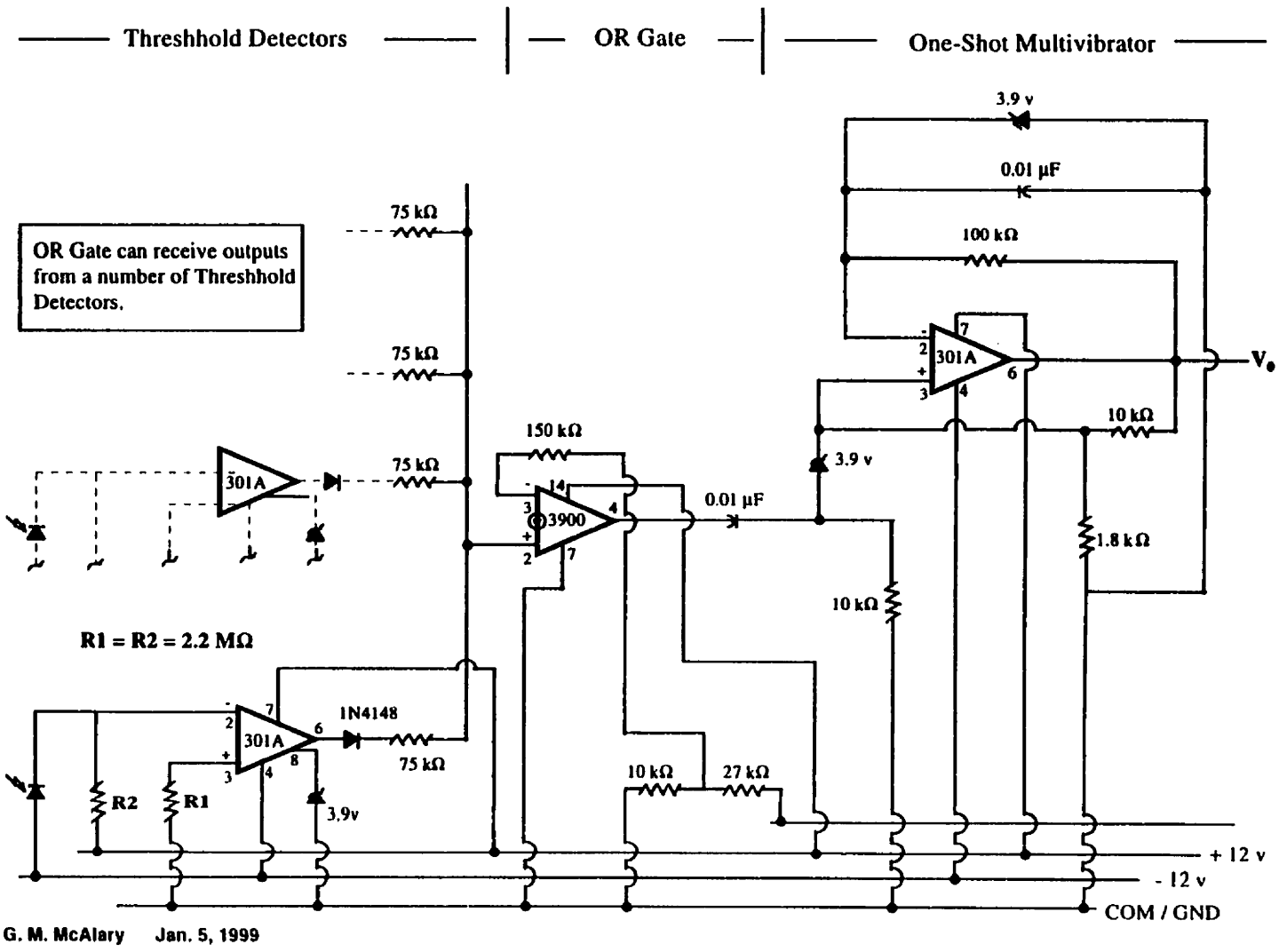

Fig. G.3 Schematic of Signal Processing Circuit, MOD 2.

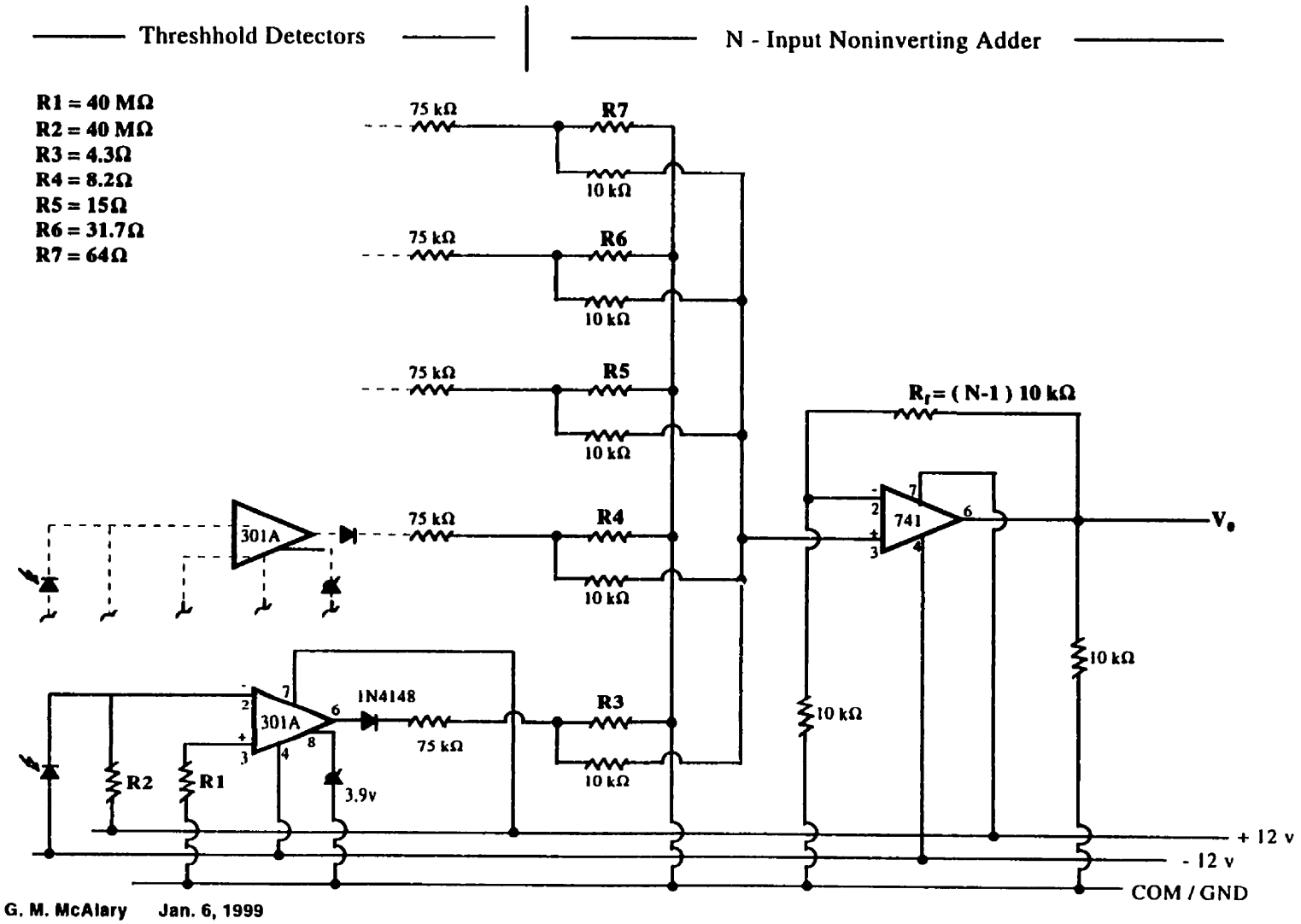

Appendix H: Oscilloscope Waveform Profile

The Mod 2 Signal Processing Circuit allowed for the individual identification of photodiode signals. Table H.1 shows the voltage signal values for every photodiode installed on the FPD. It should be noted that the signal voltage for each photodiode was approximately twice the value of the preceding photodiode signal. This geometric progression prevented the summation of signals from a number of photodiodes from being mistaken for the signal from one of the later photodiodes.

Oscilloscope Channel 1		Oscilloscope Channel 2	
Photodiode No.	V_{sig}	Photodiode No.	V_{sig}
1	0.22	1	0.11
2	0.39	2	0.22
3	0.86	3	0.41
4	1.58	4	0.82
		5	1.52

Table H.1 Voltage signal values for photodiodes.

The output signal from the processing circuit ($\mathbf{V_o}$) was the summation of all the signals from those photodiodes which were illuminated. For example, if V_o = 1.45 volts was measured for channel 2, then the only photodiodes which were illuminated at the time were photodiodes number 2, 3, and 4.

Figure H.1 shows a typical oscilloscope screen display of the photodiode signals obtained from the MOD 2 signal processing circuits. The top waveform was from channel 1, while the bottom waveform was from channel 2. The green numbers represent

the voltage levels for photodiodes 1, 2, 3 and 4 on channel 1. Note that the summation of the voltage signals from photodiode 1 and 2 are distinctly lower than the single voltage signal from photodiode 3.

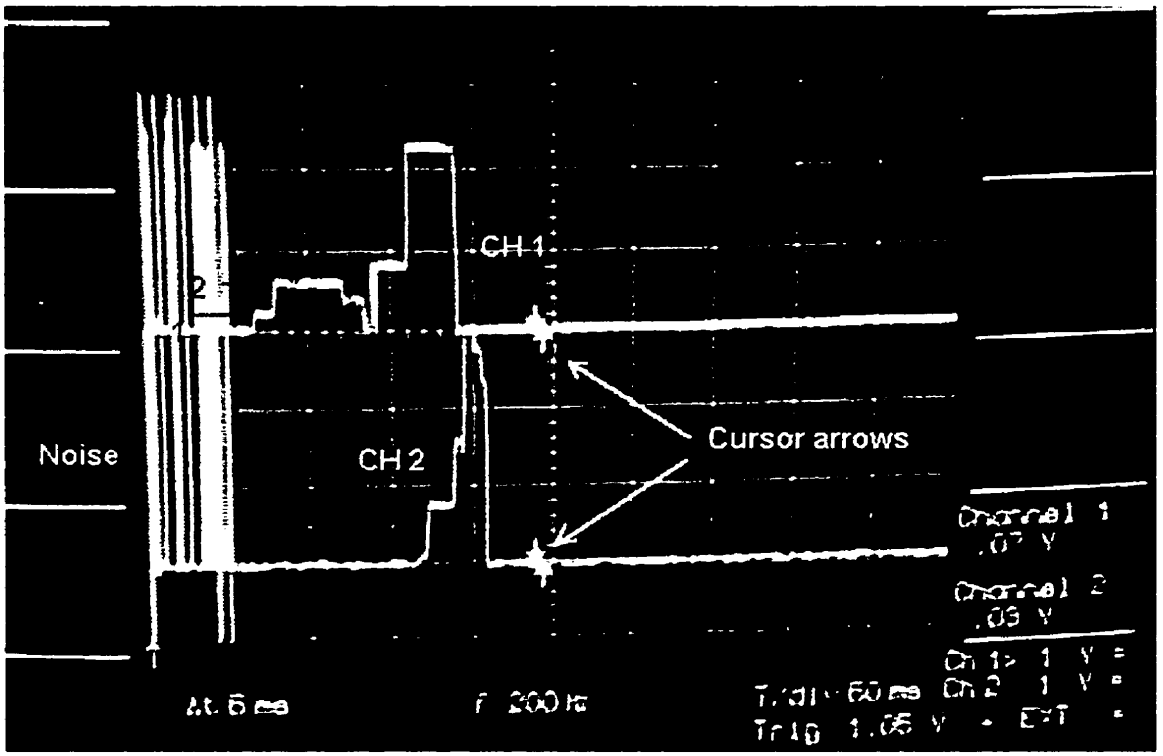

Fig. H.1 Typical oscilloscope screen display of photodiode signal waveforms.

Electromagnetic Interference (EMI) is shown as noise at the leftmost part of the screen. This EMI was due to the activation of the ignition transformer. As mentioned in Chapter 3, this undesirable condition was turned into a benefit by using the EMI to trigger the beginning of signal acquisition by the oscilloscope.

The LECROY oscilloscope used in this research project had the capability to expand the waveform. This allowed for better resolution of the time differences between corresponding photodiode signals. The cursor arrows could be moved along the

waveforms by using the appropriate knobs on the oscilloscope. One arrow would be moved to the point on the waveform where an abrupt jump to a new voltage level took place. This vertical line of the waveform, as shown in Fig. H.1 as a red highlighting mark, indicated the time when a photodiode was beginning to be illuminated by a flame front. The second cursor arrow would be moved to the next vertical line of the waveform. This line indicated the time when the neighboring photodiode was beginning to be illuminated. The time difference (delta t) between these cursor positions was the time that the flame front propagated between those specific photodiodes.

Appendix I: Ignition Circuit

Initiation of the combustion of the mixture inside the FPD was achieved by an ignition system. This system used a transformer to convert a 120 volt AC current to a 10,000 volt DC current. The high voltage resulted in an arc between the electrodes of the spark plug. The spark plug protruded into the FPD chamber which contained the combustible gas mixture.

The system as originally conceived used a simple AC push-button switch between the transformer and 120 VAC power cord. In the interest of safety, this system was replaced by a relay arrangement as shown in Fig. I.1. In this configuration, the push-button ignition switch controlled a low voltage DC current. A relay separated the high voltage side of the system from the low voltage DC side. The ignition switch was placed between the instrumentation power supply and the coil of the relay. When the switch was closed, the coil was energized. This in turn closed the high voltage switches in the relay.

Approximately 3 meters of leadwire separated the ignition switch from the relay. This allowed the operator to step away from the FPD during firing. This provided additional safety and permitted the operator a broader view of the flame front propagation through the FPD.

Fig. I.1 Schematic of Ignition Circuit.

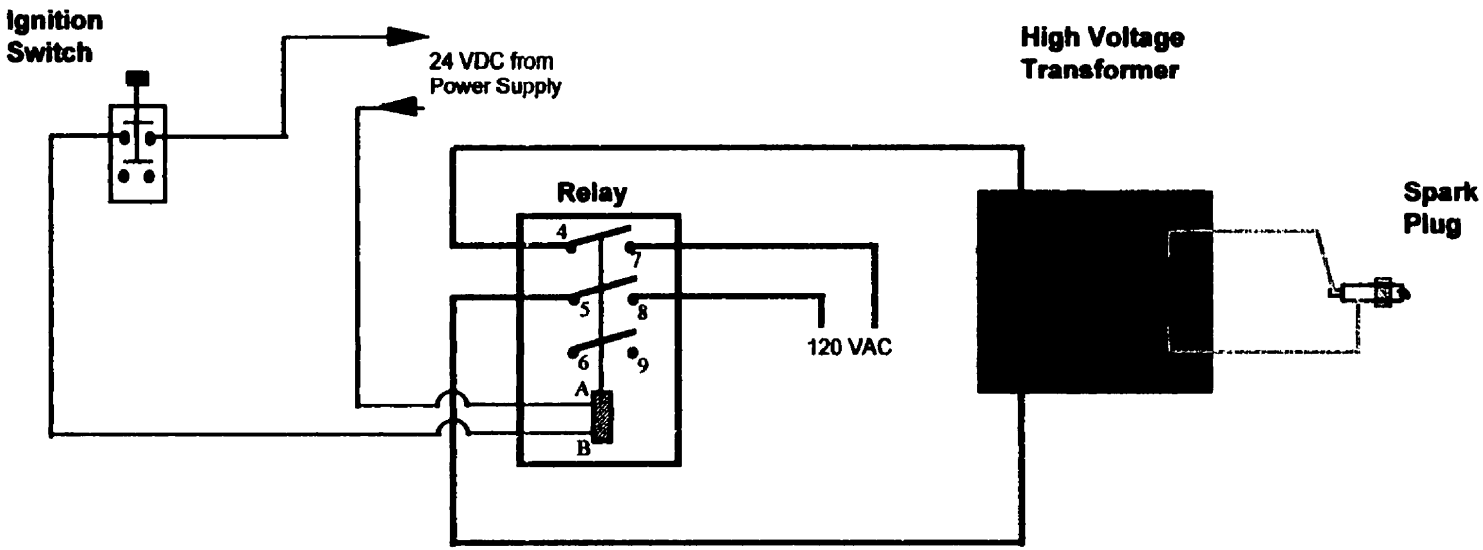

G. M. McAlary Jan. 5, 1999

Appendix J: Time Delay Circuits

The Time Delay Circuits were used during the Schlieren phase of the FPD tests. These circuits were to introduce a time delay between ignition of the mixture, and activation of the impulse current from the thermocouple time constant tester.

The first system used a mechanical time delay relay. This system had a minimum time delay of 100 ms. This delay duration was found to be too long for the test conditions. The mechanical relay system was then replaced by an electronic time delay circuit. The descriptions of both these systems follow.

J.1 Mechanical Time Delay Circuit

The schematic of the Mechanical Time Delay Circuit is shown in Fig. J.1. The key component of this circuit was a programmable time delay relay. This relay was a POTTER & BRUMFIELD type, purchased from ELECTROSONICS. It could be used for AC or DC current and could be programmed for one of eight functional modes. The time delay was adjustable between 0.1 sec. to 100 minutes.

For this application, the time delay relay was programmed for a "Recycle- initially off" mode. The time delay range was set to the lowest range (0.1 to 1.0 seconds). The relay was powered from the instrumentation power supply. Initiation of the time delay was achieved by the closing of the ignition switch. This in turn closed the switches in the

relay. In essence, the Time Delay Relay was activated by one of the switches in the ignition relay. After the time delay had elapsed, a switch in the Time Delay Relay was closed. This completed the circuit which bypassed the push-button on the TC Time Constant Tester. An impulse current was produced by the Time Constant Tester which heated the thermocouple wire installed in the FPD.

J.2 Electronic Time Delay Circuit

Once it was found that the mechanical time delay circuit was deficient, an alternative was found in the form of an electronic circuit. A simple electronic time delay circuit diagram was found on the World Wide Web at **http:// www.pacsi.org/public/education/gallery/high_speed_photos/fpaper.html**. This site was produced by the North Carolina School of Science and Mathematics in Durham North Carolina. The site dealt with the activities of the school photography club, specifically with the club's efforts in high speed photography.

The schematic of the time delay circuit used in this application is shown in Fig. J.2. The component symbols can be referenced to the legend in Fig. G.1. This circuit used a 556 Timer which consisted of an integrated circuit containing two 555 type timers. The first timer was started by grounding the input. This produced a square wave pulse at pin 5. By adjusting the 1 MΩ variable resistor, the width of the pulse could be changed. This pulse signal went to the trigger of the second timer at pin 8. When the level of the pulse signal dropped to zero, the second timer began. The second timer produced a 50 ms pulse signal at pin 9.

The silicon controlled rectifiers (SCR) were used as triggers which were controlled by the pulse signals from the timers. With this circuit, the minimum time delay obtained was approximately 4 ms.

Figure J.3 is a schematic which shows how the electronic time delay circuit was connected to the ignition switch and TC Time Constant Tester. A 9 volt battery was used to power the circuit. The input was grounded when the ignition switch was closed. This resulted in the immediate triggering of SCR 1. A light emitting diode (LED) was connected to this SCR. The LED was used as a visual indicator of the ignition time. It was placed in view of the high speed camera when recording Schlieren images of the timeline progression.

At the end of the desired time delay, SCR 2 was triggered. This closed the circuit of the bypassed push-button switch on the TC Time Constant Tester.

Fig. J.1 Schematic of Mechanical Time Delay Circuit.

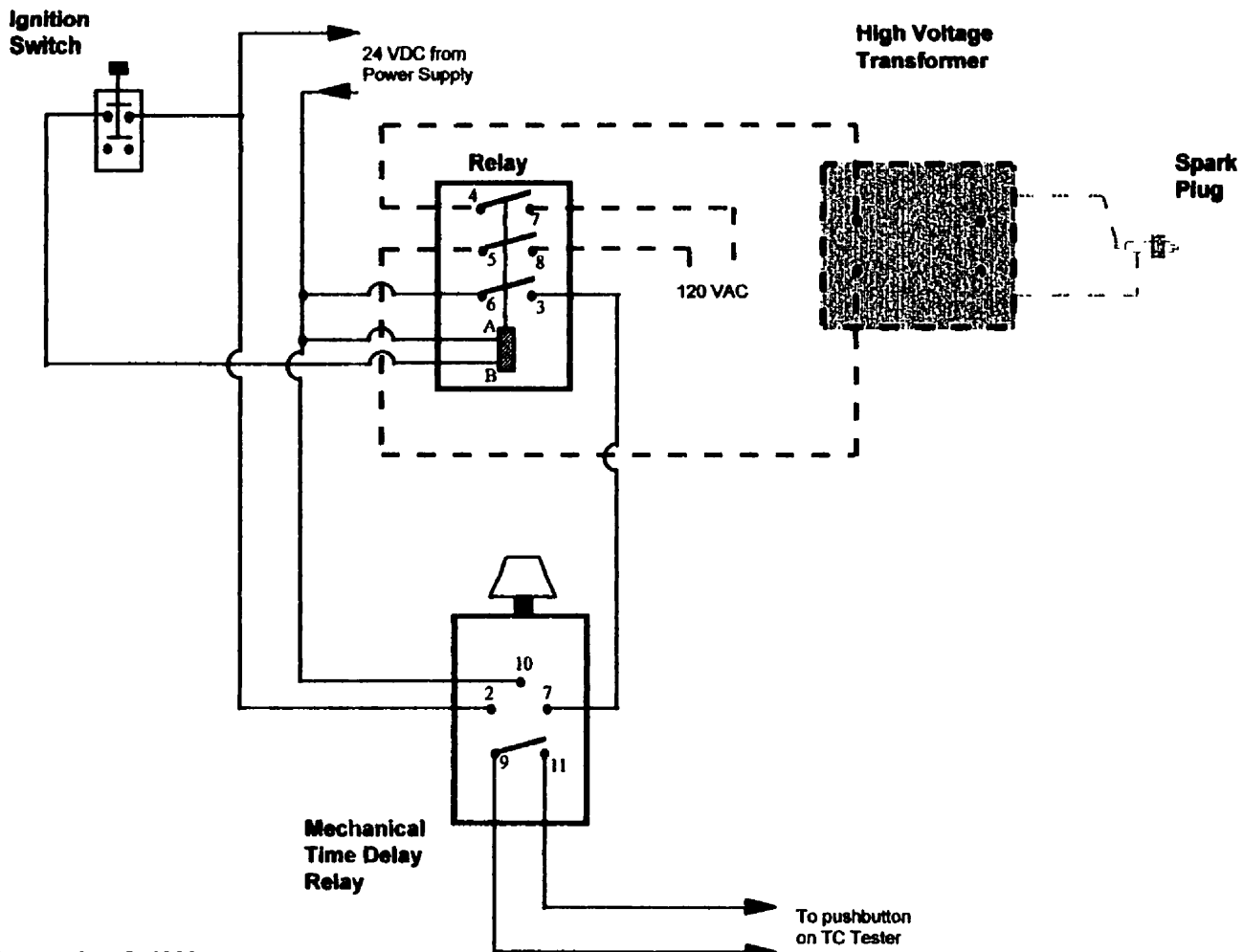

Fig. J.2 Schematic of Electronic Time Delay Circuit.

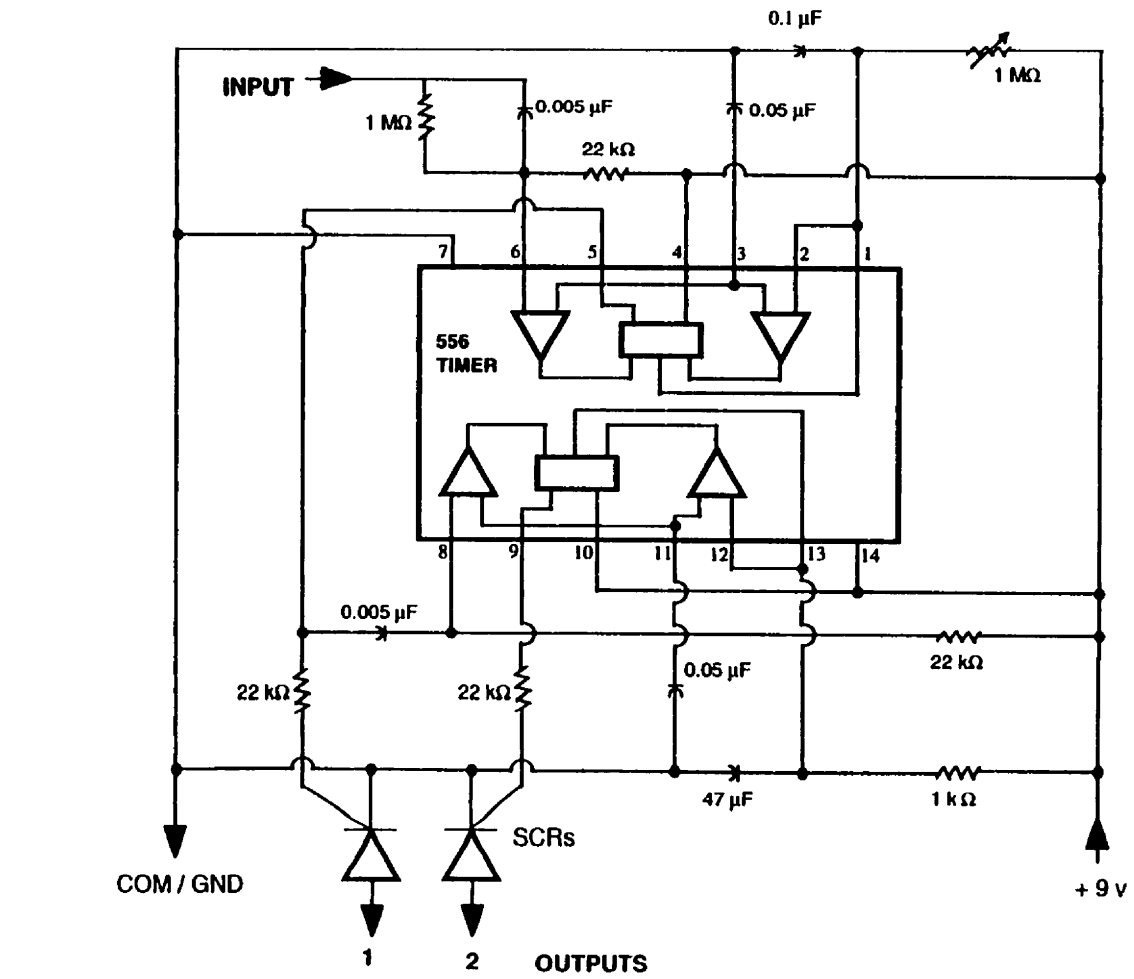

G. M. McAlary Jan. 8, 1999

Fig. J.3 Schematic of electronic time delay circuit and connections to the ignition switch and TC Time Constant Tester.

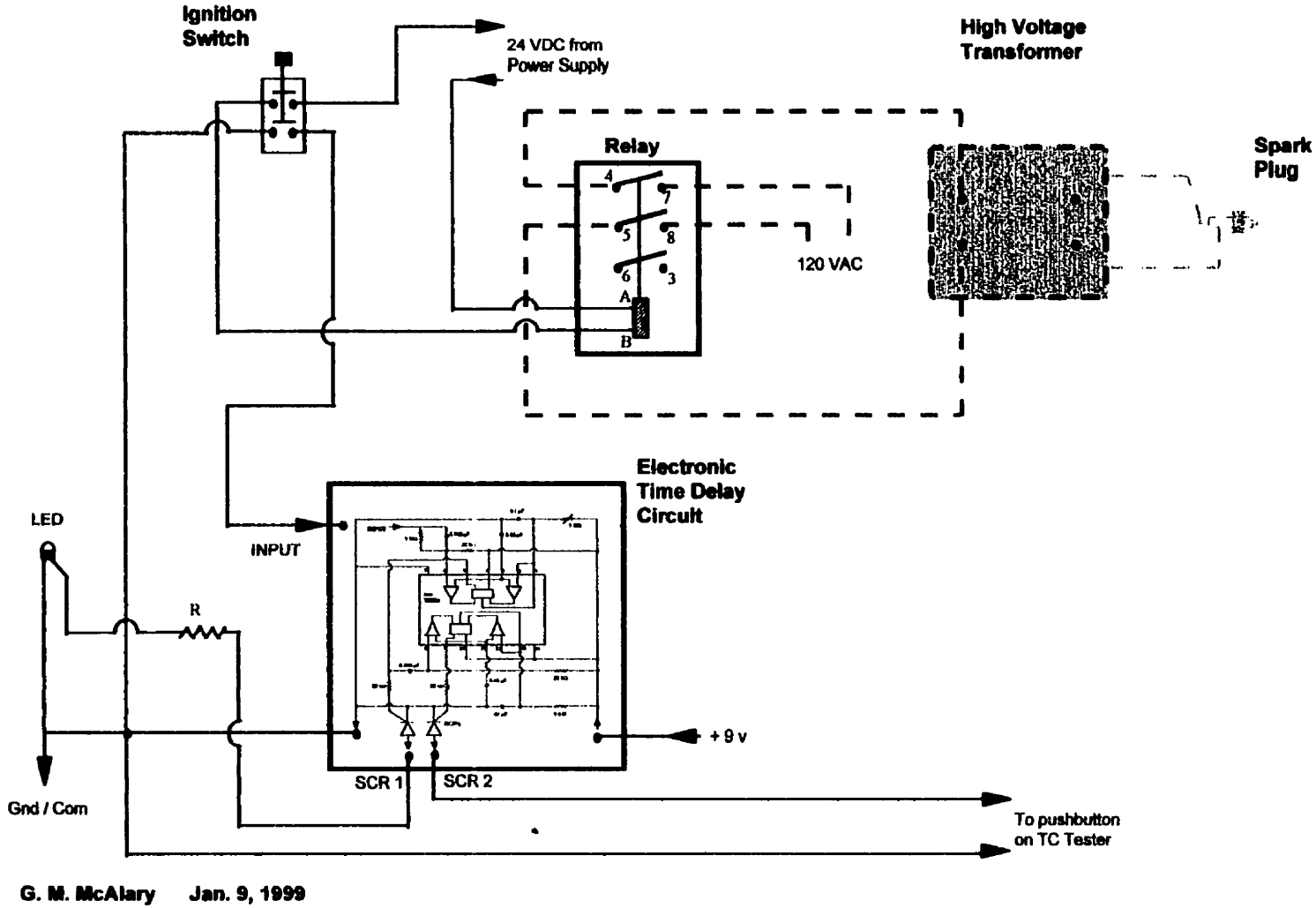

Appendix K: Schlieren Apparatus

The following figures show a schematic of the Schlieren apparatus as used in this research project, and a photograph of the test arrangement with the FPD.

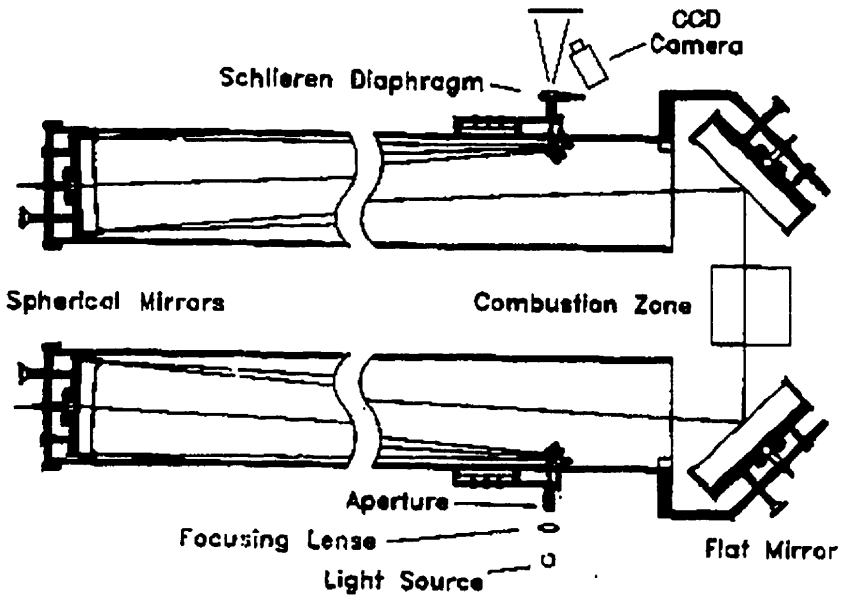

Fig. K.1 Schematic of Schlieren apparatus.

Appendix L: Preliminary Raw Test Data

Table L.1: Preliminary data obtained during FPD commissioning tests.

Test #	Date	ϕ	Oscilloscope Sample Rate (Hz)	Video (Y/N)	Time between photodiodes #1 and #2 (ms)	Calculated Velocity (m/s)	Calculated Re	Calculated Dn	Notes
1	4/14/98	1.2	500	Y	-	-	-	-	
2	4/14/98	1.2	1000	Y	9.0	11.11	25089	16726	
3	4/14/98	1.2	2000	Y	10.5	9.52	21505	14337	max vacuum -> -99.5 kPa .Only photodiodes 1 and 2 used. Full circuit used
4	4/14/98	1.2	2000	Y	12.5	8.00	18064	12043	max vacuum -> -99.5 kPa .Only photodiodes 1 and 2 used. Full circuit used
5	4/15/98	1.4	500	N	10.0	10.00	22580	15053	max vacuum -> -99.5 kPa . Half circuit used (ie. measure op-amp signals)
6	4/15/98	1.4	2000	N	15.5	6.45	14568	9712	" " remaining tests use Photodiodes 1 & 2 and half circuit signals
7	4/16/98	1.4	2000	Y	-	-	-	-	max vacuum -> -99.5 kPa . No signal from photodiodes
8	4/16/98	1.4	1000	Y	11.0	9.09	20527	13685	max vacuum drawn on duct -> -99.5 kPa .
9	4/16/98	1.4	1000	Y	13.0	7.69	17369	11579	" "
10	4/16/98	1.4	2000	Y	13.5	7.41	16726	11151	" " Last run from this cylinder mix.
11	4/16/98	1.6	2000	Y	-	-	-	-	" " flame seems slow, no signal from photodiodes
12	4/16/98	1.6	500	Y	14.0	7.14	16129	10752	" " appears faster than previous flame.
13	4/16/98	1.6	2000	Y	23.5	4.26	9609	6406	" " large time difference
14	4/16/98	1.6	2000	Y	13.5	7.41	16726	11151	" " Last run from this cylinder mix.
15	4/16/98	1.6	2000	Y	19.5	5.13	11579	7720	" " Made up new mix (Equiv ratio = 1.6). Enough for an additional two test runs.
16	4/16/98	1.6	2000	Y	15.5	6.45	14568	9712	" " Last run from this cylinder mix.
17	4/16/98	0.8	2000	Y	-	-	-	-	" " No signal from photodiodes. Possibly too fast a sampling rate.
18	4/16/98	0.8	500	Y	-	-	-	-	" " No signal from photodiodes. Not enough light to energize photodiodes.
19	4/16/98	0.8	1000	Y	41.0	2.44	5507	3672	" " Room lights remain on. Flame went all the way around bend.
20	4/16/98	0.8	1000	Y	51.0	1.96	4427	2952	max vacuum drawn on duct -> -99.5 kPa .
21	4/16/98	1.0	1000	Y	13.0	7.69	17369	11579	" "
22	4/16/98	1.0	2000	Y	15.5	6.45	14568	9712	" "
23	4/16/98	1.0	2000	Y	20.5	4.88	11015	7343	max vacuum drawn on duct -> -99.0 kPa .
24	4/16/98	1.0	2000	Y	25.5	3.92	8855	5903	max vacuum drawn on duct -> -99.0 kPa . Fuzzy playback on video tape.

Test #	Date	ϕ	Oscilloscope Sample Rate (Hz)	Video (Y/N)	Time between photodiodes #1 and #2 (ms)	Calculated Velocity (m/s)	Calculated Re	Calculated Dn	Notes
25	4/16/98	1.1	2000	Y	14.5	6.90	15572	10382	
26	4/16/98	1.1	2000	Y	17.5	5.71	12903	8602	
27	4/16/98	1.1	2000	Y	19.5	5.13	11579	7720	
28	4/16/98	1.1	2000	Y	24.5	4.08	9216	6144	

Test Conditions:

Propane type: BERNZOMATIC

distance between photodiodes: 10 cm

Photodiode #1 is at 132 cm location on FPD.
Photodiode #2 is at 142 cm location on FPD.

All tests were conducted with a 2 minute wait from filling of duct with gas mixture, to ignition of mixture.
Video camera used is S-VHS type with 30 frames per second frame rate.

$Re = v * D_h \cdot rho / mu$ where $D_h = 3.387$ cm, $rho = 1.20$ kg/m^3, $mu = 1.80 \times 10^{-5}$ N s / m^2

$Dn = Re / [R/a]^{0.5}$, where R = mean radius of curvature = 7.62 cm, and $a = D_h = 3.387$ cm

Table L.2: Preliminary data obtained during evaluation of digital VHS camera.

Test #	Date	Sample Rate (kHz)	Video Y/N	ϕ	Time between signals (ms) CH1 (PD1 - PD2) 146 cm	CH1 (PD2 - PD3) 156 cm	CH2 (PD4 - PD5) 197 cm	Notes
29	4/26/98	5,000	Y	1.6	-	-	-	max vacuum drawn on duct -> -100 kPa .
30	4/26/98	50	Y	1.6	7.25	11.3	-	max vacuum -> -99.5 kPa
31	4/26/98	125	Y	1.6	-	-	-	max vacuum -> -100 kPa
32	4/26/98	62.5	Y	1.6	12.1	15.3	-	max vacuum -> -100 kPa
33	4/26/98	62.5	Y	1.4	13.9	13.4	-	max vacuum -> -100 kPa
34	4/26/98	25	Y	1.4	10.8	11.2	-	
35	4/26/98	25	Y	1.4	-	-	-	max vacuum -> -100 kPa, lost data, did not lock waveform
36	4/26/98	25	Y	1.4	11.5	10.8	14.8	max vacuum -> -100 kPa, last run on this mixture batch
37	4/26/98	25	Y	1.2	12.7	11.9	14.0	max vacuum -> -100 kPa
38	4/26/98	25	Y	1.2	8.3	12.7	14.0	max vacuum -> -100 kPa
39	4/26/98	25	Y	1.2	9.5	10.3	13.5	max vacuum -> -100 kPa
40	4/26/98	25	Y	1.2	10.4	11.1	13.8	max vacuum -> -100 kPa
41	4/26/98	25	Y	1.0	15.4	20.8	-	max vacuum -> -100 kPa, no PD #4, PD#5 signal pick up
42	4/26/98	25	Y	1.0	13.8	18.3	17.4	max vacuum -> -100 kPa
43	4/26/98	25	Y	1.0	13.2	16.9	19.3	max vacuum -> -100 kPa
44	4/26/98	25	Y	1.0	19.2	21.8	-	max vacuum -> -100 kPa, no PD #4, PD#5 signal pick up
45	4/26/98	25	Y	0.85	-	-	-	max vacuum -> -100 kPa, no signals
46	4/26/98	25	Y	0.85	-	-	-	max vacuum -> -100 kPa, no signals, tried use of flourescent lamp for backlighting
47	4/26/98	25	Y	0.85	33.8	-	-	max vacuum -> -100 kPa, used 1 set of overhead flourescent lamps for backlighting
48	4/26/98	25	Y	0.85	33.9	-	-	max vacuum -> -100 kPa, used 2 sets of overhead flourescent lamps for backlighting

Test Conditions:

Propane type: BERNZOMATIC

distance between photodiodes: 10 cm

Photodiode #1 is at location 141 cm on FPD.
Photodiode #2 is at 151 cm location on FPD.
Photodiode #3 is at 161 cm location on FPD.
Photodiode #4 is at 192 cm location on FPD.
Photodiode #5 is at 202 cm location on FPD.

All tests were conducted with a 2 minute wait from filling of duct with gas mixture, to ignition of mixture.

Video camera used is CANON OPTURA digital VHS camera with 30 frames per second frame rate.

Appendix M: Raw Test Data

Table M.1: Time signals for photodiode configuration AA

Time between signals (ms)

Test #	Date	PD Config.	Sample Rate (kHz)	Video Y/N	ϕ	[10 cm] CH1 PD1-PD2 83 cm	[10 cm] CH1 PD3-PD4 161 cm	[5.98 cm] CH1- CH2 PD4-PD1 169 cm	[5.98 cm] CH2 PD1-PD2 175 cm	[5 cm] CH2 PD2-PD3 181 cm	[5 cm] CH2 PD4-PD5 200 cm	TIME	Notes
49	5/13/98	AA	25	Y	1.6	15	26.44	-	-	3.48	1.68		P_{fuel}=19 in Hg, P_{tot} = 70.52 psig, -100 kPa vac.
50	5/13/98	AA	25	Y	1.6	-	-	-	-	-	-		-100 kPa vac.
51	5/13/98	AA	25	Y	1.6	-	-	-	-	-	-		-100 kPa vac.
52	5/13/98	AA	25	Y	1.6	-	-	-	-	-	-		P_{fuel}=19 in Hg, P_{tot} = 70.52 psig, -100 kPa vac.
53	5/13/98	AA	25	Y	1.6	-	-	-	-	-	-		-100 kPa vac. ~25 sec to fill FPD, Press. of tank = 53 psig
54	5/13/98	AA	25	Y	1.6	-	-	-	-	-	-		-100 kPa vac. ~40 sec to fill FPD, Press. of tank = 35 psig
55	5/13/98	AA	25	Y	1.6	-	-	-	-	-	-		-100 kPa vac. ~75 sec to fill FPD, Press. of tank = 17 psig
56	5/13/98	AA	125	Y	1.6	-	-	-	-	-	-		P_{fuel}=19 in Hg, P_{tot} = 70.52 psig, Bernzomatic propane
57	5/13/98	AA	25	Y	1.6	-	-	-	-	-	-		Bernzomatic propane
58	5/13/98	AA	125	Y	1.6	-	-	-	-	-	-		Bernzomatic propane
59	5/13/98	AA	25	Y	1.6	7.96	-	-	-	-	-		Bernzomatic propane
60	5/13/98	AA	50	Y	1.0	5.12	17.6	-	4.01	1.96	2.34		P_{fuel}=22 in Hg, P_{tot} = 81.85 psig,
61	5/13/98	AA	50	Y	1.0	13.61	17.94	-	6.56	4.1	4.04		Press. of tank= 63 psig
62	5/13/98	AA	50	Y	1	15.84	17.4	-	3.8	3.66	4.52		Press. of tank= 46 psig
63	5/13/98	AA	50	Y	1	13.98	18.9	-	5.2	3.55	4.58		Press. of tank= 28 psig, end press. of tank = 10 psig
64	5/13/98	AA	50	Y	1.2	7.36	18.16	-	5.6	4.56	5.68		P_{fuel}=21 in Hg, P_{tot} = 76.65 psig,
65	5/13/98	AA	50	Y	1.2	11.56	20.7	-	5.2	4.32	8.2		Press. of tank= 59 psig
66	5/13/98	AA	50	Y	1.2	7.76	14.4	-	4.39	3.32	6.02		Press. of tank= 41 psig
67	5/13/98	AA	50	Y	1.2	9.6	15	6.28	3.73	4.3	5.52		Press. of tank= 23.5 psig
68	5/13/98	AA	50	Y	1.4	9.68	17.6	8.66	5.32	2.72	7.3		P_{fuel}=20 in Hg, P_{tot} = 73.07 psig,
69	5/13/98	AA	50	Y	1.4	9.72	12.8	6.64	4.04	3.01	7.66		Press. of tank= 55 psig
70	5/13/98	AA	50	Y	1.4	10.56	13.88	8.36	6.42	4.58	5.8		Press. of tank= 37 psig
71	5/13/98	AA	50	Y	1.4	10.76	18.32	8.76	5.3	2.41	6.2		Press. of tank= 19 psig
72	5/13/98	AA	50	Y	1.6	-		-	-	-	-		P_{fuel}=19 in Hg, P_{tot} = 70.52 psig, long duration spark
73	5/13/98	AA	25	Y	1.6	-	-	-	-	-	-		Press. of tank= 52.5 psig
74	5/13/98	AA	50	Y	1.6	-	-	-	-	-	-		Press. of tank= 34.5 psig
75	5/13/98	AA	50	Y	1.6	12.64	-	-	-	-	-		Press. of tank= 17 psig
76	5/13/98	AA	50	N	2	-	-	-	-	-	-		P_{fuel}=16 in Hg, P_{tot} = 73.57 psig, slow faint flame

Time between signals (ms)

Test #	Date	PD Config.	Sample Rate (kHz)	Video Y/N	ϕ	[10 cm] CH1 PD1-PD2 83 cm	[10 cm] CH1 PD3-PD4 161 cm	[5.98 cm] CH1- CH2 PD4-PD1 169 cm	[5.98 cm] CH2 PD1-PD2 175 cm	[5 cm] CH2 PD2-PD3 181 cm	[5 cm] CH2 PD4-PD5 200 cm	TIME	Notes
77	5/13/98	AA	50	N	2	-	-	-	-	-	-		Press. of tank= 55.5 psig, faint, quenched before bend
78	5/13/98	AA	50	N	2	-	-	-	-	-	-		Press. of tank= 38 psig, faint, quenched before bend
79	5/13/98	AA	50	N	2	-	-	-	-	-	-		Press. of tank= 20 psig,
80	5/14/98	AA	50	N	0.8	-	-	-	-	-	-		P_{fuel}=23 in Hg, P_{tot} = 89.9 psig, quenched before bend
81	5/14/98	AA	50	Y	0.8	-	-	-	-	-	-		Press. of tank= 71.5 psig, multiple fire of spark
82	5/14/98	AA	50	N	0.8	-	-	-	-	-	-		Press. of tank= 54 psig
83	5/14/98	AA	50	Y	0.8	-	-	-	-	-	-		Press. of tank= 36 psig, quench after bend
84	5/14/98	AA	50	Y	0.8	-	-	-	-	-	-		Press. of tank= 18.5 psig, quench after bend
85	5/14/98	AA	50	N	0.6	-	-	-	-	-	-		P_{fuel}=25 in Hg, P_{tot} = 83.66 psig, quenched before midpoint
86	5/14/98	AA	50	N	0.6	-	-	-	-	-	-		Press. of tank= 66 psig, no ignition
87	5/14/98	AA	50	N	0.6	-	-	-	-	-	-		Press. of tank= 30 psig, no ignition, kernel around spark
88	5/14/98	AA	50	N	0.6	-	-	-	-	-	-		Press. of tank= 12 psig, no ignition, kernel around spark
89	5/14/98	AA	50	Y	1.8	-	-	-	-	-	-		P_{fuel}=15 in Hg, P_{tot} = 89.61 psig, multiple fire, slow start
90	5/14/98	AA	50	Y	1.8	-	-	-	-	-	-		Press. of tank= 71.5 psig, bluish flame
91	5/14/98	AA	50	Y	1.8	-	-	-	-	-	-		Press. of tank= 54 psig, bluish flame
92	5/14/98	AA	50	N	1.8	-	-	-	-	-	-		Press. of tank= 18.5 psig, slow start, rapid end
93	5/14/98	AA	50	N	1.8	-	-	-	-	-	-		
94	5/14/98	AA	25	N	1.6	16.52	58	16.8	16.24	16.7	2.14		P_{fuel}=16 in Hg, P_{tot} = 93.93 psig, wavers around midpoint
95	5/14/98	AA	25	N	1.6	23.6	49.2	16.4	8.2	7.64	-		
96	5/14/98	AA	25	N	1.6	17.9	49.2	16.3	9	7.97	7.44		
97	5/14/98	AA	25	N	1.6	22.1	-	14	10.12	7.2	2.44		
98	5/14/98	AA	25	N	1.6	10.44	32.8	9.48	7.44	5.92	2.46		
99	5/14/98	AA	25	N	0.8	9.5	-	-	-	-	-		P_{fuel}=23 in Hg, P_{tot} = 89.90 psig,
100	5/14/98	AA	25	N	0.8	25.4	-	-	-	-	-		
101	5/14/98	AA	25	N	0.8	-	-	-	-	-	-		
102	5/14/98	AA	25	N	0.8	25.3	-	-	-	-	-		
103	5/14/98	AA	25	N	0.8	-	-	-	-	-	-		
104	5/14/98	AA	25	N	0.9	5.88	39.9	8.3	7.56	2.28	-		P_{fuel}=22 in Hg, P_{tot} = 92.16 psig
105	5/14/98	AA	50	N	0.9	-	-	-	-	-	-		
106	5/14/98	AA	50	N	0.9	17.52	27.4	16	7.2	1.92	-		
107	5/14/98	AA	50	N	0.9	16.16	31.8	8.92	7.92	7.64	-		
108	5/14/98	AA	50	N	0.9	-	-	-	-	-	-		last run from this air bottle
109	5/14/98	AA	50	N	1.8	-	-	-	-	-	-		P_{fuel}=16 in Hg, P_{tot} = 82.62 psig

Time between signals (ms)

Test #	Date	PD Config.	Sample Rate (kHz)	Video Y/N	ϕ	[10 cm] CH1 PD1-PD2 83 cm	[10 cm] CH1 PD3-PD4 161 cm	[5.98 cm] CH1- CH2 PD4-PD1 169 cm	[5.98 cm] CH2 PD1-PD2 175 cm	[5 cm] CH2 PD2-PD3 181 cm	[5 cm] CH2 PD4-PD5 200 cm	TIME	Notes
110	6/2/98	AA	50	N	0.6	-	-	-	-	-	-		P_{fuel}=25 in Hg, P_{tot} = 83.66 psig, quench before midpoint
111	6/2/98	AA	50	N	0.6	-	-	-	-	-	-		no ignition
112	6/2/98	AA	50	N	0.6	-	-	-	-	-	-		no ignition
113	6/2/98	AA	50	N	0.6	-	-	-	-	-	-		no ignition
114	6/2/98	AA	50	N	0.6	-	-	-	-	-	-		no ignition, last shot from mixture
115	6/2/98	AA	50	N	0.65	-	-	-	-	-	-		P_{fuel}=25 in Hg, P_{tot} = 76.28 psig, -99 kPa vac, quenched
116	6/2/98	AA	50	N	0.65	-	-	-	-	-	-		-99 kpa, no ignition
117	6/2/98	AA	50	N	0.65	-	-	-	-	-	-		-99 kPa, no ignition, flame kernel around spark
118	6/2/98	AA	50	N	0.65	-	-	-	-	-	-		-99 kPa, no ignition, flame kernel around spark
119	6/2/98	AA	50	N	0.7	-	-	-	-	-	-		P_{fuel}=24 in Hg, P_{tot} = 87.16 psig, -99 kPa vac, waver +quench
120	6/2/98	AA	50	N	0.7	-	-	-	-	-	-		-99.5 kPa, no ignition, kernel around spark
121	6/2/98	AA	50	N	0.7	-	-	-	-	-	-		-99.5 kPa, multiple fire, flame prop. to end of straight sect
122	6/2/98	AA	50	Y	0.7	-	-	-	-	-	-		multiple fire, quenched in bend
123	6/2/98	AA	50	N	0.7	-	-	-	-	-	-		multiple fire, no ignition
124	6/2/98	AA	50	N	0.7	-	-	-	-	-	-		P_{fuel}=24 in Hg, P_{tot} = 87.16 psig, -98.5 kPa vac, waver &quench
125	6/2/98	AA	50	N	0.7	-	-	-	-	-	-		-98.5 kpa vac, no ignition
126	6/2/98	AA	50	N	0.7	-	-	-	-	-	-		-98.5 kpa vac, wavers near midpoint, then quenched
127	6/2/98	AA	50	Y	0.7	-	-	-	-	-	-		-98.5 kpa vac, no ignition
128	6/2/98	AA	50	Y	0.7	-	-	-	-	-	-		-98.5 kpa vac, no ignition
129	6/3/98	AA	50	Y	0.75	-	-	-	-	-	-		P_{fuel}=23.5 in Hg, P_{tot} = 88.6 psig, -98.5 kPa vac, quench @ bend
130	6/3/98	AA	50	N	0.75	-	-	-	-	-	-		-98.5 kpa vac, multi-fire, slow, hesitant to propagate
131	6/3/98	AA	50	N	0.75	-	-	-	-	-	-		-98.5 kpa vac, no ignition
132	6/3/98	AA	50	N	0.75	-	-	-	-	-	-		-98.5 kpa vac, multi-fire, slow, hesitant to propagate
133	6/3/98	AA	50	N	0.75	-	-	-	-	-	-		-98.5 kpa vac, no ignition
134	6/3/98	AA	50	N	0.75	-	-	-	-	-	-		P_{fuel}=23.5 in Hg, P_{tot} = 88.6 psig, waver then quench @ midpt.
135	6/3/98	AA	50	N	0.75	-	-	-	-	-	-	10:19 AM	-99 kPa vac, no ignition
136	6/3/98	AA	50	N	0.75	-	-	-	-	-	-	10:26 AM	-99 kPa vac, no ignition, flame femel near spark
137	6/3/98	AA	50	N	0.75	-	-	-	-	-	-	10:34 AM	-99 kPa vac, no ignition
138	6/3/98	AA	50	N	0.75	-	-	-	-	-	-	10:55 AM	-99 kPa vac, no ignition
139	6/3/98	AA	50	Y	0.8	-	-	-	-	-	-	11:15 AM	P_{fuel}=23 in Hg, P_{tot} = 89.9 psig, quenched in bend
140	6/3/98	AA	50	N	0.8	-	-	-	-	-	-	11:19 AM	-99 kPa vac, quenched after bend
141	6/3/98	AA	50	Y	0.8	-	-	-	-	-	-	11:26 AM	-99 kPa vac, quenched in latter half of bend
142	6/3/98	AA	50	Y	0.8	-	-	-	-	-	-	11:30 AM	-99 kPa vac, quenched in latter half of bend

Time between signals (ms)

Test #	Date	PD Config.	Sample Rate (kHz)	Video Y/N	ϕ	[10 cm] CH1 PD1-PD2 83 cm	[10 cm] CH1 PD3-PD4 161 cm	[5.98 cm] CH1- CH2 PD4-PD1 169 cm	[5.98 cm] CH2 PD1-PD2 175 cm	[5 cm] CH2 PD2-PD3 181 cm	[5 cm] CH2 PD4-PD5 200 cm	TIME	Notes
143	6/3/98	AA	50	Y	0.8	-	-	-	-	-	-	11:35 AM	-99 kPa vac, quenched in latter half of bend
144	6/3/98	AA	50	Y	0.8	-	-	-	-	-	-	12:38 PM	P_{fuel}=23 in Hg, P_{tot} = 89.9 psig, - 99 kPa vac., quench in bend
145	6/3/98	AA	50	Y	0.8	-	-	-	-	-	-	12:42 PM	-99 kPa vac, quenched in latter half of bend
146	6/3/98	AA	50	N	0.8	-	-	-	-	-	-	12:58 PM	use light to improve PD threshhold resolution
147	6/3/98	AA	50	N	0.8	-	-	-	-	-	-	1:08 PM	ignition
148	6/3/98	AA	50	N	0.8	-	-	-	-	-	-	1:14 PM	ignition
149	6/3/98	AA	50	N	0.85	-	-	-	-	-	-	1:34 PM	P_{fuel}=22.5 in Hg, P_{tot} = 91.1psig, - 99 kPa vac., signals inconcl.
150	6/3/98	AA	25	N	0.85	24.8	33.8	-	-	-	-	1:43 PM	-99 kPa vac, other signals inconclusive
151	6/3/98	AA	25	N	0.85	-	35.4	-	-	-	-	1:56 PM	-99 kPa vac, other signals inconclusive
152	6/3/98	AA	25	N	0.85	-	65.2	49.3	-	-	-	2:01 PM	-99 kPa vac, other signals inconclusive
153	6/3/98	AA	25	N	0.85	-	51.4	-	-	-	-	2:11 PM	-99 kPa vac, other signals inconclusive
154	6/3/98	AA	25	N	0.85	-	34.6	-	-	-	-	2:46 PM	P_{fuel}=22.5 in Hg, P_{tot} = 91.1psig, - 99 kPa vac.,
155	6/3/98	AA	25	N	0.85	-	-	-	-	-	-	2:53 PM	multi-fire, ignition, no PD data
156	6/3/98	AA	25	N	0.85	-	-	-	-	-	-	2:56 PM	-99 kPa vac, multi-fire
157	6/3/98	AA	50	Y	0.85	-	-	-	-	-	-	3:04 PM	-99 kPa vac,
158	6/3/98	AA	50	Y	0.85	-	-	-	-	-	-	3:31 PM	P_{fuel}=22.5 in Hg, P_{tot} = 91.1psig, - 99 kPa vac.,
159	6/3/98	AA	50	Y	0.85	-	-	-	-	-	-	3:34 PM	-99 kPa vac,
160	6/3/98	AA	50	Y	0.85	-	-	-	-	-	-	3:37 PM	-99 kPa vac,
161	6/3/98	AA	50	Y	0.85	-	-	-	-	-	-	3:44 PM	-99 kPa vac,
162	6/3/98	AA	50	Y	0.85	-	-	-	-	-	-	3:50 PM	-99 kPa vac, multi-fire
163	6/3/98	AA	50	Y	0.9	-	-	-	-	-	-	4:22 PM	P_{fuel}=22 in Hg, P_{tot} = 92.15 psig, - 99 kPa vac.,
164	6/3/98	AA	50	Y	0.9	-	-	-	-	-	-	4:29 PM	-99 kPa vac,
165	6/3/98	AA	50	Y	0.9	-	-	-	-	-	-	4:34 PM	-99 kPa vac,
166	6/3/98	AA	50	Y	0.9	-	-	-	-	-	-	4:39 PM	-99 kPa vac, probably need backlighting to obtain signals
167	6/3/98	AA	50	Y	0.9	-	-	-	-	-	-	4:43 PM	-99 kPa vac,
168	6/4/98	AA	50	N	0.9	16.32	-	-	-	-	-	8:43 AM	P_{fuel}=22 in Hg, P_{tot} = 92.15 psig, - 99 kPa vac.,
169	6/4/98	AA	50	N	0.9	-	-	-	-	-	-	8:49 AM	-99 kPa vac, inconclusive signal on Ch1, PD1
170	6/4/98	AA	50	N	0.9	24.7	-	-	-	-	-	10:10 AM	P_{fuel}=23 in Hg, P_{tot} = 78.6 psig, - 99 kPa vac., other data inclus.
171	6/4/98	AA	50	N	0.9	-	41.3	-	-	-	-	10:24 AM	-99 kPa vac,
172	6/4/98	AA	25	N	0.9	25.7	-	-	-	-	-	10:30 AM	-99 kPa vac, other data inclusive
173	6/4/98	AA	25	N	0.9	15.4	98.8	-	-	-	-	10:36 AM	-99 kPa vac, other data inclusive
174	6/4/98	AA	25	Y	0.95	19.9	-	-	-	-	-	11:02 AM	P_{fuel}=21.5 in Hg, P_{tot} = 93.13 psig, - 99 kPa vac.,

Time between signals (ms)

Test #	Date	PD Config.	Sample Rate (kHz)	Video Y/N	ϕ	[10 cm] CH1 PD1-PD2 83 cm	[10 cm] CH1 PD3-PD4 161 cm	[5.98 cm] CH1- CH2 PD4-PD1 169 cm	[5.98 cm] CH2 PD1-PD2 175 cm	[5 cm] CH2 PD2-PD3 181 cm	[5 cm] CH2 PD4-PD5 200 cm	TIME	Notes
175	6/4/98	AA	50	Y	0.95	-	-	-	-	-	-	11:08 AM	-99 kPa vac,
176	6/4/98	AA	25	Y	0.95	-	-	-	-	-	-	11:13 AM	-99 kPa vac,
177	6/4/98	AA	25	Y	0.95	-	-	-	-	-	-	11:18 AM	-99 kPa vac,
178	6/4/98	AA	25	N	0.95	21.1	64.6	18.4	-	-	16.6	11:23 AM	-99 kPa vac, other data inclusive
179	6/4/98	AA	25	N	0.95	6.96	24.5	10.3	3.9	1.92	3.5	4:00 PM	P_{fuel}=21.5in Hg, P_{tot} = 93.13 psig, Rec'd Opticon CCD camera
180	6/4/98	AA	25	N	0.95	9	-	11.5	8.04	-	1.36	4:11 PM	-99 kPa vac,
181	6/4/98	AA	25	N	0.95	27.6	41.2	13.7	8.44	-	-	4:21 PM	-99 kPa vac,
182	6/4/98	AA	25	N	0.95	15.56	18.9	-	-	-	-	4:48 PM	P_{fuel}=24 in Hg, P_{tot} = 61.12 psig, -99 kPa vac.
183	6/4/98	AA	25	N	0.95	11.8	25.2	-	-	-	-	4:56 PM	-99 kPa vac, other data inclusive
184	6/4/98	AA	25	N	0.95	-	-	-	-	-	-		-99 kPa vac, other data inclusive
185	6/8/98	AA	50	Y	1	-	-	-	-	-	-	10:00 AM	P_{fuel}=21.5 in Hg, P_{tot} = 87.95 psig, -100 kPa vac.
186	6/8/98	AA	50	Y	1	-	-	-	-	-	-		-100 kPa vac, 500 frames per second
187	6/8/98	AA	50	N	1	8.36	-	-	-	-	-	10:46 AM	-100 kPa vac, 300 frames per second
188	6/8/98	AA	50	N	1	-	-	-	-	-	-	10:50 AM	-100 kPa vac, 300 frames per second, poor vid. quality
189	6/8/98	AA	50	N	1	-	-	-	-	-	-	11:04 AM	-100 kPa vac, 400 frames per second
190	6/8/98	AA	50	Y	1.1	9.96	13.12	6.28	3.04	2.67	5.16	11:32 AM	P_{fuel}=20.5 in Hg, P_{tot} = 90.12 psig, -100 kPa vac., 400 fps
191	6/8/98	AA	50	Y	1.1	14.2	14.04	6.1	2.75	3.1	5.3	11:56 AM	-100 kPa vac, 400 fps, this frame speed is best.
192	6/8/98	AA	50	Y	1.1	8.2	15.6	6.86	3.88	3.3	5.74	12:27 PM	-100 kPa vac, 400 fps, shutter speed is 1x fps
193	6/8/98	AA	50	Y	1.1	15.44	15.2	7	2.55	2.6	4.4	12:46 PM	-100 kPa vac, 500 fps
194	6/8/98	AA	50	N	1.1	19.8	17.7	6.98	3.22	2.9	4.56	1:02 PM	-100 kPa vac, 400 fps
195	6/8/98	AA	50	Y	1.2	5.8	13.76	5.88	3.62	4.11	4.55	2:38 PM	P_{fuel}=20. in Hg, P_{tot} = 86.89 psig, -100 kPa vac.
196	6/8/98	AA	50	N	1.2	12.6	12.2	5.68	3.9	2.88	5.24	3:00 PM	-100 kPa vac, 60 fps, too slow, "comet tail" images
197	6/8/98	AA	125	Y	1.2	11.84	-	-	-	-	-	3:12 PM	-100 kPa vac, O-scope sampling rate is too fast
198	6/8/98	AA	50	Y	1.2	12.28	16.08	8	2.71	2.46	5.88	3:33 PM	-100 kPa vac,
199	6/8/98	AA	50	N	1.2	9.76	15.36	6.32	3.14	2.87	5.96	3:54 PM	-100 kPa vac,
200	6/8/98	AA	50	Y	1.3	7.74	15.88	7.62	5.38	3.53	5.16	4:22 PM	P_{fuel}=19 in Hg, P_{tot} = 88.94 psig, -100 kPa vac.
201	6/8/98	AA	50	Y	1.3	12.68	21.5	6.68	4.3	1.6	6.12	4:46 PM	-100 kPa vac,
202	6/8/98	AA	50	Y	1.3	10.32	13.76	5.92	3.93	3.06	6.04	5:02 PM	-100 kPa vac,
203	6/8/98	AA	50	Y	1.3	12.64	25	10.64	1.99	3.87	7.9	5:22 PM	-100 kPa vac, similar to previous test
204	6/8/98	AA	50	N	1.3	6.02	13.88	5.7	3.44	2.56	5.56	5:46 PM	-100 kPa vac, similar to previous test
205	6/9/98	AA	50	Y	1.4	14.24	19.8	8.74	3.36	2.68	3.86	2:49 PM	P_{fuel}=18 in Hg, P_{tot} = 90.77 psig, -100 kPa vac., 400 fps
206	6/9/98	AA	50	Y	1.4	12.7	14.48	9.52	3.7	2.2	-	3:19 PM	-100 kPa vac,
207	6/9/98	AA	50	Y	1.4	11.76	11.64	10.64	4.48	2.04	-	3:37 PM	-100 kPa vac,

Time between signals (ms)

Test #	Date	PD Config.	Sample Rate (kHz)	Video Y/N	ϕ	[10 cm] CH1 PD1-PD2 83 cm	[10 cm] CH1 PD3-PD4 161 cm	[5.98 cm] CH1- CH2 PD4-PD1 169 cm	[5.98 cm] CH2 PD1-PD2 175 cm	[5 cm] CH2 PD2-PD3 181 cm	[5 cm] CH2 PD4-PD5 200 cm	TIME	Notes
208	6/9/98	AA	50	Y	1.4	8.18	15.04	13.31	2.43	4	-	3:55 PM	-100 kPa vac,
209	6/9/98	AA	50	Y	1.4	9.4	13.56	5.84	3.47	3.09	5.54	4:11 PM	-100 kPa vac,
210	6/9/98	AA	50	Y	1.5	-	-	-	-	-	-	4:40 PM	P_{fuel}=17 in Hg, P_{tot} = 92.42 psig, -100 kPa vac.,
211	6/9/98	AA	50	Y	1.5	10.48	-	-	0.94	1.62	-	4:53 PM	-100 kPa vac,
212	6/9/98	AA	50	Y	1.5	11.52	-	-	-	-	-	5:07 PM	-100 kPa vac,
213	6/9/98	AA	50	Y	1.5	14.68	14.56	7.8	4.2	1.56	-	5:22 PM	-100 kPa vac,
214	6/9/98	AA	50	Y	1.5	15.16	14.88	9.32	3.97	2.31	-	5:36 PM	-100 kPa vac,
215	6/9/98	AA	50	Y	1.6	-	-	-	-	-	-	5:57 PM	P_{fuel}=16 in Hg, P_{tot} = 90.03 psig, -100 kPa vac.,
216	6/9/98	AA	50	N	1.6	-	18.68	9.33	-	1.11	-	6:12 PM	-100 kPa vac,
217	6/9/98	AA	50	Y	1.6	-	-	-	-	-	-	6:21 PM	-100 kPa vac, need backlighting
218	6/9/98	AA	50	Y	1.6	-	-	-	-	-	-	6:33 PM	-100 kPa vac,
219	6/9/98	AA	50	Y	1.6	-	-	-	-	-	-	6:46 PM	-100 kPa vac, flame appeared faster than previous tests.?
220	6/10/98	AA	50	Y	1.7	-	-	-	-	-	-	9:26 AM	P_{fuel}=15.5 in Hg, P_{tot} = 91.63 psig, -100 kPa vac., 2 tries spark
221	6/10/98	AA	50	Y	1.7	-	-	-	-	-	-	10:03 AM	-100 kPa vac, record every third frame
222	6/10/98	AA	50	Y	1.7	-	-	-	-	-	-	10:30 AM	-100 kPa vac,
223	6/10/98	AA	50	Y	1.7	-	-	-	-	-	-	10:49 AM	-100 kPa vac,
224	6/10/98	AA	50	Y	1.7	-	-	-	-	-	-	11:13 AM	-100 kPa vac,
225	6/10/98	AA	50	Y	1.8	-	-	-	-	-	-	1:52 PM	P_{fuel}=15 in Hg, P_{tot} = 89.61psig, -100 kPa vac.,
226	6/10/98	AA	50	Y	1.8	-	-	-	-	-	-	2:10 PM	-100 kPa vac,
227	6/10/98	AA	50	Y	1.8	-	-	-	-	-	-	2:34 PM	-100 kPa vac, "snap" sound at end of propagation,
228	6/10/98	AA	50	Y	1.8	-	-	-	-	-	-	2:52 PM	-100 kPa vac,
229	6/10/98	AA	50	Y	1.8	-	-	-	-	-	-	3:20 PM	-100 kPa vac, go to 300 fps
230	6/10/98	AA	50	N	1.9	-	-	-	-	-	-	5:10 PM	P_{fuel}=14in Hg, P_{tot} = 91.15psig, -100 kPa vac., quench @ bend
231	6/10/98	AA	50	N	1.9	-	-	-	-	-	-	5:16 PM	-100 kPa vac, quench before bend, fired on 1st try.
232	6/10/98	AA	50	N	1.9	-	-	-	-	-	-	5:20 PM	-100 kPa vac, quench 10 -20 cm before bend,
233	6/10/98	AA	50	N	1.9	-	-	-	-	-	-	5:25 PM	-100 kPa vac, loud "pop" sound, propagate all the way
234	6/10/98	AA	50	Y	1.9	-	-	-	-	-	-	5:33 PM	-100 kPa vac, loud "pop" , slow propagation
235	6/10/98	AA	50	N	2	-	-	-	-	-	-	6:19 PM	P_{fuel}=13.5 in Hg, P_{tot} =89.42psig, -100 kPa vac., kernel nr sprk
236	6/10/98	AA	50	N	2	-	-	-	-	-	-	6:24 PM	-100 kPa vac, quench before bend.
237	6/10/98	AA	50	N	2	-	-	-	-	-	-	6:28 PM	-100 kPa vac, quench before bend, CCD cam conking out
238	6/10/98	AA	50	N	2	-	-	-	-	-	-	6:33 PM	-100 kPa vac, quench before bend.
239	6/10/98	AA	50	N	2	-	-	-	-	-	-	6:39 PM	-100 kPa vac, quench before bend. $T_{ambient}$ = 29 °C
240	6/11/98	AA	50	Y	0.9	11.56	-	-	-	-	-	8:52 AM	P_{fuel}=22 in Hg, P_{tot} =92.15psig, -100 kPa vac., 400 fps

Time between signals (ms)

Test #	Date	PD Config.	Sample Rate (kHz)	Video Y/N	ϕ	[10 cm] CH1 PD1-PD2 83 cm	[10 cm] CH1 PD3-PD4 161 cm	[5.98 cm] CH1- CH2 PD4-PD1 169 cm	[5.98 cm] CH2 PD1-PD2 175 cm	[5 cm] CH2 PD2-PD3 181 cm	[5 cm] CH2 PD4-PD5 200 cm	TIME	Notes
241	6/11/98	AA	50	Y	0.9	-	-	-	-	-	-	9:07 AM	-100 kPa vac, 400 fps
242	6/11/98	AA	50	Y	0.9	-	-	-	-	-	-	9:22 AM	-100 kPa vac, 400 fps
243	6/11/98	AA	50	Y	0.9	-	-	-	-	-	-	9:37 AM	-100 kPa vac, 400 fps, long duration afterflash
244	6/11/98	AA	50	Y	0.9	-	-	-	-	-	-	9:55 AM	-100 kPa vac, 400 fps
245	6/11/98	AA	50	Y	0.8	-	-	-	-	-	-	10:31 AM	P_{fuel}=23 in Hg, P_{tot} =89.9 psig, -100 kPa vac., 300 fps, faint
246	6/11/98	AA	50	Y	0.8	-	-	-	-	-	-	10:50 AM	-100 kPa vac, 250 fps, record every 1 or 2 frames
247	6/11/98	AA	50	Y	0.8	-	-	-	-	-	-	11:12 AM	-100 kPa vac, 250 fps, record every 1 or 2 frames
248	6/11/98	AA	50	Y	0.8	-	-	-	-	-	-	11:36 AM	-100 kPa vac, 180 fps, record every 1 or 2 frames
249	6/11/98	AA	50	Y	0.8	-	-	-	-	-	-	12:01 PM	-100 kPa vac, 180 fps, record every 1 or 2 frames
250	6/11/98	AA	50	Y	1.85	-	-	-	-	-	-	12:49 PM	P_{fuel}=16 in Hg, P_{tot} =80.2 psig, -100 kPa vac., new air bottle
251	6/11/98	AA	50	Y	1.85	-	-	-	-	-	-	1:04 PM	-100 kPa vac, 400 fps, images too dark
252	6/11/98	AA	50	N	1.85	-	-	-	-	-	-	1:18 PM	-100 kPa vac, 300 fps, quench before bend.
253	6/11/98	AA	50	Y	1.85	-	-	-	-	-	-	1:27 PM	-100 kPa vac, 300 fps,
254	6/13/98	AA	50	N	1.1	8.24	16.92	5.8	3.19	7.28	8.16	11:17 AM	P_{fuel}=20.5 in Hg, P_{tot} =90.1 psig, -99 kPa vac.,
255	6/13/98	AA	50	N	1.1	14.12	15	7.12	3.3	3.12	5.74	11:26 AM	-99 kPa vac, good o-scope profile
256	6/13/98	AA	50	N	1.1	6.72	13.24	5.84	5.12	4.6	8.02	11:33 AM	-99 kPa vac, good o-scope profile
257	6/13/98	AA	50	N	1.1	11.72	16	6.84	3.12	3.43	5.48	11:41 AM	-99 kPa vac, good o-scope profile
258	6/13/98	AA	50	N	1.1	15	14.08	6.06	5.46	4.08	4.17	11:50 AM	-99 kPa vac, good o-scope profile
259	6/13/98	AA	50	N	1.1	6.24	15.84	7.04	5.34	4.53	4.72	12:11 PM	P_{fuel}=20.5 in Hg, P_{tot} =90.1 psig, -99 kPa vac., good profile
260	6/13/98	AA	50	N	1.1	12.4	15.72	7.48	2.56	2.69	5.54	12:18 PM	-99 kPa vac, good o-scope profile
261	6/13/98	AA	50	N	1.1	10.68	19.32	10.48	2.45	2.66	4.7	12:25 PM	-99 kPa vac, good o-scope profile
262	6/13/98	AA	50	N	1.1	11.4	14.28	8.16	3.2	4.86	7.02	12:35 PM	-99 kPa vac, good o-scope profile
263	6/13/98	AA	50	N	1.1	11.4	18.52	8.44	2.73	3.9	3.81	12:42 PM	-99 kPa vac, good o-scope profile
264	6/13/98	AA	50	N	1.3	10.6	22	7.94	4.76	4.52	6.64	1:07 PM	P_{fuel}=19 in Hg, P_{tot} =88.94 psig, -99 kPa vac., good profile
265	6/13/98	AA	50	N	1.3	13.16	15.2	5.52	3.64	3.6	5.86	1:15 PM	-99 kPa vac, good o-scope profile
266	6/13/98	AA	50	N	1.3	8.74	25.8	11.2	5.24	4.22	9.88	1:23 PM	-99 kPa vac, good o-scope profile
267	6/13/98	AA	50	N	1.3	11.32	12.72	4.48	4.27	3.36	5.82	1:30 PM	-99 kPa vac, good o-scope profile
268	6/13/98	AA	50	N	1.3	11.8	15	5.38	4.36	3.9	4.38	1:41 PM	-99 kPa vac, good o-scope profile
269	6/13/98	AA	50	N	1.3	7.78	16.52	7.66	5.18	3.1	4.48	2:03 PM	P_{fuel}=19 in Hg, P_{tot} =88.94 psig, -99 kPa vac., good profile
270	6/13/98	AA	50	N	1.3	6.5	13.52	5.18	4.84	3.43	6.32	2:10 PM	-99 kPa vac, good o-scope profile
271	6/13/98	AA	50	N	1.3	11.16	13.52	6.13	3.63	3.84	5.38	2:18 PM	-99 kPa vac, good o-scope profile
272	6/13/98	AA	50	N	1.3	12.36	27.8	11.48	5.44	3.71	7.22	2:26 PM	-99 kPa vac, good o-scope profile
273	6/13/98	AA	50	N	1.3	13.68	12.44	5.36	4.55	3.66	5.4	2:34 PM	-99 kPa vac,

Time between signals (ms)

Test #	Date	PD Config.	Sample Rate (kHz)	Video Y/N	φ	[10 cm] CH1 PD1-PD2 83 cm	[10 cm] CH1 PD3-PD4 161 cm	[5.98 cm] CH1- CH2 PD4-PD1 169 cm	[5.98 cm] CH2 PD1-PD2 175 cm	[5 cm] CH2 PD2-PD3 181 cm	[5 cm] CH2 PD4-PD5 200 cm	TIME	Notes
274	6/14/98	AA	50	N	1.2	7.74	20.2	5.8	6.66	4.57	8.1	12:10 PM	P_{fuel}=20 in Hg, P_{tot} =86.89 psig, -99 kPa vac., good profile
275	6/14/98	AA	50	N	1.2	10.4	17.52	6.6	4.43	5.28	6.48	12:18 PM	-99 kPa vac, good o-scope profile
276	6/14/98	AA	50	N	1.2	12.64	16.28	4.28	5.05	3.7	8	12:25 PM	-99 kPa vac, good o-scope profile
277	6/14/98	AA	50	N	1.2	8.1	15.32	4.7	3.81	4.11	8.1	12:32 PM	-99 kPa vac, good o-scope profile
278	6/14/98	AA	50	N	1.2	10.12	16.72	6.1	4.6	4.14	5.94	12:42 PM	-99 kPa vac, good o-scope profile
279	6/14/98	AA	50	N	1.4	10.56	18.56	8.1	4.01	4.36	4.9	1:05 PM	P_{fuel}=18 in Hg, P_{tot} =90.77 psig, -99 kPa vac., good profile
280	6/14/98	AA	50	N	1.4	5.9	28.8	11.24	1.72	5.62	11.5	1:12 PM	-99 kPa vac, some "weak" signals
281	6/14/98	AA	50	N	1.4	12.36	19.84	9.08	1.65	3.98	7.76	1:20 PM	-99 kPa vac, CH2 PD4 - PD5 anomaly
282	6/14/98	AA	50	N	1.4	12.32	19.52	13.64	2.26	4.58	11.52	1:30 PM	-99 kPa vac, CH2 PD4 - PD5 anomaly
283	6/14/98	AA	50	N	1.4	11.16	23.9	8.54	5.1	4.6	6.98	1:40 PM	-99 kPa vac, good o-scope profile
284	6/15/98	AA	50	N	1	11.44	24.6	11.6	5.68	6.1	6.76	11:28 AM	P_{fuel}=21.5 in Hg, P_{tot} =87.95 psig, -99 kPa vac.,
285	6/15/98	AA	50	N	1	-	-	-	-	-	-	11:42 AM	-99 kPa vac, wrong settings on O-scope
286	6/15/98	AA	50	Y (O-SCOPE)	1	10.8	20.9	9.08	7.52	6	3.5	11:46 AM	-99 kPa vac, good o-scope profile
287	6/15/98	AA	50	Y (O-SCOPE)	1	10.96	30.8	9.48	6.48	2.2	4.39	11:59 AM	-99 kPa vac, good o-scope profile
288	6/15/98	AA	50	Y (O-SCOPE)	1	19.8	32.4	8.92	8.46	6.74	1.44	12:09 PM	-99 kPa vac, good o-scope profile
289	6/15/98	AA	50	N	1	13.76	22.3	6.16	4.98	18.52	7.24	12:37 PM	P_{fuel}=21.5 in Hg, P_{tot} =87.95 psig, -99 kPa vac., good profile
290	6/15/98	AA	50	Y (O-SCOPE)	1	21.6	26	10.32	7.42	5.66	6.74	12:46 PM	-99 kPa vac, fair to good o-scope profile
291	6/15/98	AA	50	Y (O-SCOPE)	1	9.34	23	8.46	5.56	5.18	7.6	12:56 PM	-99 kPa vac, good o-scope profile
292	6/15/98	AA	50	Y (O-SCOPE)	1	10.2	21.9	8.16	7.18	5.02	6.1	1:15 PM	-99 kPa vac, good o-scope profile
293	6/15/98	AA	50	N	1	13.92	32.4	8.24	8.2	6.88	8.14	1:26 PM	-99 kPa vac, good o-scope profile
294	6/15/98	AA	50	N	0.9	17.36	41.3	-	0.9	2.8	-	3:40 PM	P_{fuel}=22 in Hg, P_{tot} =92.15 psig, -99 kPa vac., fair profile
295	6/15/98	AA	50	N	0.9	25.5	-	-	-	-	-	3:51 PM	-99 kPa vac, mediocre profile
296	6/15/98	AA	50	N	0.9	17.2	33.7	16.4	16.16	-	-	3:56 PM	-99 kPa vac, fair to mediocre profile
297	6/15/98	AA	25	N	0.9	24.5	-	-	-	-	-	4:03 PM	-99 kPa vac, mediocre profile
298	6/15/98	AA	25	N	0.9	28.9	-	-	-	-	-	4:12 PM	-99 kPa vac,
299	6/15/98	AA	25	N	0.9	17.32	-	9.4	8.32	6.84	16.76	4:34 PM	P_{fuel}=22 in Hg, P_{tot} =92.15 psig, -99 kPa vac.,
300	6/15/98	AA	25	N	0.9	18.16	66.4	16.76	17	-	-	4:42 PM	-99 kPa vac,
301	6/15/98	AA	25	N	0.9	-	-	-	-	-	-	4:51 PM	-99 kPa vac,
302	6/15/98	AA	25	N	0.9	-	-	-	-	-	-	4:55 PM	-99 kPa vac,
303	6/16/98	AA	50	N	1.5	12.12	21.5	-	-	-	-	9:06 AM	P_{fuel}=17 in Hg, P_{tot} =92.42 psig, -99 kPa vac.,
304	6/16/98	AA	25	Y (O-SCOPE)	1.5	8.98	16.92	7.32	3.04	5.1	7.5	9:11 AM	-99 kPa vac, good o-scope profile
305	6/16/98	AA	25	Y (O-SCOPE)	1.5	4.26	18.12	6.64	3.9	4.66	5.7	9:20 AM	-99 kPa vac, good o-scope profile

Time between signals (ms)

Test #	Date	PD Config.	Sample Rate (kHz)	Video Y/N	ϕ	[10 cm] CH1 PD1-PD2 83 cm	[10 cm] CH1 PD3-PD4 161 cm	[5.98 cm] CH1- CH2 PD4-PD1 169 cm	[5.98 cm] CH2 PD1-PD2 175 cm	[5 cm] CH2 PD2-PD3 181 cm	[5 cm] CH2 PD4-PD5 200 cm	TIME	Notes
306	6/16/98	AA	50	Y (O-SCOPE)	1.5	12.84	18.2	6.84	3.95	3.24	5.88	9:30 AM	-99 kPa vac, good o-scope profile
307	6/16/98	AA	50	Y (O-SCOPE)	1.5	13.44	13.04	6.3	4.21	4.27	4.12	9:38 AM	-99 kPa vac, good o-scope profile
308	6/16/98	AA	50	N	1.5	12.92	23.5	8.5	5.76	4.34	7.84	10:03 AM	P_{fuel}=17 in Hg, P_{tot} =92.42 psig, -99 kPa vac., good profile
309	6/16/98	AA	50	Y (O-SCOPE)	1.5	9.88	19.8	8.42	5.3	4.34	6.3	10:10 AM	-99 kPa vac, good o-scope profile
310	6/16/98	AA	50	N	1.5	11.64	23.3	6.86	10.4	5.26	3.8	10:18 AM	-99 kPa vac, fair to good o-scope profile
311	6/16/98	AA	50	Y (O-SCOPE)	1.5	5.88	14.44	7.16	5.68	5.02	7.9	10:26 AM	-99 kPa vac, good o-scope profile
312	6/16/98	AA	50	N	1.5	14	16.68	7.56	3.11	4.48	6.46	10:36 AM	-99 kPa vac, good o-scope profile
313	6/16/98	AA	50	N	1.5	11.64	-	-	-	-	-	11:08 AM	P_{fuel}=18 in Hg, P_{tot} =84.13 psig, -99 kPa vac.,
314	6/16/98	AA	25	Y (O-SCOPE)	1.5	15.2	18.24	8.62	4.9	3.36	8.8	11:13 AM	-99 kPa vac, good o-scope profile
315	6/16/98	AA	25	Y (O-SCOPE)	1.5	14.52	20.6	8.54	6.18	9.16	6.86	11:20 AM	-99 kPa vac, good o-scope profile, backlighting not need.
316	6/16/98	AA	25	Y (O-SCOPE)	1.5	15.08	29.6	4.18	6.26	2.08	4.66	11:29 AM	-99 kPa vac, good o-scope profile, backlighting not need.
317	6/16/98	AA	25	Y (O-SCOPE)	1.6	14.96	34.8	10.28	7	6.08	6.84	12:15 PM	P_{fuel}=16.5 in Hg, P_{tot} =90.03 psig, -99 kPa vac., gd profile.
318	6/16/98	AA	25	N	1.6	10.28	17.36	6.5	4.52	4.64	8.76	12:26 PM	-99 kPa vac, good o-scope profile, backlighting
319	6/16/98	AA	25	Y (O-SCOPE)	1.6	11.36	20.7	10.56	1.62	5.32	11.24	12:34 PM	-99 kPa vac, fair to good o-scope profile,
320	6/16/98	AA	25	N	1.6	10.64	31.8	6.22	5.76	4.82	13.2	12:42 PM	-99 kPa vac, good o-scope profile,
321	6/16/98	AA	25	Y (O-SCOPE)	1.6	10.84	39.6	6.12	4.6	6.28	7.58	12:51 PM	-99 kPa vac, fair o-scope profile,
322	6/16/98	AA	25	N	1.6	14.68	33.6	13.6	3.38	5.98	11.68	1:23 PM	P_{fuel}=16.5 in Hg, P_{tot} =90.03 psig, -99 kPa vac., gd profile.
323	6/16/98	AA	25	Y (O-SCOPE)	1.6	10.12	15.12	9.4	5.7	5.48	7.74	1:30 PM	-99 kPa vac, good o-scope profile,
324	6/16/98	AA	25	N	1.6	11.68	33.3	10.4	5.76	1.96	13.56	1:38 PM	-99 kPa vac, good o-scope profile, loud "whack" sound
325	6/16/98	AA	25	N	1.6	11.84	33.3	11.52	5.48	6.18	14.6	1:47 PM	-99 kPa vac, good o-scope profile, loud "whack" sound
326	6/16/98	AA	25	Y (O-SCOPE)	1.6	14.56	22.3	6.8	4.44	5.12	6.84	1:55 PM	-99 kPa vac, good o-scope profile, loud "whack" sound
327	6/16/98	AA	25	N	1.7	17.4	-	11.68	15.52	8.02	14.64	2:24 PM	P_{fuel}=16 in Hg, P_{tot} =87.94 psig, -99 kPa vac., fair profile.
328	6/16/98	AA	25	Y (O-SCOPE)	1.7	19	-	11.74	11	5.14	9.2	2:31 PM	-99 kPa vac, fair o-scope profile,
329	6/16/98	AA	25	Y (O-SCOPE)	1.7	18.68	42.3	14.24	8.42	5.22	7.5	2:40 PM	-99 kPa vac, good o-scope profile, room lights on
330	6/16/98	AA	25	N	1.7	15.96	41	8.48	7.78	5.6	10.12	2:49 PM	-99 kPa vac, good o-scope profile, room lights on
331	6/16/98	AA	25	Y (O-SCOPE)	1.7	11.2	20.4	9.42	4.2	5.48	7.44	2:58 PM	-99 kPa vac, good o-scope profile, room lights on
332	6/16/98	AA	25	N	1.7	20	58.8	8.36	16.48	7.08	-	5:08 PM	P_{fuel}=16 in Hg, P_{tot} =87.94 psig, -99 kPa vac., fair profile.
333	6/16/98	AA	25	N	1.7	26.8	50.2	7.96	16.32	7.24	17.4	5:16 PM	-99 kPa vac, fair o-scope profile,
334	6/16/98	AA	25	N	1.7	17.04	40.5	7.78	17.36	-	24.8	5:28 PM	-99 kPa vac, CH 2, PD2-PD3 inconclusive
335	6/16/98	AA	25	N	1.7	-	-	-	-	-	-	5:36 PM	-99 kPa vac, too much backlighting,
336	6/16/98	AA	25	N	1.7	15.2	18.2	15.96	15.16	-	-	5:41 PM	-99 kPa vac, fair o-scope profile,

Time between signals (ms)

Test #	Date	PD Config.	Sample Rate (kHz)	Video Y/N	ϕ	[10 cm] CH1 PD1-PD2 83 cm	[10 cm] CH1 PD3-PD4 161 cm	[5.98 cm] CH1- CH2 PD4-PD1 169 cm	[5.98 cm] CH2 PD1-PD2 175 cm	[5 cm] CH2 PD2-PD3 181 cm	[5 cm] CH2 PD4-PD5 200 cm	TIME	Notes
337	6/17/98	AA	25	N	1.7	-	-	-	-	-	-	2:09 PM	P_{fuel}=16 in Hg, P_{tot} =87.94 psig, -100 kPa vac., multi-fire
338	6/17/98	AA	25	N	1.7	-	-	-	-	-	-	2:14 PM	-100 kPa vac, wrong settings on o-scope
339	6/17/98	AA	25	N	1.7	14.44	-	-	-	-	-	2:18 PM	-100 kPa vac,
340	6/17/98	AA	25	N	1.7	-	-	-	-	-	-	2:34 PM	-100 kPa vac,
341	6/17/98	AA	25	N	1.7	16	-	-	-	-	-	3:07 PM	P_{fuel}=16 in Hg, P_{tot} =87.94 psig, -100 kPa vac., multi-fire
342	6/17/98	AA	25	Y (O-SCOPE)	1.7	15.76	58.4	8.54	-	-	16.2	3:13 PM	-100 kPa vac, fair profile, no extra flourescent lights.
343	6/17/98	AA	25	Y (O-SCOPE)	1.7	14.04	57.8	23.76	17.52	0.72	17.68	3:24 PM	-100 kPa vac, fair profile,
344	6/17/98	AA	25	N	1.7	22.3	49.8	15.62	15.68	6.36	-	3:35 PM	-100 kPa vac, fair to good profile,
345	6/17/98	AA	25	N	1.7	16.76	23	16.32	8.74	6.42	21.8	3:40 PM	-100 kPa vac, good profile,
346	6/17/98	AA	25	N	1.7	-	-	-	-	-	-	4:42 PM	P_{fuel}=17in Hg, P_{tot} =80.57psig, -100 kPa vac., multi-fire
347	6/17/98	AA	25	N	1.7	-	-	-	-	6.6	-	4:47 PM	-100 kPa vac, single fire,
348	6/17/98	AA	25	N	1.7	-	30.8	17.02	9.44	8.96	16.64	4:51 PM	-100 kPa vac, fair profile, single fire
349	6/17/98	AA	25	N	1.7	17.52	-	-	16.08	0.28	-	5:01 PM	-100 kPa vac, poor profile,
350	6/17/98	AA	12.5	N	1.8	-	-	-	-	-	-	5:40 PM	P_{fuel}=15in Hg, P_{tot} =89.61psig, -100 kPa vac., multi-fire
351	6/17/98	AA	12.5	Y (O-SCOPE)	1.8	-	17.2	65.76	-	4.76	8.8	5:45 PM	-100 kPa vac, fair to mediocre profile,
352	6/17/98	AA	25	N	1.8	44.2	0.88	115.6	16.08	8.52	-	6:00 PM	-100 kPa vac, fair to mediocre profile, flame wavering
353	6/17/98	AA	25	Y (O-SCOPE)	1.8	39.3	1.02	65.78	-	-	6.94	6:13 PM	-100 kPa vac, flame wavering near bend entrance
354	6/17/98	AA	25	Y (O-SCOPE)	1.8	32.5	1.22	41.38	24.6	8.78	35.6	6:26 PM	-100 kPa vac, flame wavering near CH2, PD4 -PD5
355	6/17/98	AA	25	N	1.8	-	26.9	-	-	-	-	6:58 PM	P_{fuel}=15in Hg, P_{tot} =89.61psig, -100 kPa vac., slow flame
356	6/17/98	AA	12.5	N	1.8	-	-	-	-	-	-	7:02 PM	-100 kPa vac, use flourescent lamp for backlighting
357	6/17/98	AA	12.5	N	1.8	49.6	16.12	99.76	-	-	-	7:07 PM	-100 kPa vac, " ", wavering of flame front
358	6/17/98	AA	12.5	Y (O-SCOPE)	1.8	-	1.16	66.4	-	-	9.12	7:18 PM	-100 kPa vac, " ", wavering of flame front
359	6/17/98	AA	12.5	N	1.8	33.2	16.72	33.04	25.6	-	-	7:28 PM	-100 kPa vac, " ", wavering of flame front, loud "whack"
360	6/18/98	AA	12.5	N	1.8	-	10.08	33.14	-	-	17.4	10:48 AM	P_{fuel}=15in Hg, P_{tot} =89.61psig, -100 kPa vac., multiple fire
361	6/18/98	AA	12.5	N	1.8	-	16.2	123.84	-	-	5.2	11:00 AM	-100 kPa vac, one shot fire, wavering
362	6/18/98	AA	12.5	N	1.8	60.2	9.6	116.2	16.44	15.56	10.92	11:08 AM	-100 kPa vac, fair to good profile, one shot ignition
363	6/18/98	AA	12.5	N	1.8	-	-	-	-	-	14.64	11:17 AM	-100 kPa vac,
364	6/18/98	AA	12.5	N	1.8	38.5	26.1	-	-	-	1.44	11:24 AM	-100 kPa vac, one shot ignition
365	6/18/98	AA	12.5	N	1.9	-	-	-	-	-	-	12:25 PM	P_{fuel}=14in Hg, P_{tot} =91.15 psig, -100 kPa vac., multiple fire
366	6/18/98	AA	12.5	N	1.9	-	-	-	-	-	-	12:29 PM	-100 kPa vac, quenched before bend.
367	6/18/98	AA	12.5	N	1.9	-	-	-	-	-	-	12:34 PM	-100 kPa vac,
368	6/18/98	AA	12.5	N	1.9	-	32.9	16.88	8.08	6.16	18.32	12:38 PM	-100 kPa vac, loud "whack", faint flame, need backlighting

Time between signals (ms)

Test #	Date	PD Config.	Sample Rate (kHz)	Video Y/N	ϕ	[10 cm] CH1 PD1-PD2 83 cm	[10 cm] CH1 PD3-PD4 161 cm	[5.98 cm] CH1- CH2 PD4-PD1 169 cm	[5.98 cm] CH2 PD1-PD2 175 cm	[5 cm] CH2 PD2-PD3 181 cm	[5 cm] CH2 PD4-PD5 200 cm	TIME	Notes
369	6/18/98	AA	12.5	N	1.9	-	108.8	-	-	-	-	12:46 PM	-100 kPa vac, propagation all the way thru.
370	6/18/98	AA	12.5	N	1.9	-	-	-	-	-	-	1:11 PM	P_{fuel}=14in Hg, P_{tot} =91.15 psig, -100 kPa vac., multiple fire
371	6/18/98	AA	12.5	N	1.9	-	-	-	-	-	-	1:14 PM	-100 kPa vac, one shot ignition
372	6/18/98	AA	12.5	N	1.9	-	-	-	-	-	-	1:19 PM	-100 kPa vac, one shot ignition
373	6/18/98	AA	12.5	N	1.9	-	-	-	-	-	-	1:23 PM	-100 kPa vac, loud "whisp", one shot ignition
374	6/18/98	AA	12.5	N	1.9	200	84.4	-	-	-	-	1:28 PM	-100 kPa vac, low "whisp", one shot ignition
375	6/18/98	AA	12.5	N	1.8	-	-	-	-	-	-	2:50 PM	P_{fuel}=15in Hg, P_{tot} =89.61 psig, -100 kPa vac.,
376	6/18/98	AA	12.5	N	1.8	-	41.6	-	-	-	19.5	2:55 PM	-100 kPa vac, one shot ignition, wavering,
377	6/18/98	AA	12.5	N	1.8	-	50.6	-	-	-	-	3:04 PM	-100 kPa vac, one shot ignition,
378	6/18/98	AA	12.5	N	1.8	50	-	-	-	-	31.7	3:35 PM	-100 kPa vac, one shot ignition, poor profile
379	6/18/98	AA	12.5	N	1.8	61	9.2	25.26	33.1	-	54.4	3:41 PM	-100 kPa vac, one shot ignition,
380	6/18/98	AA	12.5	N	1.85	-	-	-	-	-	-	4:30 PM	P_{fuel}=15in Hg, P_{tot} =86.99 psig, -100 kPa vac., "whack" sound
381	6/18/98	AA	12.5	N	1.85	-	9.36	6.32	6.44	1.76	14.08	4:34 PM	-100 kPa vac, wavering,
382	6/18/98	AA	12.5	N	1.85	-	-	-	-	-	-	4:42 PM	-100 kPa vac,
383	6/18/98	AA	12.5	N	1.85	-	-	-	-	-	-	4:46 PM	-100 kPa vac,
384	6/18/98	AA	12.5	N	1.85	-	-	-	-	-	-	4:51 PM	-100 kPa vac,

Table M.2: Time signals for photodiode configuration BB

Time between signals (ms)

Test #	Date	PD Config.	Sample Rate (kHz)	Video Y/N	ϕ	[10 cm] CH1 PD1-PD2 83 cm	[10 cm] CH1 PD3-PD4 161 cm	[5 cm] CH2 PD1-PD2 30 cm	[5 cm] CH2 PD3-PD4 53 cm	[5 cm] CH2 PD4-PD5 58 cm	TIME	Notes
385	6/24/98	BB	50	N	1.1	7.48	-	-	2.72	4.36	12:00 PM	P_{fuel}=20.5in Hg, P_{tot} =90.12 psig, -100 kPa vac.,
386	6/24/98	BB	125	N	1.1	12.8	-	-	4.6	10.24	12:11 PM	-100 kPa vac,
387	6/24/98	BB	50	N	1.1	12.4	-	-	6.7	21.1	12:24 PM	-100 kPa vac,
388	6/24/98	BB	50	N	1.1	13.84	-	-	6.9	3.32	12:38 PM	-100 kPa vac,
389	6/24/98	BB	50	N	1.1	22.1	-	-	10.16	17.8	12:46 PM	-100 kPa vac,
390	6/24/98	BB	50	N	1.1	7.2	-	4.67	-	-	3:37 PM	P_{fuel}=20.5in Hg, P_{tot} =90.12psig, -100 kPa vac.,blownt o-scope
391	6/25/98	BB	50	N	1.1	7.62	15.36	19.5	6.86	4	11:20 AM	-100 kPa vac, good profile
392	6/25/98	BB	50	N	1.1	15.2	16.2	3.24	5.86	8.56	11:34 AM	-100 kPa vac,
393	6/25/98	BB	50	N	1.1	10.32	18.52	2.7	30.7	4.34	11:43 AM	-100 kPa vac,
394	6/25/98	BB	50	N	1.1	9.72	22.9	-	6.28	6.3	11:53 AM	-100 kPa vac, EMI of spark mixes with PD1 and PD2 sig.
395	6/25/98	BB	50	N	1.3	8.66	19.12	19.36	11.96	4.94	12:32 PM	P_{fuel}=19 in Hg, P_{tot} =88.94 psig, -100 kPa vac.,good profile
396	6/25/98	BB	50	N	1.3	13.68	30.9	-	12.16	3.33	12:40 PM	-100 kPa vac, EMI of spark mixes with PD1 and PD2 sig.
397	6/25/98	BB	50	N	1.3	9.12	17.76	5.88	9.5	3.89	1:13 PM	P_{fuel}=19 in Hg, P_{tot} =88.94 psig, -100 kPa vac.,
398	6/25/98	BB	50	N	1.3	9.86	17.04	-	7.62	10.36	1:21 PM	-100 kPa vac, EMI of spark mixes with PD1 and PD2 sig.
399	6/25/98	BB	50	N	1.3	8.52	18.28	-	11.76	3.68	1:28 PM	-100 kPa vac,
400	6/25/98	BB	50	N	1.3	8.86	21.7	-	10.44	11.08	1:37 PM	-100 kPa vac,
401	6/25/98	BB	50	N	1.3	13.84	17.6	1.85	5.28	9.5	1:50 PM	-100 kPa vac, good profile
402	6/25/98	BB	50	N	1.5	12.52	-	-	13.92	8.86	3:51 PM	P_{fuel}=17 in Hg, P_{tot} =92.42 psig, -100 kPa vac., multi-fire
403	6/25/98	BB	25	N	1.5	10.84	12.32	8.64	5.8	9.44	3:57 PM	-100 kPa vac, good profile
404	6/25/98	BB	25	N	1.5	13	26.8	0.64	16.96	10.88	4:07 PM	-100 kPa vac,
405	6/25/98	BB	25	N	1.5	3.8	23.9	8.8	3.32	3.32	4:14 PM	-100 kPa vac,
406	6/25/98	BB	25	N	1.5	14.08	17.24	-	14.44	3.84	4:24 PM	-100 kPa vac,
407	6/25/98	BB	50	N	1.0	7.92	-	2.2	13.04	2.32	5:09 PM	P_{fuel}=21.5 in Hg, P_{tot} =87.95 psig,
408	6/25/98	BB	50	N	1.0	16.16	22.2	3.69	10.6	4.44	5:16 PM	-100 kPa vac, good profile
409	6/25/98	BB	50	N	1.0	12.6	27.9	-	22.8	3.51	5:23 PM	-100 kPa vac,
410	6/25/98	BB	50	N	1.0	10.28	28.2	-	16.08	6.78	5:31 PM	-100 kPa vac,
411	6/25/98	BB	50	N	1.0	11.08	30.6	6.12	15.16	10.72	5:40 PM	-100 kPa vac, good profile
412	6/26/98	BB	50	N	1.2	7.16	24	13.48	7.92	6.94	9:01 AM	P_{fuel}=20 in Hg, P_{tot} =86.89 psig, -99 kPa, good profile

Time between signals (ms)

Test #	Date	PD Config.	Sample Rate (kHz)	Video Y/N	ϕ	[10 cm] CH1 PD1-PD2 83 cm	[10 cm] CH1 PD3-PD4 161 cm	[5 cm] CH2 PD1-PD2 30 cm	[5 cm] CH2 PD3-PD4 53 cm	[5 cm] CH2 PD4-PD5 58 cm	TIME	Notes
413	6/26/98	BB	50	N	1.2	3.14	65.2	1.72	5.12	3.02	9:07 AM	- 99 kPa vac,
414	6/26/98	BB	50	N	1.2	15.8	18.6	-	5.54	11.44	9:16 AM	-99 kPa vac, EMI of spark mixes with PD1 and PD2 sig.
415	6/26/98	BB	50	N	1.2	5.02	18.08	-	3.46	9.6	9:23 AM	-99 kPa vac, EMI of spark mixes with PD1 and PD2 sig.
416	6/26/98	BB	50	N	1.2	9.74	16.68	2.51	6.16	9.58	9:32 AM	- 99 kPa vac, good profile
417	6/26/98	BB	50	N	1.4	12.12	24.8	19.1	13.76	7.26	11:17 AM	P_{fuel}=18 in Hg, P_{tot} =90.77 psig, -99 kPa, good profile
418	6/26/98	BB	50	N	1.4	14.52	14.84	-	10.76	9.12	11:26 AM	-99 kPa vac, EMI of spark mixes with PD1 and PD2 sig.
419	6/26/98	BB	50	N	1.4	5	20.8	-	12.4	3.94	11:37 AM	-99 kPa vac, EMI of spark mixes with PD1 and PD2 sig.
420	6/26/98	BB	50	N	1.4	12.84	27.3	-	10.6	3.35	11:46 AM	-99 kPa vac, EMI of spark mixes with PD1 and PD2 sig.
421	6/26/98	BB	50	N	1.4	15.16	16.4	2.68	12.88	4.28	11:57 AM	- 99 kPa vac, good profile
422	6/26/98	BB	50	N	1.6	-	-	-	-	-	1:18 PM	P_{fuel}=16.5in Hg, P_{tot} =90.03 psig, -99 kPa,
423	6/26/98	BB	25	N	1.6	11.04	41.6	-	12.52	12.64	1:23 PM	- 99 kPa vac,
424	6/26/98	BB	25	N	1.6	-	-	-	-	14.52	1:33 PM	- 99 kPa vac, inconclusive data
425	6/26/98	BB	25	N	1.6	9.4	19.08	-	18.4	15.24	1:41 PM	- 99 kPa vac,
426	6/26/98	BB	25	N	1.6	8.46	17.16	-	17.88	14.6	1:50 PM	- 99 kPa vac, similar to #425
427	6/26/98	BB	50	N	1.6	10.28	-	-	16.64	13.96	2:26 PM	P_{fuel}=16.5in Hg, P_{tot} =90.03 psig, -99 kPa, slow start
428	6/26/98	BB	25	N	1.6	9.32	25	9.84	16.68	3.12	2:32 PM	- 99 kPa vac, loud "whack" sound, good profile
429	6/26/98	BB	25	N	1.6	-	-	-	-	-	2:41 PM	- 99 kPa vac, loud "whack" sound, too much backlight
430	6/26/98	BB	25	N	1.6	3.6	16.44	3.18	14.64	3.08	2:46 PM	- 99 kPa vac, light "whack" sound,
431	6/26/98	BB	25	N	1.6	10.28	-	-	19.4	23.5	2:55 PM	- 99 kPa vac, light "whack" sound,
432	6/26/98	BB	25	N	1.7	24.9	32.9	-	32.3	15.68	3:35 PM	P_{fuel}=15.5in Hg, P_{tot} =91.63 psig, -99 kPa, multi-fire
433	6/26/98	BB	25	N	1.7	16.92	27.8	5.52	24.2	7.22	3:46 PM	- 99 kPa vac, light "whisp" sound, good profile
434	6/26/98	BB	25	N	1.7	26.4	25.9	5.34	23.7	2.08	3:55 PM	- 99 kPa vac, light "whisp" sound, good profile
435	6/26/98	BB	25	N	1.7	25.2	25.5	5.24	17.88	2.56	4:02 PM	- 99 kPa vac, light "whisp" sound, good profile
436	6/26/98	BB	25	N	1.7	14.76	21.3	4.74	10.64	5.98	4:10 PM	- 99 kPa vac, light "whisp" sound, good profile
437	6/30/98	BB	50	N	1.0	8.78	-	1.21	-	-	12:27 PM	P_{fuel}=21.5in Hg, P_{tot} =87.95 psig, -99 kPa,
438	6/30/98	BB	50	N	1.0	-	-	-	-	-	12:46 PM	- 99 kPa vac, low voltage signals on o-scope. ?
439	6/30/98	BB	50	N	1.0	10.56	30.9	8.78	4.46	3.37	5:38 PM	P_{fuel}=21.5in Hg, P_{tot} =87.95 psig, -99 kPa, good profile
440	6/30/98	BB	50	N	1.0	14.08	25.5	7.3	9.12	11.64	5:47 PM	- 99 kPa vac, good O-scope profile
441	6/30/98	BB	50	N	1.0	18.36	23.7	8.26	8.74	7.86	5:55 PM	- 99 kPa vac, good O-scope profile
442	6/30/98	BB	50	N	1.0	20.3	30.5	9.48	11.96	5.12	6:02 PM	- 99 kPa vac, good O-scope profile
443	6/30/98	BB	50	N	1.0	18.08	-	9.58	10.04	6.64	6:12 PM	- 99 kPa vac, no CH1, PD 4 signal.
444	7/1/98	BB	50	N	1.1	13.92	16.16	7.7	11.28	3.13	11:19 AM	P_{fuel}=20in Hg, P_{tot} =95.68 psig, -99 kPa, problems w/ trnsfrmr
445	7/1/98	BB	50	N	1.1	14.16	16.4	9.64	8.3	8.34	11:28 AM	- 99 kPa vac, good O-scope profile

Time between signals (ms)

Test #	Date	PD Config.	Sample Rate (kHz)	Video Y/N	ϕ	[10 cm] CH1 PD1-PD2 83 cm	[10 cm] CH1 PD3-PD4 161 cm	[5 cm] CH2 PD1-PD2 30 cm	[5 cm] CH2 PD3-PD4 53 cm	[5 cm] CH2 PD4-PD5 58 cm	TIME	Notes
446	7/1/98	BB	50	N	1.1	15.28	15.96	10.2	6.84	4.17	11:36 AM	- 99 kPa vac, good O-scope profile
447	7/1/98	BB	50	N	1.1	16.24	19.2	10.2	7.65	5.54	11:43 AM	- 99 kPa vac,
448	7/1/98	BB	50	N	1.2	9.84	16.32	9.14	8.64	2.57	12:09 PM	P_{fuel}=20in Hg, P_{tot} =86.89 psig, -99 kPa,
449	7/1/98	BB	50	N	1.2	12.12	18.28	5.65	11.4	3.57	12:16 PM	- 99 kPa vac,
450	7/1/98	BB	50	N	1.2	15.72	17.64	4.59	12.4	3.22	12:23 PM	- 99 kPa vac,
451	7/1/98	BB	50	N	1.2	11.8	18.16	3.46	9.5	6.08	12:30 PM	- 99 kPa vac,
452	7/1/98	BB	50	N	1.2	14.76	15.8	7.24	12	6.26	12:39 PM	- 99 kPa vac,
453	7/1/98	BB	50	N	1.3	7.68	17.88	9.4	8.86	5.38	1:06 PM	P_{fuel}=19in Hg, P_{tot} =88.94 psig, -99 kPa vac,
454	7/1/98	BB	50	N	1.3	10.44	18.16	3.79	10.12	3.69	1:13 PM	- 99 kPa vac,
455	7/1/98	BB	50	N	1.3	14.84	17.4	2.44	3.88	8.5	1:22 PM	- 99 kPa vac,
456	7/1/98	BB	50	N	1.3	16.6	17.4	3.02	9.84	4.18	1:29 PM	- 99 kPa vac,
457	7/1/98	BB	50	N	1.4	12.32	17.72	4.58	15.12	-	1:54 PM	P_{fuel}=18in Hg, P_{tot} =90.77 psig, -99 kPa vac,
458	7/1/98	BB	50	N	1.4	10.56	19.28	7.06	11.2	3.36	2:03 PM	- 99 kPa vac,
459	7/1/98	BB	50	N	1.4	10.48	21.6	8.06	11.12	4.22	2:09 PM	- 99 kPa vac,
460	7/1/98	BB	50	N	1.4	10.64	19.12	4.54	12.4	3.02	2:18 PM	- 99 kPa vac,
461	7/1/98	BB	50	N	1.4	13.24	16.6	1.55	11.4	3.4	2:26 PM	- 99 kPa vac,
462	7/1/98	BB	50	N	1.5	12.56	14.52	-	-	-	4:23 PM	P_{fuel}=17in Hg, P_{tot} =92.42 psig, -100 kPa vac,
463	7/1/98	BB	25	N	1.5	14.08	13	4.58	15.28	8.2	4:28 PM	- 100 kPa vac, use flourescent backlighting
464	7/1/98	BB	25	N	1.5	-	14.48	4.82	17.96	1.82	4:35 PM	- 100 kPa vac,
465	7/1/98	BB	25	N	1.5	25	16.64	5.3	10.6	2.34	4:43 PM	- 100 kPa vac,
466	7/1/98	BB	25	N	1.5	13.64	14	8.42	11.92	5.54	4:52 PM	- 100 kPa vac,
467	7/1/98	BB	25	N	1.6	19.5	9.52	-	16.16	6.8	5:21 PM	P_{fuel}=16in Hg, P_{tot} =93.93 psig, -100 kPa vac,
468	7/1/98	BB	25	N	1.6	10.6	7.42	9.12	21.7	1.8	5:28 PM	- 100 kPa vac, "whack" sound
469	7/1/98	BB	25	N	1.6	12.72	5.2	4.54	16.16	10.28	5:37 PM	- 100 kPa vac, "whack" sound, good profile
470	7/1/98	BB	25	N	1.6	12.76	5.6	10.28	17.52	2.76	5:45 PM	- 100 kPa vac, "whisp" sound, good profile
471	7/1/98	BB	25	N	1.6	12.36	9.68	9	18.04	1.22	5:52 PM	- 100 kPa vac, "whack" sound,
472	7/1/98	BB	25	N	1.7	22.9	8.24	-	18.2	14.4	6:20 PM	P_{fuel}=16in Hg, P_{tot} =87.94 psig, -100 kPa vac, slow, "whisp"
473	7/1/98	BB	25	N	1.7	6.12	0.56	8.12	12.6	3.58	6:30 PM	- 100 kPa vac, "whisp" sound, good profile, fast
474	7/1/98	BB	25	N	1.7	8.74	7.36	10.16	19.28	2.66	6:38 PM	- 100 kPa vac, "whisp" sound, good profile,
475	7/1/98	BB	25	N	1.7	17.32	21	9.04	18.92	4.1	6:46 PM	- 100 kPa vac, light "whack" sound,
476	7/1/98	BB	25	N	1.7	11.48	1.42	12.88	18.16	4.4	6:55 PM	- 100 kPa vac, loud "whack" sound, good profile
477	7/2/98	BB	12.5	N	1.8	41.1	75.2	-	32.3	1.36	8:47 AM	P_{fuel}=15in Hg, P_{tot} =89.61 psig, -100 kPa vac,"whack", multi-fire
478	7/2/98	BB	12.5	N	1.8	38.5	28.5	6.12	58.4	5.52	8:55 AM	- 100 kPa vac, light "whack" sound,

Time between signals (ms)

Test #	Date	PD Config.	Sample Rate (kHz)	Video Y/N	ϕ	[10 cm] CH1 PD1-PD2 83 cm	[10 cm] CH1 PD3-PD4 161 cm	[5 cm] CH2 PD1-PD2 30 cm	[5 cm] CH2 PD3-PD4 53 cm	[5 cm] CH2 PD4-PD5 58 cm	TIME	Notes
479	7/2/98	BB	12.5	N	1.8	25	26.4	5.36	32.2	0.96	9:04 AM	- 100 kPa vac, loud "whack" sound,
480	7/2/98	BB	12.5	N	1.8	24.7	23.8	2.24	25.9	0.28	9:14 AM	- 100 kPa vac, "whisp" sound,
481	7/2/98	BB	25	N	1.8	33.4	27.6	5.38	39.6	1.02	9:23 AM	- 100 kPa vac, "whisp" sound,
482	7/2/98	BB	25	N	1.8	40.9	-	-	48.9	1.08	9:50 AM	P_{fuel}=15in Hg, P_{tot} =89.61 psig, -100 kPa vac, slow start
483	7/2/98	BB	12.5	N	1.8	41.7	40.4	1	33.9	0.64	9:55 AM	- 100 kPa vac, "whisp" sound,
484	7/2/98	BB	12.5	N	1.8	41.7	43.1	1.12	17.44	0.8	10:04 AM	- 100 kPa vac, loud "whack" sound, probable wavering
485	7/2/98	BB	25	N	1.8	33.6	33.8	5.54	41.7	5.8	10:11 AM	- 100 kPa vac, loud "whack" sound, slight wavering
486	7/2/98	BB	25	N	1.8	24.3	24.6	2	42	0.5	10:20 AM	- 100 kPa vac, "whisp" sound,
487	7/2/98	BB	25	N	0.9	17.48	17.56	-	-	-	10:50 AM	P_{fuel}=22in Hg, P_{tot} =92.15 psig, -100 kPa vac,
488	7/2/98	BB	50	N	0.9	24.5	17.4	14.52	31.3	1.52	10:59 AM	- 100 kPa vac, good O-scope profile
489	7/2/98	BB	50	N	0.9	32.6	18.28	8.78	31.1	1.46	11:06 AM	- 100 kPa vac, good O-scope profile
490	7/2/98	BB	50	N	0.9	25.2	17.68	8.76	31.6	1.35	11:13 AM	- 100 kPa vac, "whisp" sound,
491	7/2/98	BB	50	N	0.9	32.9	19.76	9.18	31.2	1.4	11:21 AM	- 100 kPa vac, light "whack" sound
492	7/2/98	BB	25	N	0.9	24.2	15.8	1.9	6.28	0.9	11:52 AM	P_{fuel}=22in Hg, P_{tot} =92.15 psig, -100 kPa vac,
493	7/2/98	BB	50	N	0.9	24.9	17.52	7.98	33.4	0.26	11:59 AM	- 100 kPa vac, "whisp" sound,
494	7/2/98	BB	50	N	0.9	24.7	18.28	14.84	32.1	1.15	12:07 PM	- 100 kPa vac, "whisp" sound,
495	7/2/98	BB	50	N	0.9	25.3	18.84	8.54	32.1	1.26	12:15 PM	- 100 kPa vac, "whisp" sound,
496	7/2/98	BB	50	N	0.9	33	25.1	13.76	30.6	1.49	12:23 PM	- 100 kPa vac, "whisp"
497	7/2/98	BB	25	N	0.8	25	52.8	-	-	2.18	1:30 PM	P_{fuel}=23in Hg, P_{tot} =89.90 psig, -100 kPa vac,
498	7/2/98	BB	25	N	0.8	32.9	38.9	-	25.3	6.98	1:36 PM	- 100 kPa vac, "whispy", quench in bend.
499	7/2/98	BB	25	N	0.8	41.2	35.4	-	31.6	1.5	1:42 PM	- 100 kPa vac, quench in bend.
500	7/2/98	BB	25	N	0.8	41.2	34.1	-	47.9	1.54	1:48 PM	- 100 kPa vac, flame front wavering, quench in bend.
501	7/2/98	BB	25	N	0.8	50	-	-	48.5	1	1:55 PM	- 100 kPa vac, slow
502	7/2/98	BB	25	N	0.8	47.7	-	1.88	-	-	2:19 PM	P_{fuel}=23in Hg, P_{tot} =89.90 psig, -100 kPa vac, waver,quench
503	7/2/98	BB	25	N	0.8	33.3	33.4	-	-	-	2:27 PM	- 100 kPa vac, quench
504	7/2/98	BB	25	N	0.8	33.2	30.7	-	-	1.24	2:34 PM	- 100 kPa vac, quench, other data inconclusive
505	7/2/98	BB	25	N	0.8	32.5	28.1	-	22.8	1.98	2:42 PM	- 100 kPa vac, quench in latter half of bend.
506	7/2/98	BB	25	N	0.8	41.8	41.6	-	32.3	16.96	2:50 PM	- 100 kPa vac, wavering

Table M.3: Time signals for photodiode configuration CC

Time between signals (ms)

						[10 cm]	[10 cm]	[5 cm]	[5 cm]	[5 cm]	[10 cm]		
Test #	Date	PD Config.	Sample Rate (kHz)	Video Y/N	ϕ	CH1 PD1-PD2 83 cm	CH1 PD3-PD4 161 cm	CH2 PD1-PD2 112 cm	CH2 PD2-PD3 117 cm	CH2 PD4-PD5 144 cm	CH2- CH1 PD5-PD3 151 cm	TIME	Notes
507	7/3/98	CC	50	N	1.1	9.82	20.1	7	3.45	5.82	9.36	9:03 AM	P_{fuel}=20.5in Hg, P_{tot} =90.12 psig, -100 kPa vac, good profile
508	7/3/98	CC	50	N	1.1	15	18.2	4.68	6.96	4.42	8.32	9:12 AM	- 100 kPa vac, good O-scope profile
509	7/3/98	CC	50	N	1.1	17.84	16.72	4.68	5.7	4.4	7.32	9:21 AM	- 100 kPa vac, good O-scope profile
510	7/3/98	CC	50	N	1.1	8.66	18.56	2.48	6	3.18	9.96	9:29 AM	- 100 kPa vac, good O-scope profile
511	7/3/98	CC	50	N	1.1	14.92	19.8	5.84	3.75	7.38	8.18	9:39 AM	- 100 kPa vac, good O-scope profile
512	7/3/98	CC	50	N	1.3	10	16.64	10.24	5.26	5.3	9.72	10:07 AM	P_{fuel}=19.0in Hg, P_{tot} =88.94 psig, -100 kPa vac, good profile
513	7/3/98	CC	50	N	1.3	12.88	17.56	9.58	5.7	7.18	7.52	10:15 AM	- 100 kPa vac, good O-scope profile
514	7/3/98	CC	50	N	1.3	13.08	23.6	8	7.88	7.84	13.68	10:23 AM	- 100 kPa vac, good O-scope profile
515	7/3/98	CC	50	N	1.3	10.84	23.2	4.45	7.24	1.72	13.44	10:32 AM	- 100 kPa vac, very good O-scope profile
516	7/3/98	CC	50	N	1.3	9.32	14.32	3.74	4.9	5.7	5.42	10:41 AM	- 100 kPa vac, good O-scope profile
517	7/3/98	CC	50	N	1.5	15.52	-	7.34	15.92	6.54	-	11:09 AM	P_{fuel}=17.0in Hg, P_{tot} =92.42psig, -100 kPa vac, backlighting
518	7/3/98	CC	25	N	1.5	8.84	23.3	0.74	6.82	2.75	5.98	11:18 AM	- 100 kPa vac, double "whack" sound
519	7/3/98	CC	25	N	1.5	15.88	27.9	1.68	9.36	5.12	11.08	11:26 AM	- 100 kPa vac,
520	7/3/98	CC	25	N	1.5	13.16	17.68	0.48	8.6	3.06	8.62	11:34 AM	- 100 kPa vac, strong "whisp" sound
521	7/3/98	CC	25	N	1.5	17.12	25.6	10.2	5.74	9.22	14.52	11:44 AM	- 100 kPa vac,
522	7/3/98	CC	25	N	1.6	23.5	57.2	0.42	18.9	-	-	1:25 PM	P_{fuel}=16.0in Hg, P_{tot} =93.93 psig, -100 kPa vac, backlighting
523	7/3/98	CC	25	N	1.6	22.7	47.9	-	-	-	-	1:32 PM	- 100 kPa vac, "whisp" sound
524	7/3/98	CC	25	N	1.6	8.76	34.8	-	-	2.2	24.8	1:42 PM	- 100 kPa vac, "whisp" sound, fair O-scope profile
525	7/3/98	CC	25	N	1.6	16.44	32.8	-	-	2.46	23.2	1:52 PM	- 100 kPa vac, "whisp" sound, fair O-scope profile
526	7/3/98	CC	25	N	1.6	8.16	31.1	-	-	2.14	11.52	2:02 PM	- 100 kPa vac, "whack" sound
527	7/3/98	CC	50	N	1.4	9.92	18.52	14.32	10.04	9.36	12.64	2:44 PM	P_{fuel}=18.0in Hg, P_{tot} =90.77psig, -100 kPa vac, gd profile
528	7/3/98	CC	50	N	1.4	8.2	15.16	15.12	9.22	3.19	10.32	2:57 PM	- 100 kPa vac, good profile
529	7/3/98	CC	50	N	1.4	11.44	13.92	5.02	4.38	6.04	8.88	3:05 PM	- 100 kPa vac, good profile
530	7/3/98	CC	50	N	1.4	9.18	14.4	4.69	4.78	4.48	8.86	3:12 PM	- 100 kPa vac, good profile
531	7/3/98	CC	50	N	1.4	12.04	14	5.36	4.61	4.17	8.68	3:20 PM	- 100 kPa vac, good profile
532	7/3/98	CC	50	N	1.2	7.98	17.04	7.72	4.44	4.82	9.96	4:53 PM	P_{fuel}=20in Hg, P_{tot} =86.89 psig, -100 kPa vac, gd profile
533	7/3/98	CC	50	N	1.2	9.32	17.24	3.85	6.96	4.59	8.2	5:01 PM	- 100 kPa vac, good profile
534	7/3/98	CC	50	N	1.2	5.1	26	2.77	9.68	8.18	10.44	5:09 PM	- 100 kPa vac, good profile

Time between signals (ms)

Test #	Date	PD Config.	Sample Rate (kHz)	Video Y/N	ϕ	[10 cm] CH1 PD1-PD2 83 cm	[10 cm] CH1 PD3-PD4 161 cm	[5 cm] CH2 PD1-PD2 112 cm	[5 cm] CH2 PD2-PD3 117 cm	[5 cm] CH2 PD4-PD5 144 cm	[10 cm] CH2- CH1 PD5-PD3 151 cm	TIME	Notes
535	7/3/98	CC	50	N	1.2	22.6	19.04	3.11	15.4	7.66	10.6	5:17 PM	- 100 kPa vac, good profile
536	7/3/98	CC	50	N	1.2	15.92	17.08	5.52	5.12	5.76	12.08	5:26 PM	- 100 kPa vac, good profile
537	7/4/98	CC	50	N	1.0	10.48	17.28	0.82	16.04	5.2	10.24	10:54 AM	P_{fuel}=21.5in Hg, P_{tot} =87.95 psig, -100 kPa vac, gd profile
538	7/4/98	CC	50	N	1.0	9.48	19.68	4.13	7.42	4.82	15.4	11:02 AM	- 100 kPa vac, good profile, backlighting
539	7/4/98	CC	50	N	1.0	18.96	21.5	4.27	9.24	7.02	7.8	11:11 AM	- 100 kPa vac, good profile
540	7/4/98	CC	50	N	1.0	9.54	30.7	-	17.96	-	-	11:20 AM	- 100 kPa vac, fair profile
541	7/4/98	CC	50	N	1.0	23.2	26.8	0.63	16.8	2.99	22.1	11:28 AM	- 100 kPa vac,
542	7/4/98	CC	50	N	0.9	16.64	25.3	-	-	1.03	13.4	11:57 AM	P_{fuel}=22in Hg, P_{tot} =92.15 psig, -100 kPa vac, fair profile
543	7/4/98	CC	50	N	0.9	16.2	31.8	10.32	6.18	9.8	16.64	12:05 PM	- 100 kPa vac, good profile
544	7/4/98	CC	50	N	0.9	25	31.4	13.16	11.36	3.88	17.16	12:14 PM	- 100 kPa vac, good profile
545	7/4/98	CC	50	N	0.9	16.4	-	1.41	15.44	5.5	-	12:23 PM	- 100 kPa vac, "whisp", no CH1, PD3 signal
546	7/4/98	CC	50	N	0.9	25	-	0.58	10.8	1.13	-	12:32 PM	- 100 kPa vac, no CH1, PD3 signal
547	7/4/98	CC	25	N	0.8	40.3	-	0.88	10.88	-	-	12:57 PM	P_{fuel}=23in Hg, P_{tot} =89.90 psig, -100 kPa vac, wavering
548	7/4/98	CC	25	N	0.8	7.36	-	16.4	8.08	11.32	-	1:04 PM	- 100 kPa vac, multi-fire, wavering near 181 cm location
549	7/4/98	CC	25	N	0.8	25	-	0.4	18.68	2.14	-	1:13 PM	- 100 kPa vac, whisp, wavering near 181 cm location
550	7/4/98	CC	25	N	0.8	33.5	-	14.92	11.44	2.42	-	1:21 PM	- 100 kPa vac, whisp, wavering, whisp then quench
551	7/4/98	CC	25	N	0.8	-	-	-	-	-	-	1:29 PM	- 100 kPa vac, multi-fire,slow, quench in bend
552	7/4/98	CC	25	N	1.7	-	-	-	-	-	-	2:03 PM	P_{fuel}=16in Hg, P_{tot} =87.94 psig, -100 kPa vac, whisp
553	7/4/98	CC	25	N	1.7	34.1	-	-	18.64	1.42	-	2:08 PM	- 100 kPa vac, "whack" sound, fixed PD3 lead
554	7/4/98	CC	25	N	1.7	33.5	-	0.86	25.8	1.84	-	2:15 PM	- 100 kPa vac, poor O-scope profile
555	7/4/98	CC	25	N	1.7	41.3	51.6	5.12	11.4	1.68	48	2:23 PM	- 100 kPa vac, wavering near 151 cm location
556	7/4/98	CC	25	N	1.7	39.9	28.2	5.34	10.72	1.66	32.1	2:35 PM	- 100 kPa vac, "whisp" sound, wavering
557	7/4/98	CC	50	N	1.2	7.94	17.64	8.36	3.75	7.96	8.62	3:10 PM	P_{fuel}=20in Hg, P_{tot} =86.89 psig, -100 kPa vac, good profile
558	7/4/98	CC	50	N	1.2	12.52	13.56	4.49	4.01	3.85	8.36	3:20 PM	- 100 kPa vac, good O-scope profile
559	7/4/98	CC	50	N	1.2	18.8	13.36	5.18	4.04	7.54	7.42	3:25 PM	- 100 kPa vac, good O-scope profile
560	7/4/98	CC	50	N	1.2	12.56	17.8	6.66	4.3	5.06	10.32	3:32 PM	- 100 kPa vac, good O-scope profile
561	7/4/98	CC	50	N	1.2	9.08	14	6.34	4.06	7.28	7.8	3:41 PM	- 100 kPa vac, good O-scope profile
562	7/4/98	CC	50	N	1.3	10.16	17.04	7.88	4.82	5.6	10.64	6:00 PM	P_{fuel}=19.0in Hg, P_{tot} =88.94 psig, -100 kPa vac, good profile
563	7/4/98	CC	50	N	1.3	14.96	24.8	6.76	6.3	7.12	9.92	6:07 PM	- 100 kPa vac, good O-scope profile
564	7/4/98	CC	50	N	1.3	10.56	14.64	4.5	3.17	4.47	7.32	6:13 PM	- 100 kPa vac, good O-scope profile
565	7/4/98	CC	50	N	1.3	12.04	17.2	3.77	5.64	8.48	8.86	6:21 PM	- 100 kPa vac, good O-scope profile
566	7/4/98	CC	50	N	1.3	12.2	16.2	5.32	3.39	7.18	8.3	6:29 PM	- 100 kPa vac,
567	7/4/98	CC	50	N	1.4	13.32	20.9	11	7.02	9.1	14.32	7:00 PM	P_{fuel}=18.0in Hg, P_{tot} =90.77 psig, -100 kPa vac, good profile

Time between signals (ms)

Test #	Date	PD Config.	Sample Rate (kHz)	Video Y/N	ϕ	[10 cm] CH1 PD1-PD2 83 cm	[10 cm] CH1 PD3-PD4 161 cm	[5 cm] CH2 PD1-PD2 112 cm	[5 cm] CH2 PD2-PD3 117 cm	[5 cm] CH2 PD4-PD5 144 cm	[10 cm] CH2- CH1 PD5-PD3 151 cm	TIME	Notes
568	7/4/98	CC	50	N	1.4	13.56	18.36	4.98	4.49	5.72	12.08	7:07 PM	- 100 kPa vac, good O-scope profile
569	7/4/98	CC	50	N	1.4	15.48	21.3	9.2	3.91	6.46	11	7:14 PM	- 100 kPa vac, good O-scope profile
570	7/4/98	CC	50	N	1.4	12.24	16.64	4.68	6.98	4.98	9.88	7:22 PM	- 100 kPa vac, good O-scope profile
571	7/4/98	CC	50	N	1.4	13.8	14.76	3.94	4.92	3.87	7.18	7:30 PM	- 100 kPa vac, good O-scope profile
572	7/5/98	CC	25	N	1.5	1.2	31.6	-	-	1.3	26.5	11:29 AM	P_{fuel}=17.0in Hg, P_{tot} =92.42 psig, -100 kPa vac, backlighting
573	7/5/98	CC	25	N	1.5	8.38	19.2	-	-	-	-	11:36 AM	- 100 kPa vac, loud "whack", possible wavering
574	7/5/98	CC	25	N	1.5	6.66	30.4	-	10.88	1	31.8	11:44 AM	- 100 kPa vac, loud "whack", possible wavering
575	7/5/98	CC	25	N	1.5	8.86	23.7	0.86	10.96	1.34	23.9	11:52 AM	- 100 kPa vac, "whisp", no wavering
576	7/5/98	CC	25	N	1.5	9.5	23.6	-	16.44	-	-	12:00 PM	- 100 kPa vac, "whop", other data inconclusive
577	7/5/98	CC	50	N	1.0	8.3	21.4	-	10.16	0.62	17.8	12:26 PM	P_{fuel}=21.0in Hg, P_{tot} =94.04 psig, -100 kPa vac, backlighting
578	7/5/98	CC	50	N	1.0	0.41	18.64	-	17.64	2.51	22	12:32 PM	- 100 kPa vac, small del t at PD1 - PD 2 for CH2
579	7/5/98	CC	50	N	1.0	16.6	21.8	4.66	9.92	2.49	15.96	12:42 PM	- 100 kPa vac, good O-scope profile
580	7/5/98	CC	50	N	1.0	11.12	24.9	1.04	8.7	2.87	21.6	12:51 PM	- 100 kPa vac, good O-scope profile
581	7/5/98	CC	50	N	1.0	18.76	27.6	1.85	9.52	4.72	12.16	12:58 PM	- 100 kPa vac, good O-scope profile
582	7/5/98	CC	50	N	1.1	7.74	20.9	9.84	5.2	8.58	9.26	1:26 PM	P_{fuel}=20.5in Hg, P_{tot} =90.12 psig, -100 kPa vac, backlighting
583	7/5/98	CC	50	N	1.1	13.76	25.8	9.8	6.14	8.24	14.76	1:33 PM	- 100 kPa vac, "whop" sound, good O-scope profile
584	7/5/98	CC	50	N	1.1	10.16	20.9	3.42	4.1	1.62	9.48	1:37 PM	- 100 kPa vac, good O-scope profile
585	7/5/98	CC	50	N	1.1	9.82	18.36	3.32	5.68	7.72	8.44	1:46 PM	- 100 kPa vac, good O-scope profile
586	7/5/98	CC	50	N	1.1	10.64	17.04	4.56	4.09	4.17	11.4	1:54 PM	- 100 kPa vac, good O-scope profile
587	7/5/98	CC	50	N	0.9	16.08	25.4	4.6	8.88	7.66	15.56	2:23 PM	P_{fuel}=22in Hg, P_{tot} =92.15 psig, -100 kPa vac, backlighting
588	7/5/98	CC	50	N	0.9	17.36	32.8	11.24	7.88	9.72	18.6	2:31 PM	- 100 kPa vac, "whisp pop" sound, good O-scope profile
589	7/5/98	CC	50	N	0.9	16.4	33	5.06	10.56	9.32	17.84	2:40 PM	- 100 kPa vac, good O-scope profile,
590	7/5/98	CC	50	N	0.9	17.36	34.4	5.44	17.68	10.36	23	2:48 PM	- 100 kPa vac, good O-scope profile,
591	7/5/98	CC	50	N	0.9	25.2	-	15.64	12.16	10.84	-	2:56 PM	- 100 kPa vac, "whisp", slower than other flame fronts
592	7/5/98	CC	25	N	0.8	-	-	-	-	-	-	3:21 PM	P_{fuel}=23in Hg, P_{tot} =89.90 psig, -100 kPa vac, backlighting
593	7/5/98	CC	25	N	0.8	24.9	-	1.28	33.8	16.52	-	3:25 PM	- 100 kPa vac, multiple fire, wavering
594	7/5/98	CC	25	N	0.8	19	-	15.96	18.36	2.88	-	3:33 PM	- 100 kPa vac, wavering near 130 cm location
595	7/5/98	CC	25	N	0.8	26.2	-	6.12	26.7	11.16	-	3:41 PM	- 100 kPa vac, multi-fire, wavering near 130 cm location
596	7/5/98	CC	25	N	0.8	51.4	-	15.56	34.7	1.7	83.4	3:49 PM	- 100 kPa vac, slow flame, quench in bend
597	7/5/98	CC	12.5	N	1.8	-	-	-	-	-	-	4:22 PM	P_{fuel}=15.0in Hg, P_{tot} =89.61 psig, -100 kPa vac, multi-fire
598	7/5/98	CC	12.5	N	1.8	55.6	-	5.28	11.16	0.48	74.8	4:27 PM	- 100 kPa vac, "whisp" sound, wavering
599	7/5/98	CC	12.5	N	1.8	49.8	122.8	15.4	11.8	1.08	59	4:35 PM	- 100 kPa vac, "whisp" sound, wavering
600	7/5/98	CC	12.5	N	1.8	34.7	42.4	-	-	-	-	4:44 PM	- 100 kPa vac, "whack" sound, other data inconclusive

Time between signals (ms)

						[10 cm]	[10 cm]	[5 cm]	[5 cm]	[5 cm]	[10 cm]		
Test #	Date	PD Config.	Sample Rate (kHz)	Video Y/N	ϕ	CH1 PD1-PD2 83 cm	CH1 PD3-PD4 161 cm	CH2 PD1-PD2 112 cm	CH2 PD2-PD3 117 cm	CH2 PD4-PD5 144 cm	CH2- CH1 PD5-PD3 151 cm	TIME	Notes
601	7/5/98	CC	12.5	N	1.8	23.8	-	0.64	17.76	-	-	4:52 PM	- 100 kPa vac, "whack" sound, other data inconclusive
602	7/6/98	CC	25	N	1.5	-	-	-	-	-	-	11:10 AM	P_{fuel}=17.0in Hg, P_{tot} =92.42 psig, -100 kPa vac, multi-fire
603	7/6/98	CC	25	N	1.5	26.6	18.26	0.8	9.12	1.32	8.3	11:14 AM	- 100 kPa vac, good profile, P_{atm} and RH important
604	7/6/98	CC	25	N	1.5	32.8	30.1	5.06	10.16	5.12	18.6	11:24 AM	- 100 kPa vac, "whisp" sound, good profile
605	7/6/98	CC	25	N	1.5	18.2	17.84	5.82	3.2	1.16	13.32	11:31 AM	- 100 kPa vac, "whack" sound, good profile
606	7/6/98	CC	25	N	1.5	39.5	20.8	9.64	4.88	5.08	11.2	11:38 AM	- 100 kPa vac, good profile
607	7/6/98	CC	50	N	0.9	34.3	22.2	4.54	3.6	4.17	9.92	12:34 PM	P_{fuel}=23.0in Hg, P_{tot} =78.66 psig, -100 kPa vac, good profile
608	7/6/98	CC	50	N	0.9	-	26.5	0.52	10.32	2.14	24.3	12:51 PM	- 100 kPa vac, "whisp" sound, fair profile
609	7/6/98	CC	50	N	0.9	24.6	32.4	0.33	18.2	2.49	25.7	12:59 PM	- 100 kPa vac, good profile
610	7/6/98	CC	50	N	0.9	25.5	41.7	15	11.44	10.6	24.8	1:08 PM	- 100 kPa vac, about 0.47 sec for propa. thru inlet section
611	7/6/98	CC	12.5	N	1.6	24	49.6	0.32	19	0.68	48.8	2:23 PM	P_{fuel}=16.0in Hg, P_{tot} =93.93 psig, -100 kPa vac, multi-fire
612	7/6/98	CC	50	N	1.6	14.72	24	14.48	3.5	0.69	31.8	2:34 PM	- 100 kPa vac, good profile
613	7/6/98	CC	50	N	1.6	19.2	33.7	1.44	16.44	1.28	33.4	2:41 PM	- 100 kPa vac, "whisp" sound, good profile
614	7/6/98	CC	50	N	1.6	16.84	31.6	14.52	3.38	1.42	26.4	2:50 PM	- 100 kPa vac, "whisp" sound, profile v. similar to # 612
615	7/6/98	CC	50	N	1.6	17.08	25.5	0.55	10.12	-	-	2:58 PM	- 100 kPa vac, "whisp" sound, possible wavering.
616	7/6/98	CC	12.5	N	1.7	23.6	49	-	-	-	-	3:34 PM	P_{fuel}=16.0in Hg, P_{tot} =87.94 psig, -100 kPa vac, multi-fire
617	7/6/98	CC	25	N	1.7	33.8	-	16.08	18.96	16.52	57.2	3:41 PM	- 100 kPa vac, "whisp pop" sound, slow flame
618	7/6/98	CC	25	N	1.7	25.9	183.6	0.96	17.6	2.22	50	3:50 PM	- 100 kPa vac, "whack" sound, large del. t for PD3-PD4
619	7/6/98	CC	25	N	1.7	17.72	52	4.56	11.16	15.84	41	3:59 PM	- 100 kPa vac, loud "whack" sound, good profile
620	7/6/98	CC	25	N	1.7	23.5	33.5	0.62	10.28	5.22	25.7	4:08 PM	- 100 kPa vac, "whisp" sound, good profile
621	7/6/98	CC	12.5	N	1.8	24.7	-	5.56	10.76	2.52	91.8	4:42 PM	P_{fuel}=15.0in Hg, P_{tot} =89.61 psig, -100 kPa vac, multi-fire
622	7/6/98	CC	12.5	N	1.8	51.4	270	1.4	26.5	2.48	133.6	4:51 PM	- 100 kPa vac, hesitation in exiting FPD
623	7/6/98	CC	12.5	N	1.8	43.9	-	1.36	26.9	6.32	66.2	4:58 PM	- 100 kPa vac, hesitation/wavering near PD 3-PD4
624	7/6/98	CC	12.5	N	1.8	32.3	178.4	15.96	18.4	17.48	56.8	5:07 PM	- 100 kPa vac, whispy, wavering near PD 3-PD4
625	7/6/98	CC	12.5	N	1.8	24.8	41.4	14.96	10.96	2.04	33.6	5:17 PM	- 100 kPa vac,
626	7/7/98	CC	25	N	0.8	-	-	4.66	10.64	1.36	40.9	8:48 AM	P_{fuel}=23.0in Hg, P_{tot} =89.90 psig, -100 kPa vac, quench
627	7/7/98	CC	25	N	0.8	26.8	-	0.76	26.8	1.6	66	8:55 AM	- 100 kPa vac, multi-fire, wavering, quench in bend
628	7/7/98	CC	25	N	0.8	31.3	49.2	0.52	26.8	2.36	57.2	9:05 AM	- 100 kPa vac, multi-fire, wavering, quench in bend
629	7/7/98	CC	25	N	0.8	25.6	49.8	15.16	19.4	16.44	59	9:13 AM	- 100 kPa vac, multi-fire, wavering,
630	7/7/98	CC	25	N	0.8	42.7	75.4	16.12	36.1	2.04	100	9:25 AM	- 100 kPa vac, one shot fire, wavering, very slow flame
631	7/7/98	CC	25	N	1.655	17.84	-	4.32	19.44	-	-	12:09 PM	P_{fuel}=16 in Hg, "whack" sound, slow flame, last of air from bot.
632	7/7/98	CC	25	N	1.655	23.6	48.8	-	18.6	1.78	49.8	12:15 PM	- 100 kPa vac, "whisp

Time between signals (ms)

						[10 cm]	[10 cm]	[5 cm]	[5 cm]	[5 cm]	[10 cm]		
Test #	Date	PD Config.	Sample Rate (kHz)	Video Y/N	ϕ	CH1 PD1-PD2 83 cm	CH1 PD3-PD4 161 cm	CH2 PD1-PD2 112 cm	CH2 PD2-PD3 117 cm	CH2 PD4-PD5 144 cm	CH2- CH1 PD5-PD3 151 cm	TIME	Notes
633	7/7/98	CC	25	N	1.655	18.68	49.8	14.92	11.44	0.16	58.2	12:22 PM	- 100 kPa vac, *whisp
634	7/7/98	CC	25	N	1.655	24.6	35.6	1.74	24.2	14.72	32.9	12:30 PM	- 100 kPa vac, *whisp
635	7/7/98	CC	25	N	1.655	16.64	32.7	0.44	11	4.9	25.1	12:42 PM	- 100 kPa vac, *whisp

Table M.4: Test conditions and settings for Timeline tests.

Test #	Date	ϕ	Approx. Pulse Time Delay (sec)	TC Tester Pulse Current (ma)	TC Tester Pulse Duration (ms)	CCD Camera FPS	TIME	Notes
636	8/21/98	1.2	0.100	12.2	5.4		10:50 AM	P_{fuel} = 20.5 in Hg, P_{tot} = 81.77psig, no record
637	8/21/98	1.2	0.100	12.2	5.4			no ignition, tighten fittings, no record
638	8/21/98	1.4	0.100	12.2	5.4	300		P_{fuel} = 19.0 in Hg, P_{tot} = 81.92psig, no record
639	8/24/98	1.2	0.100	14.7	5.5	300	12:10 PM	P_{fuel} = 20.5 in Hg, P_{tot} = 81.77psig, -99.5 kPA vac., too dark, no record
640	8/24/98	1.2	0.100	14.7	5.5	180	12:20 PM	-99.5 kPA vac., "boundary layer" starts before wire is activated,
641	8/24/98	1.2	0.100	14.7	5.5	120	12:30 PM	-99.5 kPa vac., no record
642	8/24/98	1.2	0.100	15	6	250	1:51 PM	-99.5 kPa vac., no record
643	8/24/98	1.4	0.100	15	6	250	2:55 PM	P_{fuel} = 18.0 in Hg, P_{tot} = 90.77psig, -99.5 kPA vac., slow flame, record
644	8/24/98	1.4	0.100	15	6	250	4:11 PM	-99.5 kPa vac.,timeline not discernable, no record
645	8/24/98	1.4	0.200	15	6	250	4:32 PM	-99.5 kPa vac.,timeline dissipates, no record
646	8/24/98	1.4	0.300	15	6	250	4:45 PM	-99.5 kPa vac.,wire activated after flame front passes, no record
647	8/24/98	1.4	0.100	15	6	250	4:53 PM	-99.5 kPa vac., no record
648	8/24/98	1.5	0.100	15	6	250	5:20 PM	P_{fuel} = 18.0 in Hg, P_{tot} = 84.13 psig, -99.5 kPA vac., no record
649	8/24/98	1.5	0.100	15	6	250	5:30 PM	-99.0 kPa vac., no record
650	8/24/98	1.5	0.100	15	6	250	5:35 PM	-99.0 kPa vac., no record
651	8/24/98	1.5	0.100	15	6	250	5:44 PM	-99.0 kPa vac., no record
652	8/26/98	1.4	0.100	10	5.5	300	11:01 AM	P_{fuel} = 19.0 in Hg, P_{tot} = 81.92 psig, - 99.5 kPa vac., test wire in duct.
653	8/26/98	1.4	0.100	13	5.5	300	11:19 AM	- 99.5 kPa vac., test wire does not ignite gas, no record
654	8/26/98	1.4	0.100	13	5.5	300	11:31 AM	- 99.5 kPa vac., wire affects flow, timeline diffuses quickly, record images
655	8/26/98	1.4	0.100	15	6	300	12:07 PM	- 99.5 kPa vac., TC wire break, event # 4004, record images, no timeline
656	8/26/98	1.4	0.100	15	6	400	1:52 PM	- 99.5 kPa vac., record images, no timeline
657	8/26/98	1.4	0.100	15	6	400	2:22 PM	- 99.5 kPa vac., similar to # 656, no record
658	8/26/98	1.4	0.100	15	6	400	2:28 PM	- 99.5 kPa vac., some hesitation in flame propagation, no record
659	8/26/98	1.4	0.100	15	6	400	2:35 PM	- 99.5 kPa vac., some hesitation, similar to #658, no record
660	9/2/98	1.4	0.007	15	6	300	12:22 PM	elect. time delay,P_{fuel} = 18.0 in Hg, P_{tot} = 90.77 psig, - 99.0 kPa vac.
661	9/2/98	1.4	0.027	15	6	300	12:31 PM	- 99.0 kPa vac., no record
662	9/2/98	1.4	0.033	15	6	300	4:12 PM	- 99.0 kPa vac., no record
663	9/2/98	1.4	0.070	15	6	300	4:23 PM	- 99.0 kPa vac., no record
664	9/2/98	1.4	0.100	15	6	300	4:32 PM	- 99.0 kPa vac., no record
665	9/2/98	1.4	0.006	15	6	300	5:00 PM	P_{fuel} = 18.0 in Hg, P_{tot} = 90.77 psig, - 98.5 kPa vac.,

Test #	Date	ϕ	Approx. Pulse Time Delay (sec)	TC Tester Pulse Current (ma)	TC Tester Pulse Duration (ms)	CCD Camera FPS	TIME	Notes
666	9/2/98	1.4	0.006	15	6	300	5:32 PM	- 98.5 kPa vac., no record
667	9/2/98	1.4	0.033	15	6	300	5:40 PM	- 98.5 kPa vac., no record
668	9/2/98	1.4	0.006	15	6	250	5:50 PM	- 98.5 kPa vac., no record
669	9/2/98	1.4	0.021	15	6	300	6:05 PM	- 98.5 kPa vac., no record
670	9/4/98	1.4	0.006	15	6	250	1:45 PM	P_{fuel} = 18.0 in Hg, P_{tot} = 90.77 psig, - 99.0 kPa vac., no record
671	9/4/98	1.4	0.006	15	6	250	1:54 PM	- 99.0 kPa vac., no record
672	9/4/98	1.4	0.012	15	6	250	2:05 PM	- 99.0 kPa vac., no record

Appendix N: Atmospheric Conditions for Tests

Table N.1: Atmospheric conditions for days during tests.

Date	Atmospheric Pressure (kPa)	Atmospheric Temperature (°C)	Relative Humidity (%)	Room Temperature (°C)	Notes
6/2/98	99.9	-	-	-	
6/3/98	100.5	-	62	18	
6/4/98	100.7	-	81	20	AM
6/4/98	100.7	-	62	21	PM
6/8/98	101.6	-	94	20	
6/9/98	102.2	-	100	21	
6/10/98	102.0	-	72	22	
6/11/98	101.8	-	82	23	
6/13/98	100.3	-	94	24	
6/14/98	100.2	-	51	26	
6/15/98	99.9	-	100	24	
6/16/98	100.0	-	88	25	AM
6/16/98	100.3	-	88	27	PM
6/17/98	100.8	-	88	23	
6/18/98	101.3	19	94	24	AM
6/18/98	101.3	24	74	26	PM
6/24/98	101.8	20	94	25	
6/25/98	101.6	21	88	27	
6/26/98	100.8	20	94	24	AM
6/26/98	100.6	22	88	26	PM
6/30/98	99.8	21	83	24	AM
6/30/98	99.6	21	88	26	PM
7/1/98	100.0	16	94	25	AM
7/1/98	100.5	18	77	25	PM
7/2/98	101.5	16	88	23	AM
7/2/98	101.6	20	73	-	PM
7/3/98	101.7	19	83	24	
7/4/98	101.3	20	88	25	AM
7/4/98	101.3	18	94	26	PM
7/5/98	101.9	20	64	25	
7/6/98	102.1	19	83	23	
7/7/98	101.8	19	83	26	
8/21/98	102.2	19	83	24	
8/24/98	100.4	23	83	24	
8/26/98	101.2	20	88	26	
9/2/98	100.3	20	83	26	

Notes:

Atmospheric temperature, pressure and relative humidity data obtained from ENVIRONMENT CANADA. Instrumentation located at Kingston Airport.

Room temperature data obtained from digital thermometer located in Rm. 222, McLaughlin Hall, Queen's University.

Appendix O: Results of Gas Analysis of Mixture Samples

Mixture samples were produced in the Gas Mixture Cart Apparatus. Samples were tested on a ROSEMOUNT model 400A gas analyzer. Dry Air and 99.5% propane were the reactants for the mixtures. A 1.06% propane in air certified gas mixture was used to calibrate the gas analyzer.

Table O.1 shows the calculated and actual fuel ratio results of the sample mixtures. Table O.2 shows the results of the analysis of the differences in the calculated and actual fuel gauge marks.

Desired Sample Equiv. ratio	Calculated Fuel Ratio (% by vol.)	Actual Fuel Ratio (% by vol.)	% dif	Actual Equiv. ratio
0.24	0.999	1.270	-21.4	0.306
0.80	3.253	3.683	-11.7	0.910
1.00	4.033	4.397	-8.3	1.094
1.20	4.801	5.077	-5.4	1.273
1.40	5.557	6.090	-8.8	1.543
1.60	6.301	6.805	-7.4	1.737

Table O.1 Results of the calculated and actual fuel ratios of the sample mixtures.

Fuel Gauge Mark Used to Produce Sample (in Hg)	Exact Fuel Gauge Mark as Back-calculated from Actual Fuel Ratio (in Hg)	P_{tot} (psig)	% dif
29.00	28.75	30.60	0.9
26.00	25.48	44.55	2.0
25.00	24.56	45.28	1.8
24.00	23.66	45.93	1.4
23.00	22.34	46.53	3.0
22.00	21.37	47.10	2.9

Table O.2 Results of the calculated and actual pressure gauge marks.

Appendix P: Results of Tests of Air Infiltration into FPD

Figure P.1 shows the results of tests of air infiltration into the FPD. Tests were performed over the course of the experimental program.

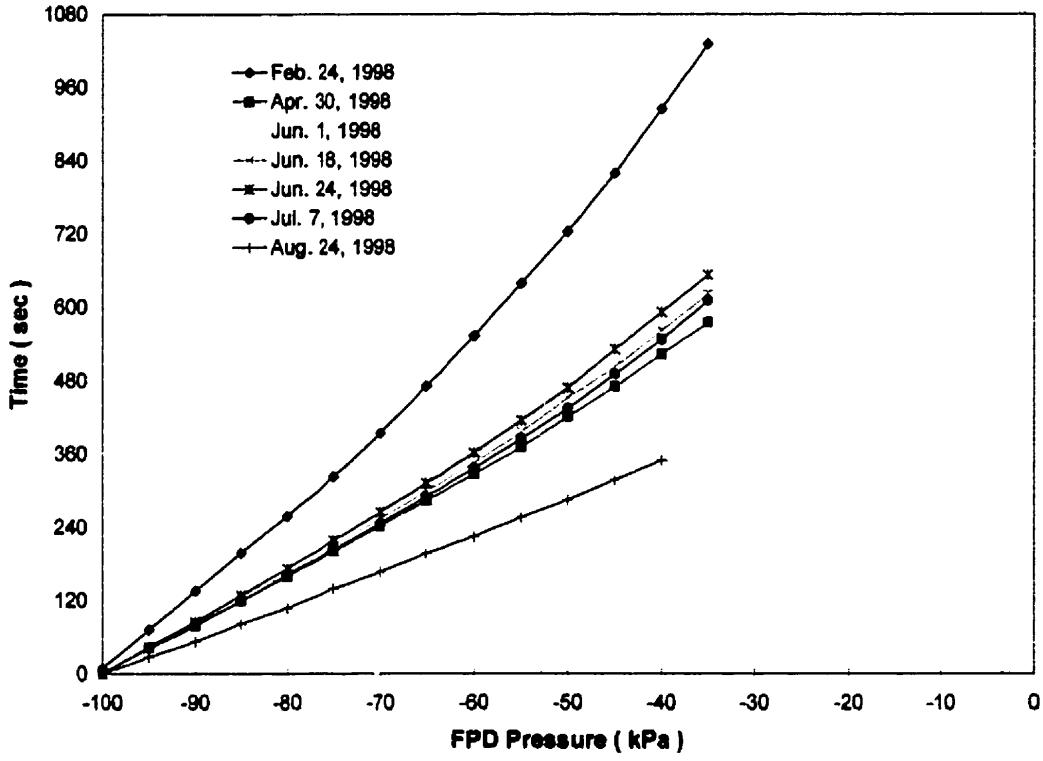

Fig. P.1 Results of air infiltration tests.

The Feb. 24, 1998 curve is representative of the rate of pressure drop in the FPD prior to finding and alleviating all discernible leaks. The Aug. 24, 1998 curve is the rate of pressure drop after installation of the thermocouple heater wires used for the timeline/Schlieren analysis. The remaining curves represent the rate of pressure drop in the FPD during the collection of the flame propagation velocity data.

Appendix Q: Results of ANOVA Study

The following tables show the results of the Analysis of Variance studies performed on the data for mixture compositions of ϕ =0.9, 1.2, and 1.6.

For each mixture composition, the velocity data was sorted according to trial number in each mixture batch. All the Trial 1 flame propagation velocities were collected to calculate average flame propagation velocities for each photodiode set location. This same procedure was used for the second, third, fourth and fifth trials for each batch.

$\phi = 0.9$

Average Flame Propagation Velocity (m/s)

Location	Trial 1	Trial 2	Trial 3	Trial 4	Trial 5
30 cm	26.32	4.85	4.53	5.76	0
53 cm	7.96	1.55	1.58	1.57	0
58 cm	0	32.89	38.86	38.36	0
83 cm	6.83	4.76	4.82	4.42	3.81
112 cm	10.94	4.65	6.84	3.33	3.20
117 cm	9.76	6.43	3.96	4.37	4.37
144 cm	22.35	11.20	12.78	4.72	24.43
151 cm	7.99	5.17	5.11	4.03	0
161 cm	3.97	3.82	3.48	4.13	0
169 cm	6.78	3.57	3.69	6.70	0
175 cm	7.55	3.52	6.00	7.55	0
181 cm	15.70	0	26.04	6.54	0
200 cm	2.98	0	0	0	0

Anova: Two-Factor Without Replication

SUMMARY	*Count*	*Sum*	*Average*	*Variance*
30 cm	5	41.464	8.297	106.468
53 cm	5	12.662	2.532	9.673
58 cm	5	110.117	22.023	409.669
83 cm	5	24.644	4.929	1.292
112 cm	5	28.959	5.792	10.427
117 cm	5	28.889	5.778	5.884
144 cm	5	75.482	15.096	67.014
151 cm	5	22.297	4.459	8.364
161 cm	5	15.403	3.081	3.022
169 cm	5	20.747	4.149	7.807
175 cm	5	24.620	4.924	10.294
181 cm	5	48.285	9.657	125.291
200 cm	5	2.983	0.597	1.780
Trial 1	13	129.139	9.934	56.030
Trial 2	13	82.412	6.339	71.925
Trial 3	13	117.700	9.054	123.557
Trial 4	13	91.512	7.039	92.772
Trial 5	13	35.807	2.754	45.170

ANOVA

Source of Variation	*SS*	*df*	*MS*	*F*	*P-value*	*F crit*
Rows	2012.226	12	167.6855	3.024509	0.00315	1.960121
Columns	406.7128	4	101.6782	[redacted]	0.137718	[redacted]
Error	2661.227	48	55.44223			
Total	5080.166	64				

Table Q.1 Results of ANOVA study for mixture composition $\phi = 0.9$.

$\phi = 1.2$

Average Flame Propagation Velocity (m/s)

Location	Trial 1	Trial 2	Trial 3	Trial 4	Trial 5
30 cm	4.59	18.96	10.89	14.45	13.41
53 cm	6.05	7.08	6.53	9.86	6.14
58 cm	13.33	15.28	9.95	6.72	6.60
83 cm	13.29	12.15	9.55	10.24	9.08
112 cm	6.23	12.06	13.85	11.79	8.47
117 cm	12.30	9.83	8.77	7.44	11.04
144 cm	8.33	11.94	6.37	8.20	7.77
151 cm	10.82	12.08	11.53	9.56	10.55
161 cm	5.65	5.56	5.91	5.90	6.30
169 cm	10.24	9.79	13.97	9.91	9.63
175 cm	12.06	13.44	12.73	17.93	16.02
181 cm	11.36	12.80	14.29	14.71	14.75
200 cm	8.65	7.79	7.28	7.91	8.40

Anova: Two-Factor Without Replication

SUMMARY	*Count*	*Sum*	*Average*	*Variance*
30 cm	5	62.307	12.461	27.878
53 cm	5	35.653	7.131	2.486
58 cm	5	51.879	10.376	15.149
83 cm	5	54.301	10.860	3.203
112 cm	5	52.406	10.481	9.424
117 cm	5	49.372	9.874	3.597
144 cm	5	42.618	8.524	4.251
151 cm	5	54.538	10.908	0.926
161 cm	5	29.326	5.865	0.084
169 cm	5	53.546	10.709	3.376
175 cm	5	72.188	14.438	6.068
181 cm	5	67.901	13.580	2.171
200 cm	5	40.033	8.007	0.292
Trial 1	13	122.892	9.453	9.392
Trial 2	13	148.753	11.443	12.584
Trial 3	13	131.624	10.125	9.203
Trial 4	13	134.620	10.355	12.370
Trial 5	13	128.182	9.860	10.211

ANOVA

Source of Variation	*SS*	*df*	*MS*	*F*	*P-value*	*F crit*
Rows	358.5686	12	29.88071	5.00528	2.59E-05	1.960121
Columns	29.0629	4	7.265725		0.315943	
Error	286.5522	48	5.969838			
Total	674.1837	64				

Table Q.2 Results of ANOVA study for mixture composition $\phi = 1.2$.

$\phi = 1.6$

Average Flame Propagation Velocity (m/s)

Location	Trial 1	Trial 2	Trial 3	Trial 4	Trial 5
30 cm	0	5.28	11.01	10.29	5.56
53 cm	3.05	3.10	3.09	3.00	2.72
58 cm	5.47	15.92	4.15	12.54	15.51
83 cm	6.12	8.03	7.91	9.84	9.18
112 cm	0	3.45	34.72	3.44	0
117 cm	2.64	14.29	3.04	14.79	4.94
144 cm	0	0	30.89	27.77	23.36
151 cm	2.05	3.14	3.51	4.05	8.68
161 cm	3.64	5.10	5.82	5.93	4.76
169 cm	4.59	6.40	5.03	6.36	8.29
175 cm	9.97	10.34	17.98	9.07	11.50
181 cm	6.53	17.87	13.73	8.47	8.72
200 cm	11.65	6.08	4.95	9.23	11.41

Anova: Two-Factor Without Replication

SUMMARY	*Count*	*Sum*	*Average*	*Variance*
30 cm	5	32.144	6.429	19.840
53 cm	5	14.953	2.991	0.025
58 cm	5	53.596	10.719	31.008
83 cm	5	41.075	8.215	2.023
112 cm	5	41.619	8.324	220.747
117 cm	5	39.699	7.940	37.082
144 cm	5	82.028	16.406	231.441
151 cm	5	21.437	4.287	6.568
161 cm	5	25.262	5.052	0.863
169 cm	5	30.673	6.135	2.095
175 cm	5	58.860	11.772	12.805
181 cm	5	55.320	11.064	21.561
200 cm	5	43.333	8.667	9.308
Trial 1	13	55.705	4.285	13.436
Trial 2	13	99.015	7.617	29.795
Trial 3	13	145.848	11.219	112.623
Trial 4	13	124.791	9.599	42.019
Trial 5	13	114.639	8.818	35.656

ANOVA

Source of Variation	*SS*	*df*	*MS*	*F*	*P-value*	*F crit*
Rows	772.7369	12	64.39474	1.522923	0.148862	1.960121
Columns	351.8485	4	87.96212	[redacted]	0.098015	[redacted]
Error	2029.615	48	42.28364			
Total	3154.2	64				

Table Q.3 Results of ANOVA study for mixture composition $\phi = 1.6$.